Title

Connecting the Pre-, Co-, and Post-Seismic Fault Behavior with High-Resolution Seismic Catalog, Statistics, and Source Spectra Analysis

Author

Zhou, Yijian

Publication Date

2024

UNIVERSITY OF CALIFORNIA
RIVERSIDE

Connecting the Pre-, Co-, and Post-Seismic Fault Behavior with High-Resolution Seismic Catalog, Statistics, and Source Spectra Analysis

A Dissertation submitted in partial satisfaction
of the requirements for the degree of

Doctor of Philosophy

in

Earth and Planetary Sciences

by

Yijian Zhou

September 2024

Dissertation Committee:
  Dr. Abhijit Ghosh, Chairperson
  Dr. David Oglesby
  Dr. Roby Douilly

The Dissertation of Yijian Zhou is approved:

Committee Chairperson

University of California, Riverside

Acknowledgments

A Ph.D. journey is rarely without its challenges, and mine has been no exception. However, I consider myself fortunate to have built confidence during my Master’s career, where I had nearly completed the development of my earthquake detection workflow (it was named as PALM and get published later). Yet, there was still one lingering bug in my relocation code, which was not resolved until the end of 2020. That was my first year as a Ph.D. student, and I was stuck in China due to the COVID-19 pandemic. At that time, I was also wrapping up my Master’s research, attempting to publish a case study on the Xiaojiang Fault Zone using PALM. After two rejections from JGR, we decided to publish the method separately: a decision that, in hindsight, proved to be the right one. I vividly recall the sense of accomplishment when I completed all the figures for the PALM paper while visiting Shanghai. It was the first time I truly felt independent in research, capable of seeing a project through from start to finish on my own. Even more rewarding was the positive reception PALM received, especially in China, where it has since become one of the most widely used earthquake cataloging workflows. For this reason, I would like to extend my first and heartfelt thanks to the reviewers who offered their critical comments along the way. Their constructive feedback, though difficult at times, has continually pushed me to create better works and grow as a researcher. This experience also taught me a valuable lesson: against external voices, the importance of accurately assessing my work and choosing either to confidently stand by it or to improve it, rather than becoming defensive or discouraged. This mindset has been so crucial to my growth that I find myself grateful for having naturally embraced it.

I would like to extend my second thanks to my advisor, Abhijit Ghosh, who offered me my only Ph.D. opportunity in 2019. Abhi is truly a unique scholar, always bringing fresh perspectives to our discussions. I am deeply grateful for the freedom he afforded me throughout my Ph.D. journey, allowing me to pursue my own curiosities rather than using me solely to further his own ideas. I am also deeply grateful to the rest of my committee members, David Oglesby and Roby Douilly. David, thank you for teaching the very first course I took at UCR. Our discussions on earthquake physics profoundly shaped my research perspectives. You have always been a reliable advisor, and your genuine kindness serves as a role model for me, showing me what it means to be a great teacher and mentor. Roby, thank you for being such a supportive advisor and friend. It has been incredibly encouraging to see you use my software in your research, and having you as a source of information during my job search has been invaluable. Moreover, the faculty in our EPS department have been incredibly supportive and inclusive, fostering an environment that has guided me through a journey of self-discovery and professional development. I would especially like to thank Heather Ford, who is exceptionally knowledgeable and takes education seriously, while also dedicates herself to community service, making academia a better place. Gareth Funning has not only been an outstanding scientist but also an approachable friend who genuinely cares about students' well-being and always offers valuable insights.

My third thanks go to my collaborators and peers, who have not only made things happen but also broadened my horizons. Among them, I would like to acknowledge my previous advisors, Shiyong Zhou and Han Yue, who continue to follow my progress and provide timely advice on my research career. I am also grateful to Lihua Fang, who granted me access to numerous seismic datasets from China, offered opportunities to co-advise his students, and consistently advertise my works. I would also like to thank Qingkai Kong, who offered me the opportunity to work as student summer intern at LLNL, where I gained not only decent pay but also valuable connections. Special thanks go to Longtan Wang and Hongyang Ding, students from PKU whom I mentored: their sharp thinking and willingness to tackle challenging technical problems, which are essential but not always highly recognized, have been invaluable. I also want to recognize the members of my discussion group: Chunmei Ren, Heng Luo, Baoning Wu, Binhao Wang, Hao Zhang, Shenjian Zhang, Zeyan Zhao, Naidan Yun, and many others, who have been constant sources of opinions, techniques, and support across various research fields. I am inspired by the examples set by early-career scientists like Wenyuan Fan, Junle Jiang, Weiqiang Zhu, Shujuan Mao, Jiaqi Li, Haoran Meng, Ruijia Wang, and Yifang Cheng, who have shaped my vision for the future. Lastly, I owe a special thanks to Zhigang Peng, an established scientist with whom I share similar research interests. Although we have not yet collaborated, he has provided constructive feedbacks as an Associate Editor and candid pieces of advice as a friend. Zhigang has truly been a guide, showing me how to survive and thrive in academia.

Finally, I would like to thank my peers and friends, who have made my Ph.D. life fun and colorful. I am grateful to the Hewett Club committee members, Chenyi Tu and Heather McCandless, as well as the former members Phillip Boan, Zhexing Li, Hsin-Yu Lee, and Adriana Rizzo, whose dedication and hard work made the fantastic speaker series possible. I also want to thank my travel buddies, Zhexing Li, Shouwei Li, Chenyi Tu, Hsin-Yu Lee, Xianglin Ren, and Yu-Chi Lee, who have been reliable friends both on and off campus. My heartfelt thanks go to my officemates and classmates: Evan Marschall, Shankho Niyogi, Beth Shallon, Norma Contreras, Karlee Rivera, Andre Mere, Binayak Parida, Li-Chieh Lin, Lupita Bravo, Celeste Hofstetter, Adam Margolis, as well as my former classmates Jordan Cortez and Andrew Birkey, who joined Zoom courses with me during the midnights while I was in China. My life has also been enriched by my badminton and tennis peers, including Shouwei, Hsin-Yu, Zhexing, Yu-Chi, and Anthony Dominguez at UCR; as well as Krittanon (Pond) Sirorattanakul, Shuo Cao, Guanli Wang, Ruolin Deng, Zitong (Jerry) Wang, Guannan Dong, and Mateo Acosta at Caltech. My tennis skills even served a practical purpose, as they helped me impressed Jean-Philippe, my future supervisor at Caltech, before he knew much about my research. My last special thanks go to my partner, Yuexin Li, who has been a part of all the activities mentioned above and so much more. For example, she proposed most of our lunch/dinner plans, travel plans, and shopping plans over the past years, pulling me away from my minimalist lifestyle.

The text of this dissertation, in part, is a reprint of the material as it appears in: Zhou et al. (2021b), Zhou et al. (2024), Ding et al. (2023), Zhou et al. (2022b) and Zhou et al. (2022a). The co-author Dr. Abhijit Ghosh listed in those publications supervised the research which forms the basis for this dissertation.

To my mother, Rongyan Li, and my father, Benhua Zhou.

ABSTRACT OF THE DISSERTATION

Connecting the Pre-, Co-, and Post-Seismic Fault Behavior with High-Resolution Seismic Catalog, Statistics, and Source Spectra Analysis

by

Yijian Zhou

Doctor of Philosophy, Graduate Program in Earth and Planetary Sciences
University of California, Riverside, September 2024
Dr. Abhijit Ghosh, Chairperson

The earthquake dynamics is determined by the preset conditions of fault zone. However, the fault properties at seismogenic depth are hard to constrain, especially for the preseismic phase, during which the fault motion is relatively slow. To better characterize the fault behavior at different stages, we utilize high-resolution seismic catalog to image fault geometry, make statistics on seismicity, and analyze the source spectra. Through case studies spanning continental faults, foreshock sequences, and large earthquakes, this dissertation underscores the pivotal role of microseismicity in illuminating the connection of fault behavior before, during, and after a large earthquake.

In the first part of the dissertation, I introduce two earthquake detection workflows: (1) PALM (Zhou et al., 2021b), which integrates phase Picking, Association, Location, and the Matched filter technique to achieve high-completeness detection for intense sequences; (2) LoSAR (Zhou et al., 2024), which Localized a Self-Attention RNN picker to build long-term catalogs with detectability comparable to that of matched filter. These tools offer a generalized approach for earthquake detection, making them suitable for seismic networks commonly deployed worldwide. Systematic tests demonstrate that our methods achieve higher detection completeness and accuracy compared to contemporary algorithms. Additionally, their high temporal stability and computational efficiency make them particularly helpful for studying fault zones and earthquake physics.

In the second part of the dissertation, I conducted case studies on fault zones and seismic sequences across diverse tectonic settings, including the East Anatolian Fault Zone in SE Turkey, Xiaojiang fault zone and Yangbi foreshock sequence in SE Tibet, and Ridgecrest-Coso region in California. Our findings revealed key seismicity characteristics related to large earthquakes: (1) Major fault zones often feature subsidiary structures that produce increased microseismicity and elevated b-values, potentially skewing overall b-value estimates; (2) Quiescence along major faults prior to large earthquakes is common, typically accompanied by low b-values, serving as indicators of high seismic hazard; (3) Seismicity depth distribution remains stable before and after large events, useful for inferring fault locking depth; and (4) Foreshock sequences can be more than a triggered cascade, with both inter-event stress transfer and aseismic process play important roles.

Contents

List of Figures .... **xiii**

List of Tables .... **xxii**

1 Introduction **1**

1.1 Development of Earthquake Detection Techniques 4

1.2 Structure of This Dissertation 7

2 Generalized Earthquake Detection and Location Architecture: Phase Picking, Association, Location, and Matched Filter (PALM) **8**

2.1 Introduction 8

2.2 Method and Data 12

2.2.1 Workflow of PALM 12

2.2.2 PAL: Picking, Association, and Location 12

2.2.3 MESS: Match, Expand, Shit, and Stack 19

2.3 Results and Discussions 23

2.3.1 Phase Picking Results 23

2.3.2 Detection Results 25

2.3.3 Location Results 28

2.4 Conclusions 31

3 Construction of Long-term Seismic Catalog with Deep Learning: A Workflow for Localized Self-Attention RNN (LoSAR) **33**

3.1 Introduction 33

3.2 Methods 35

3.2.1 Overview of the LoSAR Workflow 35

3.2.2 Self-Attention RNN (SAR) Model for Phase Picking 40

3.3 Comparison of Cataloging Workflows 45

3.3.1 Case 1: Ridgecrest-Coso Region (2008-2019/07) 46

3.3.2 Case 2: East Anatolian Fault Zone (2020-2023/04) 55

3.4 Conclusions 67

4 High-Resolution Seismicity Imaging and Characterization of Fault Behavior 68

4.1 Introduction 68

4.2 Early Aftershocks of the 2023 Kahramanmaraş Earthquake Doublet 70

4.3 Erkenek-Pütürge Fault Segment (EPF) of EAFZ 83

4.4 2019 Ridgecrest-Ruptured Faults 88

4.5 Microseismicity Along Xiaojiang Fault Zone (SE Tibetan Plateau) 93

4.6 General Characteristics of Microseismicity 118

5 Untangling Foreshock Triggering Mechanisms with Source Spectra Analysis and Coulomb Stress Modeling 120

5.1 Introduction 120

5.2 Data and Methods 123

5.2.1 Seismic Catalog 123

5.2.2 Spectral Ratio Analysis 124

5.2.3 Multi-Point-Source Moment Tensor Inversion 127

5.3 Results and Discussion 128

5.3.1 Rupture Directivity and Source Parameters 128

5.3.2 Analysis of the Largest Foreshock 131

5.3.3 Construction of Fault Model 133

5.3.4 Coulomb Stress Evolution 138

5.3.5 Interpretation of Inter-event Triggering 141

5.3.6 Implications on Foreshock Triggering Models 151

5.4 Conclusions 153

6 Conclusions and Perspectives for Future Work 155

6.1 Remaining Problems in Earthquake Detection 156

6.2 Seismic Source Parameters 157

6.3 Slow Earthquakes 158

References 161

List of Figures

2.1 Workflow of PALM. Input and output results are denoted by squares. Detection and location operations are plotted in ellipse patches. Modules for detection and location purpose are plotted in blue and orange, respectively. 11

2.2 Algorithm of PAL picker. (a) Detection of P arrival. Z-channel waveform (velocity record) and STA/LTA function are plotted in black lines. Trigger level and time are plotted by dashed horizontal gray line and yellow star, respectively. The P phase window is bounded by a gray dashed rectangle. (b) Picking of P-wave. Red dashed and solid lines plot initial and corrected (final) P picks, respectively. (c) Detection of S arrival. Original and PCA filtered horizontal (E-N) channel amplitude are plotted in the top and bottom panels. The time of maximum filtered amplitude is marked by a yellow star. The S phase window is marked as a gray dashed rectangle and gray double arrow. The red double arrow marks the first half of the window between P and the yellow star (i.e. P window). (d) Picking of S-wave. The labels are identical as (b). (e) Detailed illustration of S picking algorithm. Characteristic functions are plotted in black lines. The earliest and latest boundary derived from STA/LTA and long-window Kurtosis picker are marked by gray dashed lines. The initial and final S-pick are marked by red dashed and solid lines. 13

2.3 Phase association process. (a) Temporal association. E-channel waveforms at different stations are plotted in different colors. Vertical solid gray lines mark the picked P- and S-arrival times. Yellow stars denote the estimated origin times. (b) Spatial association. Red triangles show the locations of seismic stations. Circles are centered at the stations with corresponding epicentral distances estimated from the picked P- and S-arrival times. The yellow stars denote the estimated epicenter. 16

2.4 Algorithm of MESS. (a) Matched filter. Template and raw waveforms are plotted in red and gray lines, respectively. The resulting cross-correlations are plotted in black. (b) Stacking strategy. Original and expanded cross-correlations are plotted in gray and black lines, respectively. 18

2.5 (a) Phase picking performance of PAL, STA/LTA, and Kurtosis algorithms are evaluated as deviation from the SCSN picks and plotted as histograms using slash-filled, gray-filled, and blank bars, respectively. Detection accuracy is defined as the ratio of picks with an absolute deviation of 0.5s. Phase picking precision is presented by mean ± std (sec) value for the detected phases. (b) P-wave detection accuracy and picking precision for different window lengths. Solid lines with dot, triangle, and square marker denote STA/LTA with long window length set to 2s, 4s, and 6s, respectively. Dashed line with circle marker denotes picking result by Kurtosis picker. In the upper panel, blue and red lines plot phase detection accuracy assuming a maximum picking deviation (dt) of 0.5s and 0.2s, respectively. In the lower panel, blue and red lines plot mean and std values of picking deviation, respectively. Adopted parameters are highlighted by yellow-filled dots. (c) Same as (b), but for S pick. 22

2.6 (a) Comparison of frequency magnitude distribution (FMD). PAL and SCSN catalogs are plotted in yellow and blue symbols, respectively. Cumulated and non-cumulative distribution are plotted as circles and triangles, respectively. (b) Same as (a) but for the MFT detected catalogs: MESS, Shelly (2020), and Ross et al. (2020), which are plotted as red, green, and cyan symbols respectively. (c) Seismic rate comparison. Results from different catalogs are plotted in the same colors as (a-b). Significant events (M>4.5) are marked by yellow asterisks. 25

2.7 Location comparison for template events. (a), (b) and (c) plot locations of catalog obtained by PAL+HypoInverse, PAL+HypoDD, and SCSN catalog, respectively. Earthquakes are plotted in dots color-coded by their hypocentral depths and the marker size scaled with magnitude. Cross-sections are plotted in blue dashed squares. Profiles of catalog depth distribution along profile OO' are denoted as blue dots. 27

2.8 Location comparison for MFT catalogs. Markers have the same meaning as Figure 2.7. 28

3.1 The Localized Self-Attention RNN (LoSAR) workflow. The blue and yellow modules denote the detection and location algorithms, respectively. PAL refers to an rule-based cataloging workflow developed by Zhou et al. (2021b); SAR refers to Self-Attention RNN phase picking model developed in this study. CT/dt.ct and CC/dt.cc refer to catalog-based and cross-correlation-based differential travel time, following the hypoDD terminology. The ph2dt_cc module is a CC-based differential time calculation method developed in this study. 35

3.2 Demonstration of differential travel time measurement with waveform cross-correlation. The two events are named as "detection" and "template", travel time and differential travel time are abbreviated as "tt" and "dt", respectively. 37

3.3 The SAR model structure and training sample slicing strategy. (a) SAR model structure. The filtered 3-channel seismogram is plotted in black curves, and the red vertical lines mark the P&S arrival times. The data processing units are denoted by: xi for the i^{th} input time step; Gf and Gb for forward and backward Grated Recurrent Unit (GRU); y_i for the i^{th} output of the GRU RNN; Q/K/V for Query, Key, and Value input in the multi-head self-attention terminology, and they are all set as the RNN output (i.e. y) in the case of self-attention; "Linear" for fully-connected layer; "MatMul" for matrix multiplication; "Concat" for concatenation; z_i for the i^{th} output of the multi-head self-attention layer; "N/P/S prob" for Noise, P wave, and S wave prediction probability (b) Training sample slice strategy. Blue, red and pink waveforms for negative, positive, and augmented positive samples, respectively. 41

3.4 Study region and catalog comparison for Case 1: Ridgecrest-Coso (2008-2019/07). (a-b) plot the LoSAR catalog generated in this study, with preseismic period and aftershock period shown separately. Seismicity is plotted as dots that have its depth denoted by color. Active faults are plotted as black lines; surface rupture caused by the 2019 Ridgecrest earthquakes are marked by white lines. The area of Coso Geothermal Field (CGF) is marked by a red circle. The insets show location of the study area in a larger scale, with the San Andreas Fault (SAF) and Eastern California Shear Zone (ECSZ) marked. (c-d) are the same as (a-b), but for the relocated SCSN catalog (Hauksson et al., 2012). The blue box in (b) & (d) marks the location coverage in Figure 3.5a-b. 45

3.5 Comparison of FMD and magnitude-time sequence. The blue, green, and red color denote the SCSN catalog, the QTM catalog, and the LoSAR catalog in this study, respectively. (a-c) plot the FMD comparison for the total aftershock detections, well located aftershocks, and the preseismic period (2008-2017), respectively. The dots and triangles denote cumulative and non-cumulative distribution in FMD. (d-f) plot the magnitude-time comparisons for the preseismic period (2008-2017). The thick black lines denote the magnitude of completeness in the current panel, and the colored dash lines plot that for two other catalogs. 51

3.6 Study region and catalog comparison for Case 2: EAFZ (2020-2023/04). (a-b) plot the LoSAR catalog generated in this study, with preseismic period and aftershock period shown separately. Seismicity are dots that have its depth denoted by color. Active faults are plotted as black lines; responsible faults for the 2023 earthquake doublet are marked by red lines. The insets show location of the study area in a larger scale. (c-d) are the same as (a-b), but for the relocated AFAD catalog by Lomax (2023). 55

3.7 Comparison of location results with different association algorithms for RC-Coso preseismic period (2008-2019/06). (a-c) plot the map-view distribution of the hypoInverse location results, where the input phase files are generated by PhaseNet (PHN) + PAL associator, PHN + GaMMA (all picks), and PHN + GaMMA (only paired P&S picks), respectively. 59

3.8 Comparison of location results with different association algorithms for EAF pre-postseismic period (2020-2023/01). (a-f) plot the map-view distribution of the hypoInverse location results, where the input phase files are generated by PhaseNet (PHN) + PAL associator, PHN + GaMMA (all picks), and PHN + GaMMA (only paired P&S picks), respectively. (a-c) plot the preseismic period (2020-2023/01) and (d-f) plot the aftershock period (2023/02-04). 61

3.9 Comparison of phase picking and association performance. The blue, cyan, orange, and red markers denote the results by different pickers and associators. (a & e) plot the number of picks. The P & S picks are marked by darker and lighter colors. The paired P&S picks are filled by color; (b & f) plot the number of associated picks; (c & g) plot the FMD comparison, where circles and triangles denote cumulative and non-cumulative numbers, respectively; (d & h) plot the number of unassociated picks on each station. (a-d) and (e-h) plot the Case 1 (Ridgecrest-Coso) and Case 2 (EAFZ), respectively. 62

4.1 Comparison of cataloging results. (a-b) plot the overall distribution of aftershocks by the PALM method and Lomax (2023), respectively. Events are plotted as dots with the color coded by depth, and size proportional to magnitude. Inset in (a) shows a regional tectonic overview, with the red rectangle indicating the study area. Major plate-boundary faults are abbreviated as EAF: Eastern Anatolian Fault, NAF: Northern Anatolian Fault, and DSF: Dead Sea Fault. Inset in (b) shows the depth distribution of the PALM catalog, Lomax (2023), and AFAD. (c-d) show a zoom-in view of the PALM catalog around the two mainshocks. The epicenter of mainshocks obtained by this study, Lomax (2023), and

AFAD are plotted by red star, green circle, and blue rectangle, respectively. The solid purple lines denote the fault traces from the GEM Global Active Faults Database; the solid black lines are the surface ruptures of activated mapped faults provided by USGS; the dashed lines in (c) are the unmapped faults interpreted along with microseismicity. The transparent boxes in (c) plot the interpreted fault planes with different dip angles. 73

4.2 Relation of hypocentral distances and travel-time. (a-b) display the hypocentral distance and time relation according to the initial hypocenters obtained by the PAL and AFAD catalogs, respectively. The red and blue dots represent the P- wave and the S- wave phases, respectively. 74

4.3 Detailed aftershock distribution and interpretation of fault structure. (a) shows the map-view of aftershocks by the PALM method, events in which are plotted as dots with size proportional to magnitude. Orange and crimson dots in each filled area are projected to the gray rectangle's southeast side that is subparallel to the EAF and the SF, respectively, to get the along-fault profiles. Dots in each dashed rectangle are projected to the longer side of the rectangle to get the normal-fault profiles. Events not included in the filled rectangles are plotted as gray. Black stars represent the epicenter of M>6 events, and the same projection strategy as dots is applied to stars. The slender colored rectangle is the surface projection of the USGS-NEIC finite fault model. The solid purple lines are the same as that in Figure 4.1. Focal mechanism solutions for the M>6 events are from GCMT. Inset in (a) shows the depth distribution of events by the PALM method along the SF and EAF. The top three panels in (b) show the normal-fault profiles resulting from (a). Lines indicate the fault dip inferred from the aftershock distribution. The bottom panel of (b) and (c) show the along-fault profiles for the SF and EAF, respectively, in which the USGS-NEIC finite fault model for the two mainshocks are also projected. The convention of the color-coded dots in (b-c) is the same as that in (a). 76

4.4 Temporal behavior of aftershocks. (a) Left panel shows the magnitude-time sequence of the PALM and AFAD catalogs. Vertical solid lines divide major evolution periods. The right panel shows the FMD comparison. (b) plots the map-view event distribution of the PALM catalog during T1, T2, and T3. Endpoints of along-fault profiles shown in Figure 4.2a are also marked. The solid purple lines are the same as that in Figure 4.1a. (c) shows the temporal evolution in seismicity along the profiles of the EAF and the SF shown in Figure 4.3a. The time is calculated from the original time of M1, and the distance is calculated along the southeast side longer side of the filled rectangles in Figure 4.3a. Note that time is displayed in logarithmic scale. The convention of the color-coded dots is the same as that in Figure 4.3a. Horizontal solid lines represent the time separation same as that in (a). 79

4.5 Seismicity and fault geometry interpretation for the Erkenek-Pütürge fault segment (EPF) of EAFZ. (a-b) plot the map-view distribution of postseismic (2023/02-04) and preseismic period (2020-2023/01) seismicity. The events in current panel / time period are color coded by the depth, and the seismicity in the other time period is plotted as white dots in the bottom. (c) plot the fault-normal cross-sections. The 2023 aftershocks and preseismic events are denoted in blue and green, respectively. The interpreted fault dip is marked as black lines. (d) plot the along-strike cross-section. The coseismic slip of the 2023 Mw 7.8 obtained by Ren et al. (2024) is plotted in orange-red contours, the coseismic slip and afterslip slip of the 2020 Mw 6.8 obtained by Cakir et al. (2023) are plotted as orange and black contours, respectively. 82

4.6 B-value mapping and detailed fault structure interpretation of the EPF area. (a-b) B-value mapping results with the LoSAR catalog and that by Lomax (2023) during the preseismic period. The active faults and 2023-ruptured faults are plotted by gray and orange-red lines, respectively. The red box marks the spatial coverage of (c-d). (c-d) provide a zoom-in plot for part of the EPF. (c) plot the distribution of CC-relocated LoSAR catalog. The white solid and dashed lines show interpreted faults. (d) plot the focal mechanism solutions of Mw>4 events during 2020-2023/04 from AFAD. 85

4.7 Seismicity on the Ridgecrest faulting area before and after the 2019 earthquakes. (a-b) plot the preseismic period of relocated SCSN catalog (Hauksson et al., 2012) and LoSAR catalog in this study, respectively, and (c) for the LoSAR catalog aftershock period. Note that the dot size and transparency for the preseismic (a-b) and aftershock (c) period are set differently, because of the very different seismicity rate. In the map view plots (upper panels), the seismicity is plotted as dots that have its color denoting the depth and size varies with the magnitude. The active faults are plotted as black lines; the surface ruptures are marked by white lines. The reference points and spatial coverage of the along-fault cross-section is marked by blue dashed rectangle. The hollow black stars denote the largest foreshock and the mainshock of the 2019 Ridgecrest sequence. In the cross-sections (lower panels), the rupture model by Yue et al. (2021b) is plotted as different shades of red. The Garlock Fault (GF) on the surface and seismicity-interpreted depth extension is marked by red lines. The black lines are the imaged cross faults by seismicity. 86

4.8 Distribution of Ridgecrest seismicity before the 2019 mainshock. (a-c) plot the relocated SCSN catalog, well-located QTM catalog, and relocated LoSAR catalog, respectively. 87

4.9 Focal mechanism solutions (FMS) for the Ridgecrest-Coso preseismic period (2008-2019/06). The red beach balls and dark blue dots denote the M>2 FMSs from Cheng et al. (2023) and relocated LoSAR catalog present in this study. 88

4.10 Comparison of b-value mapping results for the RC-Coso region during preseismic period with different seismic catalogs. (a-c) plot the b-value mapping results with the relocated SCSN catalog (Hauksson et al., 2012), the QTM catalog (Ross et al., 2019b), and the LoSAR catalog in this study, respectively. The active faults and surface ruptures are plotted by gray and black lines, respectively. The M>5 earthquakes after 1946 are marked by yellow stars. The area of Coso Geothermal Field (CGF) is marked by red circle in the map view and by horizontal line in the cross section. The coseismic slip by Yue et al. (2021b) is plotted as black contours in the cross section. Annotations in the map view include: R_{slice}, the slicing radius for each grid in b-value calculation; N_{min}, the minimum number of events above the complete magnitude to calculate b-value; MC, the magnitude of completeness. 90

4.11 (a) Tectonic setting of the Sichuan-Yunnan block. Active tectonic blocks are marked by colored patches. The horizontal movement of the blocks is indicated by gray arrows. Fault traces are plotted in gray lines. The Xianshuihe Fault (XSH Ft.), Anninghe-Zemuhe Fault (AZ Ft.), and Xiaojiang Fault (XJ Ft.) are highlighted by black lines. The focal spheres are solutions in the region since 1976 from the GCMT catalog. The black triangles denote broadband seismic stations used in this study (see Figure 2 for details). In the inset map, the red box indicates the study region. Blue lines show boundaries of tectonic blocks, while plate boundaries are marked by orange lines with ticks. (b) Seismicity and b-value of the study region. The background color shows the b-value, whereas red dots are epicenters of seismic events of magnitude 1.5-7.0 during 2016-2019 from the regional catalog of CSES. 92

4.12 Seismic stations along the XJF used in this study. Blue triangles denote broadband stations; orange squares denote daily GPS stations. Black dots are the detected micro-seismic events. Historical earthquakes of magnitudes M ≥ 6 are denoted by red stars. Focal mechanism solutions from the GCMT catalog since 1976 and the CSES catalog since 2009 are shown by gray and black focal spheres, respectively. Black lines depict active faults, and that of XJF are thickened. 95

4.13 Detection and location result. (a) and (b) plot the CSES regional catalog during 2009 to 2019 and PALM catalog during 2016 to 2019, respectively. Earthquake epicenters are shown in dots that colored by depths. The black lines depict fault traces. Three areas (one on and off the major fault) are marked by red, blue and green dashed rectangles, whose depth distribution and frequency-magnitude distribution are plot in (c) and (d) respectively. 98

4.14 Seismicity pattern around XJF. (a) and (b) Map view of shallow (0-10km) and deep (10-30km) seismicity, respectively. Events are shown in dots colored by depths. Gray lines are fault traces. Blue rectangular and OO' mark the endpoints of the overall cross-section; Green frames from AA' to GG' mark the endpoints of the local cross-sections in (d). (c) and (d) plots overall and local cross-sections, where microseismic events are plotted as black and blue dots, respectively. Inter-seismic coupling ratio (ISC) from Li et al. (2021a) is color-coded in (c). Vertical lines in (d) mark the dipping direction of the major fault. Fault zone conductors detected by Li et al. (2019) are marked by brown patches in (d). 100

4.15 Distribution of repeating earthquakes. The left panel (a) is an overview of the whole region, and the right panels (b) show zoom-in plots of repeater distributions in the dashed boxes in (a). Locations of repeating sequences with more than 10 events are denoted by open stars. The colored events in (b) are clusters separated by waveform similarity analysis. 103

4.16 Repeating sequence analysis. (a) Repeating sequences. Horizontal and vertical axes are origin time and sequence index, respectively. Note that the sequence indexes are sorted by latitude. Gray dots denote repeating events, with the size proportional to the magnitude. (b) Periodicity of sequence. Histogram plots the number of sequences with respect to the COV value of recurrence interval. Gray dots mark the sequence duration and its COV value. (c) Histogram for the magnitude distribution of repeaters. 105

4.17 Temporal evolution of seismic rate in different area. The black and colored lines plot total and clustered seismic rate, with the color of different clusters the same as Figure 4.15. Gray patches mark the spontaneous active period of micro-seismicity in different clusters. . 107

4.18 (a) Location of three GPS stations are denoted as green triangles. Earthquakes in background and off-fault structures are plotted as gray and red dots, respectively. The arrows mark the deformation of block. (b) E, N and Vertical component of relative displacement across the XJF and off-fault branches are plotted as gray and blue curves, respectively. (c) E, N and V component of relative velocity across the off-fault structures are plotted as blue curves in each panel. Smoother seismicity rate in area A are plotted as red curves. 108

4.19 Maps of (a) b-value, (b) b-value uncertainty, and (c) magnitude of completeness Mc. Events and fault traces are plotted in gray dots and black lines, respectively. Red stars mark the epicenters of the 1733 and 1833 historical earthquakes. 110

4.20 Conceptual model of XJF. Crust with different depth and different properties are separated by color. Faults traces and planes are plotted in black lines and gray patches. White dots plot characteristic seismic clusters. Black arrows mark the block motion. 113

5.1 Tectonic background and foreshock sequence. (a) Tectonic background of the Yangbi earthquake. In the main plot, fault traces are plotted by black lines, and come from Wang et al. (2021a). The interseismic background seismicity and Yangbi seismic sequence are plotted by blue and orange dots respectively, with the focal depth color-coded. Focal mechanism of GCMT since 1976 is plotted by black beachballs. Blue triangles mark the broadband stations. In the insert plot, the plate boundary and active block boundary are plotted by orange and blue lines, respectively. Main blocks, i.e. Qiangtang block (QT), Bayan Har block (BH), Chuandian block (CD), and South China block (SC), are noted, with their relative motion marked. (b) The Yangbi foreshock sequence. The study time period is divided by the major foreshocks (f1, f2, and F1) and the mainshock (M). Seismic catalog comes from Zhou et al. (2021a). The focal mechanisms of the mainshock and largest foreshocks are determined by multi-point-source inversion, and that of the first two smaller foreshocks comes from Yang et al. (2021). 119

5.2 Spectral ratio comparison for directivity determination. (a), (b), and (c) plot the spectral ratio comparison of the foreshock f1, f2, and F1, respectively. The first and second line show the comparison along fault-parallel and fault-normal direction. The station used for the comparison is shown in the inset, with their color represent the quadrant. Each line represents a spectral ratio observation on one station, with the color mark its azimuthal quadrant. The frequency bands with significant contrasts are highlighted by gray patches. 127

5.3 Spectral ratio analysis. (a), (b), and (c) plot the spectral ratio analysis of the foreshock f1, f2, and F1, respectively. The black lines, solid red lines, and dashed red lines denote the spectral ratio on single stations, stacked spectral ratio, and the best fit to Boatwright model to the stacked spectral ratio. The vertical gray line marks the estimated corner frequency. 128

5.4 Multi-point-source (MPS) inversion for the largest foreshock (F1) and its two immediate aftershocks (F2 & F3). (a) Waveform of F1, F2, and F3. The Z-channel waveform is band-pass filtered to 1-20Hz, and is aligned with the initial P wave arrival of F1. The onset of P waves of F1 is marked by vertical red line, and that of the second subevent of F1 (i.e. F1_2) is marked by dashed red line. The earthquake signal of F1-3 are highlighted in blue. The relative remote stations with the S wave of F1 and P wave of F2 overlapped are marked in red. (b) The MPS inversion result of F1-3. The subevents of the whole sequence are marked in blue, with their centroid location distributed on the preset mesh grids. Note that F1 is separated by two subevents, and the summarized moment tensor plot in red, with a comparison with that by GCMT plot in light-red. 129

5.5 Spectral ratio analysis of F2. (a) & (b) are two sets of spectral ratio comparisons along fault-parallel and fault-normal direction, respectively. The dash lines are the stacked and averaged spectral ratio. (c) plots the stacked and fitted spectral ratio. The markers have the same meaning as in Figure 5.3. (d) shows the station distribution used in this analysis. Seismic stations are plotted in triangles, fault traces are plotted in black lines, and reference fault-parallel and fault-normal trend are marked by red dashed lines. 130

5.6 Fault geometry interpretation and MPS inversion of the mainshock. (a) Interpretation of fault geometry. The solid black lines are the mapped fault, the dashed black line is the unmapped major fault, and the dashed dark-blue lines are the unmapped conjugate faults. The blue beachballs mark the MPS-inversed focal mechanisms of the foreshock F1-3, and the hollow black stars mark their epicenters. (b) Simplified fault geometry and MPS inversion result of the mainshock. The solid red and blue line marks the simplified fault trace associated with the mainshock and the largest foreshock. The red beachballs mark the focal mechanisms of the mainshock subevents, and their centroid locations are marked by hollow stars. 133

5.7 Distribution of seismic events and finite rupture model. (a) Map view, (b) cross-section along strike, and (c) fault-normal cross-sections. Events in different periods are denoted by colors. Four major foreshocks are marked by hollow stars. The simplified faults associated with the mainshock (Fault_M) and the largest foreshock (Fault_F) are denoted as thick black lines. The rupture length and area are marked by color line and patch in (a) and (b). The coseismic slip contour by Wang et al. (2022a) is plotted in (b). Repeating earthquakes pre- and post-mainshock is plotted in solid squares and hollow diamonds, respectively. 135

5.8 Evolution of Coulomb stress change. (a), (b), and (c) plot cumulated Coulomb stress change after f1, after f2, and after F1, respectively. The hypocenters are marked by stars. The upper and lower panels plot the map view with Fault_M as the receiver fault, and the cross-sections on Fault_M and Fault_F. Contours of 0.02 MPa and 0.05 MPa Coulomb stress increase are marked by dashed lines. 137

5.9 Coulomb stress change induced by f2 with Fault_F as the receiver fault at a depth of 5 km. 138

5.10 Coulomb stress evolution with F1 as a purely uni-lateral rupture. The symbols have the same meaning as in Figure 5.8. 139

5.11 Repeater detection. (a-c) Repeater waveforms. The nearest four stations are plotted, with the Z-channel seismograms band-pass filtered to 1-20 Hz. (d-e) Relationship between CC values and frequency band. The CC values between each event pairs are calculated under different frequency band. The low corner frequency is kept as 1 Hz, with the high corner frequency ranges from 10-20 Hz. 141

5.12 Migration pattern and interpretation of triggering mechanism. (a-b) plot seismicity migration along strike, with linear time scale. The reference points OO’ are the same as in Figure 5.7. The extension of different asperities and their rupture directivity are marked by vertical lines with arrow. (c-d) plot aftershock evolution after f1 and f2, with the time plot in log-scale. (e) summarize our interpretation of foreshock mechanism. (f) plot fault-parallel cross-section, with the rough boundary of asperity delineated by solid lines. The coseismic slip model by Wang et al. (2022a) is plotted by gray dashed contours and color patches. Repeating earthquakes pre-, and post-mainshock are plotted in solid squares and hollow diamonds, respectively. 144

List of Tables

5.1 Comparison with published results on Yangbi foreshock mechanisms..............146

Chapter 1

Introduction

Earthquakes represent one of the most severe natural hazards, leading to significant economic losses and numerous casualties. Unfortunately, accurately predicting earthquakes is widely regarded as impossible due to the chaotic nature of fault systems (Geller et al., 1997). Nevertheless, seismic hazard can still be assessed by characterizing fault structures, slip behaviors, and stress states (Kaneko et al., 2010; Ader et al., 2012; Ulrich et al., 2019). Additionally, earthquake forecasting may be possible by identifying precursory signals (e.g. Kato et al., 2012; Bouchon et al., 2013; Bletery and Nocquet, 2023). Observing small earthquakes has proven beneficial in these efforts for several reasons: (1) small earthquakes occur much more frequently than large ones, allowing for direct imaging of fault geometry at depth (e.g. Waldhauser and Ellsworth, 2002; Shelly and Hardebeck, 2019); (2) different fault slip behaviors and stress levels can be inferred from characteristics of microseismicity, such as its magnitude distribution (e.g. Tormann et al., 2013; Nanjo, 2020); (3) small earthquakes may act as potential precursors to larger events (e.g. Bouchon et al., 2013; Trugman and Ross, 2019). Thus, constructing high-resolution seismic catalogs with high detectability and location precision is fundamental to these analyses.

In recent years, earthquake detection techniques have advanced rapidly alongside the increasing quantity and quality of data, largely driven by the growth of deep learning. My Ph.D. career coincides with this period of rapid progress in AI-driven seismology

(Mousavi and Beroza, 2022). My research encompasses two main areas: technically, the development of earthquake cataloging algorithms; and scientifically, the use of seismicity to investigate fault zone dynamics and earthquake physics. In this dissertation, I will present my research on generalized workflows for constructing high-quality seismic catalogs and how these catalogs provide valuable insights into fault behavior and earthquake mechanics.

1.1 Development of Earthquake Detection Techniques

Traditionally, earthquakes have been routinely monitored using energy-based algorithms, such as short-term average over long-term average (STA/LTA), supplemented by manual inspections for complete detection and quality control. Since STA/LTA does not capture the features of the whole waveform, a relatively high triggering threshold is required to reduce false detections, which limits its detectability. For example, the Southern California Seismic Network (SCSN) produces its routine catalogs in this manner (Hutton et al., 2010). Due to its semi-automated nature, the SCSN catalog suffers from inconsistent detection completeness through time, which potentially affects statistical studies based on it. One strategy to enhance the routine catalog is to treat them as templates and utilize waveform cross-correlation to find similar events from continuous data, a method known as template matching or matched filter technique (MFT). The MFT approach is particularly effective for intense sequences, such as aftershocks and seismic swarm, where researchers usually focus on a short period of time to capture faulting complexity (e.g. Shelly et al., 2016; Ross et al., 2017b). However, the performance of MFT depends heavily on the quality of the templates, and routine catalogs are not always available. Additionally, large-scale waveform cross-correlation is computationally expensive, particularly when the number of templates is large, and the time period is extended. These limitations make MFT a less generalizable approach.

To address these challenges, I developed two workflows for detecting earthquakes across various scenarios: (1) PALM (Zhou et al., 2021b), which integrates phase Picking, Association, Location, and the Matched filter technique to achieve high-completeness detection for intense sequences; (2) LoSAR (Zhou et al., 2024), which Localized a Self-Attention RNN picker to build long-term catalogs with detectability comparable to that of matched filter. Zhou et al. (2021b) introduced a generalized earthquake detection workflow, referred to as PAL (Picking, Association, and Location), which combines several rule-based algorithms to enhance the picking and association performance. Unlike traditional pickers that cannot discriminate P and S wave arrivals, PAL picks P and S waves in pairs and significantly improves S-picking accuracy using a hybrid STA/LTA-Kurtosis algorithm. This manner of phase picking also make the PAL associator efficient. Systematic tests demonstrate that the PAL associator is considerably more scalable than other machine learning-based algorithms (Zhou et al., 2024). In terms of event detection ability, our tests on the 2019 Ridgecrest aftershock sequence show that PAL realized about twice the number of detections compared to the SCSN catalog, with significantly improved temporal consistency (Zhou et al., 2021b). This reliable detection forms the foundation for the subsequent matched filter process, making PALM adaptable to various station distributions and tectonic settings (e.g. Lu et al., 2021; Zhou et al., 2021a; Zhou et al., 2022b; Ding et al., 2023).

Instead of treating PAL detections as templates for MFT, LoSAR employs these detections as local training samples to optimize the neural network (Zhou et al., 2024). This approach is motivated by the fact that both STA/LTA and deep learning is efficient in handling big data, but deep learning methods show much higher detection ability and picking precision (e.g. Zhu and Beroza, 2018; Zhou et al., 2019; Mousavi et al., 2020; Yu and Wang, 2022; Sun et al., 2023). However, growing evidences suggest that AI pickers can suffer from inconsistent performance among data in different regions (e.g. Chai et al., 2020; Jiang et al., 2021a; Münchmeyer et al., 2022; Zhu et al., 2022b; Park et al., 2023; Zhong and Tan, 2024). This indicates a lower generalizability compared to rule-based algorithms, such as STA/LTA. Thus, the LoSAR workflow combines the high generalizability of PAL with the superior detectability of the SAR picker by training a localized SAR model using local PAL detections, thereby avoiding the need for trans-region applications. We apply LoSAR to two distinct regions: (1) the Ridgecrest-Coso region (2008-2019), and (2) the East Anatolian Fault Zone (EAFZ, 2020-2023/04). Through detailed comparisons, we demonstrate that LoSAR offers slightly higher detection completeness than the QTM matched filter catalog (Ross et al., 2019b), while boosts an over 100 times faster processing and a superior temporal stability, avoiding low-magnitude gaps during background periods. Against PhaseNet (Zhu and Beroza, 2018) and GaMMA (Zhu et al., 2022d), two established AI-driven phase picker and associator, LoSAR proves more scalable and generalizable, achieving roughly 2.5 times more event detections in the EAFZ case, along with a ~7 times higher phase association rate.

In summary, PALM and LoSAR are powerful tools for resolving fine-scale seismicity. They work effectively with conventional networks and continuous data, making them widely applicable to current seismic observational conditions. As these technical advances continue, new scientific insights into fault zones and earthquake physics can be uncovered, which forms another key aspect of my Ph.D. research.

1.2 Structure of This Dissertation

In this dissertation, I will begin by detailing the PALM and LoSAR workflows in the following two chapters, including their algorithms and systematic tests. In Chapter 4, I present four case studies that use microseismicity to characterize fault zone behavior during pre- and post-seismic periods and explore how seismicity relates to earthquake potential. Chapter 5 focuses on how foreshocks trigger each other and the mainshock, highlighting the crucial role of high-resolution catalogs in distinguishing various triggering mechanisms. Finally, in Chapter 6, I will summarize the conclusions of this dissertation and suggest possible directions for future research.

Chapter 2

Generalized Earthquake Detection and Location Architecture: Phase Picking, Association, Location, and Matched Filter (PALM)

2.1 Introduction

The detection and location of seismic events are basic procedures to generate earthquake catalogs. A catalog with high completeness and high resolution provides a detailed image of 3D fault geometry (Waldhauser and Ellsworth, 2002; Hayes et al., 2012; Shelly et al., 2016; Ross et al., 2017a), which facilitates the fault model construction to perform slip model inversions (e.g. Yue et al., 2017; Sun et al., 2018). The spatiotemporal pattern and magnitude scaling also provide insights into the physical processes on fault, e.g. slow slip migration (Peng and Zhao, 2009; Kato et al., 2016) and fluid diffusion (Di Luccio et al., 2010; Chen et al., 2012); The power-law distribution of events at different magnitude is described by the b-value, which is observed to be correlated with stress level, fault roughness and fault strength (Scholz, 1968; Schorlemmer and Wiemer, 2005; Spada et al., 2013). In general, an ideal earthquake catalog should have high completeness and location precision, and consistent performance over a long time scale. To realize such objective in modern networks, which typically includes hundreds to thousands of stations, it requires high-performance detection and location architecture to perform automatic and systematic scanning over continuous waveforms.

The detection of earthquakes is usually based on a network of seismic stations. Typical detection workflows involve (1) phase picking on single stations, and (2) associate picks into events. Before the application of artificial intelligence (AI) seismology, automatic phase picking is usually realized with energy-based characteristic functions, e.g. short-term-average over long-term-average (STA/LTA) (Allen, 1978), which capture the abrupt change of amplitude in the seismograms. This type of methods presents high computational efficiency, but tend to introduce a high false detection rate and does not discriminate P- and S-wave well. To overcome this limitation, proper association algorithms enable more accurate detection, though station records with a low signal-to-noise ratio (SNR) may still be missed. The phase association is usually realized by the temporal and spatial correlation between picks (Johnson et al., 1997; Patton et al., 2016; White et al., 2019), but difference exists in the format of input picks: for example, Chen and Holland (2016) does not assign P or S to the picks, and let the associator decide each pick to be P/S; Zhang et al. (2019) need P & S picks, but they do not come in pairs, which also lead to low efficiency.

In more recent years, two types of algorithms present better detection performance: AI and matched filter technique (MFT). AI-based phase pickers incorporate the features of complete waveform (i.e., P&S phases), instead of solely the phase arrivals (Zhu and Beroza, 2018; Zhou et al., 2019; Mousavi et al., 2020). With numerous labeled training samples, AI models are able to detect and pick emergent phase arrivals. However, training samples are not always available, and pre-trained models cannot guarantee comparable performance as that on the training set (Zhu et al., 2019; Chai et al., 2020). Such attempts in this direction include transfer learning (Zhu et al., 2019; Chai et al., 2020), and building a global training set (Mousavi et al., 2019a; Liu et al., 2020b). Even so, AI applicants still suffer from the difficulty in collecting and preprocessing training data, and building efficient training pipelines for big data as well. Thus, though a promising and fast-developing direction, AI pickers need more case studies to validate its effectiveness and robustness.

Matched filter augments the initial detections (i.e., templates) by cross-correlating with raw data (Turin, 1960; Gibbons and Ringdal, 2006). This correlation-based algorithm can detect signal lower than the noise level, and can thus obtain the most complete catalog (Shelly et al., 2007). However, the detectability of MFT is determined by the diversity of template waveforms, which requires a rather complete catalog and high seismicity rate. Moreover, the cross-correlation is computationally expensive, even adopting Graphics Processing Unit (GPU) acceleration. These shortcomings limit the applicability of MFT to certain situations, e.g. aftershock detection, where enough templates can be available, and only a few days' scanning is required. Thus, an ideal automatic detection workflow should provide reliable baseline detections as templates, and an efficient MFT implementation based on GPU acceleration.

The location of earthquakes is usually based on arrival times picked for each event. Typical location processes include (1) absolute location, where each event is located individually, minimizing the difference between observed and predicted travel time (Geiger, 1912; Klein, 2002); and (2) relative location, where differential travel times for event pairs are measured to constrain the relative location (Waldhauser and Ellsworth, 2000; Zhou et al., 2001; Trugman and Shearer, 2017). In such workflow, the absolute location process obtains an accurate overall location, and the relative relocation help resolves a detailed image of seismicity. An accurate absolute location calls for high-quality phase picking, proper choice of velocity model, adequate coverage of network, and fine-tuned location parameters (Husen and Hardebeck, 2010; Lomax, 2020). The picking of S arrival is especially important in this process, since the S-P time constrains the length of ray path, which reduces the trade-off between origin time and epicentral depth in the inversion. However, S arrival is more difficult to precisely pick in comparison with P arrivals, because its initial arrival is often contaminated by the tail of P-wave. This results in large uncertainty in determining the hypocentral depths. The relative relocation process resolves fine structure with double-difference (DD) algorithm. Note that CC-based differential travels times reach a theoretical resolution below sampling rate (Frémont and Malone, 1987), and is thus always applied in company with MFT applications in recent years (Shelly et al., 2016; Ross et al., 2019b), which result in both high detectability and high-resolution relocation.

The above progress makes possible a high-performance earthquake detection and location applying to modern networks. However, people still need to combine modules from different researches, which possibly brings about low efficiency pipelines and even errors. We acknowledge some successful cases following such strategy, e.g., Mendoza et al. (2019); White et al. (2019), but a seamless and open-source architecture sequentially performing event detection, location and match-filter from raw data is still in urgent need to the seismic community. In this study, we present PALM, a newly developed detection and location architecture applied to raw continuous waveforms, which incorporates phase picking, phase association, location, and matched filter. PALM is independent of any a priori information about earthquakes, while gives high-completeness detection and high-resolution location. We apply it to the 2019 Ridgecrest, California M_w 7.1 (RC) aftershock sequence, and compare our result with two other MFT catalogs: Shelly (2020b) and Ross et al. (2019a) to validate its performance.

2.2 Method and Data

2.2.1 Workflow of PALM

The workflow of PALM includes two modules (Figure 2.1): (1) PAL, i.e. picking, association, and location, an STA/LTA-based algorithm for initial detection, and (2) MESS, i.e. match, expand, shift, and stacking, a matched filter detector that augments the initial PAL catalog. Each module contains detection and location stages, and process raw continuous waveforms. Details of PAL and MESS are presented in the following sections. Suggestions for software usage can be found in the electronic supplement.

2.2.2 PAL: Picking, Association, and Location

The initial catalog is obtained by PAL process, which includes three steps (Figure 2.1): (1) Picking: the picker firstly picks P- and S-arrivals from the continuous waveform; (2) Association: the associator groups phases to different events for location purpose; and

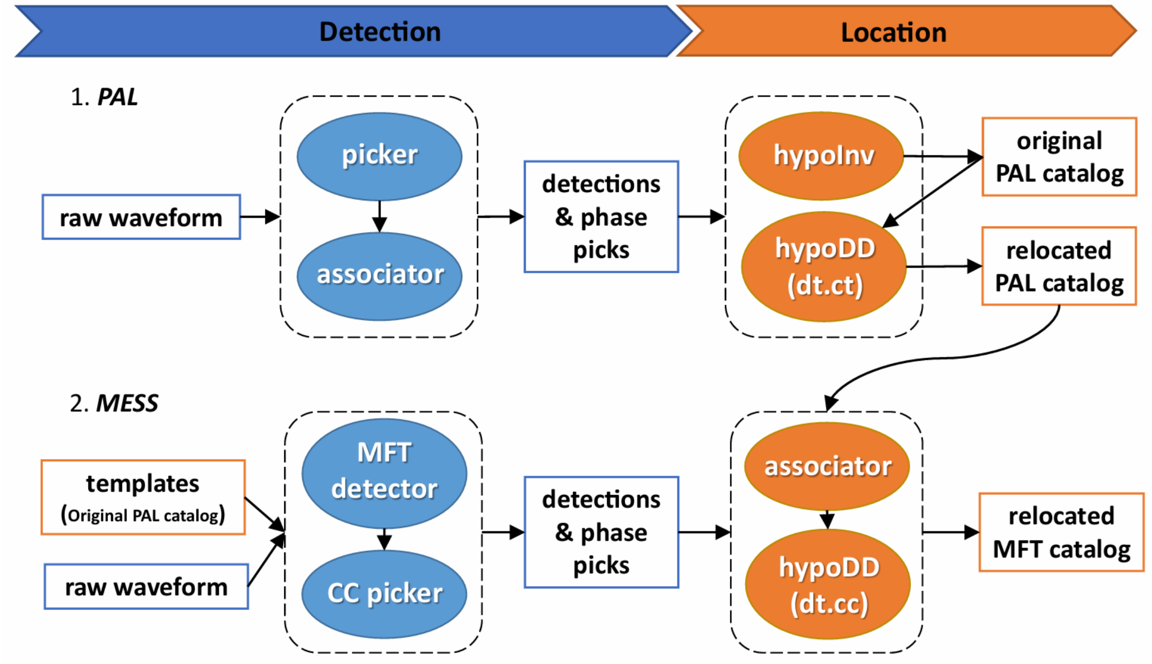

Figure 2.1. Workflow of PALM. Input and output results are denoted by squares. Detection and location operations are plotted in ellipse patches. Modules for detection and location purpose are plotted in blue and orange, respectively.

(3) Location: events are located and relocated with standard algorithm, i.e. HypoInverse (Klein, 2002) and HypoDD (Waldhauser, 2001).

2.2.2.1 PAL Picker

The PAL picker picks P&S arrivals in pairs, following a "detect and pick" strategy (Figure 2.2). It is realized with a combination of STA/LTA (Allen, 1978) and Kurtosis (Baillard et al., 2013) algorithm, whose definitions are:

$$S_d(t_i) = \frac{\Delta t_{LTA}}{\Delta t_{STA}} \cdot \frac{\sum_{t_i}^{t_i+\Delta t_{STA}} d(\tau_i)}{\sum_{t_i-\Delta t_{LTA}}^{t_i} d(\tau_i)} \tag{2.1}$$

where S_d is the STA/LTA function for the input waveform (time series) d; Δt_{STA} and Δt_{LTA} are the window lengths for STA and LTA calculation, respectively. And

$$K_d(t_i) = \frac{\frac{1}{N}\sum_{t_i-\Delta t_K}^{t_i}\left(d(\tau_i) - \bar{d}\right)^4}{\left[\frac{1}{N}\sum_{t_i-\Delta t_K}^{t_i}\left(d(\tau_i) - \bar{d}\right)^2\right]^2} \tag{2.2}$$

where K_d is the kurtosis function of data (d); Δt_K and N is the window length and number of sample points for kurtosis calculation; d and $\bar{d}$ are the input data (time series) and mean value of $d(\tau)$ for $t_i - \Delta t_K < \tau_i \le t_\mathrm{i}$. The raw data are preprocessed by removing the mean and linear trend, tapering, and bandpass filtering to the frequency band of local earthquakes. In the case of RC, we apply a 2-40Hz bandpass filter. Then picking operation is performed to the processed data.

The P arrivals are detected on Z-component with STA/LTA algorithm (Figure 2.2a). The characteristic function S_{p_det} is calculated on the kinematic energy of vertical component:

$$S_{p\_det}(t) = S_{z^2}(t) \tag{2.3}$$

where z is Z-channel velocity. Note that the Δt_{STA} is relatively long for the detection purpose. For RC data, we set $\Delta t_{STA} = 0.8s$ and $\Delta t_{LTA} = 6s$. A detection is declared at the triggering time t_{p_trig} , if S_{p_det} reaches the triggering threshold S_{p_thres} , i.e. $S_{p\_det}\left(t_{p\_trig}\right) = S_{p\_thres}$. We set $S_{p\_thres} = 12$ in RC based on the estimation of the SNR. Precise P arrivals (t_P) is picked around the triggering time, by an STA/LTA operation calculated on vertical energy, but with a shorter Δt_{STA} (Figure 2.2b). We set $\Delta t_{STA} = 0.4s$ and $\Delta t_{LTA} = 2s$ for P arrival picking in RC. The initial picking is made at the peak of STA/LTA function, which is then corrected on the Z-velocity by finding the first peak backward.

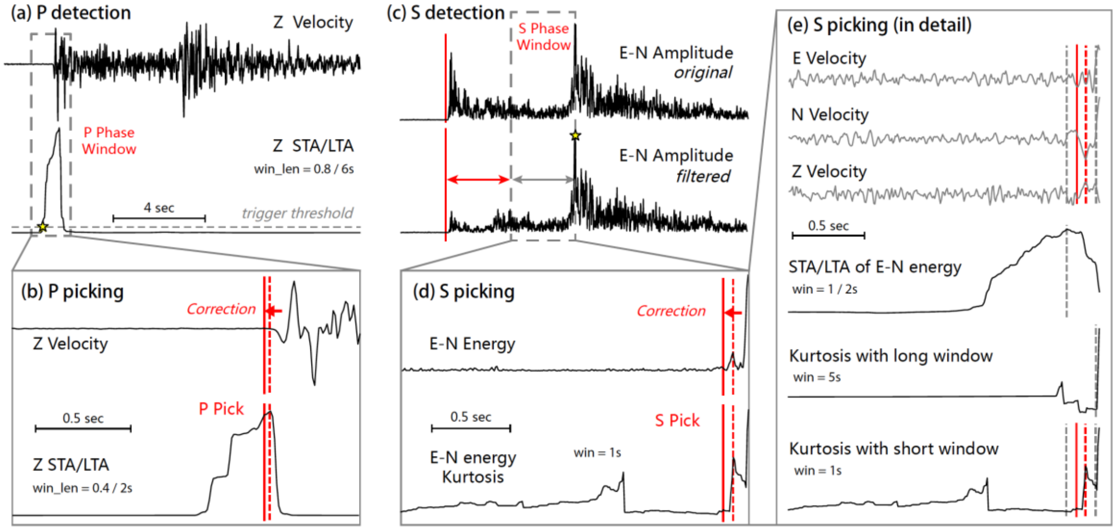

Figure 2.2. Algorithm of PAL picker. (a) Detection of P arrival. Z-channel waveform (velocity record) and STA/LTA function are plotted in black lines. Trigger level and time are plotted by dashed horizontal gray line and yellow star, respectively. The P phase window is bounded by a gray dashed rectangle. (b) Picking of P-wave. Red dashed and solid lines plot initial and corrected (final) P picks, respectively. (c) Detection of S arrival. Original and PCA filtered horizontal (E-N) channel amplitude are plotted in the top and bottom panels. The time of maximum filtered amplitude is marked by a yellow star. The S phase window is marked as a gray dashed rectangle and gray double arrow. The red double arrow marks the first half of the window between P and the yellow star (i.e. P window). (d) Picking of S-wave. The labels are identical as (b). (e) Detailed illustration of S picking algorithm. Characteristic functions are plotted in black lines. The earliest and latest boundary derived from STA/LTA and long-window Kurtosis picker are marked by gray dashed lines. The initial and final S-pick are marked by red dashed and solid lines.

S-wave arrivals are detected on the horizontal components (E and N channels) (Figure 2.2c). The triggering time for S-wave t_{s_trig} is defined as the time when the S-wave amplitude $A_S(t)$ reaches its peak value:

$$A_S\left(t_{s_{trig}}\right) = max[A_S(t_i)]\,, \text{for } t_P < t_i < t_P + \Delta t_S \qquad (2.4)$$

where Δt_S is the searching window for S-wave following the picked P arrival time t_P. The S-wave amplitude A_S is defined as:

$$A_S(t_i) = \begin{cases} \sqrt{x^2(t_i) + y^2(t_i)} \times P_{filter} & , \text{for } t_P < t_i \leq t_P + \Delta t_{filter} \\ \sqrt{x^2(t_i) + y^2(t_i)} & , \text{for } t_P + \Delta t_{filter} < t_i < t_P + \Delta t_S \end{cases} \qquad (2.5)$$

where P_{filter} is a polarization filter based on a similar strategy to Ross and Ben-Zion (2014); Δt_{filter} is the time window in which the polarization filter is applied. We set $\Delta t_{filter} = 2s$ in RC to remove the possible contamination from P-wave. The S arrival is thus constrained between $t_P + (t_{s\_trig} - t_P)/2$ and t_{s_trig} (namely "S window").

Precise S arrival time t_S is picked by the kurtosis of horizontal energy, with a small Δt_K (i.e. K_{short}) to capture emergent change in amplitude (Figure 2.2d-e). The correct peak in K_{short} is further constrained by STA/LTA, S_{s_det} and long-window kurtosis K_{long} in the S window (Figure 2e):

$$\begin{cases} S_{s\_det}(t_{min}) = \max\left(S_{s\_det}\right) \\ K_{long}(t_{max} + \Delta t_{corr}) = \max(K_{long}) \end{cases}, \tag{2.6}$$

where t_{min} and t_{max} are the earliest and latest boundary of the peak in K_{short}; Δt_{corr} is the time correction made by finding the first trough backward. In RC, we set $\Delta t_{STA} = 1s$ and $\Delta t_{LTA} = 2s$ to calculate S_{s_det}; set $\Delta t_K = 1s$ and $\Delta t_K = 5s$ to calculate K_{short} and K_{long}, respectively. The initial picking is made at the peak of K_{short}, which is then corrected on the horizontal energy by finding the first peak backward.

The PAL picker provides precise P- and S-picks for correctly detected phases. However, it may yield false detections due to impulsive noise signal (Withers et al., 1998; Yue et al., 2018). We conduct a subsequent phase association process to remove false detections.

2.2.2.2 PAL Associator

The P/S arrivals are associated to different events based on their spatial and temporal relations at different stations (Figure 2.3). The temporal association is realized by clustering the estimated origin times (Figure 2.3a). The origin time t_o at a given station is estimated as:

$$t_o = \frac{t_P \cdot v_P - t_S \cdot v_S}{v_P - v_S} \tag{2.7}$$

where v_P and v_S are the average P- and S-wave velocities in the crust, respectively. In the case of RC, phase picks are grouped into the same events, if their origin time estimations deviate within 2s. Temporally associated phase picks are retained for further process in the spatial association.

Epicentral distances can be roughly estimated from $t_S - t_P$, drawing a location circle centered by the station (Figure 2.3b). For point source (earthquake), these circles from different stations converge near the real epicenter. This convergence serves as a criterion for spatial association, which can eliminate arrivals inconsistent with the common convergence point (i.e. false detection). This spatial association is realized by a 3-D grid search for the epicentral location that minimizes the travel time residual ε defined as:

$$\varepsilon = \sum_{i=1}^{N} \varepsilon_i = \sum_{i=1}^{N} \left| \left(t_o + T_{P,i} \right) - t_{P,i} \right|, \qquad \text{for } \varepsilon_i < \varepsilon_{max} \tag{2.8}$$

where $T_{P,i}$ and ε_i are the respective P wave theoretical travel time and residual at the i^{th} station; N is the number of stations whose travel time residual fall below the threshold ε_{max}. We set $\varepsilon_{max} = 1.5s$ for the RC events, considering the uncertainty in travel time estimation. A minimum number of stations is required for a robust location, which is set as $N \geq 4$ here.

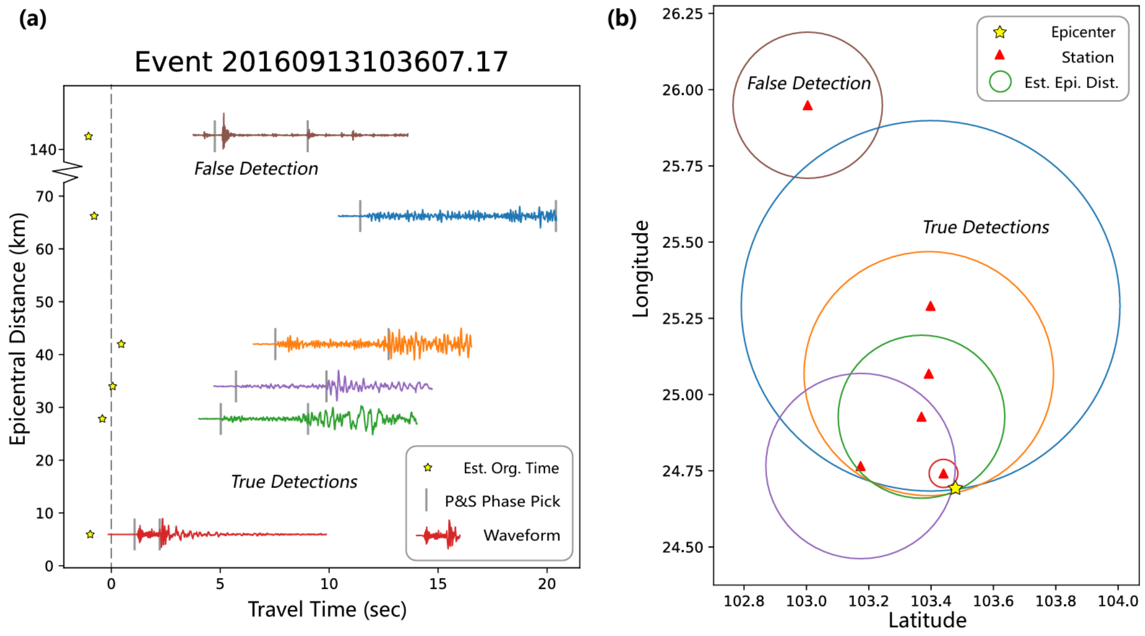

Figure 2.3. Phase association process. (a) Temporal association. E-channel waveforms at different stations are plotted in different colors. Vertical solid gray lines mark the picked P- and S-arrival times. Yellow stars denote the estimated origin times. (b) Spatial association. Red triangles show the locations of seismic stations. Circles are centered at the stations with corresponding epicentral distances estimated from the picked P- and S-arrival times. The yellow stars denote the estimated epicenter.

Finally, we estimate the local magnitude M_L using the S-wave amplitude, according to the classical definition by Richter (1935):

$$M_L = median\left(log_{10}\left(A_{S,i}\right) + log_{10}(r_i) + 1\right) \tag{2.9}$$

where $A_{S,i}$ is the S-wave amplitude (in μm) at the i^{th} station; r_i is the corresponding hypocentral distance in km. Note that we do not include distance attenuation and station correction term for wider applicability, since they are path- and site-dependent, and are not available in most cases (Boore, 1989). This results in a similar magnitude scale in California, and thus suitable for the case of RC (Hutton and Boore, 1987; Uhrhammer et al., 2011).

The PAL associator utilize pairs of P-S picks to realize stable and efficient association, which is different from previous algorithms, e.g. Chen and Holland (2016). This may also result in more missed detections when the network is rather sparse or the noise level is high. Such problem can be solved in the following MESS detection procedure.

2.2.2.3 PAL Locator

We adopt standard location and relocation procedures in the location stage, because the PAL detector and associator produce absolute arrival times. The detected events are first located using HypoInverse (Klein, 2002), which is an absolute location method based on gradient descent inversion. Then, the locations are refined by HypoDD (Waldhauser, 2001), using the catalog-derived differential time (namely *dt.ct*) (Figure 2.1). The original PAL catalog serves as template events for MESS detection, and the relocated PAL location is applied in relocating MESS detection results.

For RC events, we employ the 1-D velocity model used by Shelly (2020b), which is a 1-D approximation of the 3-D CVM-S model (Kohler et al., 2003). In the absolute location using HypoInverse, we apply a cosine distance weighting factor that changes from 1 at 30km to 0 at 90km; as also a residual weighting function that ranges from 1 at 0.3s to 0 at 0.9s of maximum residual, for P&S picks. In the HypoDD relocation, we set WDCT=5 km and apply 4 iterations of inversion, considering the average inter-event distance.

2.2.3 MESS: Match, Expand, Shift, and Stack

2.2.3.1 MESS Detection

The initial PAL detections are augmented by MESS, a matched filter detector that consists of four steps: Match, Expand, Shift, and Stack. In this process, both event detection and phase picks are realized by cross-correlation, which is accelerated by GPU. The details of the MESS are described as following:

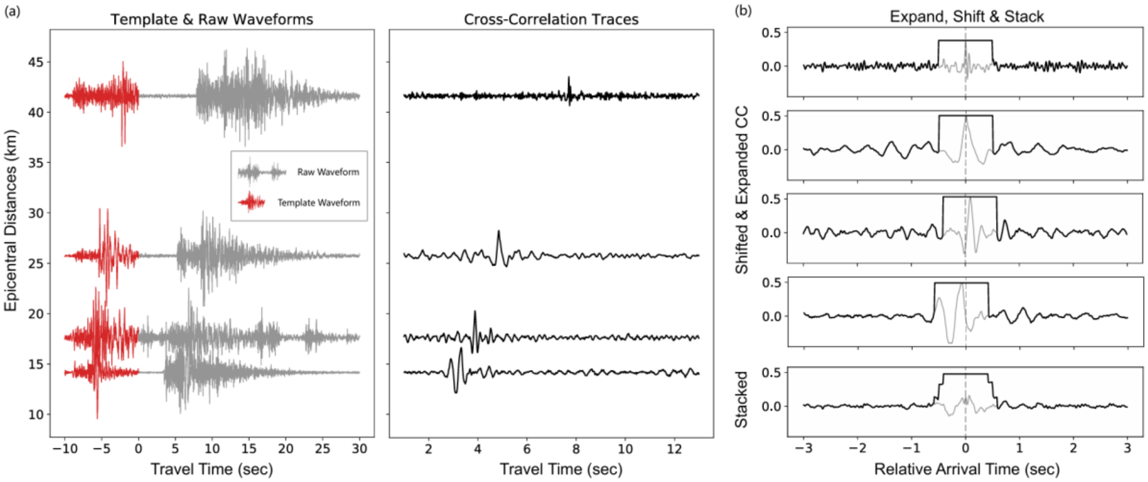

Figure 2.4. Algorithm of MESS. (a) Matched filter. Template and raw waveforms are plotted in red and gray lines, respectively. The resulting cross-correlations are plotted in black. (b) Stacking strategy. Original and expanded cross-correlations are plotted in gray and black lines, respectively.

(1) Match: the similarity between template and raw data is quantified by the cross-correlation (Figure 2.4a):

$$CC_0(t_i) = \frac{\sum_{\tau_i=t_i}^{t_i+\Delta t_{temp}} d_{raw}(\tau_i) \cdot d_{temp}(\tau_i - t_i)}{\sqrt{\sum_{\tau_i=t_i}^{t_i+\Delta t_{temp}} d_{raw}^2(\tau_i)} \cdot \sqrt{\sum_{\tau_i=0}^{\Delta t_{temp}} d_{temp}^2(\tau_i)}}, \tag{2.10}$$

where d_{raw} and d_{temp} are the raw and template waveforms, respectively, and Δt_{temp} is the length of template waveform. For the RC data, the template uses 10s-windows, from 1s before to 9s after the P arrival, so as to cover both P- and S-waves for accurate detection. Both template and raw waveforms are preprocessed in the same way as in the PAL process.

(2) Expand: a peak value expanding operation is imposed on the cross-correlation functions (Figure 2.4b):

$$CC_{exp}(t_i) = \begin{cases} CC_{peak}\ , for\ t_{peak} - \Delta t_{exp}/2 < t_i \le t_{peak} + \Delta t_{exp}/2 \\ CC_0(t_i) \qquad\qquad\qquad\qquad , otherwise \end{cases} \tag{2.11}$$

where CC_{peak} and t_{peak} are the amplitude and time of the CC$_0$ peaks, respectively; Δt_{exp} is the length of expansion. The expansion operation is designed to reconcile location differences between the templates and detected events, because a direct summation fails to align peak CC values at the origin time of detected event, which limits the detectability (see the comparison in Figure 2.4b). We set $\Delta t_{exp} = 1s$ in RC, which corresponds to a searching radius of about 3km around the template event.

(3) Shift: The expanded cross-correlation is shifted by the P-wave travel time of the template event (Figure 2.4b):

$$CC(t_i) = CC_{exp}(t_i + T_P) \tag{2.12}$$

where T_P is the P-wave travel time of the template event. Given that the template event has a similar location to the detected event, this time shift can roughly align the cross-correlations from different stations.

(4) Stack: The migrated CCs from different stations are stacked (Figure 4b):

$$CC_{stack}(t_i) = \frac{1}{N} \cdot \sum_{i=1}^{N} CC_i\,(t_i)\,, \tag{2.13}$$

where N is the number of stations. Multi-trace stacking suppresses uncorrelated random noises, further reducing the false detection rate. We set the detection criterion as $CC_{stack} \geq 0.25$, and the origin time t_o is determined as the peak time on CC_{stack}.

The P&S arrival times are then picked by waveform cross-correlation. The template window for CC picking ranges from 0.5 s-pre to 1.5s-post the P arrival, and 0.5s-pre to 2.5 s-post the S arrival, considering the length of signal in RC. The S amplitude is also individually measured for magnitude estimation using the same method as that for PAL detections.

2.2.3.2 MESS Relocation

The MESS detections are relocated by HypoDD (Waldhauser, 2001), using the correlation measured differential time as the *dt.cc* file (Figure 2.1). Detections from different templates are firstly associated based on their origin time. In RC, we associate detections with estimated t_o within 2 s as one detection, and its origin time is the t_o estimation by the template with maximum CC_{stack} value. The differential travel time between the template and detected event can be obtained by:

$$\Delta T = t_{cc} - t_o - T_{temp} \, , \tag{2.14}$$

where t_{cc} is the correlation picked arrival time, t_o is the origin time of the detected event, and T_{temp} is the travel time of the template event. The initial location of the templates is shifted to the relocated PAL catalog location, while the initial location of newly detected events is set to the average of template locations that detected it.

For RC events, we adopt the same velocity model as for PAL location. For robust relocation, each event is required to be detected by at least 3 templates with *dt* from 4 stations. We utilize only *dt.cc* to relocate MESS detections, with the WDCC=4 km for 5 iterations of relocation.

2.2.4 SCSN Data

We use the aftershock catalog of the 2019 Ridgecrest earthquake to validate the performance of the PALM pipeline. The detected arrival time and relocated catalog is compared with published results. We utilize publicly available Southern California Seismic

Network (SCSN) data to build RC aftershock catalog (Cochran et al., 2020; Hauksson et al., 2020). Broad-band and short-period stations that distribute within approximately 100 km from the mainshock epicenter are incorporated, which covers the source region well. The average distance between stations is about 10-20km. This selection of stations is similar to that used by Shelly (2020b) and Ross et al. (2019a). We apply PALM from 2019-07-04 to 2019-07-16 enabling direct comparison with Shelly (2020b) and Ross et al. (2019a) catalog.

2.3 Results and Discussions

2.3.1 Phase Picking Results

Phase picking is the fundamental step for event detection and location in the PAL architecture. We test the PAL picker on the PAL-recalled SCSN events, and use SCSN picks as a reference, which contains about 100,000 P&S pick pairs. We made a detailed comparison between PAL, STA/LTA, and Kurtosis picker picking results. Here, both STA/LTA and Kurtosis picker pick the peak time in the characteristic functions, as defined by Equation (1) and (2), respectively. The choice of channel is also kept the same with PAL picker: pick P arrivals on Z-vertical velocity waveforms and S arrivals on EN-horizontal energy. The picking operation is performed over ±1 s time window reference to the SCSN arrival times.

We first compare the distribution of picking deviation (*dt*) for the three pickers (Figure 2.5a). The phase detection accuracy is defined as the ratio of picks with dt<0.5s to the total number, which measures the stability of a picker. The phase picking precision is

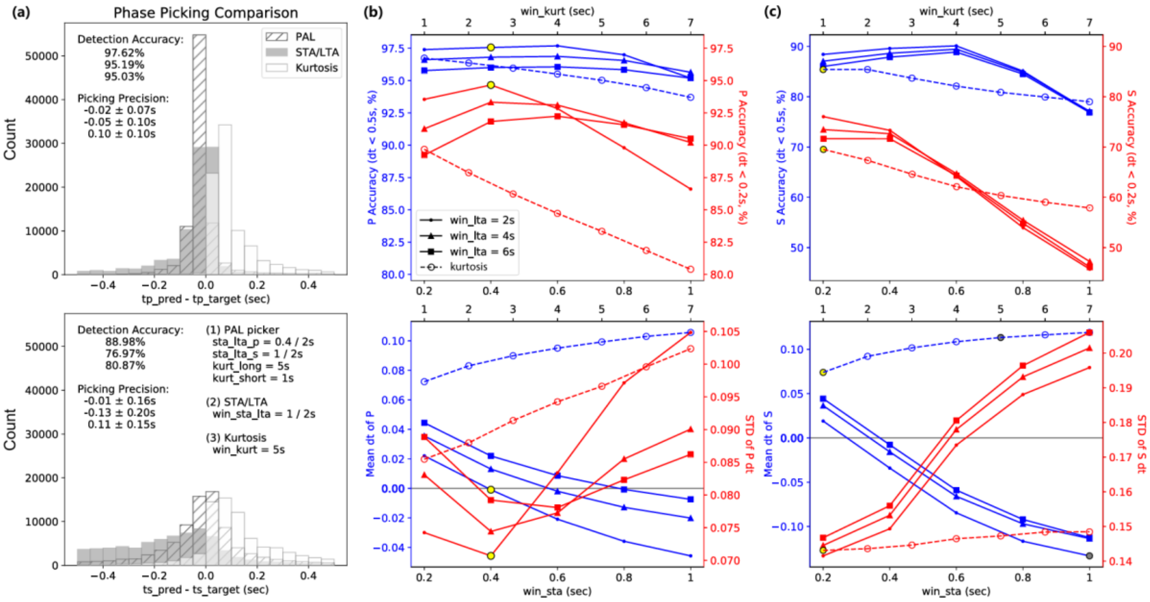

Figure 2.5. (a) Phase picking performance of PAL, STA/LTA, and Kurtosis algorithms are evaluated as deviation from the SCSN picks and plotted as histograms using slash-filled, gray-filled, and blank bars, respectively. Detection accuracy is defined as the ratio of picks with an absolute deviation of 0.5s. Phase picking precision is presented by mean ± std (sec) value for the detected phases. (b) P-wave detection accuracy and picking precision for different window lengths. Solid lines with dot, triangle, and square marker denote STA/LTA with long window length set to 2s, 4s, and 6s, respectively. Dashed line with circle marker denotes picking result by Kurtosis picker. In the upper panel, blue and red lines plot phase detection accuracy assuming a maximum picking deviation (*dt*) of 0.5s and 0.2s, respectively. In the lower panel, blue and red lines plot mean and std values of picking deviation, respectively. Adopted parameters are highlighted by yellow-filled dots. (c) Same as (b), but for S pick.

expressed as the mean ± std of the detected phases, whereby the mean value evaluates the systematic picking deviation and the std evaluates the picking concentration. As shown in Figure 5a, the PAL picker outperforms STA/LTA and Kurtosis picker for both P & S picks, being stable in detection, precise in picking, and has little systematic deviation. In contrast, STA/LTA tends to pick ahead of SCSN, and has low picking precision. This bias is more serious for S-waves, which has low-SNR. The Kurtosis picker has high picking precision, but also results in lagged picks, which is also reported by previous studies (Baillard et al., 2013; Ross and Ben-Zion, 2014). Further improvement can be made with AI methods (Zhu and Beroza, 2018; Zhou et al., 2019; Mousavi et al., 2020), especially for the S-wave picking. However, as stated in the Introduction Section, the generalization of AI methods is still a problem and needs further investigation, but is out of the scope of this paper.

We further explore the performance of STA/LTA and Kurtosis picker with different window lengths (Figure 2.5b-c), which helps to illustrate the advantage in PAL picker, as it combines the strengths of the two traditional pickers. In P picking (Figure 2.5b), STA/LTA have higher detection ability and picking precision than Kurtosis, under most combinations of window length. For STA/LTA method, the mean *dt* drops with increasing Δt_{STA}, and the best performance is obtained with a $\Delta t_{STA} = 0.4s$ and $\Delta t_{LTA} = 2s$. When picking S arrivals (Figure 2.5c), the Kurtosis picker is more robust to different window lengths, and has significantly higher picking precision compared with STA/LTA, however, the Kurtosis picks are consistently later than the SCSN picks by about 0.1 s, which is caused by the emergent arrival of S wave. Though the S-wave initial arrival shows up as a peak in kurtosis function, the growing amplitude afterward leads to a larger kurtosis amplitude (Figure 2.2). On the other hand, STA/LTA gives consistent ahead picking when $\Delta t_{STA} > 0.5s$. Thus, the STA/LTA and long-window kurtosis provide a stable constraint on S arrival times. Based on this constraint, the PAL picker utilizes short-window kurtosis to reveal more emergent change in amplitude, without sacrificing the picking stability.

2.3.2 Detection Results

We evaluate the detection performance of PALM by comparing with the public SCSN catalog (Hutton et al., 2010; Hauksson et al., 2020), Shelly (2020b)'s and Ross et al. (2019a)'s catalog.

We first compare the number of detections in the source area (117.28°W to 117.8°W and 35.49°N to 36.01°N). PAL detected 27,024 events, ~80% more than that in the SCSN catalog, showing higher detection ability (Figure 2.6a). The relocated MESS catalog contains 59,159 events, a comparable number of that in Ross et al. (2019a) and more than 1.5 times of that in Shelly (2020b) (Figure 2.6b). Note that Ross et al. (2019a) employed templates from 2019-07-04 to 2019-07-24, which is 8-days more than that used by Shelly (2020b) and this study. We also measures the recall rate of PALM, Shelly (2020b) and Ross et al. (2019a)'s catalog on SCSN catalog to estimate the detection completeness, which results in 90.05%, 93.53%, and 94.83% recall rate for the three catalogs, respectively. A slightly higher recall rate for Shelly (2020b) and Ross et al. (2019a)'s catalog is reasonable, since they use SCSN catalog as template, and that matched filer tend to recall template events themselves (i.e. self-detection). Most of the missed events come from a poor event connection in the relocation process. It is worth noting that the detection number by MFT depends on the association process as well (see the "MESS Relocation" section), which determines the robustness in relocation. Thus, a small difference in the number of events can be neglected in evaluating the quality of catalog.

The frequency magnitude distribution (FMD) are compared in Figure 2.6 to examine the consistency along magnitude dimension. The SCSN catalog presents a significant b-value change for events between M 1-3.4 and M 3.5-6, which violates the G-R law (Gutenberg and Richter, 1944) indicating incompleteness for events smaller than M3.4. This bias does not exist in the PAL catalog, which provides a better estimation for b-value (Wiemer and Wyss, 2000; Woessner and Wiemer, 2005). After matched filter, the

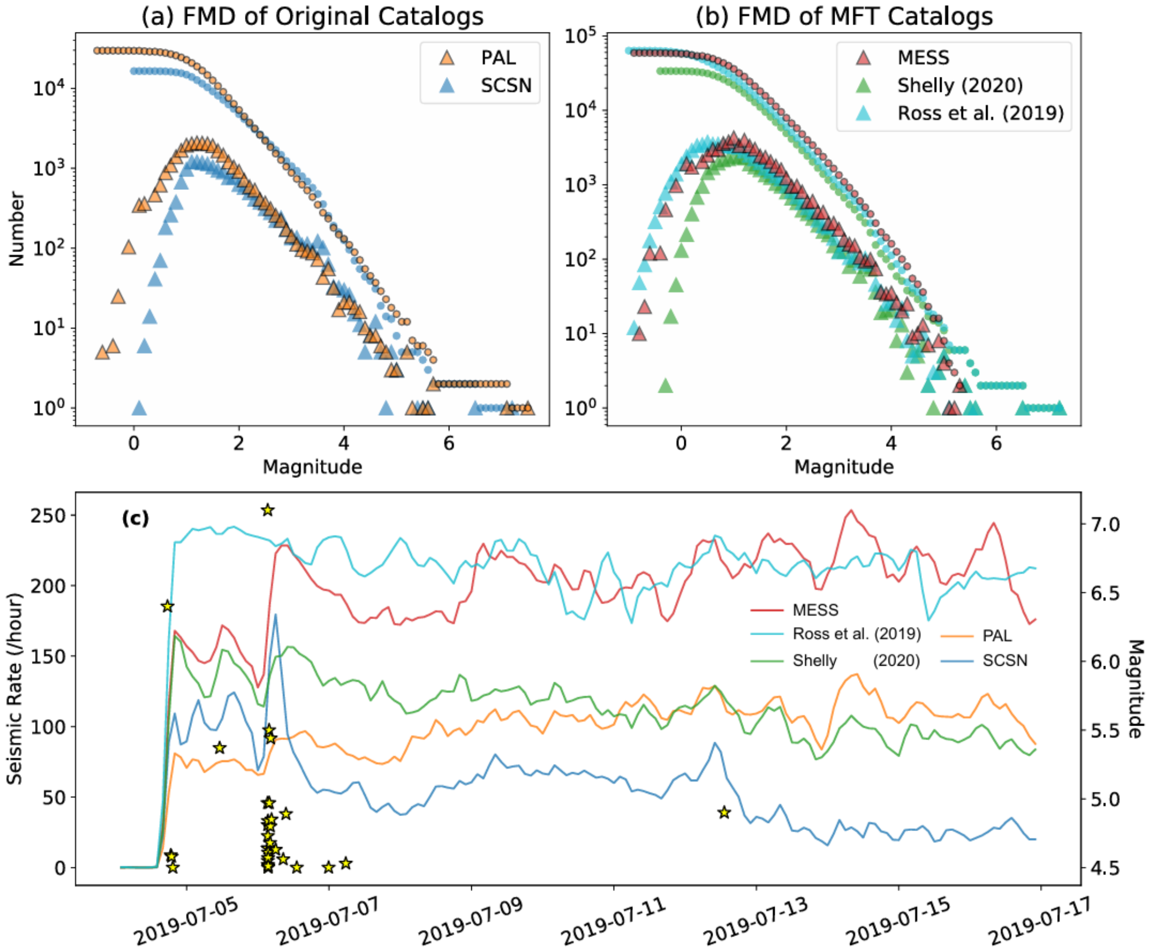

Figure 2.6. (a) Comparison of frequency magnitude distribution (FMD). PAL and SCSN catalogs are plotted in yellow and blue symbols, respectively. Cumulated and non-cumulative distribution are plotted as circles and triangles, respectively. (b) Same as (a) but for the MFT detected catalogs: MESS, Shelly (2020), and Ross et al. (2020), which are plotted as red, green, and cyan symbols respectively. (c) Seismic rate comparison. Results from different catalogs are plotted in the same colors as (a,b). Significant events (M>4.5) are marked by yellow asterisks.

complete magnitude of Ross et al. (2019a)'s catalog is pushed to ~0.5 under maximum curvature criteria (Wiemer and Wyss, 2000), but it is obvious that the bias between M0.5-2.0 still exists, which may alter further analysis on b-value. Such problem does not exist in the result by MESS and Shelly (2020b), while MESS show much higher detectability. Thus, the quality of template catalog determines the matched filter result, and the PALM architecture renders good matched filter performance.

The temporal variation of detection rate is compared in figure 6c to examine the temporal consistency. Expected temporal behaviors of early aftershock sequence are: (1) abrupt increase immediately after a significant event, and geometrical decrease further afterward, as described by the Omori's law (Utsu, 1961; 1970); and (2) consistent overall seismicity rate over such short period (16 days, in this study), while some possible fluctuations included. However, the initial detections, i.e. the SCSN and PAL catalog, show systematic bias (Figure 2.6c): the SCSN catalog shows an artificial drop in detection rate after 2019-07-12. This phenomenon is not reflected by other catalogs, thus it reflects some temporal detection issue of the SCSN catalog. The PAL catalog doesn't show a sharp seismic activity increase after the major events, i.e. the M_w 6.4 foreshock and the M_w 7.1 mainshock, indicating magnitude completeness change during intensive seismic activities right after major events. After MFT augmentation, the detection rate in MESS show a sudden increase after large events (Figure 2.6c). This abrupt increase can also be seen in Shelly (2020b)'s catalog, yet not presented in Ross et al. (2019a)'s catalog after the mainshock.

2.3.3 Location Results

The location of PAL and SCSN catalog are compared in Figure 2.7. The PAL+HypoDD catalog qualitatively shows a similar level of location clustering and lineation as the SCSN catalog, which is more concentrated than the HypoInverse catalog (Figure 2.7a), but the PAL cross-section does not show concentration at certain depths as in the SCSN catalog (Figure 2.7c), which is a common artifact in the absolute location with 1-D velocity model. The PAL+HypoDD relocation (Figure 2.7b) clearly outlines basic fault structures in RC, e.g. the orthogonal sub-faults cutting the NW-striking main fault, and the two branches in the southeast side. In comparison with the SCSN catalog, the relocated PAL catalog recovers more detailed and complete fault geometrical structure features, due to the abundance of detections. This also leads to more robust matched filter detection throughout the study region, especially for the SE end of the mainshock rupture, where seismicity in the SCSN catalog is relatively sparse (Figure 2.7c).

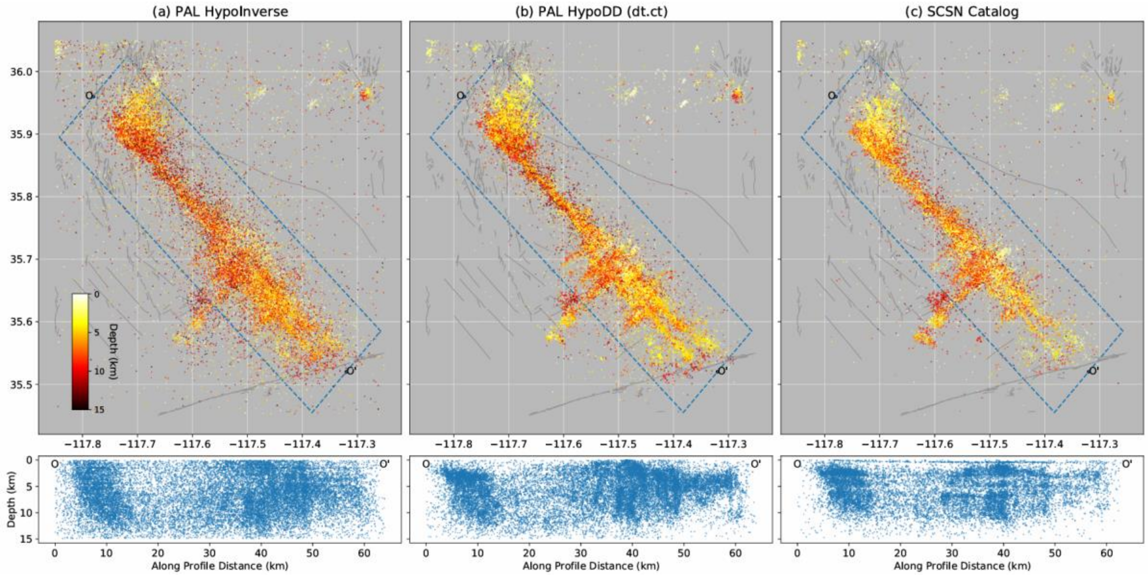

Figure 2.7. Location comparison for template events. (a), (b) and (c) plot locations of catalog obtained by PAL+HypoInverse, PAL+HypoDD, and SCSN catalog, respectively. Earthquakes are plotted in dots color-coded by their hypocentral depths and the marker size scaled with magnitude. Cross-sections are plotted in blue dashed squares. Profiles of catalog depth distribution along profile OO' are denoted as blue dots.

The relocated MFT catalogs, i.e. the MESS, Ross et al. (2019a) and Shelly (2020b)'s catalogs, are shown in the same manner in Figure 8. Detailed fault structures are consistently revealed by three MFT catalogs, including: the location and strikes of secondary faults perpendicular to the main fault; the deep clusters on Garlock fault, and the complex swarm in the NW end of co-seismic rupture, etc. Owing to the high-resolution CC-based differential time measurement, a comparable resolution is achieved by the three MFT catalogs. The relocation resolution of MESS and Shelly (2020b)'s catalog appears to be higher than that of Ross et al. (2019a), which may be caused by the difference in the relocation algorithm, i.e. Ross et al. (2019a)'s from GrowClust (Trugman and Shearer, 2017), but MESS and Shelly (2020b)'s by HypoDD (Waldhauser, 2001). The HypoDD algorithm tends to remove events showing in-consistent arrivals with other events, while the GrowClust algorithm treats them as low-weighted events.

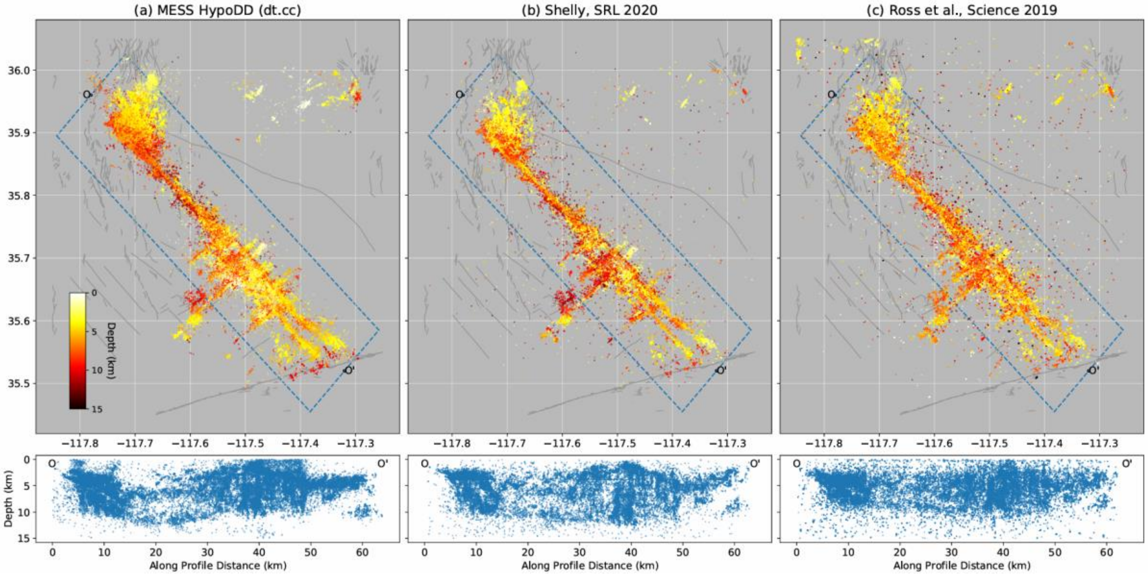

Figure 2.8. Location comparison for MFT catalogs. Markers have the same meaning as Figure 2.7.

Despite the consistency of general patterns of the three catalogs, the depth distribution of these catalogs varies. The most significant difference occurs in the NW side of the mainshock epicenter (~15-25 km along-profile distance, Figure 2.8), where large coseismic slips are observed at shallow portion (~0-5 km, (Ross et al., 2019a; Goldberg et al., 2020; Jin and Fialko, 2020). In such area, we expect to see a deficit in aftershock activity (Wetzler et al., 2018), and the MESS catalog fit this pattern better than Shelly (2020b)'s and Ross et al. (2019a)'s result. This may come from difference in phase association and the absolute location process, which are not included in Shelly (2020b)'s and Ross et al. (2019a)'s research, thus serves as a good case to show the advantage of a complete detection and location workflow. Differences also exist in the relocation process: though both starting from SCSN locations, Ross et al. (2019a) and Shelly (2020b)'s catalog deviate from each other for ~2km in the depth distribution (Figure 2.8). Again, this is partly due to different relocation methods, since GrowClust does not explicitly constrain the separation distance of event pairs. Such deviation can be enlarged with different template locations. However, in the relocation process, we are keeping track of the consistency between MESS and the relocated templates (i.e. PAL+HypoDD), so that no systematic deviations are introduced. Thus, the small differences between the MESS, Ross et al. (2019a) and Shelly (2020b)'s catalog reflect the uncertainty introduced by the relocation method and starting locations of template events.

2.4 Conclusions

We developed an earthquake detection and location architecture, which sequentially performs phase picking, association, location, and match-filter techniques. The design of PALM is specified to directly apply to continuous seismograms and to produce high-resolution catalogs, not requiring a reference catalog. This architecture is particularly useful for large-scale seismicity monitoring networks without detailed visual inspection, such as the on-building seismicity monitoring network in the Sichuan-Yunnan province of China (Wu et al., 2019b). We adopted PALM to the 2017 Ridgecrest aftershock sequence and compare the catalog with several published catalogs. The comparison demonstrates that:

1. PAL picker realizes robust phase detection and high picking precision, with an optimal combination of STA/LTA and Kurtosis algorithm.

2. PAL achieves high detectability and accurate location, which serves as a sound foundation for the following matched filter detection.

3. MESS augmented the PAL detections and gives high-resolution relocation with cross-correlation.

4. PALM can recover an un-biased and fine fault structure from continuous data.

Chapter 3

Construction of Long-Term Seismic Catalog with Deep Learning: A Workflow for Localized Self-Attention RNN (LoSAR)

3.1 Introduction

Microseismicity provides a direct indication to the fault structure and slip behavior at depth. Such strategy is especially useful when the fault slips at a high rate, e.g. during early aftershock period (e.g. Zhou et al., 2022a; Ding et al., 2023; Shelly et al., 2024), or other intense seismic sequences (e.g. Ross et al., 2020; Tan et al., 2021; Gong and Fan, 2022). However, a huge portion of faults generate low seismicity rate during the interseismic period because of a high locking ratio or a low fault slip rate (e.g. Jiang and Lapusta, 2016; Bletery et al., 2020; Chamberlain et al., 2021; Uchida and Bürgmann, 2021; Zhou et al., 2022b), while, unfortunately, these faults are also prone to large earthquakes (Sykes, 2021; Lay and Nishenko, 2022). To study such low-seismicity faults, a long-term observation is always necessary. For example, Schurr et al. (2020) built a seismic catalog for 7 years before the 2014 Iquique earthquake, and found that the pre-mainshock seismicity complements the coseismic slip; Sugan et al. (2023) observed a 8-year migration of seismicity towards the nucleation area of the 2016 central Italy seismic sequence.

Technically, the construction of long-term catalogs requires a workflow that is both computationally efficient and of high detection completeness, which is still a challenging task.

Currently, two types of cataloging workflow can realize a state-of-the-art performance: (1) the PAL-style workflow that follows "phase Picking – phase Association – event Location" procedure (e.g. Zhou et al., 2021b; Zhang et al., 2022c; Zhu et al., 2022c), and (2) the matched filter technique (MFT) that utilizes pre-detected events as templates to detect similar events (e.g. Ross et al., 2019a; Shelly, 2020b; Neves et al., 2022). The detection completeness of PAL-style workflows is basically dependent on the phase picking algorithm. In recent years, algorithms based on artificial intelligence (AI), specifically deep learning, realize outstanding phase picking performance in terms of the detectability and picking precision (e.g. Zhu and Beroza, 2018; Zhou et al., 2019; Mousavi et al., 2020; Yu and Wang, 2022; Sun et al., 2023). Most of these models, e.g. PhaseNet (Zhu and Beroza, 2018), are trained on regional or global datasets, aiming at building a general model that works for various data not included in the training set. However, systematic tests show that the AI pickers can suffer from inconsistent performance among data in different regions (e.g. Chai et al., 2020; Jiang et al., 2021a; Münchmeyer et al., 2022; Zhu et al., 2022b; Park et al., 2023; Zhong and Tan, 2024), especially for ocean-bottom seismograms (Bornstein et al., 2024; Niksejel and Zhang, 2024). This indicates a lower generalizability compared with traditional rule-based algorithms, such as short-term-average over long-term average (STA/LTA). The MFT methods can realize even higher detection ability than AI pickers (e.g. Mousavi et al., 2019b; Zhou et al., 2021a; Yoon and

Shelly, 2024), but its low computational efficiency makes it difficult to process big data (Ross et al., 2019b). Moreover, the detection results of MFT may be biased by incomplete templates (e.g. Herrmann and Marzocchi, 2020). In summary, the AI-based picker is the most promising method that combines both high efficiency and high detectability, whereas further improvements are needed to realize a consistent picking performance on a large spatiotemporal range of data.

In this study, we introduce a novel cataloging workflow powered by deep learning, featuring the Localization of Self-Attention RNN (LoSAR) for phase picking, tailored with local data. This approach effectively addresses the challenge of generalization faced by deep learning models. We apply the LoSAR workflow on two cases that covers a local-to-regional scale and years-to-decade time length, in order to demonstrate its advantage in building long-term catalogs.

3.2 Methods

3.2.1 Overview of the LoSAR Workflow

As reviewed in the Introduction section, the first-generation AI pickers attempt to provide a pre-trained model suitable for all datasets, which has not been very successful so far. Instead, we designed a new workflow that generates a local training set to obtain a locally optimized neural network (Figure 3.1). This workflow is composed of a detection module followed by a location module, and the detection module consists of two major steps: the model training step and the model application step.

In the model training step of the earthquake detection module, we utilize the PAL method (Zhou et al., 2021b) to construct a local training set (Figure 3.1). PAL utilizes rule-base algorithms for phase picking and association, thus does not have generalization problem as for deep learning. Tests on the 2019 Ridgecrest aftershock sequence show that PAL realizes around 2 times the number of detections by the Southern California Seismic Network (SCSN) (Zhou et al., 2021b), and PAL has been successfully applied in multiple regions and seismic sequences (e.g. Zhou et al., 2021a; Zhou et al., 2022b; Ding et al., 2023). Since the detection of PAL is basically made by the STA/LTA algorithm, which detects both earthquakes and pulse-like noises (e.g. anthropogenic noise or data glitches), we usually set a relatively high triggering threshold to avoid high false detection ratio and to reliably detect high signal-to-noise ratio (SNR) events. The PAL detections serve as the training set for our deep learning model, which can realize stable detections for weak signals. Note that deep learning models usually require a large number of training samples to tune the hyper-parameters, but the number of training samples is dependent on the model complexity. Thus, for light-weight models (e.g. Zhou et al., 2019; Yu and Wang, 2022), as that used in this study (see the next subsection for details), a relatively small training set is required to optimize the neural network (Mousavi et al., 2020; Zhou et al., 2021a).

After the model training step, we simply substitute the PAL picker with the locally-trained SAR picker (LoSAR), and associate the LoSAR picks with PAL associator (Figure 3.1). The PAL associator groups pairs of P&S picks into events based on their travel time-location relationship, and it also obtains a grid-searched location in the meantime. The magnitude calculation is also completed by the PAL associator in the local magnitude scale

(M_L), based on the S-wave amplitude and hypocentral distance (please refer to Zhou et al., 2021b for more details). We will show in this paper that this LoSAR workflow realizes >2.5 times more event detections compared with PAL, and is of a much higher detection stability and accuracy. It also generalizes well among very different tectonic settings, spatial scales, and network configurations.

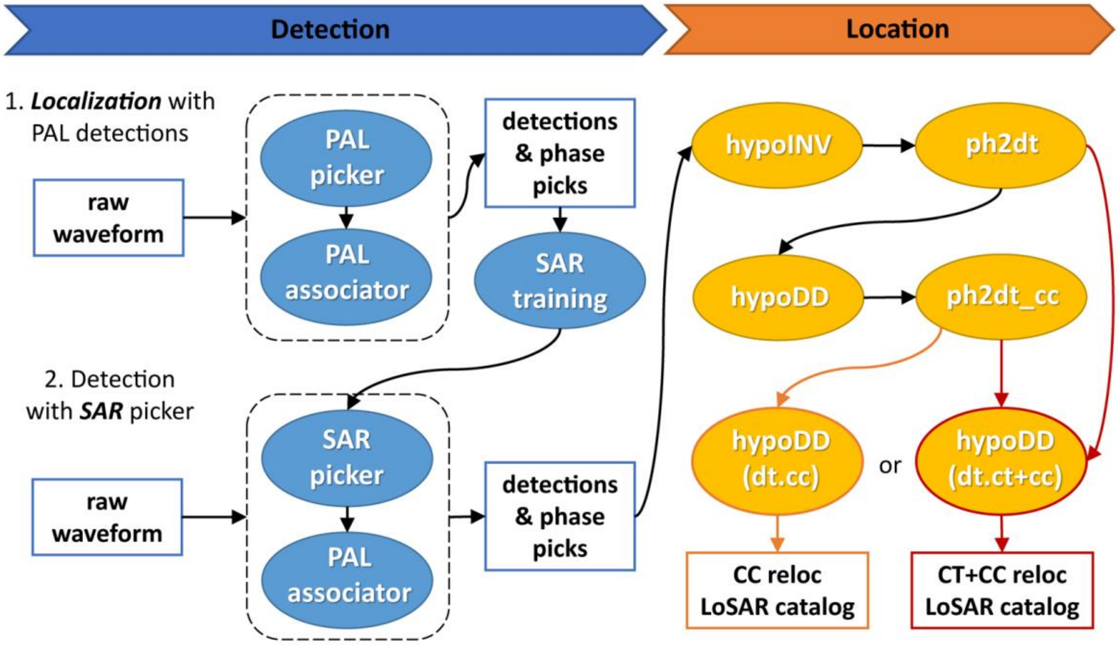

Figure 3.1. The Localized Self-Attention RNN (LoSAR) workflow. The blue and yellow modules denote the detection and location algorithms, respectively. PAL refers to an rule-based cataloging workflow developed by Zhou et al. (2021b); SAR refers to Self-Attention RNN phase picking model developed in this study. CT/*dt.ct* and CC/*dt.cc* refer to catalog-based and cross-correlation-based differential travel time, following the hypoDD terminology. The *ph2dt_cc* module is a CC-based differential time calculation method developed in this study.

To locate and relocate the detections, we build interface for HypoInverse (abbreviated as HypoINV thereafter, Klein, 2002) and HypoDD (Waldhauser and Ellsworth, 2000; Waldhauser, 2001) (Figure 3.1). HypoINV is a widely adopted algorithm for absolute location, which minimize the travel times in an iterative manner, where the weight for the phases are adaptively determined based on their epicentral distance and residual time (Klein, 2002). HypoDD is a double-difference (DD) relocation algorithm that minimizes the differential travel times between event pairs to constrain their relative locations (Waldhauser and Ellsworth, 2000). Given that the fault structure is manifested by the relative locations in seismicity imaging, the relocation process can significantly improve the imaging resolution (e.g. Waldhauser and Ellsworth, 2000; Trugman and Shearer, 2017; Lomax and Savvaidis, 2022). Notably, the differential time (*dt*) data used in hypoDD can come from catalog picks (CT, i.e. *dt.ct*) or cross-correlation (CC, i.e. *dt.cc*), and they can be jointly inversed or used individually. The best practice of using *dt.ct* and *dt.cc* comes from their different characteristics: *dt.ct* covers a larger inter-event distance, whereas the precision is relatively low, because it is dependent on the phase picking and location accuracy; *dt.cc* realize a sub-sampling-rate measurement for the differential time and is unaffected by picking errors, but it covers a much smaller distance, because it relies on waveform similarity between event pairs (as summerized in Waldhauser, 2001). Thus, jointly using *dt.ct* and *dt.cc* in some way is usually suggested. In our LoSAR workflow, we provide two approaches of combining *dt.ct* and *dt.cc* (Figure 3.1): (1) sequentially relocate with only *dt.ct* and *dt.cc*, and (2) relocate with *dt.ct* in the first step and jointly inverse *dt.ct & dt.cc* in the second relocation. The first approach is suitable for a relatively dense seismic network, because the near-source stations tend to have higher CC values; the second approach can maintain more events under a relatively sparse network, while also take advantage of the high-precision *dt.cc* data.

The calculation of differential times is the fundamental step for hypoDD relocation. The hypoDD software (Waldhauser, 2001) provides a *ph2dt* module that calculate the *dt.ct*

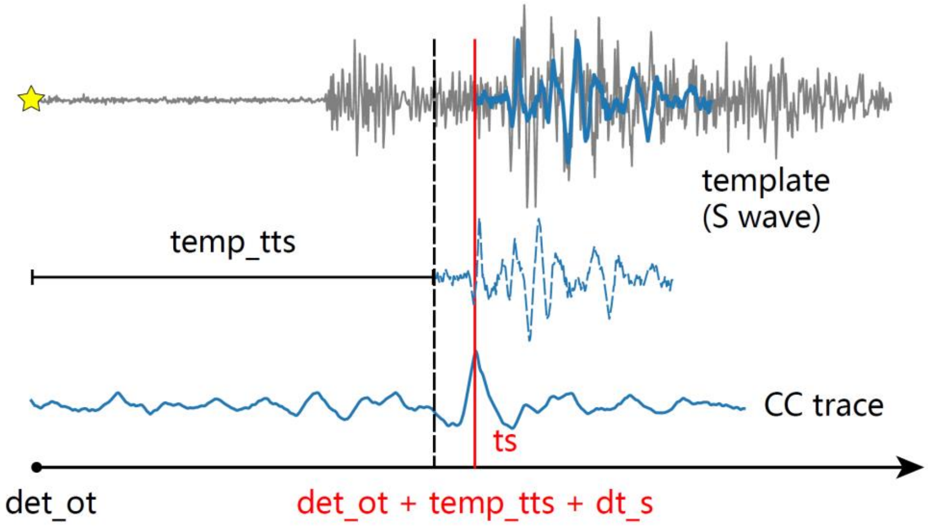

Figure 3.2. Demonstration of differential travel time measurement with waveform cross-correlation. The two events are named as “detection” and “template”, travel time and differential travel time are abbreviated as “tt” and “dt”, respectively.

data from the input phase file. It forms a chain of *dt*-links between events by searching neighboring events within a certain radius. For each event, a maximum number of neighboring events are preset in this process, in order to lower down the computational complexity and model errors. Following a similar strategy, we develop a *ph2dt_cc* module to calculate the high-precision *dt.cc* data with waveform cross-correlation (Figure 3.2). It first finds all possible event pairs by comparing the location differences and the common station picks. For each event pair, only events within a certain hypocentral separation and with certain number of shared stations are selected as candidates. To control the quality of *dt* measurements, we only use stations within an epicentral distance of about 100 km, and too small events (e.g. $M_L<0$) cannot be linked to each other. To avoid too many measurements, we also limit the maximum number of stations for each event pair, and each event can only be linked to a maximum number of neighbors. Secondly, we calculate the CC-derived *dt* for each candidate event pair. In the CC calculation, users can set the window length, which channel to use, and the filtering frequency band. The weight for each phase used in the hypoDD is determined by the square root of CC value. After the CC calculation, we further select the *dt* measurements by discarding that with a too large *dt* or a too small CC, and the minimum number of station criteria still applies afterwards. Detailed parameters will be given for each real case in the following sections.

3.2.3 Self-Attention RNN (SAR) Model for Phase Picking

The performance of a deep learning model is decided by multiple factors, including the model structure, target function (labeling strategy), training data, and training parameters. Here, we introduce a new phase picking neural network stemming from our previous work (Zhou et al., 2019), but incorporates the recent advances in this field targeting at the above factors (Figure 3.3).

We adopt a Self-Attention RNN (SAR) model for phase picking. RNN is a typical deep learning model for sequence modelling, and has been widely adopted in various tasks related to time series, including speech recognition (e.g. Graves and Jaitly, 2014; Hannun et al., 2014) and natural language processing (e.g. Cho et al., 2014; Sutskever et al., 2014). Compared with Transformer (Vaswani et al., 2017), which is recently proven to be powerful in sequence-related tasks, RNNs have much fewer parameters, thus are more data-efficient and require less computational resources, making them a practical choice for small datasets (Ezen-Can, 2020; Peng et al., 2023). RNNs process sequences in a recurrent manner: generating outputs for each time step by integrating the current input with a hidden state that captures previously encountered sequence information. Zhou et al. (2019) first adopt a 2-layer bi-directional Gated Recurrent Unit (GRU) RNN in the phase picking task, where the RNN is trained to classify each 1-s time step as noise, P-wave, or S-wave. In this study, we adopt the same GRU structure with 2 bi-directional layers, and 128 hidden size, but divide the raw data into frames of a much smaller step length (0.5 s) and stride (0.1 s) to increase the theoretical phase picking precision (Figure 3.3a). Moreover, we add a multi-head self-attention layer (Bahdanau et al., 2014; Vaswani et al., 2017) after the GRU layers (Figure 3.3a).

Multi-head self-attention is a mechanism that enhances the performance by allowing the model to simultaneously focus on different parts of the input sequence from different representation subspaces, which makes a key component of the Transformer architecture (Vaswani et al., 2017). In a single self-attention head, the input sequence (i.e. the output of GRU layers in our case) is transformed into three vectors: queries (Q), keys (K), and values (V), which are then used to compute attention scores that determine how much focus each element of the input sequence should have on every other element. This process captures dependencies regardless of their distance in the sequence, making the model able to capture complex dependencies that span across long sequences. Multi-head self-attention improves upon this by dividing the Q-K-V vectors into multiple independent heads, performing the self-attention process parallelly. Thus, each attention head learns to focus on different features of the input sequence, allowing the model to capture a richer array of relationships within the data. The outputs of all attention heads are then concatenated and linearly transformed to produce the final output, which combines the diverse learned representations. Similar attention mechanisms have been proved effective in enhancing the seismic phase picking performance (e.g. Mousavi et al., 2020; Zhang et al., 2023a).

For the model target in the training stage, we label only the frames containing P & S arrivals as P and S, respectively, and all other frames as Noise (Figure 3.3a). This labeling strategy forms a small but finite weight for the P&S arrival times, which guides the model to focus on these features and makes more stable phase detection. Since the invention of such labeling strategy by Zhu and Beroza (2018) for PhaseNet, it has been widely adopted by most of the following deep learning models (e.g. Mousavi et al., 2020; Yu and Wang, 2022; Sun et al., 2023). In the model prediction stage, instead of treating the SAR output as classifications, we only use the output prediction probability, so that users can set the detection threshold based on their own problems. In line with PhaseNet, we also set the default triggering threshold for SAR as 0.3 to balance the detection completeness and accuracy. We regard a group of consecutive frames with a prediction probability above the threshold as a P or S pick, and take the median time of these frames as the picked phase arrival. For the cases when multiple P and S picks exist in a sliding window, we group these picks into all possible P&S pairs, only requiring that the S wave always arrives later than the P wave in a pair. Also, since we apply SAR in a sliding window manner, and that the sliding windows have about half the length overlapping, we will merge the picks from different windows if they have similar P&S picks.

The training samples fundamentally determine how the model behaves. To train the SAR model with the local earthquakes detected by PAL, we design a sampling strategy to properly balance the model’s ability of detecting weak signals and identifying different

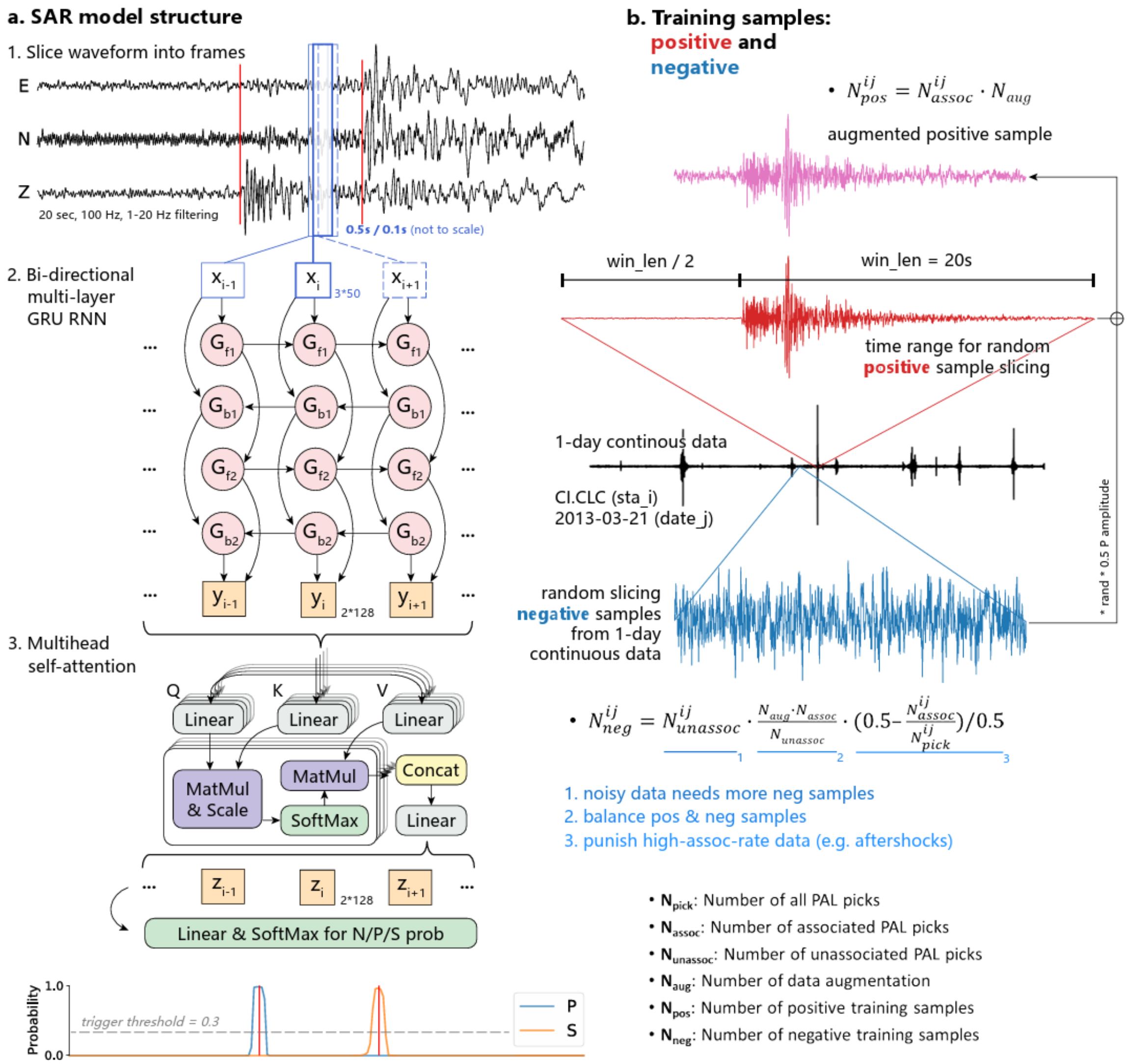

Figure 3.3. The SAR model structure and training sample slicing strategy. (a) SAR model structure. The filtered 3-channel seismogram is plotted in black curves, and the red vertical lines mark the P&S arrival times. The data processing units are denoted by: x_i for the ith input time step; G_f and G_b for forward and backward Grated Recurrent Unit (GRU); y_i for the ith output of the GRU RNN; Q/K/V for Query, Key, and Value input in the multi-head self-attention terminology, and they are all set as the RNN output (i.e. y) in the case of self-attention; "Linear" for fully-connected layer; "MatMul" for matrix multiplication; "Concat" for concatenation; z_i for the ith output of the multi-head self-attention layer; "N/P/S prob" for Noise, P wave, and S wave prediction probability (b) Training sample slice strategy. Blue, red and pink waveforms for negative, positive, and augmented positive samples, respectively.

types of noises (Figure 3.3b). We slice both positive (i.e. earthquakes) and negative (i.e. noise) samples for training. The positive samples are sliced surrounding the PAL-picked

P&S arrivals (Figure 3.3b). We randomly position the P arrival at the first half of the time window, so that the model has a consistent detection ability for random signal positions that it will encounter in the real applications. Data augmentation was employed to increase the diversity of the training set and improve the generalizability of the SAR model. This involves adding real noise, randomly sliced from the same station-date for a specific P&S pick. For each augmented sample, the noise amplitude is scaled by a random ratio between 0 and 0.5, multiplied by the maximum P-wave amplitude. In this way, the number of positive samples is:

$$N_{pos}^{ij} = N_{assoc}^{ij} \cdot N_{aug} \, , \tag{3.1}$$

where i & j is the station and date index, respectively; N_{pos} is the number of positive samples; N_{assoc} is the number of associated picks; N_{aug} is the number of augmentations set by the users. Note that the users need to set the number of augmentations, so that the number of positive samples is large enough (empirically, >100,000). The negative samples are sliced randomly in each station-date pair (Figure 3.3b), while excluding the time ranges that has PAL-picked P&S arrivals. The number of negative samples on a certain station-date is decided by the number of associated and unassociated PAL picks on that station-date:

$$N_{neg}^{ij} = N_{unassoc}^{ij} \cdot \frac{N_{aug} \cdot N_{assoc}}{N_{unassoc}} \cdot \frac{0.5 - \frac{N_{assoc}^{ij}}{N_{pick}^{ij}}}{0.5} \, , \tag{3.2}$$

where i & j is the station and date index, respectively; N_{neg} is the number of negative samples; N_{pick}, N_{assoc} & $N_{unassoc}$ are the number of all picks, number of associated and unassociated picks, respectively; N_{aug} is the number of augmentations set by the users. The logic for each term of this equation is that: (1) the number of unassociated PAL picks indicate the noise level, the more noise a station-date is, the more negative samples we need to slice on it; (2) the number of positive and negative samples need to be balanced in the training process; (3) the pick association ratio indicate the true positive rate of the PAL picks, and a large number of unassociated picks and a high association rate can occur together in an intense sequence (e.g. aftershock sequences), thus we should reduce the number of negative samples in this case. Note that if the association ratio is larger than 0.5, we do not slice any negative samples on that station-date. In this way, we can obtain a temporally stable number of negative samples. We will show in this study that the above sampling strategy realizes stable detection performance.

The training of SAR is performed in a mini-batch manner. We feed both positive and negative samples in each iteration, and train for about 15-20 epochs to make about 100,000 total training iterations. Note that with the third term of Equation 3.2, the total number of negative samples will be smaller than the positives, thus we feed 128 positives and a smaller number of negatives so that they experience the same number of epochs. We adopt the Adam optimizer (Kingma and Ba, 2014) with a learning rate of 10^{-4}. As will be shown in the real cases here and in our previous experiments for RNN (Zhou et al., 2019), the SAR model behaves very stable in the training process, without showing any signs of overfitting.

3.3 Comparison of Cataloging Workflows

To test the detectability and generalizability of our LoSAR workflow, we apply it to two cases that differ in tectonic settings and spatiotemporal scales: (1) the Ridgecrest-Coso (California) region from 2008 to 2019/07, covering its long-term preseismic period and 20-days' early aftershocks; and (2) the East Anatolian Fault Zone (EAFZ, Turkey) from 2020 to 2023/04, which covers ~3 years' preseismic period and ~3 months' aftershocks. Both cases contain large earthquakes that significantly change the seismicity rate and patterns, which makes the cataloging more difficult, and is thus suitable for technical discussions. In these cases, we compare LoSAR with other popular cataloging workflows in terms of earthquake detection completeness, stability, and phase association rate.

3.3.1 Case 1: Ridgecrest-Coso Region (2008-2019/07)

3.3.1.1 Background and Motivation

The 2019 Ridgecrest, California sequence comprised a M_w 6.4 foreshock on 2019/07/04, followed by a M_w 7.1 mainshock on 2019/07/06, and was featured by intense aftershock activities that reveal widespread orthogonal structures (Ross et al., 2019a; Shelly, 2020b). It is associated with a young fault system (Goldberg et al., 2020; Hauksson and Jones, 2020; Xu et al., 2020) and the majority of the ruptured faults are not mapped before the earthquake (Thompson Jobe et al., 2020). Tectonically, the Ridgecrest sequence is situated within the East California Shear Zone (ECSZ), an approximately 100-km-wide band dominated by right-lateral strike-slip faults that accommodates the relative motion between the Pacific and North American plates (Oskin et al., 2008; Spinler et al., 2010; Tymofyeyeva and Fialko, 2015). In this study, we focus on an area not only covering the Ridgecrest ruptures, but also two close-by tectonic units (Figure 3.4): (1) the central Garlock fault (McGill and Sieh, 1993; Ganev et al., 2012; Hatem and Dolan, 2018), a major

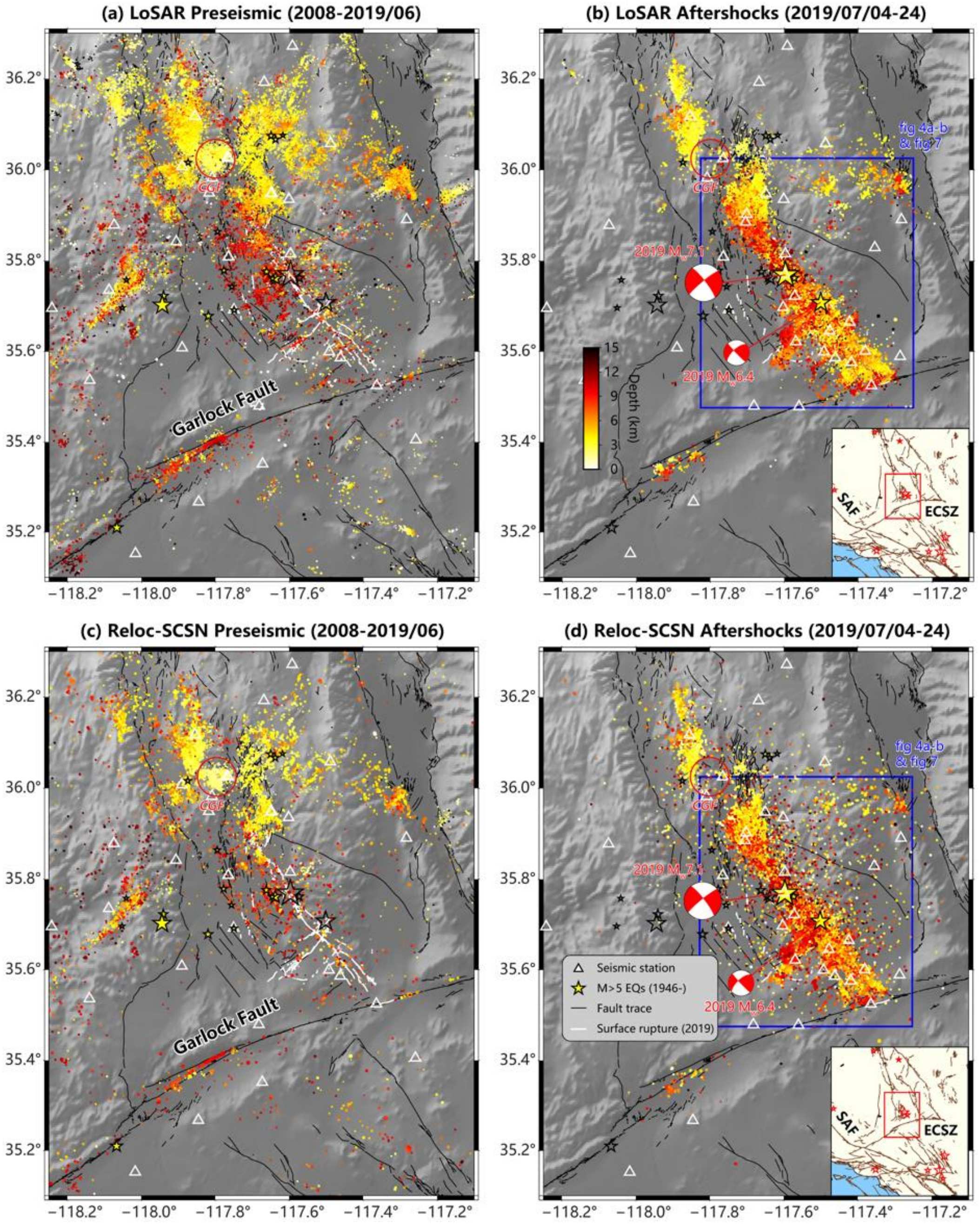

Figure 3.4. Study region and catalog comparison for Case 1: Ridgecrest-Coso (2008-2019/07). (a-b) plot the LoSAR catalog generated in this study, with preseismic period and aftershock period shown separately. Seismicity is plotted as dots that have its depth denoted by color. Active faults are plotted as black lines; surface rupture caused by the 2019 Ridgecrest earthquakes are marked by white lines. The area of Coso Geothermal Field (CGF) is marked by a red circle. The insets show location of the study area in a larger scale, with the San Andreas Fault (SAF) and Eastern California Shear Zone (ECSZ) marked. (c-d) are the same as (a-b), but for the relocated SCSN catalog (Hauksson et al., 2012). The blue box in (b) & (d) marks the location coverage in Figure 3.5a-b.

fault cutting off the Ridgecrest faults on its south; and (2) the Coso Geothermal Field (CGF), one of the largest three geothermal fields in California that has been inducing intense seismicity for decades (Schoenball et al., 2015; Trugman et al., 2016; Im et al., 2021).

We work on a time period from 2008 to 2019, because of the significant improvement in the seismic network starting from 2008 (Hutton et al., 2010), and to overlap with the decade-long QTM matched filtering catalog that covers 2008-2017 (Ross et al., 2019b). This time frame offers an exceptional opportunity to directly compare our novel workflow with MFT. For the aftershock period, we also align our investigations with the MFT catalog by Ross et al. (2019a), which spans the first 20 days since the M_w 6.4 foreshock. Both time periods of the QTM catalog utilize the routine SCSN catalog as templates, adopting a detection threshold of 12 times the median absolute deviation of CC, and are relocated with Growclust (Trugman and Shearer, 2017) that inverse the CC-based differential times. Also involved in the comparison is the relocated SCSN catalog (Hauksson et al., 2012), which has a similar number of detections as the routine SCSN catalog, but has a much higher relocation precision that comes from the CC-based relocation. To make a fair comparison, we utilize the same set of stations maintained by SCSN, which is composed of broad-band and short-period stations of 3- and 1-component recordings, along with several near-source temporary stations deployed after the 2019 mainshock (Figure 3.4).

3.3.1.2 Detection and Location

For this case, we run the LoSAR workflow for the ~11-year preseismic period and the 20-day aftershock period separately, due to the considerable differences in station distribution (Figure 3.4) and seismicity rate. This approach also allows for an assessment of the workflow's performance under two end-member situations: a scenario of very intense sequence observed by a rather dense seismic network, and a pure interseismic period (no large earthquakes) with regular observational condition. We set the LoSAR parameters specifically for the preseismic period, since it is less investigated; and we keep the same set of parameters for the aftershock period to make the results more comparable. In running PAL, we set the STA/LTA triggering threshold as 12 (defined by energy), S wave searching window as 12 s after the P pick, in line with the scale of study region and the average inter-station distance. For PAL association, we require at least 4 stations to have an original time deviation <1.2 s, and a maximum P-wave travel time residual <0.8 s. The PAL obtains 61,053 / 451,694 and 49,737 / 440,942 event detections / associated picks for the preseismic and aftershock period, respectively. In running SAR, we set the window length as 20 s and the sliding stride as 10 s in the predictions for continuous data. We augment the original training samples by 2 times, making a total of 812,771 / 451,689 positive / negative samples for training in the preseismic period, and 792,784 / 123,018 positive / negative training samples for the aftershock period. Note that there are ~10% remaining samples serve as the validation set. The waveforms in a time window are band-pass filtered to 1-20 Hz and normalized in both the training and application stage. We made 15 epochs of training until the accuracy is stable. As described in the last section, we apply the local-trained SAR picker and the same PAL associator to enhance the PAL detections. This gives 165,393 / 1,277,974 and 122,933 / 1,078,038 event detections / associated picks for the preseismic and aftershock period, respectively. In summary, for Ridgecrest-Coso, the LoSAR workflow achieves a ~2.5-2.7-fold increase in detection number compared to PAL.

To locate and relocate the LoSAR detections, considering a rather dense network, we adopt the first approach described in Section 3.2.1 (Figure 3.1), utilizing *dt.ct* and *dt.cc* separately for a two-step relocation. Similar as the detection part, we adopt the same set of location parameters for both the preseismic and aftershock period. For the hypoINV absolute location, the distance weighting is configured as follows: 0-50 km assign full weight, >100 km zero weight, and 50-100 km is assigned a cosine tapered in between. A similar weighting scheme is employed for the time residual between 0.25 and 0.75 s. For S waves, the weights are further adjusted by a factor of 0.6, considering a larger picking error relative to P waves. The above weighting strategy results in 95.4% events well located, and an average lateral and vertical uncertainty of 1.11 km and 2.22 km, respectively. In the hypoDD relocation process with *dt.ct*, we pair events within 8 km (i.e. WDCT, in hypoDD terminology), P & S waves weighted respectively as 1 and 0.6, and inverse for 4 iterations. This results in a relative location error of about 120 m for epicenter and 150 m for depth, under the least square criteria by hypoDD. Given that the least-square location error reported by hypoDD tends to significantly underestimate the real uncertainty, we test the *dt.ct* relocation results under different velocity models, and found highly consistent distributions. In the final CC relocation stage, we measure the waveform-based differential time on 1-20 Hz band-pass filtered waveforms, with the P and S window length set as 2.5 s and 4 s, starting from 0.5 s and 0.2 s before the phase arrival, respectively. We do not calculate *dt* between $M_L<0$ earthquakes to lower down the computational costs. A maximum number of 200 neighboring events are preset in the candidate neighbor selection step, sorted by the separation distance. After the CC calculation, we discard the measurements with CC<0.35, or *dt_p*>0.5 s, or *dt_s*>0.8 s, and the event pairs with <4 stations fulfilling these criteria are further dropped. The above selections finally maintain 18,421,488 P and 12,506,600 S differential time measurements for the preseismic period. For the aftershocks, these numbers are 13,718,530 for P and 8,422,550 for S. In the hypoDD relocation process, we link events within 4 km (i.e. WDCC, in hypoDD terminology), set both P and S waves' weights as 1 and inverse for 4 iterations, because S waves have higher stability in waveform cross-correlation. Finally, we obtained 101,193 and 61,578 well-relocated events for the preseismic and aftershock period, respectively. For both catalogs, the average relocation error reported by hypoDD is about 40 m and 60 m along horizontal and vertical directions, respectively. Note that this location error is in the relative and average sense, and reflects more about the goodness of data fitting, instead of the real uncertainty.

3.3.1.3 Catalog Comparisons

The cataloging methodology and parameters outlined in the last subsection yield the seismicity distribution shown in Figure 3.5. The LoSAR catalog and the relocated SCSN catalog exhibit an overall consistent distribution, particularly in areas of major intense clusters. Nonetheless, the LoSAR catalog demonstrates a significantly enhanced detection capability, rendering previously indistinct seismicity structures much more discernible (Figure 3.4). To make a more comprehensive and quantitative comparison, we plot the frequency-magnitude distribution (FMD) and magnitude-time sequences of the relocated SCSN, the QTM catalog, and the LoSAR catalog for both the aftershock and preseismic period (Figure 3.5).

FMDs serve to illustrate not only the total number of detections, but also the distribution of events across different magnitude bins. Ideally, a FMD should adhere to the GR law (Gutenberg and Richter, 1944), meaning that for the magnitude range above a completeness threshold (approximately the magnitude of maximum non-cumulative distribution, Wiemer and Wyss, 2000), the occurrence frequency of earthquakes is expected to follow a power-law distribution relative to their magnitudes (i.e. a linear relationship when plotted on a logarithmic scale). Furthermore, the objective of earthquake detection is also to achieve the smallest possible magnitude of completeness, or equivalently, the largest possible cumulative count. Applying the above criteria to analyze the FMDs, it becomes evident that LoSAR has a comparable or superior detectability compared with QTM, especially for the preseismic period (Figure 3.5a-c). While QTM shows a higher detection ability for the intense aftershock sequence (Figure 3.5a), it is noteworthy that ratio of well-located events determined by the Growclust algorithm falls below 35% (Figure 3.5b). This result also suggests that a trade-off between the quantity of detections and the quality of their locations, emphasizing the necessity of keeping comparable relocation precision for an equitable comparison of detectability across methodologies. In addition to overall event counts, the slope of these FMDs also offer critical insights. First, an apparent inconsistency in detection completeness exists in both the SCSN and QTM catalogs between the M 0-2 and M >2 events, as evidenced by the varying slopes in the FMDs (Figure 3.5a-c). Second, also for the SCSN & QTM catalog,

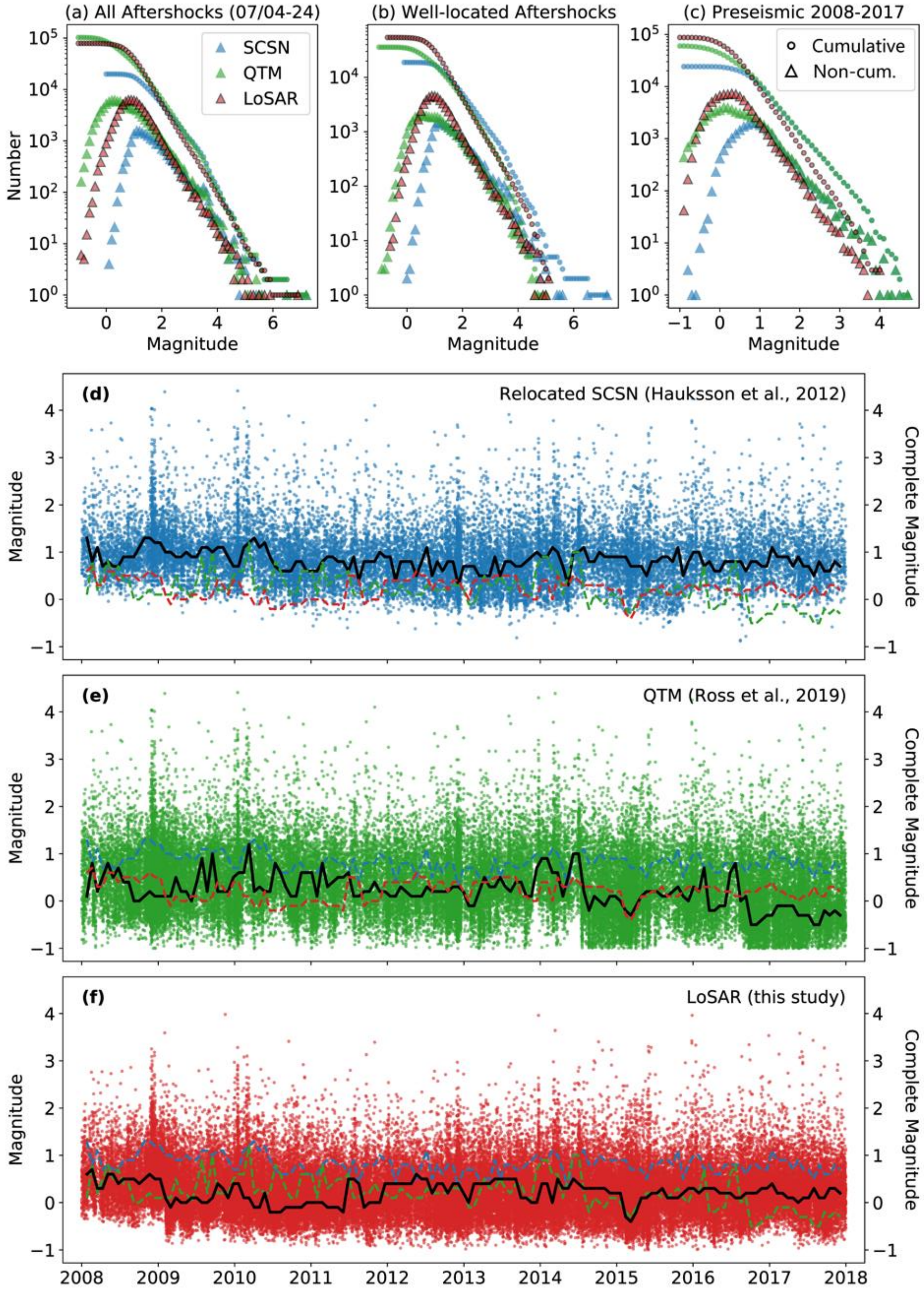

Figure 3.5. Comparison of FMD and magnitude-time sequence. The blue, green, and red color denote the SCSN catalog, the QTM catalog, and the LoSAR catalog in this study, respectively. (a-c) plot the FMD comparison for the total aftershock detections, well located aftershocks, and the preseismic period (2008-2017), respectively. The dots and triangles denote cumulative and non-cumulative distribution in FMD. (d-f) plot the magnitude-time comparisons for the preseismic period (2008-2017). The thick black lines denote the magnitude of completeness in the current panel, and the colored dash lines plot that for two other catalogs.

there is a noticeable shift in the FMDs' slope around M 3.5 (Figure 3.5a-c). This shift is partially caused by the adoption of different magnitude scales (e.g. M_l, M_w, or M_{lr}, as detailed at https://scedc.caltech.edu/eq-catalogs/change-history.html), which can affect the catalog-based b-value studies. The LoSAR catalog does not exhibit the aforementioned issues, demonstrating a consistent detection performance across the magnitude range in this study.

The magnitude-time sequence reveals the temporal evolution of seismicity, which is modulated by external sources, such as tectonic loading, as well as internal triggering between earthquakes (Ogata, 1988; Zhuang et al., 2002; Zaliapin and Ben-Zion, 2020; Hsu et al., 2024). Thus, statistical studies will require a catalog to have temporally stable detection capability for both the intense sequences and the background seismicity. In our case in the Ridgecrest-Coso preseismic period, we observe that the SCSN catalog is not temporally consistent, displaying high detectability mainly during the intense seismic sequences (Figure 3.5d). This pattern arises from the SCSN catalog's compilation process, which involves a semi-automated detection supplemented by manual inspections, particularly for intense seismic sequences (as detailed at https://scedc.caltech.edu/eq-catalogs/change-history.html). The issue of temporal inconsistency is not alleviated, but being exacerbated in the QTM catalog, as indicated by the highly variable lower magnitude limit (Figure 3.5e). It is probably due to the fact that earthquakes within an intense sequence tend to have high waveform similarity, making them easy to be detected by matched filtering; Conversely, the background seismicity comes from a wider variety of faults and asperities, which inherently diminishing the effectiveness of matched filter. In contrast, our

LoSAR catalog realizes markedly improved stability in detection throughout this 11-year period (Figure 3.5f), without showing any notable gaps in the detection of lower magnitude events. This robustness suggests that the SAR model is adept at capturing the statistical features of seismic events over a large spatiotemporal range, thus making it a more generalized algorithm for long-term earthquake detection.

In our final comparison, we assess the computational efficiency of the LoSAR workflow against QTM. The entire LoSAR process (including running PAL) is executed within ~7 days with 1 Nvidia GeForce RTX 2080 GPU card and 1 Intel Xeon E5-2695 CPU. Contrarily, the construction of the QTM catalog requires 200 Nvidia P100 GPU cards, with a runtime exceeding 60 days. Although the study area of QTM is ~20 times larger, there is still a 100-fold difference in computational efficiency. This significant difference is attribute to the computationally intensive nature of cross-correlation and that the linear increase in runtime with the addition of templates in matched filtering.

In conclusion, the LoSAR workflow not only exhibits superior detection capabilities and stability compared to the matched filter approach, but also significantly outperforms in computational efficiency. This makes it particularly advantageous for applications across extensive spatiotemporal scales.

3.3.2 Case 2: East Anatolian Fault Zone (2020-2023/04)

3.3.2.1 Background and Motivation

On February 6, 2023, Southeast Turkey's Kahramanmaraş region was struck by an M_w 7.8 earthquake followed by another M_w 7.6 within ~9 hours, marking one of the largest continental earthquake doublets ever documented (Dal Zilio and Ampuero, 2023; Hussain et al., 2023; Jia et al., 2023; Xu et al., 2023b; Zhang et al., 2023b; Ren et al., 2024). The 2023 Turkey earthquake doublet occurs on the East Anatolian Fault Zone (EAFZ), a roughly ~600-km-long fault zone defining the plate boundary between the Anatolian and Arabian plates (Figure 3.6). Driven by the collision between the Arabian and Eurasian plates, the Anatolian plate is extruded westward at a rate of approximately 20-25 mm/yr, along with a counterclockwise rotation (McClusky et al., 2000; Bulut et al., 2012; Barbot and Weiss, 2021; Güvercin et al., 2022). This plate motion give rise to the predominantly left-lateral strike-slip characteristics observed along the EAFZ. Additionally, the fault slip rate along the EAFZ is relatively low, ranging from ~4 mm/yr on the SW segments to ~10 mm/yr on the central and NE segments (Cavalié and Jónsson, 2014; Walters et al., 2014; Aktug et al., 2016; Weiss et al., 2020). It is noteworthy that the two mainshocks of the 2023 doublet are associated with different fault systems (Figure 3.6): the first M_w 7.8 mainshock (denoted as *M1*) occurs on the major plate boundary faults, whereas the second M_w 7.6 mainshock (denoted as *M2*) ruptures the intraplate faults. The distinct aftershock patterns observed across this dual faults suggest contrasting fault properties (Ding et al., 2023; Güvercin, 2024).

In this study, we build a seismic catalog covering the entire EAFZ, a task that presents technical challenges due to the large spatial extent, and the relatively sparse seismic network, with its inter-station distances ranging from about 30 to 60 km (Figure 3.6). This network density is representative of most regions outside of the well-monitored areas like California and Japan. We start our analysis from 2020, because of the significant enhancement of Turkey seismic network in that year, spurred by a M_w 6.8 earthquake on

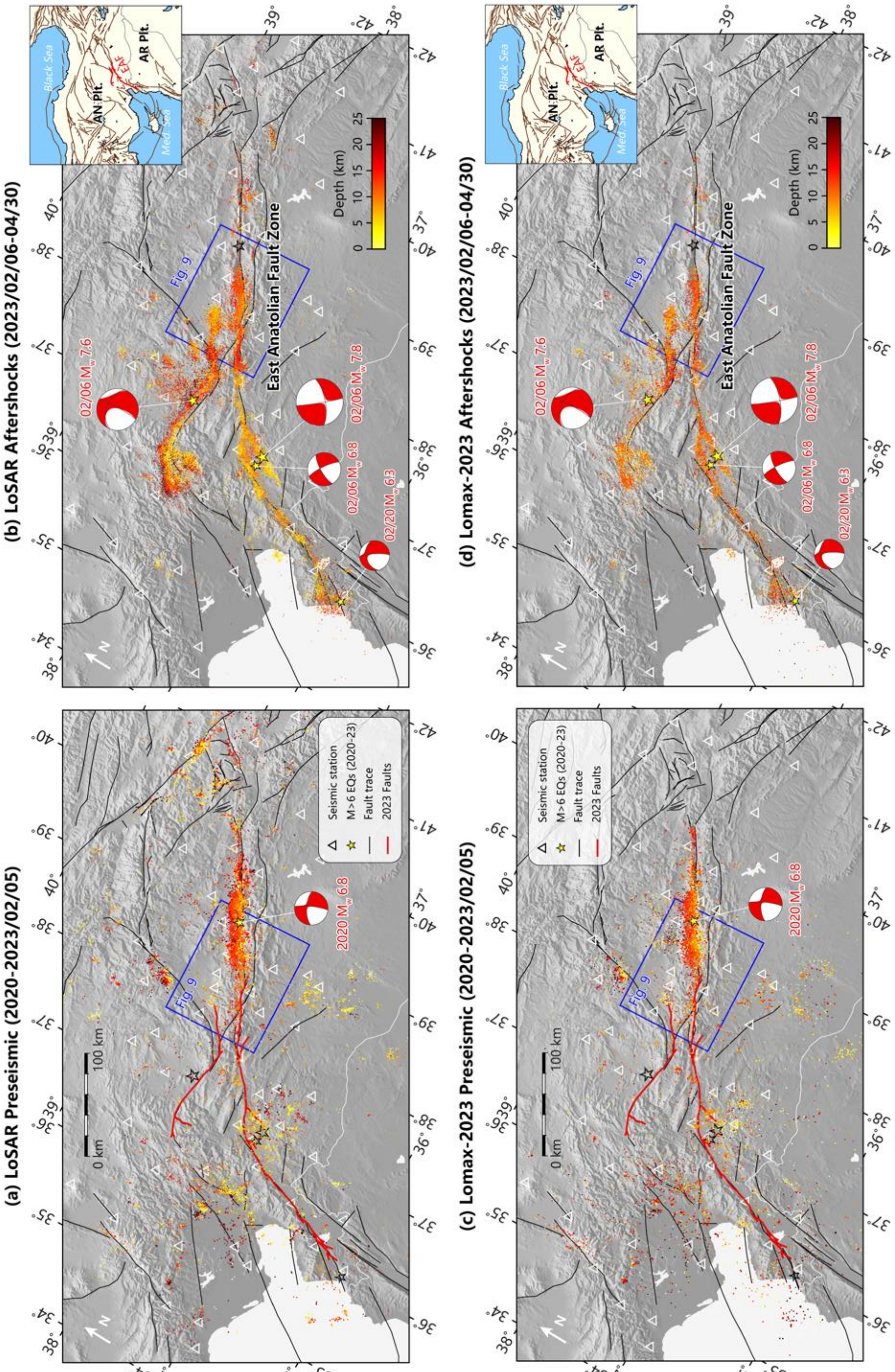

Figure 3.6. Study region and catalog comparison for Case 2: EAFZ (2020-2023/04). (a-b) plot the LoSAR catalog generated in this study, with preseismic period and aftershock period shown separately. Seismicity are dots that have its depth denoted by color. Active faults are plotted as black lines; responsible faults for the 2023 earthquake doublet are marked by red lines. The insets show location of the study area in a larger scale. (c-d) are the same as (a-b), but for the relocated AFAD catalog by Lomax (2023).

January 24, 2020, that ruptured the NE side of the 2023 rupture zones (Gallovič et al., 2020; Lin et al., 2020; Melgar et al., 2020; Pousse-Beltran et al., 2020). Our study extends over a 3-month aftershock period to 2023/04, which expands our previous rapid work that only covers 1 months' early aftershocks (Ding et al., 2023) and the 2-month aftershock period examined by Güvercin (2024). We combine 3-channel broad-band stations from multiple networks, including the TU network from the Disaster and Emergency Management Presidency (AFAD) and the KO network from the Kandilli Observatory and Earthquake Research Institute (KOERI). Instead of discussing this case in the EAFZ alone, we will combine the previous case in the Ridgecrest-Coso to compare the generalization ability of different phase picking and association algorithms in earthquake detection. This is motivated by the fact that the two cases are associated with contrasting tectonic settings, spatiotemporal scales, and network configurations.

3.3.2.2 Detection and Location

Contrary to our first case in Ridgecrest-Coso, for this case in EAFZ, we execute the LoSAR workflow over a combined ~3.5-year pre-postseismic period. This approach offers additional validation of LoSAR's capability to handle highly variable seismicity rates. The detection and location parameters for this EAFZ case largely align with those used in the Ridgecrest-Coso case, with the exception of several parameters adjusted to accommodate the expanded scope and density of the network.

In running PAL, the phase picker utilizes the same triggering threshold, but an 18-s S wave search window, which corresponds to a ~150-km epicentral distance. The PAL associator maintains a 4-station requirement, but different in the limit for original time deviation as <1.6 s and the P-wave travel time as <1.2 s. These specifications resulted in 47,416 / 295,494 event detections / associated picks. In running SAR, we set a larger window length of 25 s and maintain the same 10-s sliding stride. We augment the original training samples by 2 times, making a total of 516,168 / 322,894 positive / negative training samples. Similarly, ~10% remaining samples are used for validation. We applied the same data preprocessing, and made 20 epochs of training until the accuracy is stabilized. After applying the locally-trained SAR picker and the same PAL associator, we got 140,119 / 929,944 event detections / associated picks, which represents a ~3-fold increase in the number of detections compared to PAL.

To locate and relocate these detections, we adopt the second approach described in Section 3.2.1 (Figure 3.1), utilizing both *dt.ct* and *dt.cc* in the second round of relocation. For the hypoINV absolute location, we also weight the phases by its epicentral distance and residual times, but set a less restrictive set of parameters to account for the sparser network: the distance weighting is configured as 0-80 km full weight, >160 km zero weight, and 80-160 km cosine tapered; the time residual weighting is configured in the same way between 0.4 s and 1.2 s. Similar as for Ridgecrest-Coso, the S-wave weights are further adjusted by a factor of 0.6. The hypoINV outputs ~93.1% well located events, with an average lateral and vertical uncertainty of 2.48 km and 3.73 km, respectively. Note that the location error is highly variable across our study region, due to the heterogenous station distribution. In the first round of hypoDD relocation with *dt.ct,* we pair events within 20 km (i.e. WDCT, in hypoDD terminology), and P & S waves weighted as 1 & 0.6, inversed for 4 iterations. The relocation uncertainty is also correlated with the station density, ranging from about 180-280 m for epicenter and 250-550 m for depth, under the least square criteria by hypoDD. For CC-based differential time measurements, we filter the waveforms to 1-12 Hz, considering the sparser network, while keeping the same P and S windows as in Ridgecrest-Coso. We only calculate *dt* between $M_L>0.5$ earthquakes and other events. We limit a maximum number of 50 neighboring events in the candidate selection step, and we require CC>0.3, *dt_p*<1 s, and *dt_s*<1.75 s, in addition to a minimum number of 4 stations fulfilling these criteria. The above processes finally obtain 3,719,995 P and 2,961,716 S differential times. For the final hypoDD relocation process that combines *dt.ct & dt.cc*, we made 2 sets of inversions. In the first round, we set WDCC and WDCT as 4 km and 10 km, and weighted the *dt.ct* data strongly; in the second round of inversion, the WDCC and WDCT are set to 2 km and 5 km, with the *dt.cc* being dominantly weighted. Using this weighting scheme, we benefit from both the high-precision *dt.cc* data and the wide coverage of *dt.ct* that helps maintain more events in relocation. Finally, we obtained 93,680 well-relocated events, with an average relocation error ranging from about 40-80 m and 70-120 m along horizontal and vertical directions, respectively. Furthermore, aiming for a higher-resolution catalog (at the cost of reducing the number of detections), and for a more realistic estimation of location uncertainty, we also applied the first approach outlined in Section 3.2.1 (Figure 3.1) to relocate the LoSAR detections. We exclusively used dt.cc for relocation, setting WDCC as 2 km and performing the inverse over 4 iterations. This yielded 56,656 events with a much lower relocation uncertainty and an overall consistent distribution of seismicity. However, it is important to note that this relocation approach results in a considerable reduction of events above the completeness magnitude, rendering it less suitable for b-value analysis.

The detection and location strategies elaborated above result in a significantly enhanced catalog compared with the relocated AFAD catalog produced by Lomax (2023), as show in Figure 3.6. Such advancement is made possible by a much higher detectability and relocation precision. Similar as in Ridgecrest-Coso, the LoSAR catalog exhibit ideal FMDs and magnitude-time series in EAFZ, effectively capturing the seismicity features for both the preseismic and postseismic period.

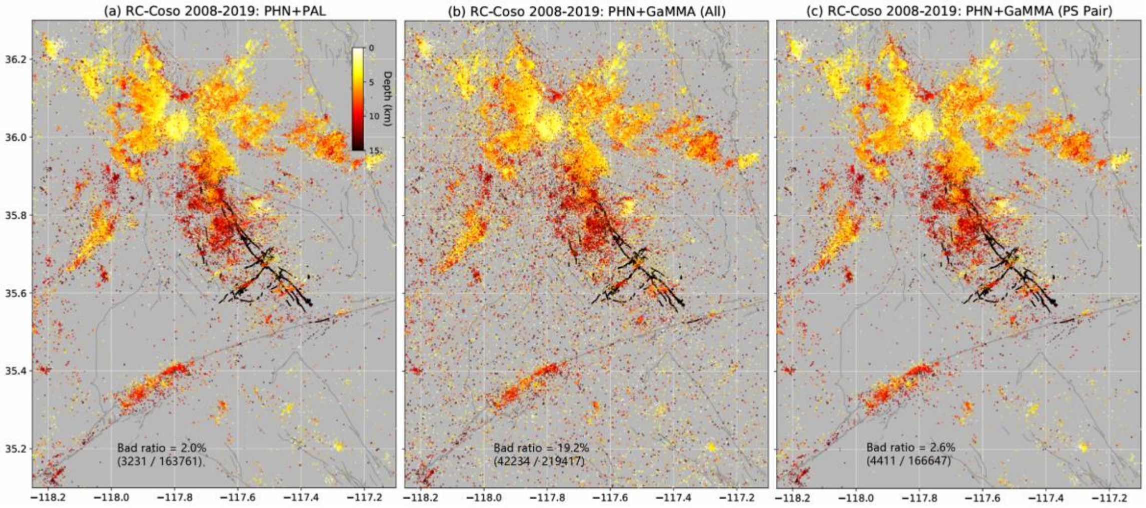

Figure 3.7. Comparison of location results with different association algorithms for RC-Coso preseismic period (2008-2019/06). (a-c) plot the map-view distribution of the hypoInverse location results, where the input phase files are generated by PhaseNet (PHN) + PAL associator, PHN + GaMMA (all picks), and PHN + GaMMA (only paired P&S picks), respectively.

3.3.2.3 Comparisons with Both Cases

Utilizing this case in the EAFZ pre-postseismic period, along with our previous case in the Ridgecrest-Coso preseismic period, we conduct detailed comparisons against PhaseNet (Zhu and Beroza, 2018) and GaMMA (Zhu et al., 2022d), both of which are considered as the state-of-the-art phase picking and association algorithms, and are being widely adopted in cataloging workflows (e.g. Zhang et al., 2022c; Zhu et al., 2022c). Through these comparisons, we can evaluate the scalability of these algorithms across different tectonic environments, spatiotemporal ranges, and network densities.

In executing PhaseNet and GaMMA, we adhere primarily to their default parameters and the behaviors anticipated for typical users, which are intended to be broadly applicable. For PhaseNet, we use 30-s time windows that slide in 15-s steps. They are larger than what we set for SAR picker in the two cases, and should have enough coverage. The waveforms are high-pass filtered above 1 Hz. We keep the default triggering threshold at 0.3. Picks from overlapping sliding windows are merged using a 0.5-s window, where the picks with higher prediction probabilities are selected. Note that PhaseNet pick P & S arrivals independently, and we pair them up to combine with the PAL associator. The phase pairing strategy is consistent with that used for the SAR picker; however, it necessitates manually setting an S-wave search window, which we keep the same as for PAL picker in the two cases. For GaMMA, we set the criterion at a minimum of 8 phases to declare an event detection, aligning this requirement with the 4-station criterion of the PAL associator that we applied in both the EAFZ and Ridgecrest-Coso cases. It is important to highlight that the association results from GaMMA do not necessarily ensure paired P and S phases for each station. However, we observed that directly utilizing the GaMMA outputs for hypoINV lead to a significant number of events unconstrained (Figures 3.7 & 3.8). Consequently, we opted to refine the GaMMA outputs by excluding the stations with only single P or S picks and imposed a requirement for a minimum of 4 stations.

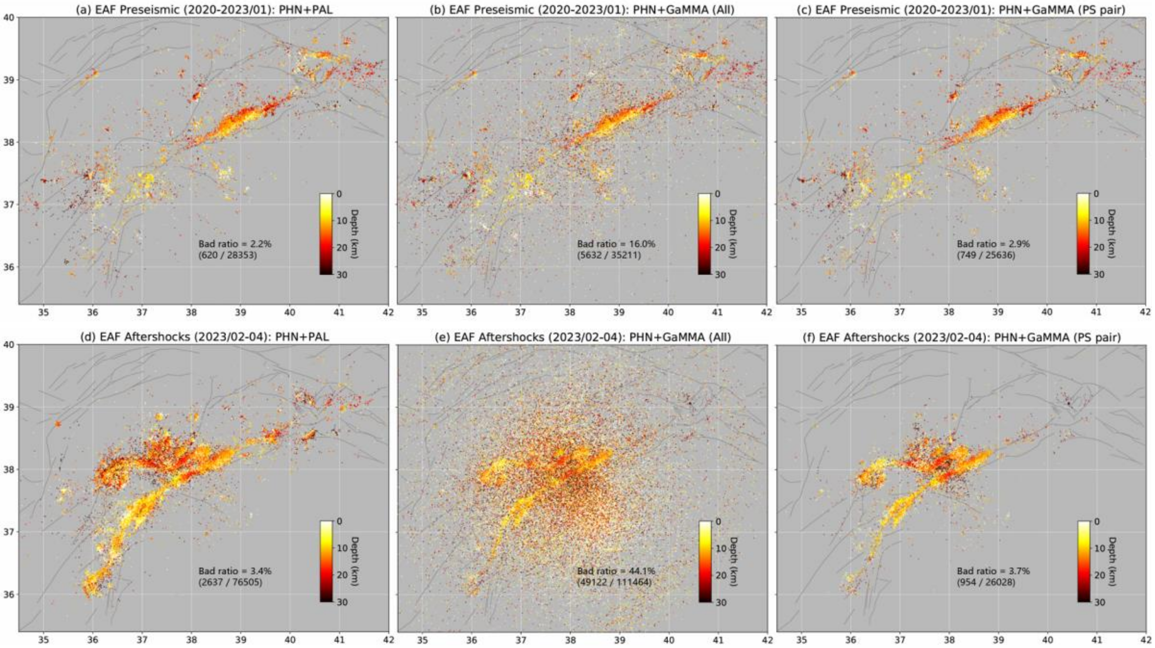

Figure 3.8. Comparison of location results with different association algorithms for EAF pre-postseismic period (2020-2023/01). (a-f) plot the map-view distribution of the hypoInverse location results, where the input phase files are generated by PhaseNet (PHN) + PAL associator, PHN + GaMMA (all picks), and PHN + GaMMA (only paired P&S picks), respectively. (a-c) plot the preseismic period (2020-2023/01) and (d-f) plot the aftershock period (2023/02-04).

We first compare the number of associated picks and the association ratio (Figure 3.9a-b & e-f). We assume that the association process filters out most of the false picks, thus the number of associated picks represents the phase detection completeness, and the association ratio indicate the detection accuracy. In the Ridgecrest-Coso case, all three combinations of AI-driven picker-associator setups (i.e. PhaseNet+GaMMA, PhaseNet+PAL, and LoSAR) achieved a similar number of associated picks, with an association ratio around 10% (Figure 3.9a-b). This performance markedly outperforms that of the STA/LTA method, as represented by PAL, demonstrating the advanced picking accuracy and completeness afforded by deep learning methodologies that learn from waveform features. Note that PhaseNet is originally trained on Northern California data,

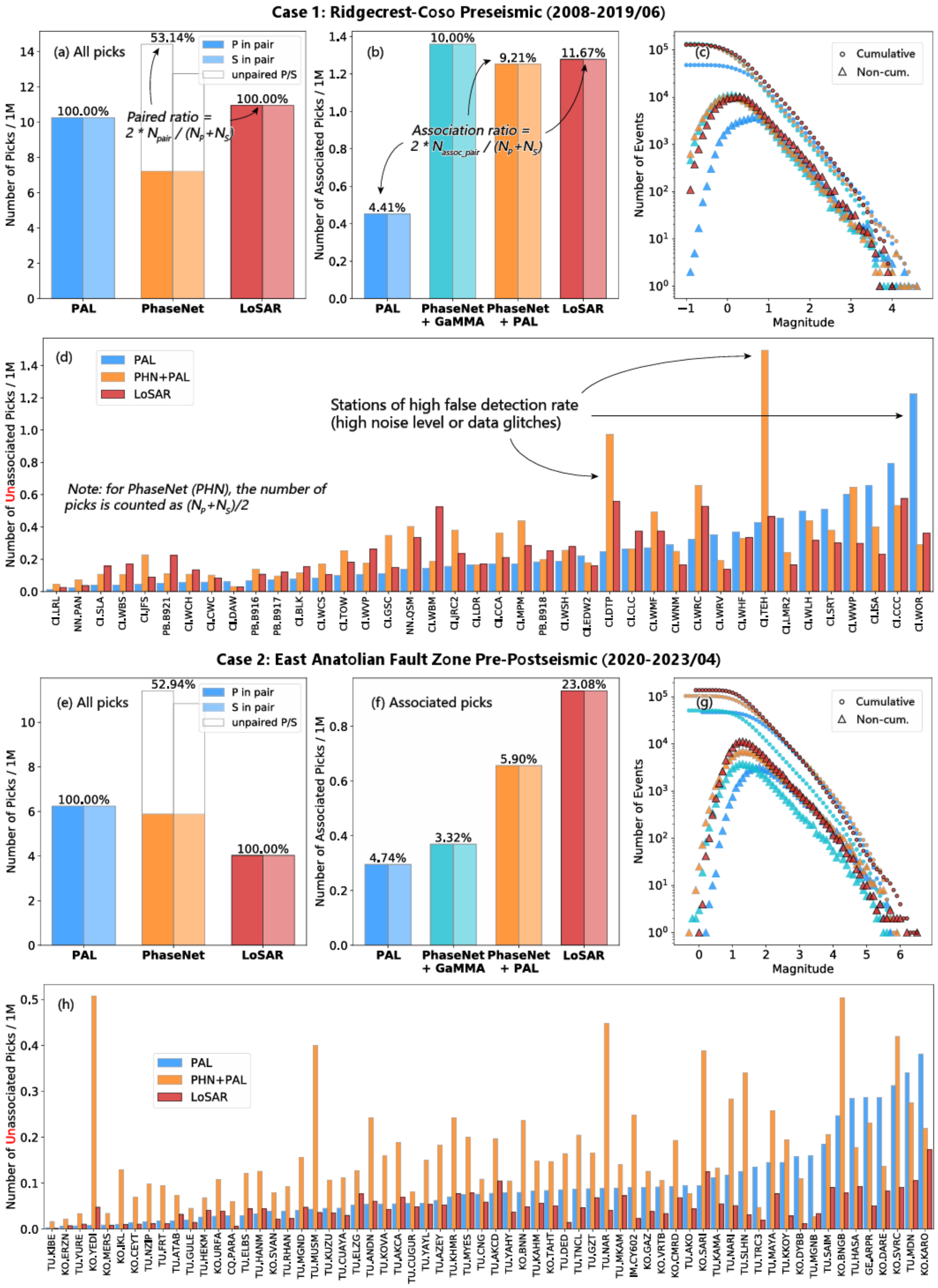

Figure 3.9. Comparison of phase picking and association performance. The blue, cyan, orange, and red markers denote the results by different pickers and associators. (a & e) plot the number of picks. The P & S picks are marked by darker and lighter colors. The paired P&S picks are filled by color; (b & f) plot the number of associated picks; (c & g) plot the FMD comparison, where circles and triangles denote cumulative and non-cumulative numbers, respectively; (d & h) plot the number of unassociated picks on each station. (a-d) and (e-h) plot the Case 1 (Ridgecrest-Coso) and Case 2 (EAFZ), respectively.

thus is intrinsically localized for the Ridgecrest-Coso case. Moreover, all three methods recalled ~97% events in the SCSN catalog, showing great consistency in event detection. In contrast, in the EAFZ case, the number of associated picks by LoSAR surpasses that of PhaseNet+PAL by ~1.5 times, and ~2.5 times more than PhaseNet+GaMMA (Figure 3.9e-f). Furthermore, both PhaseNet+PAL and PhaseNet+GaMMA demonstrate significantly lower association ratios (5.9% and 3.3%, respectively) in comparison to LoSAR’s 23.1%, as well as to their performances in the Ridgecrest-Coso case (~10%). This result indicates that PhaseNet is less tailored for the EAFZ data, and that GaMMA suffers from a much larger-scale network with sparse station distributions. By comparing the FMDs (Figure 3.9c & g), it is evident that the three AI-driven picker-associator combinations show high consistency in Ridgecrest-Coso, as previously noted. However, PhaseNet+GaMMA displays noticeable discrepancies for the EAFZ case, missing a significant portion of events above the complete magnitude. Excluding this particular instance, the remaining seven catalogs across both cases display consistent FMDs for the portion above completeness magnitude, aligning with the expectations set by the G-R law.

Lastly, we examine the number of unassociated picks across all stations in both cases (Figure 3.9d & h). Given the presumption that a large portion of the unassociated picks represent false detections, the spread of unassociated picks across stations serves as an indicator of a phase picker’s detection stability. In our analysis, we compare three phase pickers: PAL, PhaseNet, and LoSAR, employing PAL (based on STA/LTA) as the benchmark for evaluating PhaseNet and LoSAR. The rationale behind this comparison stems from the high sensitivity of STA/LTA algorithms to pulse-like noises (e.g. data glitches), which often results in a higher volume of unassociated picks. Consequently, when PhaseNet or LoSAR generate significantly more unassociated picks than PAL, it suggests a high false detection rate for low-SNR phases. In both cases, there is no correlation in the number of unassociated picks between PAL and the two AI-based pickers (Figure 3.9d & h), demonstrating the AI pickers' effective ability to discriminate against pulse-like noises. This performance aligns with expectations due to their design to analyze whole-waveform characteristics. However, even in the case of Ridgecrest-Coso (Figure 3.9d), a few stations were identified where PhaseNet produced a significantly higher number of unassociated picks compared to PAL. Such instability of PhaseNet is notably severer in EAFZ, where multiple stations recorded more than twice the unassociated picks than PAL (Figure 3.9h). These observations suggest that PhaseNet may be sensitive to certain types of low-SNR noises. A similar behavior is also observed with LoSAR's picking results, albeit to a lesser extent (Figure 3.9d). The above observations highlight a potential area for improvement in AI-picker's noise discrimination capabilities, and a multi-station-based picking algorithm could offer a solution (e.g. Feng et al., 2022; Sun et al., 2023).

In summary, our comparative analysis across cases with divergent characteristics demonstrate the LoSAR's superiority in detection completeness and stability over PhaseNet, as well as PAL's greater scalability in phase association compared to GaMMA. These attributes position LoSAR as a notably robust workflow for compiling long-term, large-scale seismic catalogs.

3.4 Conclusions

In this study, we introduce LoSAR, an innovative deep learning-driven workflow for constructing long-term seismic catalogs. It is designed based on the idea of training a deep learning model with local data. By applying LoSAR to two distinct cases in the Ridgecrest-Coso and EAFZ region, we demonstrated that LoSAR realizes a detection ability comparable to MFT, while offering markedly improved temporal stability and computational efficiency. Through direct comparisons with other state-of-the-art phase picking and association algorithms, we conclude that LoSAR has superior scalability and generalizability. These advantages position LoSAR as an ideal tool for building catalogs of a large spatiotemporal scale.

Chapter 4

High-Resolution Seismicity Imaging and Characterization of Fault Behavior

4.1 Introduction

Leveraging the high-resolution catalogs developed by our novel algorithms, we conduct practical analysis in characterizing fault behaviors before and after a large earthquake. Our investigations to be presented in this chapter covers: (1) early aftershocks of the 2023 Turkey Mw 7.8 & 7.6 earthquake doublet, (2) preseismic fault behavior of the Erkenek-Pütürge fault segment (EPF) of EAFZ, (3) Ridgecrest-Coso region, and (4) the Xiaojiang fault zone in SE Tibet. These case studies provide insights into seismic hazard assessment prior to large earthquakes and rapid responses following significant events. As a general strategy, we utilize seismicity distribution to infer the fault geometry and using b-value as an indicator of stress level. We mainly focus on spatial patterns, because the examinations of temporal seismicity evolution and b-value variation demand more rigorous analysis and statistical techniques, thus fall beyond the scope of this chapter.

The seismicity imaging technique relies on the understanding that earthquakes, regardless of their size, occur on faults, including both major and subsidiary ones. Consequently, the clustered seismicity serves as a tool to detect geologically hidden faults, and to direct delineate fault structures at depth with a high resolution (e.g. Waldhauser and

Schaff, 2008; Hauksson et al., 2012; Ross et al., 2019b; Shelly, 2020b). However, the occurrence of seismicity is intricately linked to the stress and frictional state of faults (as reviewed in Bürgmann, 2018), which introduces several caveats in the interpretation of seismicity distribution. For example, certain fault segments can be quiescent during the interseismic period, because of the stress shadow drawn by a deeply penetrated rupture of previous large earthquakes (Jiang and Lapusta, 2016). Therefore, a lack of continuous seismicity does not necessarily imply a discontinuity in fault structure. Another commonly observed phenomenon is the complementary distribution between aftershocks and coseismic slip (Wetzler et al., 2018; Toda and Stein, 2022). In such cases, aftershocks tend to concentrate on the periphery of ruptured asperities, thereby obscure the fault dip in cross-section views. Thus, to accurately infer fault geometry, it is always recommended to jointly consider the focal mechanism solutions and the surface traces of faults or ruptures (e.g. Lu et al., 2021; Zhou et al., 2022a; Ding et al., 2023).

The b-value in the GR-law, which quantifies the relative number of large versus small earthquakes, is inversely related to the stress level, as demonstrated by numerous experimental and statistical studies (Scholz, 2015, and references therein). In this study, we obtain the spatial distribution of b-values by calculations performed on each grid cell, incorporating earthquakes within a specified radius. Given a set of earthquakes, the b-value can be estimated by the maximum-likelihood method (Aki, 1965):

$$b = \frac{\log_{10} e}{\bar{M} - M_C + \frac{\Delta M}{2}}, \tag{4.1}$$

where $\bar{M}$, M_C, and ΔM is the mean magnitude, lower cut-off magnitude, and the magnitude bin, respectively. The b-value uncertainty is estimated following Shi and Bolt (1982):

$$\delta b = 2.3 \times b^2 \times \sqrt{\sum_{i=1}^{n} \frac{(M_i - \bar{M})^2}{n(n-1)}}\ , \tag{4.2}$$

where n is the number of events. For reliable b-value estimations, we require a minimum number of events above the cut-off magnitude, typically >80. It is important to recognize that the b-value uncertainty determined by Equation 4 tend to underestimate its true variability (Woessner and Wiemer, 2005; Amorèse et al., 2010; Marzocchi et al., 2019). Therefore, we conduct additional tests to prevent over-interpretation in our applications, which includes: (1) Adjusting the slicing radius for each grid, which affect the number of events in b-value estimations; (2) Modifying the cut-off magnitude (M_C), given that b-value estimation is positively correlated with M_C (Cao and Gao, 2002; Zhou et al., 2018); and (3) whether to adopt a uniform M_C or calculate M_C individually on each grid. Note that we opt to use a uniform M_C in the main text, based on the considerations mentioned above.

4.2 Early Aftershocks of the 2023 Kahramanmaraş (SE Türkiye) M_w 7.8 & 7.6 Earthquake Doublet

4.2.1 Introduction

On 2023/02/06 (UTC), two M_w ~7.8 earthquakes struck the Türkiye-Syria boarder region near Kahramanmaraş (Figure 1a) consecutively within ~9 hours, resulting in enormous loss in life and properties (Dal Zilio and Ampuero, 2023; Erdik et al., 2023; Goldberg et al., 2023; Hussain et al., 2023; Mai et al., 2023; Melgar et al., 2023; Petersen et al., 2023). An M>7.5 earthquake doublet is extremely uncommon, and even a single continental earthquake of similar size dates back to 2016 M_w 7.8 Kaikōura earthquake. Both mainshocks of the 2023 Kahramanmaraş (Türkiye) M_w 7.9 & 7.8 doublet (abbreviated as M1 & M2 thereafter, moment magnitude measured by Jiang et al., 2023) are larger than any other earthquakes ever recorded in Türkiye during the instrumental period, and are probably the largest in pre-instrumental era as well (along with the 1939 Erzincan M7.8 and 1114 Kahramanmaraş M7.8, Karabacak et al., 2023; Karabulut et al., 2023; Mai et al., 2023). Thus, it is of great social and scientific importance to understand the mechanisms of this doublet. As shown by real-time aftershock detections, strong motion records, surface ruptures, and satellite images, the first M_w 7.9 mainshock (M1) ruptures the Eastern Anatolian Fault (EAF), a major fault that defines the Anatolia-Arabia plate boundary (Figure 1a); and the second M_w 7.8 mainshock (M2) occurs on the Sürgü Fault (SF) within the Anatolia plate. However, a major portion of both faults do not generate intensive microseismicity before the earthquake (Güvercin et al., 2022), and thus the fault geometry is poorly constrained.

Early aftershocks illuminate the seismogenic faults at depth (e.g. Shelly, 2020b; Tan et al., 2021), and its temporal evolution is indicative of postseismic fault behaviors (e.g. Jiang et al., 2021b; Zhou et al., 2022a). Traditionally, template matching is used with cataloged events to augment original detections and to enhance the relative locations. However, the quality of templates (e.g. event detection and phase picking) is highly variable among network systems, and manual catalogs always suffer from temporal inconsistency (see comparisons in Zhou et al., 2021b), thus can bias the matched filter results. This motivates the birth of PALM (Zhou et al., 2021b), a complete workflow for continuous data that consists of phase Picking, Association, Location, and Matched filter. In this study, we adopt PALM to build a high-resolution early aftershock catalog for the 2023 sequence, which directly images the structure of seismogenic faults and can facilitate future studies, such as dynamic rupture processes and earthquake triggering.

4.2.2 Catalog Construction

For the catalog construction, we downloaded continuous seismic data of 43 broad-band stations from TU & KO network ranging from 2023/02/01 to 2023/02/28. The network provides a decent coverage for ruptured area, and has an average inter-station distance of ~40 km. Note that defects do exist in the SW side, where the faults stretch into the Mediterranean Sea; and that the stations are less dense along the SF. We process the continuous data with PALM (Zhou et al., 2021b), as detailed in Chapter 2.

In running PAL, we detect P wave with an STA/LTA triggering threshold of 12 (defined by square amplitude), and search for S wave within 15 s following P. The raw data are preprocessed by a 1-20 Hz band-pass filter. In the phase association process, we require at least 4 stations that have an original time deviation <1.6 s and P travel time residual <1.2 s. We locate and relocate the 13,585 PAL detections with hypoInverse (Klein, 2002) and hypoDD (Waldhauser, 2001), respectively. In hypoInverse, we weigh different phases by the epicentral distance, time residual, and type of phase. Stations within 40-120 km and picks with a residual from 0.2-0.6 s are tapered from full to zero weight. P and S waves are weighted as 1 & 0.6, respectively. This results in only 496 out of 13,585 events (~3.6%) not well constraint by hypoInverse. The absolute location uncertainty reported by hypoInverse is about 900 m and 2100 m in horizontal and vertical direction, respectively. We further refine the relative location with hypoDD. We link the events within 20 km hypocentral separation (WDCT=20), and perform 4 iterations of inversion with 808,336 catalog-based *dt* measurements (*dt.ct*). We relocate events only within the study region (35.6-38.6°N; 35.5-39.2°E), and 12,243 out of 13,369 events (~92%) remain after this process. The relocation uncertainty reaches ~300 m & 800 m along horizontal and vertical direction, under the least-square criteria of hypoDD, and the average time residual is reduced below 0.19 s.

For MESS, we set the window length for event detection as 1 & 11 s pre- & post-P arrival, and that for P & S *dt* measurement is 2.5 s and 4 s, starting from 0.5 s before phase arrival. The raw data are preprocessed by 1-16 Hz band-pass filtering. In the detection process, we require at least 3 stations with CC>0.3. Detections from different templates are associated as one detection if the original times fall within 1.2 s. In the relocation process, we adopt only P and S *dt* <1.2 s and <2 s, respectively, and each event needs to be linked to at least 2 other events. This gives 805,835 CC-based *dt* measurements (*dt.cc*). We jointly inverse *dt.ct* and *dt.cc* with hypoDD, and set WDCT=20; WDCC=10 to let different datasets control the relative locations at different scales. Note that the weight for *dt.cc* data is set as 10 times larger than the *dt.ct* data, so that the final resolution is mostly determined by the high-resolution *dt.cc* data. After 4 iterations of inversion, we finally got 29,519 well-located events, which significantly improves the routine catalog by Disaster and Emergency Management Presidency (AFAD) in detection numbers (11,703 in the same area) and location precision (see next subsection). The final relocation uncertainty is about

70 m & 200 m in horizontal and vertical direction, with an average *dt.ct* & *dt.cc* residual of 0.23 s & 0.02 s, respectively.

Several caveats to be mentioned:

(1) The location uncertainty is an average value for all detected events, thus events in locations with poorer station coverage may have larger errors. Besides, only the distribution of a cluster of events can be interpreted, instead of individual events.

(2) Waveform of large events usually have lower similarity with smaller ones, thus the M>~5 events may be dropped in the CC-based relocation process.

(3) The local magnitudes (M_L) are estimated by S wave amplitude and hypocentral distance, and the magnitude for each event is measured independently (see Zhou et al., 2021b for more details). Thus, for large events (M>~5.5) that cause waveform clipping, the magnitudes tend to be underestimated.

4.2.3 Results and Discussions

4.2.3.1 Comparison with existing catalogs

We compare the PALM catalog with another catalog built by Lomax (2023), who utilizes NLL-SSST algorithm (Lomax and Savvaidis, 2022) to relocate the AFAD catalog. For the detection completeness, PALM catalog includes 29,519 well-relocated events with a complete magnitude (M_C) of M_L 1.4, while that of the original and relocated AFAD catalog in the same spatiotemporal range is 11,703 and 10,396, respectively, with an M_C of M_L 2.0. For the location result, the overarching difference between the two catalogs is that the PALM catalog shows a much wider depth range (Figure 4.1a-b). This difference mainly comes from the data: due to the data accessibility, Lomax (2023) only used TU

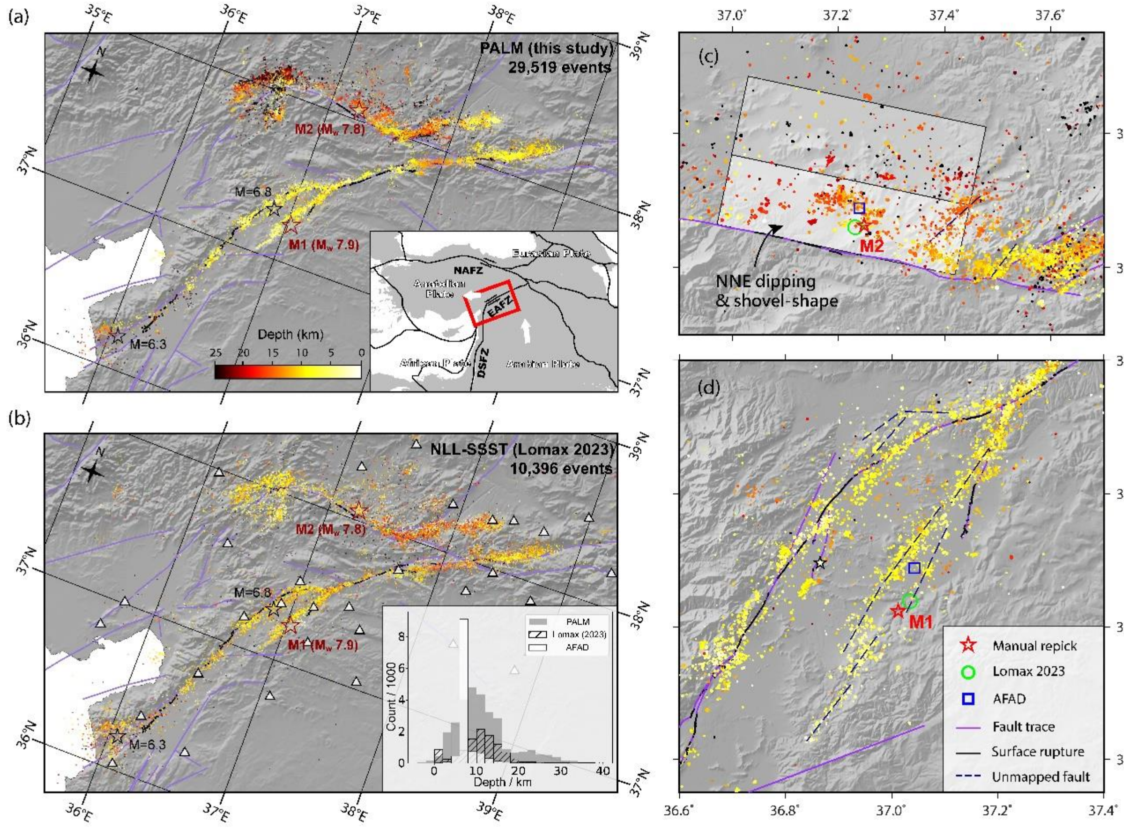

Figure 4.1. Comparison of cataloging results. (a-b) plot the overall distribution of aftershocks by the PALM method and Lomax (2023), respectively. Events are plotted as dots with the color coded by depth, and size proportional to magnitude. Inset in (a) shows a regional tectonic overview, with the red rectangle indicating the study area. Major plate-boundary faults are abbreviated as EAF: Eastern Anatolian Fault, NAF: Northern Anatolian Fault, and DSF: Dead Sea Fault. Inset in (b) shows the depth distribution of the PALM catalog, Lomax (2023), and AFAD. (c-d) show a zoom-in view of the PALM catalog around the two mainshocks. The epicenter of mainshocks obtained by this study, Lomax (2023), and AFAD are plotted by red star, green circle, and blue rectangle, respectively. The solid purple lines denote the fault traces from the GEM Global Active Faults Database; the solid black lines are the surface ruptures of activated mapped faults provided by USGS; the dashed lines in (c) are the unmapped faults interpreted along with microseismicity. The transparent boxes in (c) plot the interpreted fault planes with different dip angles.

network in the absolute location with NLL, and only KO network in the SSST relative relocation process, which is much sparser; besides, the phase picks from AFAD is much more scattered in the travel time ~ hypocentral distance plot compared with that by PAL (Figure 4.2), showing low phase picking accuracy. Other factors, including different relocation algorithm and velocity models, also add variations in the relocation results, e.g. the resolution and number of off-fault events (Figure 4.1a-b). Despite those differences, the first-order pattern of depth distribution in our PALM catalog is more consistent with the relative location between the epicenters and fault traces, the moment tensor (Figure 4.3a), and the rupture model (Figure 4.3c). See next subsection for more detailed discussions.

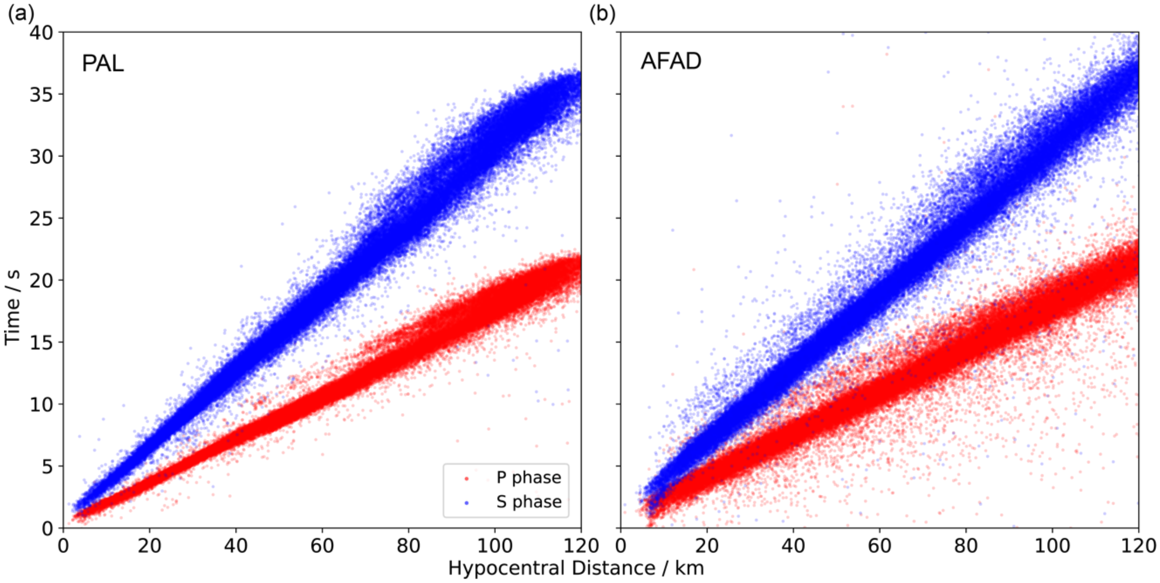

Figure 4.2. Relation of hypocentral distances and travel-time. (a-b) display the hypocentral distance and time relation according to the initial hypocenters obtained by the PAL and AFAD catalogs, respectively. The red and blue dots represent the P- wave and the S- wave phases, respectively.

We also relocate the hypocenter of two mainshocks by manually picking the first arrivals and run hypoInverse (Figure 4.1c-d). In this process, we adopt both broad-band and strong motion data, which is much denser. Note that we do not use S wave, since the complex rupture makes S arrival hard to identify, and that the S wave associated with the weak first arrival is buried under the P tails, making the S-P time overestimated. This results in a similar epicentral location with that by Lomax (2023) (Figure 4.1c-d). However, the focal depth is less well-constraint because of the lack of S picking. We tested different weighting schemes and found that the M1 hypocentral depth probably ranges from 4.5-6.0 km, and that for M2 is 7.5-10.5 km. Picking the arrivals of subsequent phases and their location migration is helpful in understanding its nucleation process (e.g. Lomax, 2020).

4.2.3.2 Structure of seismogenic fault

The PALM catalog contains abundant information on fault structures in different scales. For fine-scale features, we specifically analyze the hypocentral area of the two mainshocks (Figure 4.1c-d). For M1, the hypocentral location indicates that it nucleates from the branching fault (Figure 4.1d). Microseismicity reveals complexity of this branch, including several subparallel faults and stepovers, which are not mapped by geological field investigations even after the earthquake. Other smaller branches are also developed along the major EAF, forming an en échelon structure, as also observed in Xiaojiang fault zone (Zhou et al., 2022b) and San Andreas fault (DeLong et al., 2010). The major trend of aftershocks does not follow the surface fault trace, indicating that fault dip varies along strike.

For M2 (Figure 4.1c), aftershock distribution shows that the nucleation segment of the SF (O5-O6) is dipping to the NNE direction, and the dip angle decreases with depth (jj' & kk' in Figure 4.3b), forming a shovel shape. This fault orientation is consistent with the moment tensor (Figure 4.3a) and the location of surface fault traces. Such shovel-shape faults are commonly observed under compressional regime, e.g. the Longmenshan fault that generates 2008 M_w 7.9 Wenchuan earthquake (Lei and Zhao, 2009; Fang et al., 2013;

Zhang et al., 2022a). Besides, the microseismicity seems to show a change in fault strike near the epicenter (Figure 4.1c). A more detailed analysis on the fine-scale seismicity distribution and aftershock focal mechanisms can further constrain the fault geometry, which benefits the dynamic rupture studies.

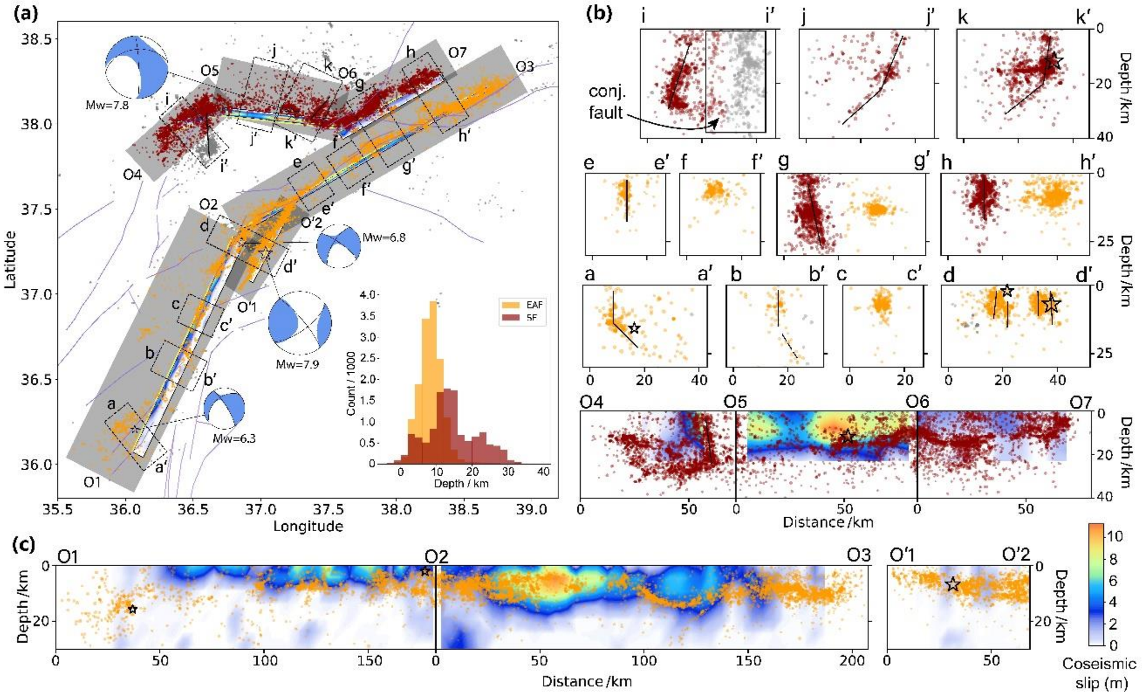

Figure 4.3. Detailed aftershock distribution and interpretation of fault structure. (a) shows the map-view of aftershocks by the PALM method, events in which are plotted as dots with size proportional to magnitude. Orange and crimson dots in each filled area are projected to the gray rectangle's southeast side that is subparallel to the EAF and the SF, respectively, to get the along-fault profiles. Dots in each dashed rectangle are projected to the longer side of the rectangle to get the normal-fault profiles. Events not included in the filled rectangles are plotted as gray. Black stars represent the epicenter of M>6 events, and the same projection strategy as dots is applied to stars. The slender colored rectangle is the surface projection of the USGS-NEIC finite fault model. The solid purple lines are the same as that in Figure 4.1. Focal mechanism solutions for the M>6 events are from GCMT. Inset in (a) shows the depth distribution of events by the PALM method along the SF and EAF. The top three panels in (b) show the normal-fault profiles resulting from (a). Lines indicate the fault dip inferred from the aftershock distribution. The bottom panel of (b) and (c) show the along-fault profiles for the SF and EAF, respectively, in which the USGS-NEIC finite fault model for the two mainshocks are also projected. The convention of the color-coded dots in (b-c) is the same as that in (a).

On a large scale, the EAF shows a much simpler fault geometry compared with the SF, featuring only one major bend near the M1 epicenter and a near-vertical fault dip, except in the SW corner, where multiple branching faults intersect. Moreover, the seismicity along EAF is generally shallower (<15 km) and more concentrated in depth, while that along the SF expands a much wider depth range (Figure 4.3b-c). The dominant depth of seismicity along EAF probably indicates the lock-creep transition zone, where stress are concentrated at the crack tip (Jiang and Lapusta, 2017). It can be validated by the good complementary pattern with the USGS-NEIC coseismic slip (Figure 4.3c, Goldberg et al., 2023). Note that several slip models have been obtained from different groups and are generally consistent (e.g. Barbot et al., 2023; Li et al., 2023b; Mai et al., 2023; Melgar et al., 2023; Xu et al., 2023a). The highly depth-concentrated seismicity also makes it harder to determine the fault dip, and the horizontally distributed aftershocks in the fault-normal profiles suggest multiple subparallel faults as discussed in the previous section (e.g. cc’ & ff’-hh’ in Figure 4.3b).

In contrast, the SF is characterized by two significant fault bends and a relatively low-angle dip that varies both with depth and along strike. From the fault-normal cross sections, the dip angle for the O4-O5 segment is about 75° to NW; the O5-O6 segment dips at ~70-80° in shallow portions, and ~40-55° in deeper portions; the mapped segment along O6-O7 (gg’) dips ~80° to SE. Aftershocks on the major portions of SF reach depths of ~35 km deep, whereas they decrease to <15 km in the eastern end, which corresponds to an unmapped branch. The deep aftershocks agree well with the thick crust in the east Anatolian Plate (Vanacore et al., 2013; Ogden and Bastow, 2021), and the ~35-km aftershock extension is still above the ~40-45-km Moho depth, thus are within the crust. The broad depth distribution of seismicity implies that the fault is partially coupled, with no abrupt transition between fully locked and fully creeping behavior. Researchers can further investigate the differences in source parameters and statistical features to gain insights into the contrasting fault behaviors.

4.2.3.3 Migration of early aftershocks

Aftershocks usually expand a wider spatial range than the rupture zone (Neo et al., 2020), and the temporal evolution provide insights on earthquake triggering mechanism (e.g. Kato and Obara, 2014; Sirorattanakul et al., 2022). In the study area, the seismicity within 5 days before the first mainshock distributes in the eastern end of rupture, which is an active segment related to the 2020 M_w 6.8 earthquake (Gallovič et al., 2020; Melgar et al., 2020; Pousse-Beltran et al., 2020; Taymaz et al., 2021). No seismicity clusters near the M1 epicenter, and a M_L 4.2 event occurred off the EAF (Figure 4.4a-b). Thus, we found no immediate foreshocks or precursors based on seismicity between Feb. 1st and M1 in our catalog (Figure 4.4a). Before the second mainshock (T1 in Figure 4.4), all seismicity occurs on the EAF, and the SF is completely quiescent. During this period, the aftershock magnitude on the western segment (O1-O2) seems to be significantly higher than the eastern segment (O2-O3). After the second mainshock (T2 in Figure 4.4), the SF is activated, while the seismicity on the O2-O3 segment of EAF is suddenly suppressed (Figure 4.4c), which can be explained by the stress shadow drawn by the coseismic slip on SF (Toda et al., 2023). The aftershock zone continues expanding on both major faults ~2 days after the second mainshock, especially to the western sides of both faults (i.e. near O1

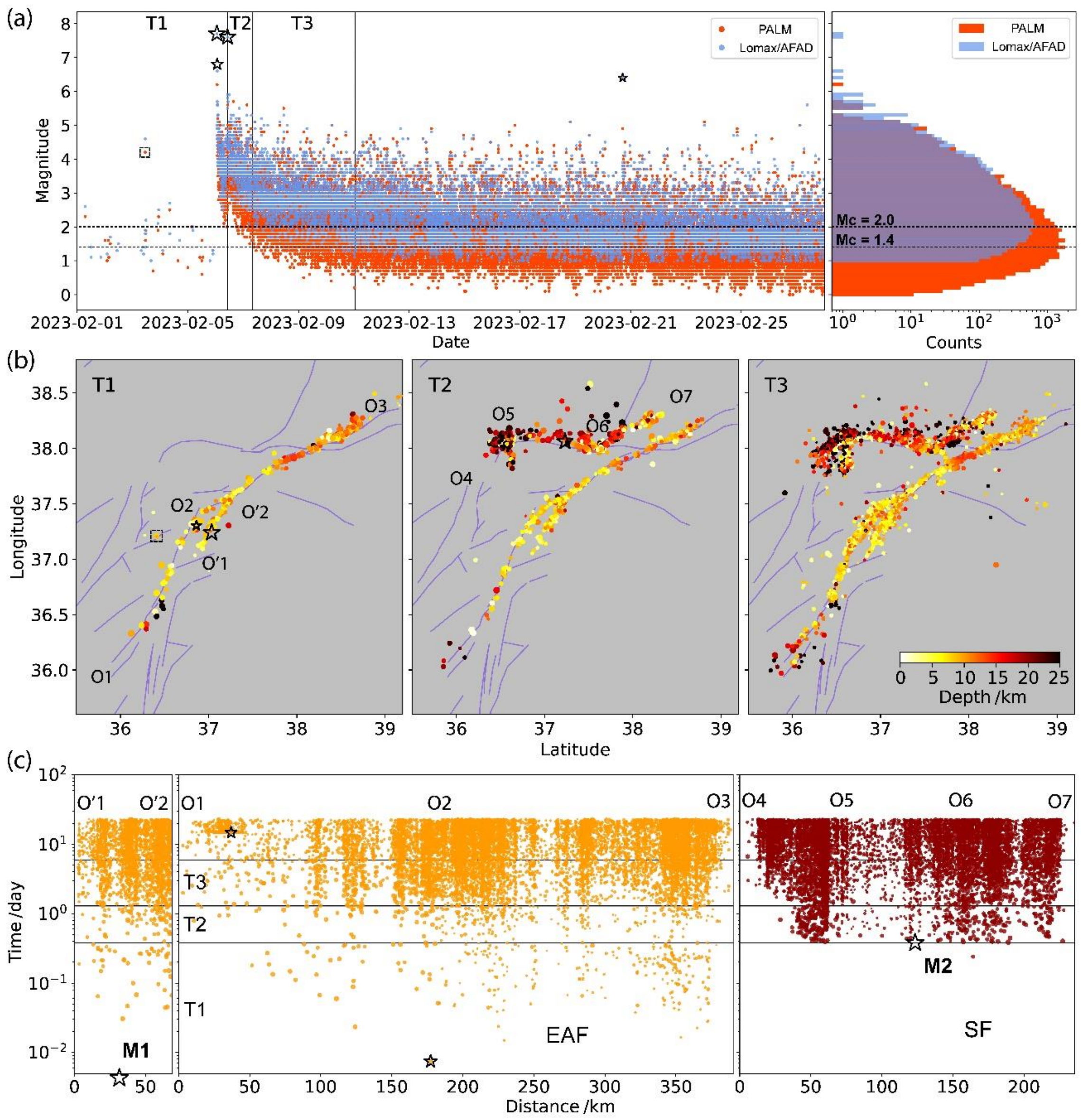

Figure 4.4. Temporal behavior of aftershocks. (a) Left panel shows the magnitude-time sequence of the PALM and AFAD catalogs. Vertical solid lines divide major evolution periods. The right panel shows the FMD comparison. (b) plots the map-view event distribution of the PALM catalog during T1, T2, and T3. Endpoints of along-fault profiles shown in Figure 4.2a are also marked. The solid purple lines are the same as that in Figure 4.1a. (c) shows the temporal evolution in seismicity along the profiles of the EAF and the SF shown in Figure 4.3a. The time is calculated from the original time of M1, and the distance is calculated along the southeast side longer side of the filled rectangles in Figure 4.3a. Note that time is displayed in logarithmic scale. The convention of the color-coded dots is the same as that in Figure 4.3a. Horizontal solid lines represent the time separation same as that in (a).

& O4), which is indicative of afterslip (e.g. Kato and Obara, 2014; Jiang et al., 2021b). Thus, it is highly plausible that the western ends of both faults exhibit aseismic fault slip and terminate rupture, whereas the eastern ends serve as barriers due to their low stress level following the 2020 M_w 6.8 event. The aftershock zone ceases to expand after T3, and a daily variation in the lower magnitude range emerges (Figure 4.4a), a common feature attributed to anthropogenic noise (e.g. Li et al., 2021b; Zhou et al., 2021a). In summary, the aftershocks of 2023 SE Türkiye sequence show intriguing temporal behavior, and our new PALM catalog provides a solid foundation for further studies on the postseismic processes.

4.2.4 Summary

In this subsection, we present a high-resolution early aftershock catalog for the 2023 SE Türkiye earthquake doublet. Our main findings are:

(1) the aftershocks on EAF are shallow (<15 km) and highly concentrated in depth, while that on the SF has a wide depth range down to ~35 km.

(2) the major portions of EAF are near-vertical, but complexities are revealed in the fine-scale, including subparallel sub-faults, unmapped branches, and stepovers.

(3) the SF has a relatively low dip angle (~40-80°) for strike-slip faults, and the segment responsible for M2 nucleation is shovel-shaped at depth.

(4) no immediate foreshocks are found in ~5 days before M1, and no seismicity exists on SF before M2.

4.3 Erkenek-Pütürge Fault Segment (EPF) of EAFZ

As reviewed in Section 3.3.2.1, the 2023 Turkey doublet is extraordinarily large for continental environments, raising questions about the mechanisms that allow an earthquake to reach such size. Instead of investigating how the rupture grows, we are curious about how it terminates. Specifically, we explore the termination of the *M1* rupture at its NE end, named as Erkenek-Pütürge fault segment (EPF), which acted as a barrier not only for *M1*, but also for the 2020 M_w 6.8 earthquake and multiple historical and paleoseismic events (Hubert-Ferrari et al., 2020; Güvercin et al., 2022; Karabacak et al., 2023). Fortunately, the observational condition for this segment of the EAFZ were optimal during our study period from 2020 to 2023, which set a solid foundation to examine the formation of this persistent barrier.

4.3.1 Fault structure interpretation

Firstly, we utilize all seismicity from 2020-2023 to image the fault structure (Figure 4.5). The map view (Figure 4.5a-b) and cross-sections (Figure 4.5c) reveal an along-strike variation in fault structure: from a single major fault in profile 01-04, to a major-secondary fault style in profile 05-10, and then to a wide fault zone from profile 11-15, and reverts to the major-secondary pattern in profile 16-18. A zoom-in plot with CC-relocated LoSAR catalog (Figure 4.6c) show that the ~10-km wide fault zone (profile 11-15) is composed of two major subparallel branches, along with several subsidiary conjugate faults in between. Intriguingly, the surface fault traces in this area also exhibit two subparallel branches with shapes similar to the seismicity observed at depth, but of a much narrower width (Figure

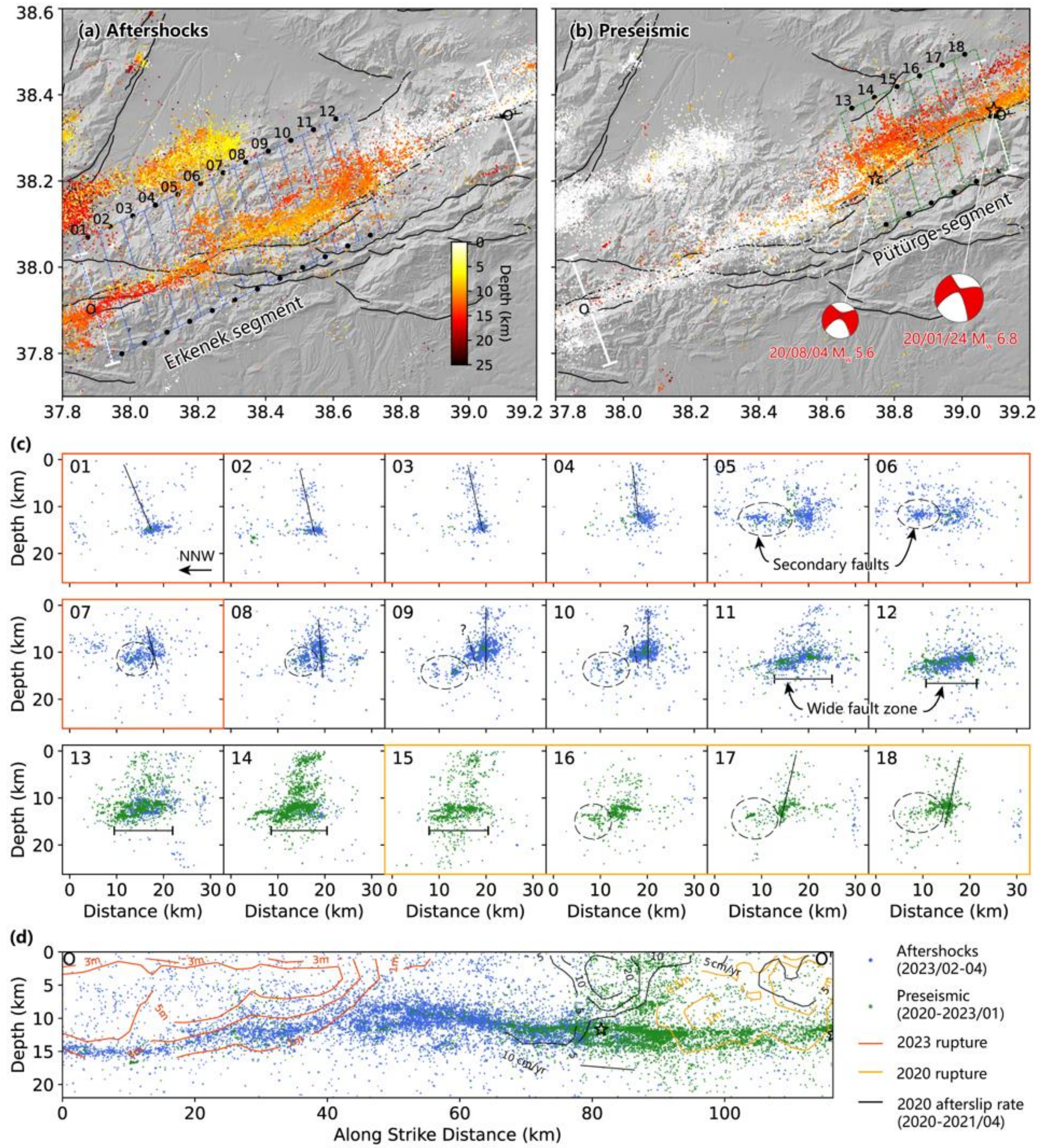

Figure 4.5. Seismicity and fault geometry interpretation for the Erkenek-Pütürge fault segment (EPF) of EAFZ. (a-b) plot the map-view distribution of postseismic (2023/02-04) and preseismic period (2020-2023/01) seismicity. The events in current panel / time period are color coded by the depth, and the seismicity in the other time period is plotted as white dots in the bottom. (c) plot the fault-normal cross-sections. The 2023 aftershocks and preseismic events are denoted in blue and green, respectively. The interpreted fault dip is marked as black lines. (d) plot the along-strike cross-section. The coseismic slip of the 2023 M_w 7.8 obtained by Ren et al. (2024) is plotted in orange-red contours, the coseismic slip and afterslip slip of the 2020 M_w 6.8 obtained by Cakir et al. (2023) are plotted as orange and black contours, respectively.

4.6c). This may imply that the fault zone broadens as it extends deeper into the crust, a scenario not commonly observed (Scholz, 1988; Ben-Zion and Sammis, 2003; Scholz, 2019). In addition to the aforementioned structural variation is a shift in the dip angle of the major fault, which gradually change from an SSE-dipping in profile 01-04 to an NNW-dipping in profile 17-18 (Figure 4.5c). This contrast in fault dip direction of the EPF is also reflected in the moment tensors of the 2023 *M1* (subevent inversion by Jia et al., 2023) and the 2020 M_w 6.8 & M_w 5.6 (Figure 4.5b). These structural variations appear to correlate with the coseismic behavior, with the unruptured segments (profile 08-14) show greater geometrical complexity, in contrast to the relatively simpler structures that were ruptured in 2023 (profile 01-07) and 2020 (profile 15-18).

4.3.2 B-value Analysis

We further examine the b-value distribution before the 2023 mainshocks (Figure 4.6a-b). Note that we exclude events occurring within 24-hr following the 2020 M_w 6.8, since it causes a transient incompleteness in the catalog that can bias the b-value estimation. However, we tested that using different time ranges do not alter the relative values in the distribution. The b-value distributions, derived from both the LoSAR catalog and that by Lomax (2023), reveal that the 2020-ruptured area is characterized by a relatively high b-value, which agree with the significant stress drop after the large earthquake. Notably, this segment also exhibits a gap of M>4 earthquakes in our study period (Figure 4.6d), further supporting a significantly reduced stress level. Another area of high b-value coincide with the area experiencing large afterslip following the 2020 mainshock (Cakir et al., 2023). In the map-view distribution (Figure 4.6a-b), the secondary faults show relatively higher b-value compared to those observed along the major fault, which suggest a contrast in the strength between major and secondary faults. The area near the NE end of the 2023 ruptures also appear to have a high b-value before the earthquake (Figure 4.6a). This area also displays highly variable focal mechanisms, indicating complex local structures. However, the reliability of this feature may be compromised due to the significantly fewer events that occurred before the 2023 mainshock. In addition to the high-b areas mentioned above, a markedly low-b area extends over 15 km length along strike, located southwest of the 2020 M_w 5.6 aftershock (Figure 4.6a-b). This area probably represents an unruptured asperity that has not experienced any M>5.5 earthquakes so far. Observations of postseismic deformation following the 2023 sequence may help to rule out the alternative hypothesis that the stress in this segment has been relieved through aseismic slips.

Back to the question posed in the beginning of this subsection, the high b-value observed in the northeastern part of the 2023 rupture could potentially decelerate the rupture process; whereas the presence of a significantly low-b area adjacent to it on the northeast starkly contrasts with the observation that the rupture terminated before reaching this region. Furthermore, given that fault stress is more variable than structural features over extended time scales, we posit that the geometrical complexity is the primary factor rendering the EPF a persistent rupture barrier.

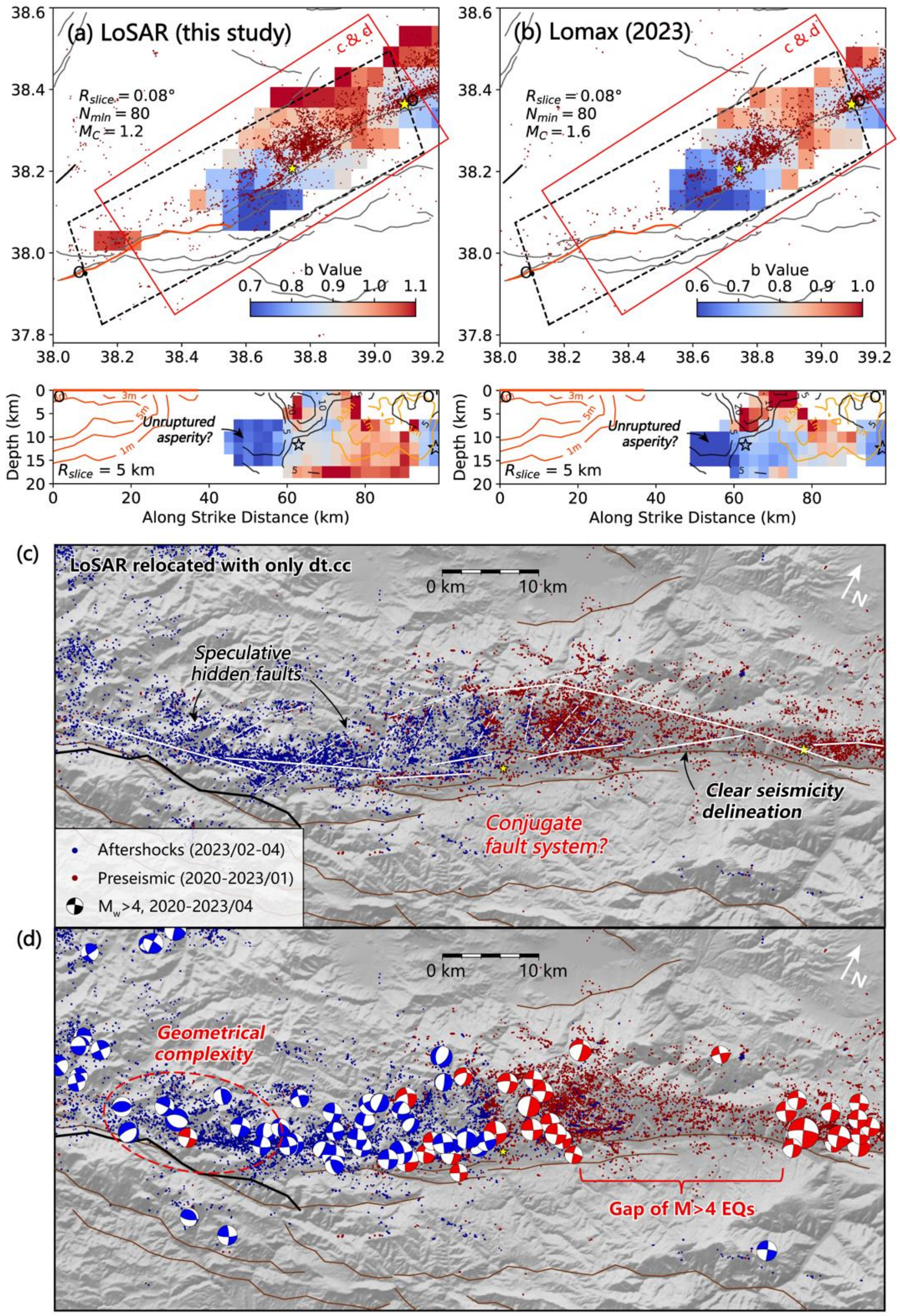

Figure 4.6. B-value mapping and detailed fault structure interpretation of the EPF area. (a-b) B-value mapping results with the LoSAR catalog and that by Lomax (2023) during the preseismic period. The active faults and 2023-ruptured faults are plotted by gray and orange-red lines, respectively. The red box marks the spatial coverage of (c-d). (c-d) provide a zoom-in plot for part of the EPF. (c) plot the distribution of CC-relocated LoSAR catalog. The white solid and dashed lines show interpreted faults. (d) plot the focal mechanism solutions of M_w>4 events during 2020-2023/04 from AFAD.

4.4 2019 Ridgecrest-Ruptured Faults

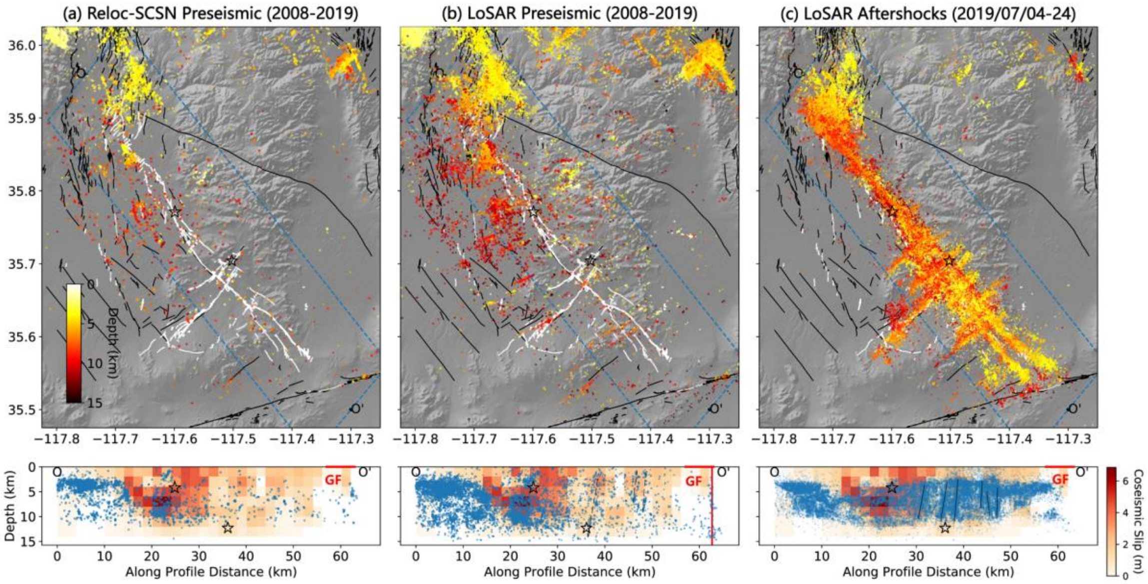

Figure 4.7. Seismicity on the Ridgecrest faulting area before and after the 2019 earthquakes. (a-b) plot the preseismic period of relocated SCSN catalog (Hauksson et al., 2012) and LoSAR catalog in this study, respectively, and (c) for the LoSAR catalog aftershock period. Note that the dot size and transparency for the preseismic (a-b) and aftershock (c) period are set differently, because of the very different seismicity rate. In the map view plots (upper panels), the seismicity is plotted as dots that have its color denoting the depth and size varies with the magnitude. The active faults are plotted as black lines; the surface ruptures are marked by white lines. The reference points and spatial coverage of the along-fault cross-section is marked by blue dashed rectangle. The hollow black stars denote the largest foreshock and the mainshock of the 2019 Ridgecrest sequence. In the cross-sections (lower panels), the rupture model by Yue et al. (2021b) is plotted as different shades of red. The Garlock Fault (GF) on the surface and seismicity-interpreted depth extension is marked by red lines. The black lines are the imaged cross faults by seismicity.

As reviewed in Section 3.3.1.1, the 2019 Ridgecrest sequence activated a largely unmapped orthogonal fault system. However, subsequent detailed geological investigation by Thompson Jobe et al. (2020) suggest that up to 50-70% of the fault traces could have been mapped before the earthquake. It is practically important to know whether those faults can be imaged by long-term seismicity, and whether this region represent a hazardous seismic gap, considering that the Ridgecrest sequence breaks a ~20-year quiescence in the ECSZ (Ross et al., 2019a; Chen et al., 2020; Hauksson and Jones, 2020).

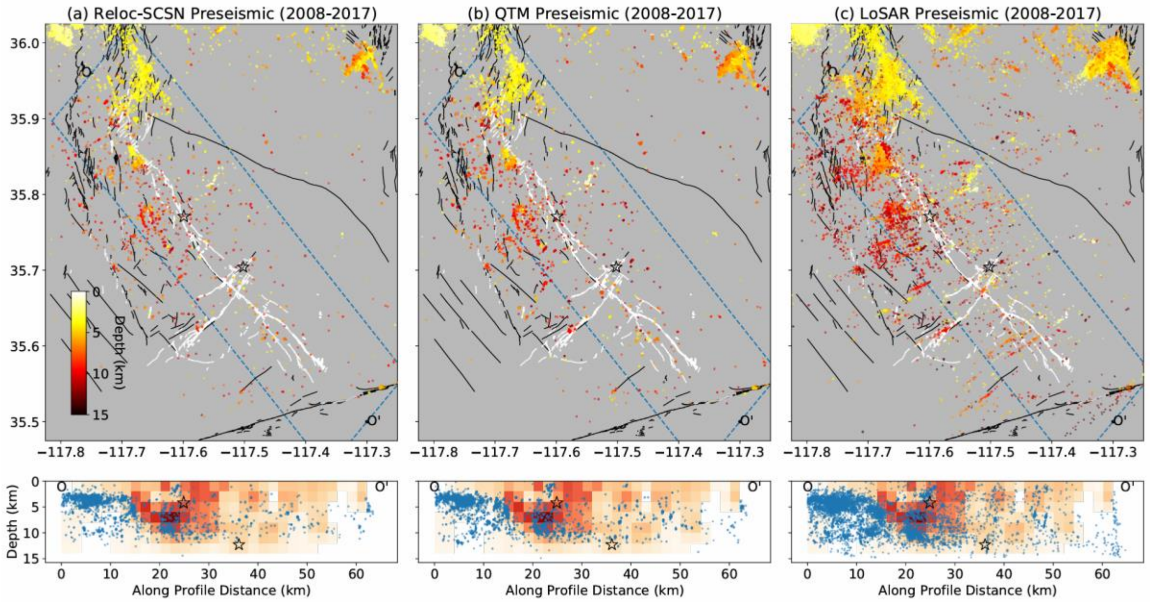

Figure 4.8. Distribution of Ridgecrest seismicity before the 2019 mainshock. (a-c) plot the relocated SCSN catalog, well-located QTM catalog, and relocated LoSAR catalog, respectively.

From the event distribution prior to the earthquake (Figure 4.7a-b), it is evident that an over 20-km-wide zone along the Ridgecrest faults is characterized by spreading microseismicity. This pattern is more distinctly observed in our LoSAR catalog compared to both the relocated SCSN catalog and the QTM catalog (Figure 4.7-4.8). Though the southern segments have much lower seismicity rate, the seismicity in the LoSAR catalog exhibit multiple clusters trending orthogonally to the main faults ruptured during the 2019 M_w 7.1 earthquake, aligning with the focal mechanisms of M>2 events within those clusters (Figure 4.9). Additionally, these orthogonal clusters appear to be further activated following the mainshock, since they collocate with the aftershocks and mapped surface traces (Figure 4.7c). The above observations suggest that multiple subparallel faults extend to the SE of the 2019 M_w 6.4 foreshock, an area where previously few fault traces had been mapped. The net effect of such a fault system is a distributed shear deformation and a low slip rate on each individual fault, which agree with the weak seismic activity observed in this region.

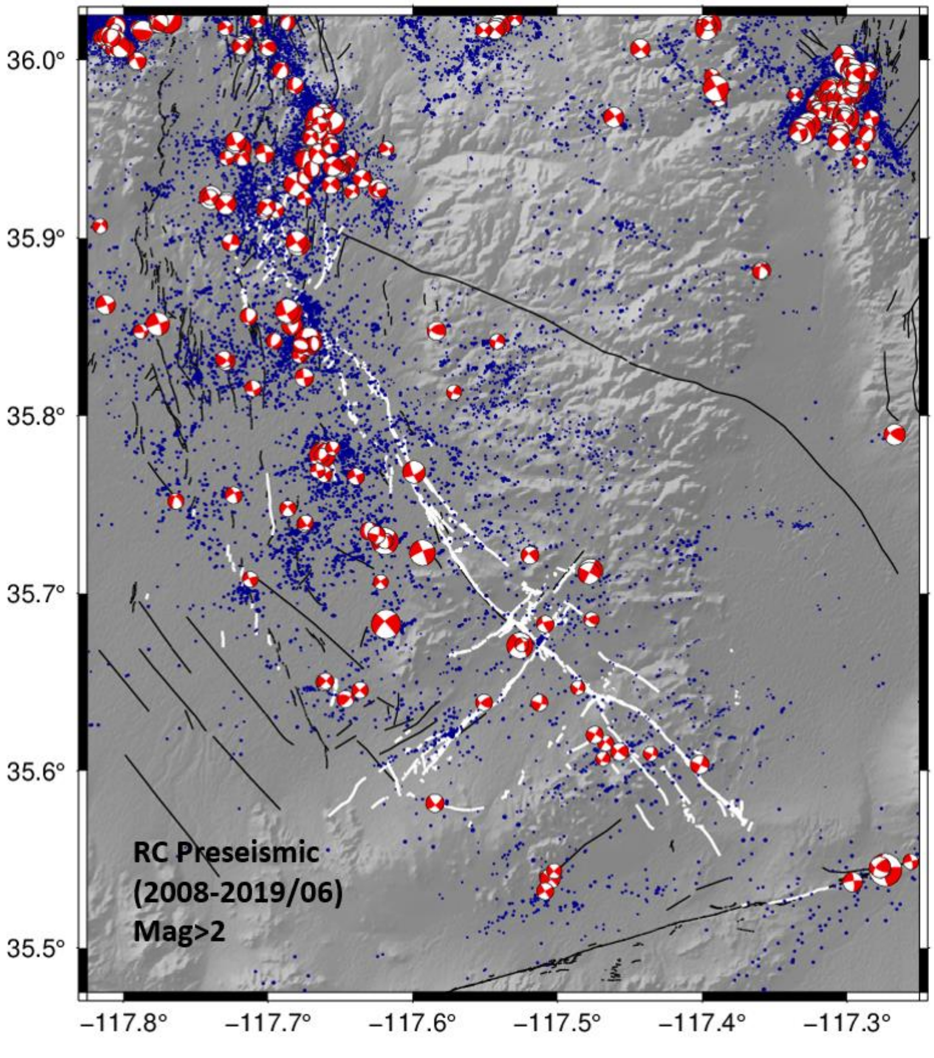

Figure 4.9. Focal mechanism solutions (FMS) for the Ridgecrest-Coso preseismic period (2008-2019/06). The red beach balls and dark blue dots denote the M>2 FMSs from Cheng et al. (2023) and relocated LoSAR catalog present in this study.

By examining the seismicity depth distribution in the cross sections (Figure 4.7), we find a similar pattern of depth contour before and after the 2019 mainshocks, despite contrasting intensities of seismic activity, both complementing the coseismic slip. Furthermore, the b-value mapping results reveal that the areas of weak seismicity in the southern segments correspond to notably low b-values (Figure 8c), indicating a high level of differential stress. The same low-b-value feature on Ridgecrest faults are also revealed with the QTM catalog (Figure 4.10b) and the SCSN catalog starting from 1980 (Nanjo, 2020), but it is not resolvable with merely ~11 years of data, due to a small number of event detections (Figure 4.10a). Collectively, these findings suggest that the southern segments were strongly locked prior to the earthquake, and can be considered as a persistent asperity primed for rupture.

It is noteworthy that the relative b-value pattern obtained from the three catalogs we examined here are consistent to the first order (Figure 4.10), although the b-value estimation with the LoSAR catalog is systematically higher by ~0.2, which is probably caused by the magnitude scale inconsistency mentioned in Section 3.3.1.3. The main difference between these results is the grid coverage of resolvable b-value, as we require at least 100 events above the magnitude of completeness. The shared features between these catalogs under various tests mentioned at the beginning of this section are physically interpretable, supporting the previously recognized inverse correlation between b-value and stress level. For example, the northern segments of Ridgecrest faults, responsible for the M_w 7.1 mainshock nucleation, are of relatively high b-value (Figure 4.10). This can be interpreted by the stress shadow effect caused by several M>5 events during the 1990s on its western subparallel faults. This contrast in preseismic b-value near the foreshock and mainshock hypocenters provides insight into the sequential occurrence of the M_w 6.4 foreshock before the M_w 7.1 mainshock.

In summary, the distributed microseismicity prior to the mainshock unveils a preexisting fault system composed of multiple subparallel branches. This system, characterized by a weak seismicity and an overall low b-value, represents a persistent asperity of potential hazard.

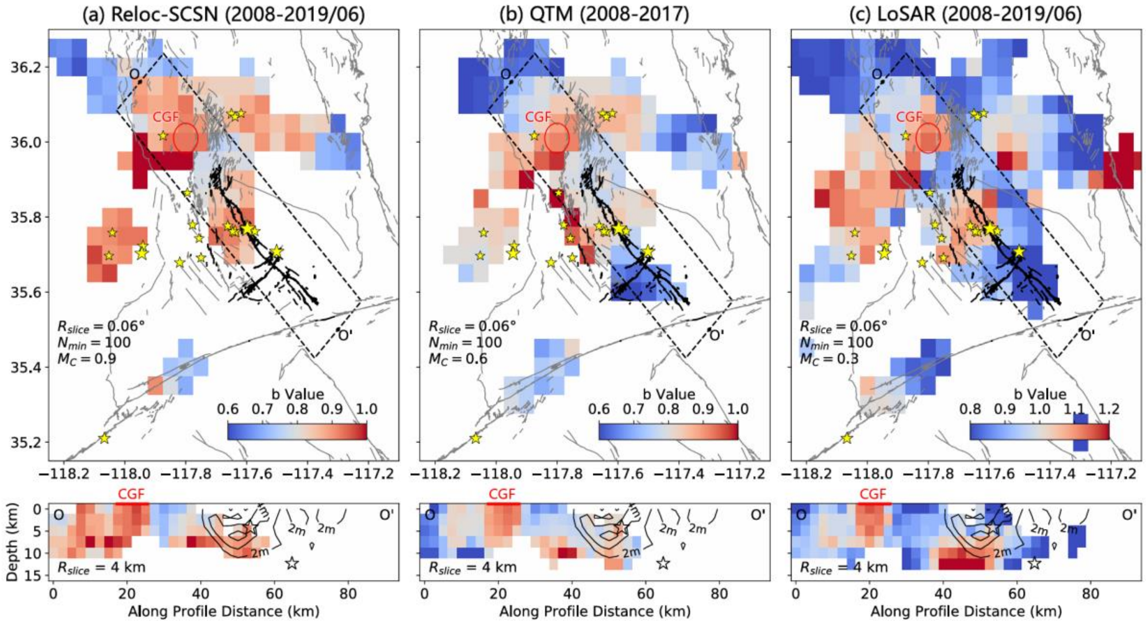

Figure 4.10. Comparison of b-value mapping results for the RC-Coso region during preseismic period with different seismic catalogs. (a-c) plot the b-value mapping results with the relocated SCSN catalog (Hauksson et al., 2012), the QTM catalog (Ross et al., 2019b), and the LoSAR catalog in this study, respectively. The active faults and surface ruptures are plotted by gray and black lines, respectively. The M>5 earthquakes after 1946 are marked by yellow stars. The area of Coso Geothermal Field (CGF) is marked by red circle in the map view and by horizontal line in the cross section. The coseismic slip by Yue et al. (2021b) is plotted as black contours in the cross section. Annotations in the map view include: R_{slice}, the slicing radius for each grid in b-value calculation; N_{min}, the minimum number of events above the complete magnitude to calculate b-value; M_C, the magnitude of completeness.

4.5 Microseismicity Along Xiaojiang Fault Zone (Southeastern Tibetan Plateau)

4.5.1 Introduction

The Xiaojiang Fault (XJF) is located in the southeastern margin of the Tibetan Plateau, which defines the displacement boundary between the South China block in the east and the Sichuan-Yunnan (also known as Chuandian) block in the west (Figure 4.11). The fault zone stretches for about 400-km in the north-south direction (Shen et al., 2003; Zhang et al., 2003). Driven by the eastward extension of the Tibetan Plateau, the rhombic Sichuan-Yunnan block moves southeastward relative to the stable South China block at a rate of 7-10 mm/yr, accompanied by a clockwise rotation (Shen et al., 2005; Wang et al., 2015; Fu et al., 2020). Strong earthquakes are active along the eastern boundary of the Sichuan-Yunnan block, which is composed of the Xianshuihe Fault (XSHF), the Anninghe-Zemuhe Fault (AZF), and the Xiaojiang Fault (Figure 4.11, Deng et al., 2003; Zhang et al., 2003). Historical earthquakes on XJF include three M7~8 and sixteen M6~7 events that occurred since 1500 A.D. (Wen et al., 2008; Ren, 2013), with the largest and latest two being the 1833 M8 Songming and the 1733 M7.5 Dongchuan earthquake. The ~200-year quiescence and long-term active behavior of large earthquake on XJF make the seismic hazard assessment of great scientific and public importance. Thus, special focus has been placed on monitoring the seismic activities, e.g., the China Seismic Experimental Sites (CSES, Wu et al., 2019b) and studying the fault behavior of the Xiaojiang fault area. However, previous studies have not reach agreement on the seismic hazard of XJF:

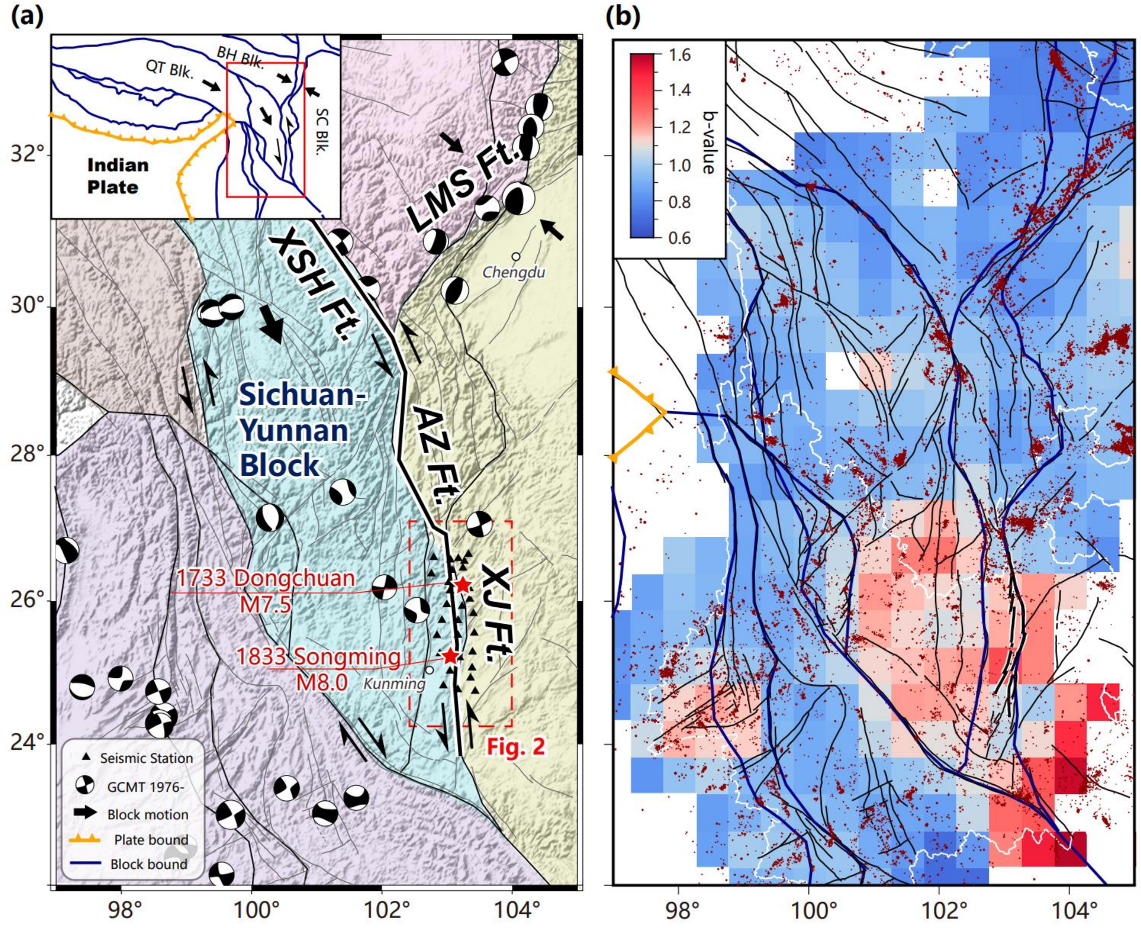

Figure 4.11. (a) Tectonic setting of the Sichuan-Yunnan block. Active tectonic blocks are marked by colored patches. The horizontal movement of the blocks is indicated by gray arrows. Fault traces are plotted in gray lines. The Xianshuihe Fault (XSH Ft.), Anninghe-Zemuhe Fault (AZ Ft.), and Xiaojiang Fault (XJ Ft.) are highlighted by black lines. The focal spheres are solutions in the region since 1976 from the GCMT catalog. The black triangles denote broadband seismic stations used in this study (see Figure 2 for details). In the inset map, the red box indicates the study region. Blue lines show boundaries of tectonic blocks, while plate boundaries are marked by orange lines with ticks. (b) Seismicity and b-value of the study region. The background color shows the b-value, whereas red dots are epicenters of seismic events of magnitude 1.5-7.0 during 2016-2019 from the regional catalog of CSES.

Adopting a simple earthquake recurrence model, the seismic hazard can be estimated by the elapsed time from the preceding large earthquake, while the near future seismic hazard along the XJF is under debate. Historical earthquakes on XJF show an irregular recurrence interval and magnitude for M6~7 events (Wen et al., 2008), while paleoseismic studies find characteristic earthquakes of M>7.5, whose recurrence interval is about 2000 years (Shen and Wang, 1999; Shen et al., 2003). However, a recent paleo-seismic study by Li et al. (2015) found a much shorter recurrence interval of 370-480 years for the characteristic events on the western branch of XJF. Based on these observations, Liu et al. (2020a) propose a high probability of an M>7 event on XJF in the near future.

Geodetic measurements provide another independent observation to estimate earthquake hazards. Wang et al. (2015) calculated the balance between the GPS measured tectonic loading and the strain release by historical earthquakes, which gives a high moment deficit on XJF indicating high potential of large earthquakes; whereas using a similar approach, Wang et al. (2011) obtained a negative moment deficit, which indicates a low potential of large earthquakes. It appears that the discrepancy of seismic hazard originates from the different remnant stress assumed by different groups.

Besides paleo-seismic and geodetic evidence, the current stress status is another probe to assess the possibility of a near-future earthquake. This can be inferred from b-value distribution (see Section 4.1), which avoids the problem of uncertain residual stress in the aforementioned geodetic method. We mapped b-value distribution in the Sichuan-Yunnan region with a regional earthquake catalog. It turned out that XJF has a relatively high b-value, which may be associated with low stress level, in comparison with AZF and XSHF that located to the north (Figure 4.11b).

Overall, the discrepancies in previous studies are probably induced from low-resolution observations, which prevent discussions on the factors that control the initiation and propagation of rupture, including the fault geometry, coupling state, stress and strength distribution.

In this study, we adopt microseismic activity to resolve the fault zone properties and to estimate the seismic hazard on XJF. To construct a high-resolution seismic catalog, we deploy temporary seismic stations and apply a newly developed earthquake detection method. Based on the catalog, we perform spatiotemporal analysis, detect potential repeaters, and map the b-value, with the purpose to infer the fault structure and strength, slip behavior, and stress status of XJF.

4.5.2. Data and Methods

4.5.2.1 Regional Networks and Data

We use continuous data from 31 broadband seismic stations along the main segment of XJF involving two sub-parallel traces of faults (Figure 4.12). The network is composed of two sub-arrays deployed by different groups, which includes 20 and 11 stations, respectively. The 20 stations deployed by Peking University utilize Trillium Compact sensor and Centaur datalogger produced by Nanometrics; The 11 stations deployed by Institute of Geophysics, China Earthquake Administration utilize Güralp 3ESPC sensor and RefTek RT-130 datalogger. The network has an average inter-station distance of 20-30km. The network was operated from September 2016 to January 2019, with a daily average of about 80% of the stations in operation.

4.5.2.2 Earthquake Detection and Location Method

We apply the PALM architecture (Zhou et al., 2021b) to build the microseismic catalog of XJF. PALM utilizes phase picking, association, location, and matched filter

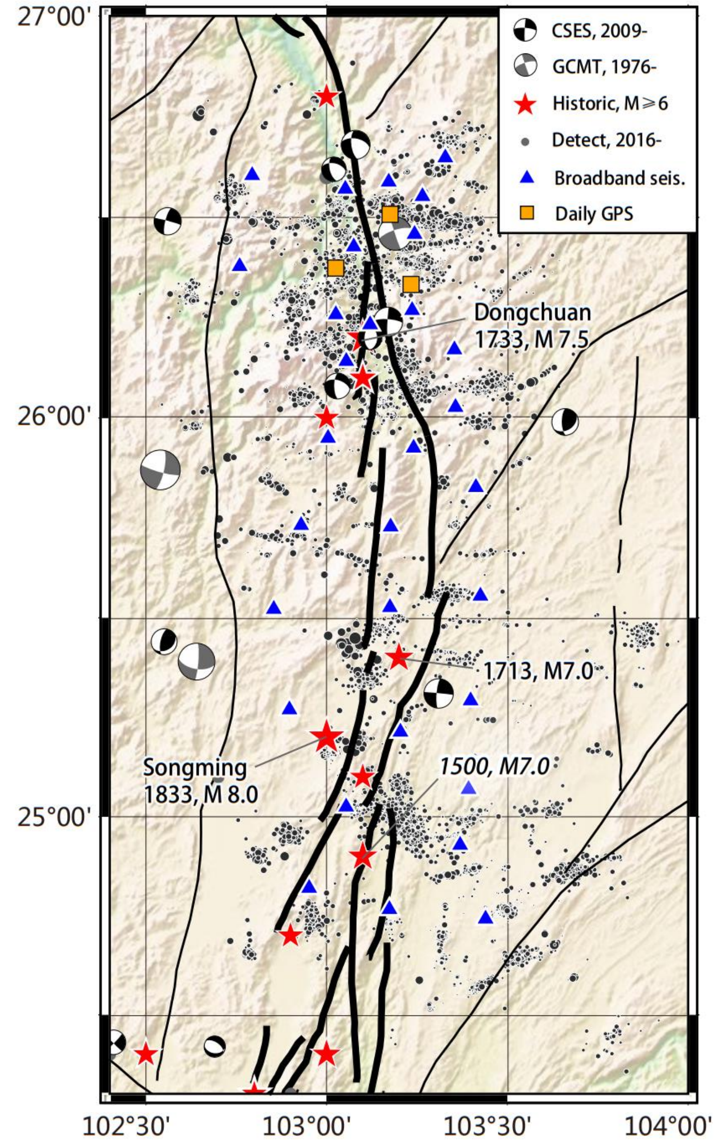

Figure 4.12. Seismic stations along the XJF used in this study. Blue triangles denote broadband stations; orange squares denote daily GPS stations. Black dots are the detected micro-seismic events. Historical earthquakes of magnitudes M ≥ 6 are denoted by red stars. Focal mechanism solutions from the GCMT catalog since 1976 and the CSES catalog since 2009 are shown by gray and black focal spheres, respectively. Black lines depict active faults, and that of XJF are thickened.

technique to automatically build a microseismic catalog (see Section 2 for details). Before feeding into PALM, the raw data is preprocessed by removing the mean value and linear trend, and band-pass filtering to 1-20Hz. The whole architecture is composed of two parts:

(1) PAL: phase picking, association and location

PAL first detects candidate phases with short-term-average over long-term-average (STA/LTA) algorithm (Allen, 1978). The P & S arrivals are then picked in pairs by a hybrid picker incorporating STA/LTA and Kurtosis algorithm. In the phase association process, the estimated origin time on each station is clustered, and then a 3D grid search is applied to search for a location with the minimum travel time residual. We require at least 4 associated stations to declare a detection. For the calculation of magnitude, we use the S-wave amplitude to calculate the local magnitude (M_L). The median estimations on different stations are adopted for stability. For event location, we first apply HypoInverse (Klein, 2002) for absolute location, and then use HypoDD (Waldhauser and Ellsworth, 2000) to refine the relative location between events. For PAL detections in XJF, we employ the 1-D velocity model of Wang et al. (2002) for both HypoInverse and HypoDD location. The stability of HypoInverse location result is tested with different velocity models. For HypoDD relocation, we only include stations within 120-km for each event, we require at least 8 differential times for each event pair, set WDCT=30-km, and apply 4 iterations, while other weighting schemes give similar results.

(2) MESS: matched filter, expand, time shift, and stacking

For MESS detections in XJF, we set the template window length as 1-s before and 11-s after P arrival, which covers both P and S waves. We set the minimum CC threshold for detection as 0.25, and require an event to be detected by at least two templates for higher accuracy. Note that detections within 2s by different templates are associated as one detection. The magnitude of MESS detections is calculated in the same way as for PAL detections. The P and S arrival times of detected events are then picked by waveform cross-correlation, but with a shorter window length to separate P & S wave: 0.5-s before to 2.5-s after the phase arrival. We input this high-resolution *dt.cc* into HypoDD (Waldhauser, 2001) for relocation. For the relocation process, we only utilize stations within 120-km for each event, and each event pair must have at least 6 differential times that have a CC higher than 0.35, and P & S differential time smaller than 1-s & 1.8-s, respectively. We set WDCC=10-km with 1 iteration to relocate the MESS detected events. The stability of the relocation result is tested with different weighting schemes. This finally leads to a location uncertainty of 300-m & 500-m in lateral and vertical direction, respectively.

4.5.3 Results and Discussion

4.5.3.1 Microseismicity Locations and Fault Structure

The PALM detection method finally gives 12,881 well-located events during the study period from 2016-09 to 2019-01. Compare with the regional catalog provided by CSES, our PALM catalog gives much improved location accuracy and catalog completeness of the regional seismicity (Figure 4.13), which is due to the dense seismic network and the effectiveness of PALM algorithm. A rough but quantitative comparison is that the regional catalog has an average uncertainty of about 2.5-km & 1.5-km in vertical and lateral directions, compared with that of 500-m & 300-m in our PALM catalog, under the least square criteria of HypoDD. The PALM detection and location procedure is well-behaved in the XJF network: (1) the initial ~4,500 detections given by PAL is augmented to ~13,000 by MESS, a ~2 times increase; (2) the location of PAL is stable and accurate under different velocity models and location parameters; (3) the location results between PAL and MESS are consistent with each other, while MESS reveals more detailed image; (4) the MESS catalog reaches a lower magnitude of completeness than PAL, but with the same FMD for the complete part.

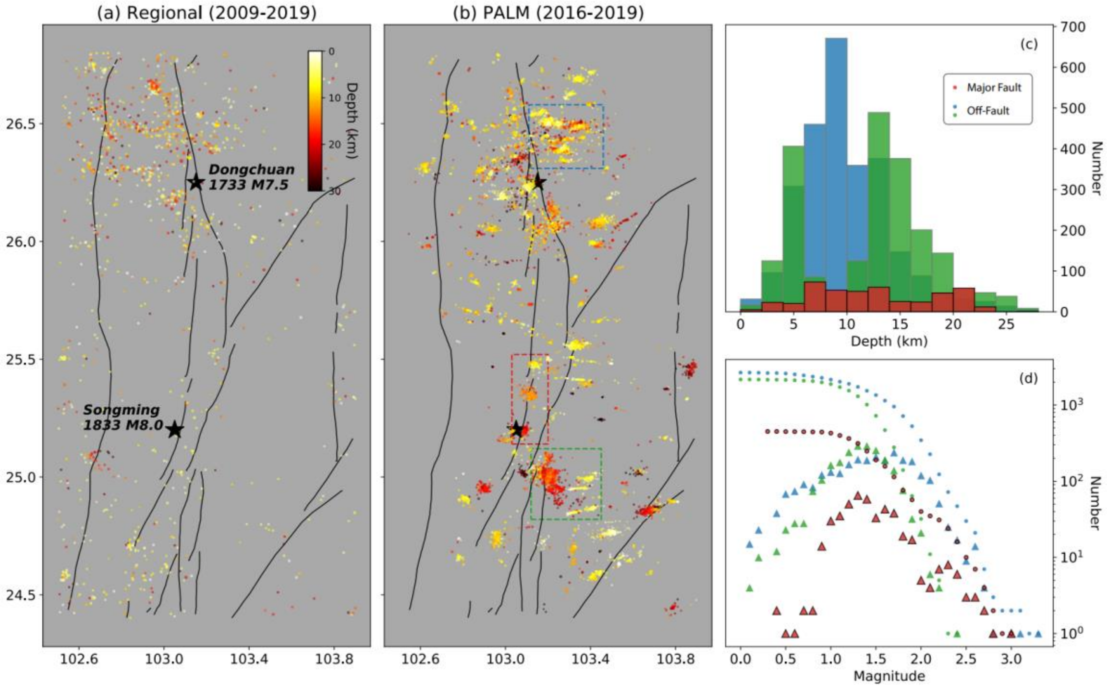

Figure 4.13. Detection and location result. (a) and (b) plot the CSES regional catalog during 2009 to 2019 and PALM catalog during 2016 to 2019, respectively. Earthquake epicenters are shown in dots that colored by depths. The black lines depict fault traces. Three areas (one on and off the major fault) are marked by red, blue and green dashed rectangles, whose depth distribution and frequency-magnitude distribution are plot in (c) and (d) respectively.

The microseismicity reveals abundant off-fault structures around XJF, which show clear lineation in the ENE-WSW direction, conjugating the main trend of the XJF (Figure 4.13-14). The seismic events on the main fault are highly clustered, with limited spatial lineation. Referring to a detailed fault mapping result from geological investigations, we find that the seismic clusters on the major fault occur on the intersections between the main fault and cross-cutting branches (Zhang and Xie, 2001; Shen et al., 2003). Such fault geometry is typical for a strike-slip fault system with subparallel branches, where conjugate faults and rhombus shaped sub-blocks are developed in between (Nicholson et al., 1986; Kilb and Rubin, 2002). Assuming that the deep micro-earthquakes occur on the junction between the main and conjugate faults, the dip angle of main fault branches can be determined in the fault vertical cross-sections (Figure 4.14d), which show a slightly east-dipping sub-vertical geometry.

The formation of the major XJF fault structure can be explained by the Riedel shear theory (Ronald et al., 1973; Davis et al., 2000). At the initial stage, conjugate faults are formed at the preferred Coulomb failure orientation, forming *én* echelon faults (R shear) and conjugate faults (R' shear) in pairs on two sides of the maximum compressional stress direction. The R and R' faults initially align in an acute angle, but with continuous shearing, the sub-blocks rotate and deform, changing it to an obtuse angle. For the XJF, the major branches (R shear) and the conjugate faults (R' shear) form an obtuse angle, which indicates that XJF is at a late stage of Riedel shear development (Nicholson et al., 1986; Kilb and Rubin, 2002).

In summary, the regional fault structure of XJF can be classified into two groups: (1) two sub-parallel NS trending major faults that show *én* echelon structure; and (2) several short conjugate faults between and off the major faults.

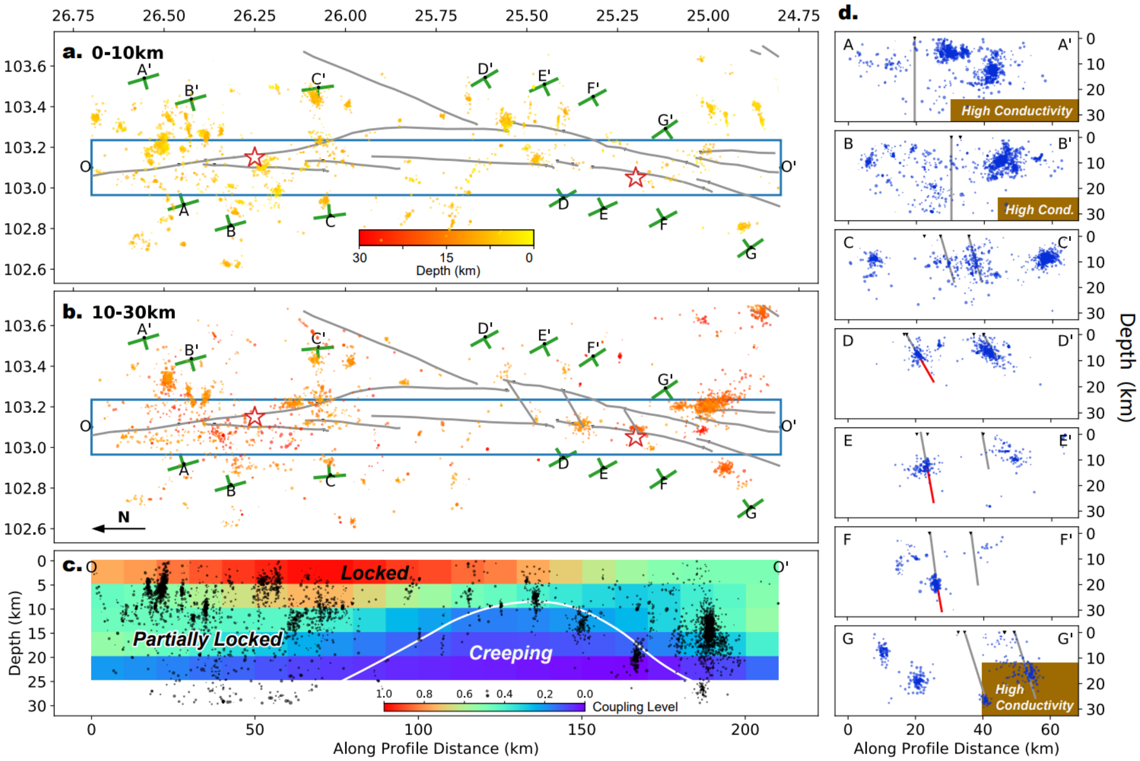

Figure 4.14. Seismicity pattern around XJF. (a) and (b) Map view of shallow (0-10km) and deep (10-30km) seismicity, respectively. Events are shown in dots colored by depths. Gray lines are fault traces. Blue rectangular and OO' mark the endpoints of the overall cross-section; Green frames from AA' to GG' mark the endpoints of the local cross-sections in (d). (c) and (d) plots overall and local cross-sections, where microseismic events are plotted as black and blue dots, respectively. Inter-seismic coupling ratio (ISC) from Li et al. (2021a) is color-coded in (c). Vertical lines in (d) mark the dipping direction of the major fault. Fault zone conductors detected by Li et al. (2019) are marked by brown patches in (d).

4.5.3.2 Locking Pattern of the Major Fault

The spatial distribution of microseismicity also provides insights into slip behaviors. On the major Xiaojiang faults, the rather low microseismicity agrees with the high locking ratio revealed by GPS measurements (Fang et al., 2005; Zhao et al., 2015; Fu et al., 2020). Such strong locking is more significant for the seismic quiescence segment in the seismic gap between the Songming and Dongchuan epicenter (from 25.5°N to 26°N) (Wen et al., 2008), which correlates well with the segment of large increase in cumulative Coulomb stress since 1713 (Shan et al., 2013). Similar quiescence of microseismicity on the major fault is also reported on the Alpine Fault of New Zealand, which is in the late stage of an earthquake cycle (Chamberlain et al., 2017).

On the western branch of XJF, we identified a special group of earthquake clusters with variable epicentral depths ranging from 25-km near 25°N to 10-km at 25.5°N (Figure 4.13b, 4.14c). Note that the XJF is currently at an interseismic period, we assume the seismic activity is mostly driven by fault creeps occurring at depth. Adopting a shear dislocation model with deep fault creep, the stress accumulation is concentrated at the boundary between creeping and locking patches, driving intense seismic activities (Jiang and Lapusta, 2017). Thus, in XJF, the spatial trend of deep seismic events is an indicator of the locking depth. In comparison with a recent interseismic locking model derived by geodetic data (Li et al., 2021a), we find a good agreement between seismicity distribution and boundary of locking-creeping patches (Figure 4.14c). This correspondence between micro-seismicity location and the locking depth also applies to the Himalayan thrust front (Ader et al., 2012) and San Andreas Fault (Waldhauser et al., 2004; Wdowinski, 2009). The fault segment between about 25.25° to 25.75° show a shallow fault creep at 10-20km, which can be a result of either fluid-induced high pore-pressure or material heterogeneities, and further studies with other high-resolution observations are needed to draw stronger conclusions.

Overall, the strong locking of major Xiaojiang Fault is well supported by both GPS studies and a low seismic rate reported here. We will provide even more lines of evidence from repeater analysis (subsection 4.5.3.3), temporal evolution of seismicity (subsection 4.5.3.4), and b-value mapping (subsection 4.5.3.5). However, the slip behavior of the off-fault structures is more difficult to revolve, on which we will show additional analysis on seismicity in subsection 4.5.3.3-3.5 and make a concentrated discussion in subsection 4.5.3.6.

4.5.3.3 Repeater Analysis

To investigate the slip behavior of subsidiary faults, we conducted repeating earthquake detection and analysis. Repeating earthquakes is usually considered as a re-rupturing of the same asperities driven by aseismic slips (Uchida and Bürgmann, 2019). The detection of repeaters requires strict criteria in both waveform similarity and location separation:

(1) High waveform similarity. We measure the cross-correlation on 1-20Hz band-pass filtered waveforms. We require a minimum CC threshold to be 0.9 for more than one station observation. The template window for cross-correlation is 10s-long (1-s before and 9-s after P arrival), covering both P and S waves. This is a relatively low threshold among other repeater studies (Uchida, 2019), but is widely adopted when location criteria are also included in the detection process (Li et al., 2011; Schmittbuhl et al., 2016; Zhang et al., 2022b).. Note that at this stage, we focus on the detection completeness, and do not rely on CC to make the final decision, since it is affected by multiple other factors besides inter-event separation, e.g. variation in noise level (Gao et al., 2021).

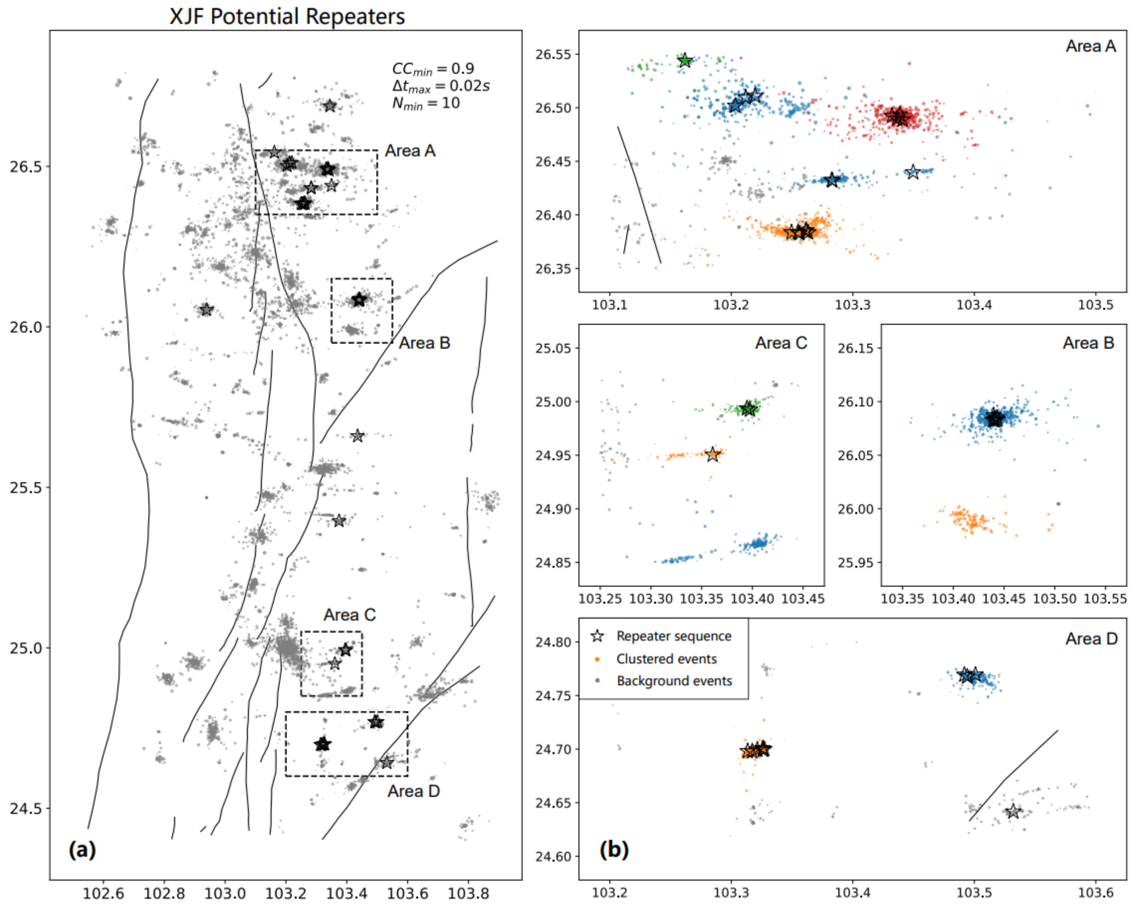

Figure 4.15. Distribution of repeating earthquakes. The left panel (a) is an overview of the whole region, and the right panels (b) show zoom-in plots of repeater distributions in the dashed boxes in (a). Locations of repeating sequences with more than 10 events are denoted by open stars. The colored events in (b) are clusters separated by waveform similarity analysis.

(2) Indistinguishable location difference. We adopt a similar strategy as in Li et al. (2011) that utilize CC-measured differential S-P time to constrain the inter-event separation. We measure the difference of S-P time on each station between a pair of events, and require a maximum deviation within 0.02 s for at least 3 stations. The ΔS-P time is measured with P&S phase window of 2-s: 0.5-s before and 1.5-s after P; 0-s before and 2-s after S. This operation avoids the uncertainty of clock error, since the operation is done on single stations. Theoretically, such strategy leads to a maximum separation of $0.02s * v_p *$

$v_s/(v_p - v_s) \approx 150m$, which is comparable to the rupture radius of an M1.5 event (Eshelby, 1957; Hanks and Kanamori, 1979).

The periodicity of sequence is analyzed with the coefficient of variation (COV) value of the recurrence interval, which is defined as the ratio of the standard deviation over the mean value of recurrent. A COV value of 0 corresponds to a purely periodic behavior, a COV value of 1 indicates a Poisson process, and COV > 1 suggests temporal clustering (Lengliné and Marsan, 2009; Li et al., 2011).

Results show that most repeaters occur on off-fault structures (Figure 4.15), which is consistent with the high coupling ratio of the major fault. The repeaters tend to occur in a random behavior (Figure 4.16a,b): the sequences' COV values range between 0.4 to 1.2, which deviates from a periodic recurrence pattern (COV=0) generated by isolated patch driven by constant aseismic slips. The high COV value indicates a temporal clustering of repeating earthquakes, which may be driven by slow-slip events with higher slip rate than background creeping. Moreover, the repeating sequences with a shorter duration show more quasi-periodic feature, while longer sequences have a higher degree of clustering (Figure 4.16b). This suggests that the short-term creep rate tends to be stable, but the long-term creep rate is influenced by episodic events.

It is worth noting that the magnitude of repeaters concentrates around M_L1.8 (Figure 4.16c), which is smaller than that in most other studies (Uchida, 2019; Uchida and Bürgmann, 2019). Such a small event size makes it hard to determine whether the repeaters detected in this study are re-rupturing the same asperity. Thus, we only consider them as possible repeaters, which differ from the ordinary repeaters that indicate stable fault creeping behavior. This result shows that the off-fault region of XJF is not freely and stably creeping, but is partially locked to near surface, which agrees with the GPS-inversed locking model by Li et al. (2021a) (Figure 4.14c). Similar near-repeating clusters are also detected adjacent to the co-seismic rupture zone of 2020 M_w 6.8 Sivrice earthquake that occurs on the East Anatolian Fault (Konca et al., 2021) and on the Anza segment of San Jacinto Fault loaded by the afterslip of moderate earthquakes (Shaddox et al., 2021), both of which report near-repeating earthquakes that recurrent irregularly and with variable magnitude, but are associated with aseismic fault slip.

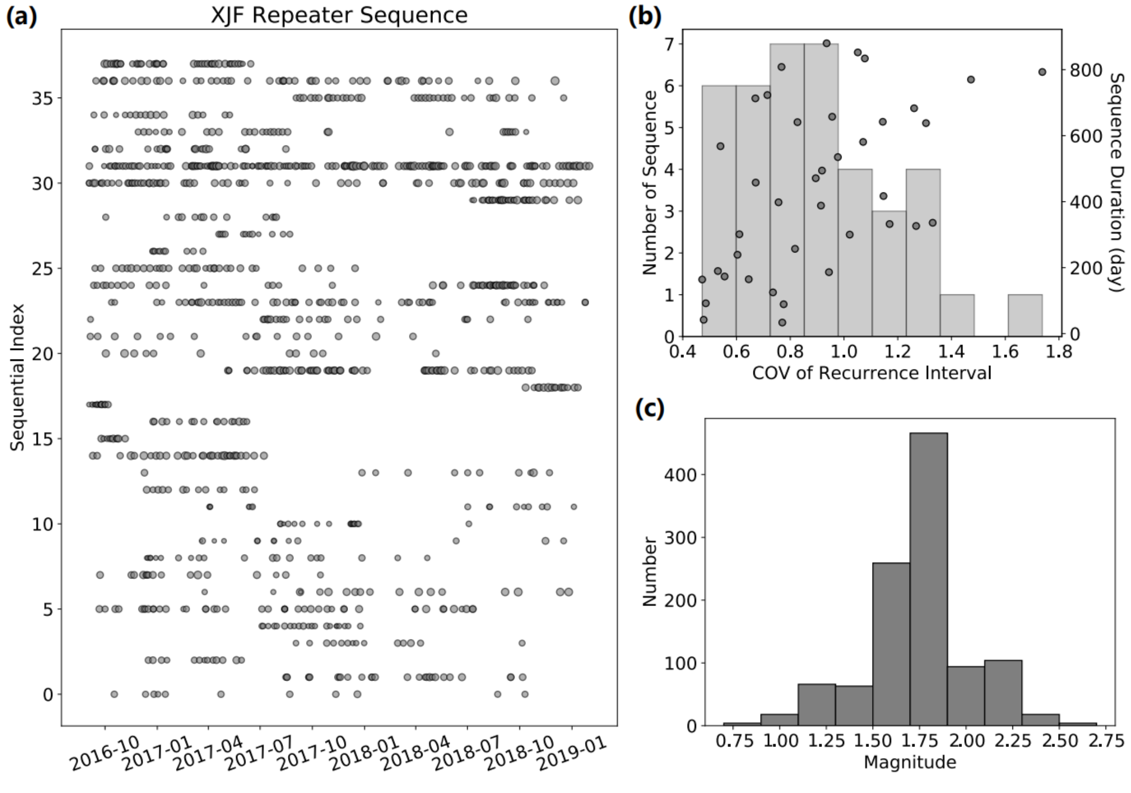

Figure 4.16. Repeating sequence analysis. (a) Repeating sequences. Horizontal and vertical axes are origin time and sequence index, respectively. Note that the sequence indexes are sorted by latitude. Gray dots denote repeating events, with the size proportional to the magnitude. (b) Periodicity of sequence. Histogram plots the number of sequences with respect to the COV value of recurrence interval. Gray dots mark the sequence duration and its COV value. (c) Histogram for the magnitude distribution of repeaters.

4.5.3.4 Temporal Evolution of Seismicity

We further analyze the temporal evolution of seismicity and the GPS time series to infer the slip behavior of off-fault structures. We first examine the seismicity rate in each separated area in Figure 5. We found that different seismic clusters in an area tend to be activated spontaneously (Figure 4.17), indicating that they are driven by the same mechanism. Note that each area is constituted by multiple faults and has a scale of 10-20km, which excludes the possibility of smaller-scale mechanisms, e.g. inter-event triggering, because the scale of seismicity clustering area is much larger than the stress influence area of such small events. On the other hand, a larger-scale mechanism that effect all areas simultaneously, e.g. tidal stress, is also not supported, because the seismic rates in different areas do not correlate with each other (Figure 4.17). A more detailed tidal modulation study may validate the contribution of tidal forces, and it is possible that the regional variation is caused by different fluid conditions, since high fluid content areas could be more influenced by tidal forces. But from the current seismicity rate pattern, we cannot tell the influence of tidal forces.

We collect displacement data of three continuous GPS stations on the northern XJF to further investigate the spatiotemporal deformation behavior of this area (Figure 4.18a). The geometry of three stations are shown in Figure 8a: Station DTB locates at the west side of the XJF, while station HNG and HDH locates on the north and south side of the off-fault branches, respectively. The original data is processed with daily solution and reference to the whole earth coordinate. We subtract the solution of HDH from the other two stations to recover relative displacement across two fault structures: HDH-DTB reflects the deformation across the XJF, and HDH-HNG reflects the deformation across the off-fault structures. It is noted that such subtraction also removes the common mode errors in the original data.

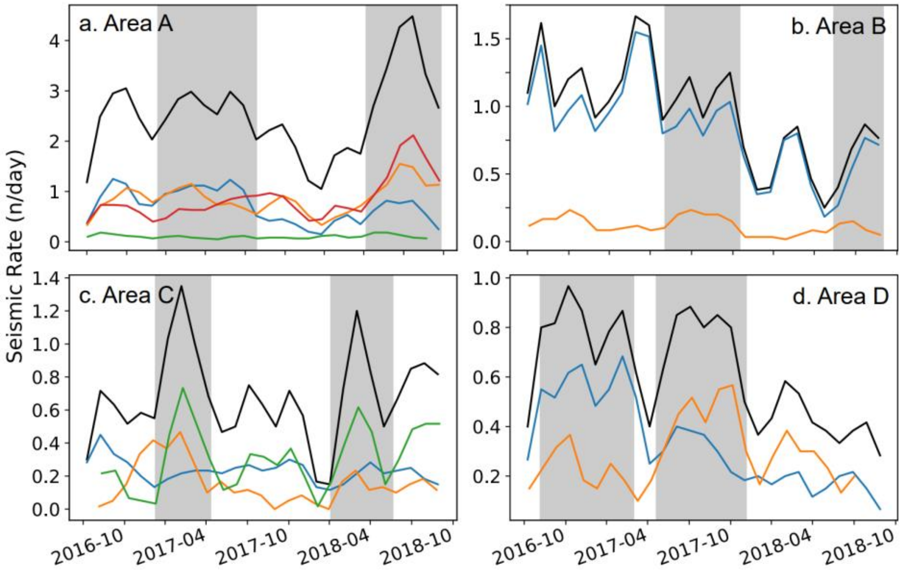

Figure 4.17. Temporal evolution of seismic rate in different area. The black and colored lines plot total and clustered seismic rate, with the color of different clusters the same as Figure 4.15. Gray patches mark the spontaneous active period of micro-seismicity in different clusters.

Time series of relative displacements are plotted in figure 8b. It is evident that the most significant deformation in this area is the left-lateral shearing in the NS direction across the XJF at an averaged velocity of ~5-mm/yr. Deformation across the off-fault structures is dominated by right-lateral shearing in the EW direction at ~1-mm/yr rate (figure 4.18b). Such sense of motion is consistent with the tectonic shear loading of the XJF, while it also indicates that the off-fault structures are undergoing slow right-lateral sense of deformation.

The seismic rate is compared with the off-fault slip rate (figure 4.18c). We recover the relative velocity from daily slips and smooth the velocity with a 60-day running window. The seismicity rate for events above M_L 2 in Area A is also smoothed with 60-day time windows. The comparison shows that the slip rates on the off-fault structures, though at a low rate, have a significant consistency with the seismicity rates (figure 4.18c). This consistency indicates a low fault strength, which may be caused by geothermal condition and high pore-pressure (Ake et al., 2005; Vidale and Shearer, 2006). Under the rate-state-dependent friction law, a high pore-pressure produce higher sensitivity between shear stress and slip rates (Lu et al., 2021), therefore even small velocity change produces high shear stress change on these off-fault structures. At the same time, high pore pressure leads to low effective normal stress and low friction. If these structures are close to failing criterion, stress excess produced by velocity increase will increase seismic activities, which explains the temporal correlation between slip rates and seismicity rates.

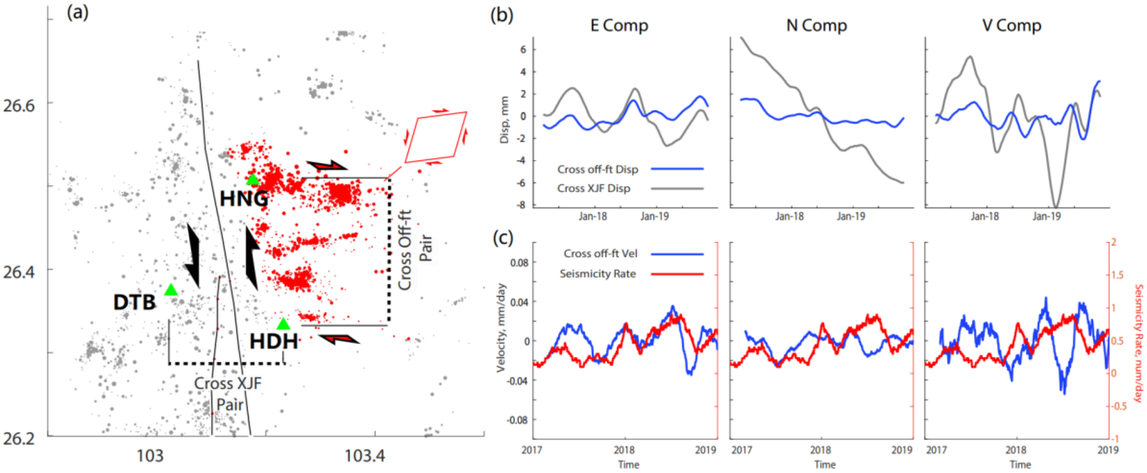

Figure 4.18. (a) Location of three GPS stations are denoted as green triangles. Earthquakes in background and off-fault structures are plotted as gray and red dots, respectively. The arrows mark the deformation of block. (b) E, N and Vertical component of relative displacement across the XJF and off-fault branches are plotted as gray and blue curves, respectively. (c) E, N and V component of relative velocity across the off-fault structures are plotted as blue curves in each panel. Smoother seismicity rate in area A are plotted as red curves.

Seismic activities on these off-fault structures, though intensive, cannot produce the observed slip rate (~1 mm/yr), thus extra aseismic creeping, maybe in a form of episodic creeps in the deep portions of off-fault branches, appears to be responsible for the synchronized seismic activities and surface deformation rates. We also processed SAR images to extract the cross-fault velocity gradients across these off-fault structures, the solution reveals no significant deformation in the shallow part of these structures. This observation indicates these structures are locked at the ground surface, while slowly creeping beneath the seismogenic depths (~20km).

4.5.3.5 b-Value Mapping

We calculate b-value using the PALM catalog. The b-value on each spatial grid, is calculated with events within a radius of 0.2°, and the grid spacing is set to 0.1°. We impose a minimum number of 200 as a number criterion for robust b-value estimation. A stability test is performed for different event association radii. The resulting b-map has complete coverage for the study region (Figure 4.19a), with an uncertainty below 0.1 for most grids (Figure 4.19b). The M_c ranges from M_L1.0~1.6 for most part of the region (Figure 4.19c), indicating high detection completeness.

On the main fault, the b-value is low along the seismic gap between the epicenter of 1733 Dongchuan and 1833 Songming earthquake (Figure 4.19a, Wen et al., 2008; Ren, 2013), indicating high stress level. This low-b feature is consistent with the low seismic rate on the main fault, which suggests strong fault coupling. The epicenter of Dongchuan and Songming earthquake lie in a transition region between high and low b-value (Figure 4.19a), which fit well with the spatial variation of interseismic fault coupling (Figure 4.14c).

Note that we also mapped several low-b area off the major Xiaojiang fault (Figure 4.19a), indicating that the western block or the Puduhe fault on the west of XJF is strong and has a high stress level.

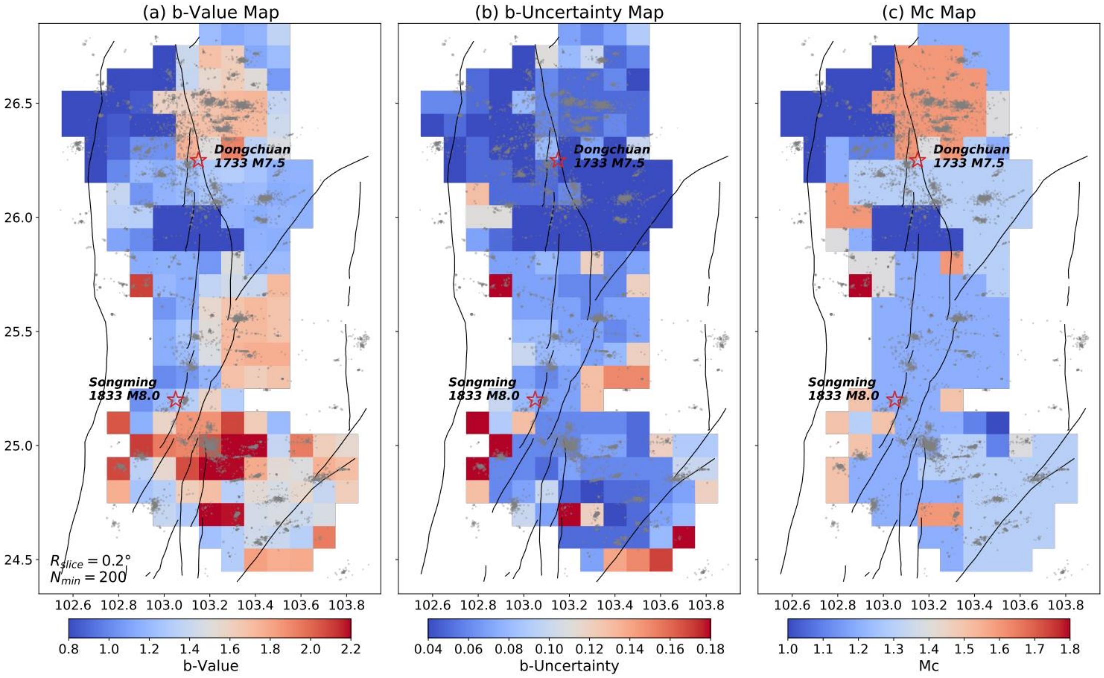

Figure 4.19. Maps of (a) b-value, (b) b-value uncertainty, and (c) magnitude of completeness Mc. Events and fault traces are plotted in gray dots and black lines, respectively. Red stars mark the epicenters of the 1733 and 1833 historical earthquakes.

In contrast to the major faults, the off-fault structures have significantly higher b-values, which are commonly associated with a low stress level (El-Isa and Eaton, 2014) or weak fault strength (Scholz, 2015). Mechanisms related to weak fault strength include: (1) velocity strengthening frictional properties (Schurr et al., 2014), (2) low-effective normal stress (Bachmann et al., 2012), and (3) geothermal or volcanic conditions (Murru et al., 2007).

Besides, our b-value mapping result also solves the contradiction between the average b-value and geodetic estimation mentioned in Section 4.5.1: regional catalog gives high average b-value on XJF (Figure 4.11b), but geodetic estimation by Wang et al. (2015) gives high moment deficit. We interpret this phenomenon as the bias of average b-value: in XJF, the off-fault structures and regional distributed shear generate distributed microseismicity with high b-value, which lead to an overestimation of b-value on the major fault. If we use the b-value on major fault to represent the current stress level of XJF, the ~0.9 b-value (Figure 4.19a) is comparable to that on AZF and XSHF, which is consistent with geodetic results (Wang et al., 2015). Thus, in adopting the b-value inference, a high-completeness catalog with detailed b-mapping is important.

4.5.3.6 Locking Behavior and Strength of the Off-fault Structures

It is noted that the XJF is under an interseismic loading period, while the most intensive microseismicity are concentrated on off-fault structures, especially in two areas near 26.5°N and 25°N east of XJF. We infer geothermal condition of these two locations may be responsible for such high seismic activity, as indicated by high conductivity (Bai et al., 2010; Li et al., 2019) and distribution of hot springs (Shi and Wang, 2017). As analyzed in detail for the NE area of XJF, this area (1) shows strong correlation between seismicity and slip rate, (2) possibly hosts repeating earthquakes, and (3) are characterized by high b-value. Therefore, off-fault structures in this area may be subject to low-frictional strength and deep episodic slow-slip events.

Considering the deformation across the off-fault structures, as also the spatial decaying of NS shearing in the normal direction of XJF, the area with intensive off-fault structures is undergoing a right-lateral shearing in the NS direction and left lateral shearing in the EW direction (Figure 4.18a). Such mode of deformation is close to a pure-shear deformation within a bulk. Elastic theory supports that a pure-shear deformation in such a geometry setting releases shear direction in both NW and EW direction. As a volume of the eastern wall of XJF, shear stress loading is partially released by the distributed shearing in this volume. Thus, the shear stress on XJF near these geothermal areas should be lower in comparison with other strongly locked areas, and may serve as stress barriers for co-seismic ruptures. At the same time, geothermal portions of XJF may cause a velocity strengthening behavior because of a low effective normal stress. Recent observations of continental strike slips events show, the co-seismic ruptures can be terminated by geothermal conditions, e.g. the 2016 Kumamoto earthquake (Yagi et al., 2016; Yue et al., 2017) and 2019 Ridgecrest earthquake (Liu et al., 2019; Wang et al., 2020; Yue et al., 2021b). The spatial segmentation of historical events along the XJF, e.g. Songming and Dongchuan earthquake, appears to be terminated by these two loci (Shen et al., 2003; Wen et al., 2008; Ren, 2013). Therefore, the fault portion between the 26° and 25.5°, may be an independent rupture segment bounded by geothermal portions on its two ends (Figure 4.19).

Considering the overall tectonic setting near the XJF, its west part shows distributed shear, with three extra NS trending sub-parallel faults, e.g. Luzhijiang fault, Yimen fault (YMF) and Puduhe fault (PDF), with ~30 km interval (Wang and Shen, 2020). The lower crust to the west side of XJF shows a low material strength, as validated by (1) a low P and S wave velocity in the lower crust (Wu et al., 2013; Bao et al., 2015; Yang et al., 2020), (2) a low-electric resistivity (Bai et al., 2010; Li et al., 2019), (3) a high attenuation (Zhao et al., 2013), (4) relatively high heat flow and concentrated hot springs (Shi and Wang, 2017), and (5) a high b-value (Figure 4.11b). Such low material strength may be generated by a radial active decay of a thick crust (~50 km) and shearing generated heat (Wang et al., 2017). Thus, we infer that a ductile lower crust with distributed shear deformation to the west side of XJF. A similar shear pattern is also found for the Songpan-Ganze block near NE boundary of the Tibetan plateau. Large earthquakes were found to occur within the shear zone instead of only on boundary faults (Yue et al., 2021a). Therefore, denser geodetic and seismic observation in this area are needed to evaluate the seismic hazard in the whole area.

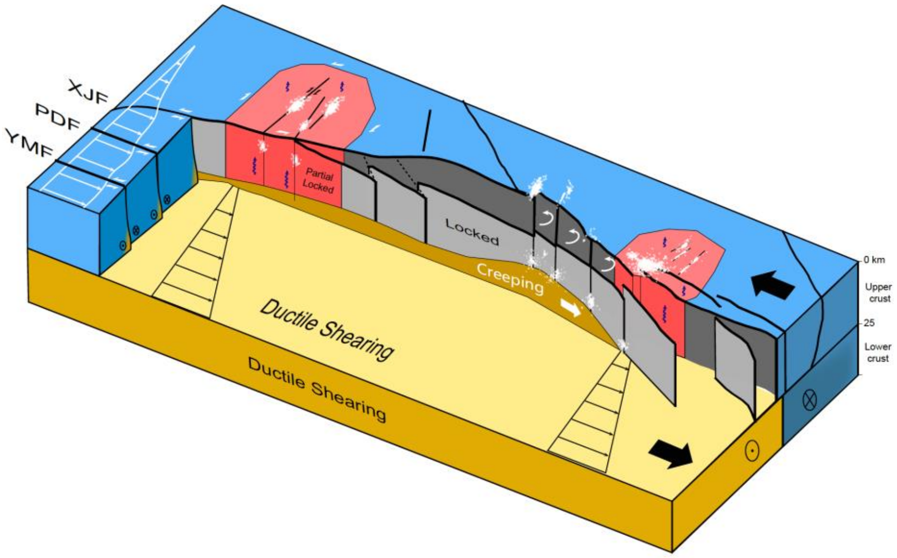

Figure 4.20. Conceptual model of XJF. Crust with different depth and different properties are separated by color. Faults traces and planes are plotted in black lines and gray patches. White dots plot characteristic seismic clusters. Black arrows mark the block motion.

4.5.3.7 Seismic Hazard of XJF

Based on the above discussions, we imaged the structure of XJF and demonstrated its slip behaviors (Figure 4.20). Here, we analyze the implications of such fault characteristics on the seismic hazard.

The major Xiaojiang fault is composed of several segments aligned in an *én* echelon pattern. Historically, this ~150-km-long fault trace is capable to create M7-8 earthquakes (Shen et al., 2003; Wen et al., 2008; Ren, 2013; Li et al., 2015). To evaluate the current potential of XJF of generating large events, we suppose that a large earthquake requires a high stress level on a large scale, which has been validated by dynamic rupture simulations (Day, 1982; Wesnousky, 2008; Yang et al., 2019). In XJF, the quiescent segment between the Dongchuan and Songming epicenters (~25.5-26°N) fulfills such criteria: (1) the lowest b-value in the study area (Figure 4.19a); (2) the largest cumulative Coulomb stress change (1-10MPa) given by Shan et al. (2013); (3) the highest locking ratio along XJF inverted from GPS (Li et al., 2021a). Thus, we conclude that this ~50-km-long gap is still susceptible to dynamic rupture, which can lead to a ~M7 earthquake if being completely ruptured.

The origin time of future large earthquake is especially hard to predict. In this discussion, we only consider which stage does XJF lie in the whole cycle. As stated in Section 4.5.1, the earthquake cycle given by paleo-seismic studies are not consistent with each other. We can revisit this problem by direct evidence from the fault slip rate and coseismic offset. Multiple GPS measurements over decades give a slip rate of 7-10 mm/yr on XJF (Shen et al., 2003; Shen et al., 2005; Wang et al., 2015; Fu et al., 2020). Adopting the field observation by Ren (2013), the coseismic offset of the 1833 Songming earthquake ranges from ~3-6m, which would lead to a maximum of 850-year recurrence interval, still much smaller than ~2000-year by Shen et al. (2003). On the other hand, the average interval is about 500 years following this estimation, which is comparable to 370-480 years given by Li et al. (2015). Thus, we prefer the paleo-earthquake result from Li et al. (2015), and infer that XJF is at its late stage of seismic cycle, considering the 200-300 years' elapse from the 1733 and 1833 events.

4.5.4 Summary

In this chapter, we obtained a high-resolution image of microseismicity in XJF with a temporal seismic network and PALM detection method. Combining spatiotemporal feature of seismicity, repeater analysis, and b-value mapping, we characterize the behavior of XJF during its interseismic period. The main conclusions include:

(1) We found that the XJF is composed of two sets of structures: the two major branches and the conjugate sub-faults. The major Xiaojiang fault includes two sub-parallel NS-trending branches, each is composed of several segments showing *én* echelon geometry. It is overall strongly locked, generating low microseismicity, low b-value, and no repeaters. The clusters on western branch show variable depth around the epicenter of 1833 Songming earthquake, delineating a fault segment with shallow locking depth.

(2) The off-fault structures form conjugate geometry with the main faults. The intense microseismicity on these sub-faults are driven by small fault slip, indicating stress loading released by distributed shear. We propose that such behavior may be caused by geothermal-induced fault weakening mechanism, which explains all observations in this and previous studies, including the potential repeating events, high b-value, and low resistivity at shallow depth. These distributed shearing areas may serve as both stress and material barriers for future large earthquakes, which bound the segment of XJF between 25.0°N and 26.5°N as an isolated rupture segment.

(3) The overall b-value in the central of XJF is low, indicating a high stress level. Considering the locking pattern of XJF and its surrounding loading environment, we infer that XJF at a late stage of interseismic loading. The segment between 25.0°N and 26.5°N may be subject to an ~M7 earthquake in the future.

4.6 General Characteristics of Microseismicity Before and After Large Earthquakes

Based on the insights from the four case studies, it is clear that fault zones are highly complex, which complicates seismic hazard assessment. However, we have identified some general characteristics of seismicity related to large earthquakes that could provide valuable insights for understanding seismic hazards.

(1) Major fault zones typically exhibit off-fault or subsidiary structures, which are generally weaker than the primary faults, as seen in the cases of the EPF in Turkey and XJF in China. These smaller structures tend to produce higher rates of microseismicity and elevated b-values. This pattern may bias the overall b-value, making detailed b-value mapping essential for accurately inferring the stress levels on the main fault.

(2) Quiescence along major faults appears to be a common pattern observed in all our cases prior to large earthquakes. This can be interpreted as a result of pervasive dynamic weakening mechanisms during ruptures (Jiang and Lapusta, 2016). Additionally, we may anticipate a more rapid decay in aftershock rates along major asperities, as also predicted by statistical simulations (Toda and Stein, 2022).

(3) Hidden faults that represent major asperities can still be detected through long-term seismicity. Based on the findings in (2), fault segments with both low seismicity rates and low b-values tend to have higher earthquake potential, as illustrated in the Ridgecrest case. Conversely, high b-values are often associated with lower stress levels (e.g., segments following large earthquakes) or weaker fault strength (e.g., subsidiary structures or geothermal fields), which indicates lower seismic hazard.

(4) The seismicity depth distribution tends to remain stable before and after large earthquakes, making it a useful tool for inferring fault locking depth and delineating persistent asperities. This pattern can also be observed in distributed shear zones, such as the Ridgecrest faults. However, further comparative studies using geodetic observations are needed. While we have proposed speculative interpretations - linking concentrated seismicity at depth to clear lock-creep separation, and distributed seismicity depth profiles to partially coupled faults - these hypotheses require additional validation.

It is important to note that our analysis of seismicity has been simple and qualitative, and there is likely much more valuable information to be uncovered within enhanced seismic catalogs. To achieve this, maintaining stable and continuous seismic observations over extended periods is crucial. Additionally, incorporating multiple observational techniques, such as InSAR and GNSS, for cross-validation can help identify more interpretable features in seismicity.

Chapter 5

Untangling Foreshock Triggering Mechanisms with Source Spectra Analysis and Coulomb Stress Modeling

5.1 Introduction

Foreshocks are known as smaller earthquakes preceding the large mainshock (Jones and Molnar, 1979). Due to the neighboring location and temporal correlation, foreshocks are considered as a possible precursory phenomenon, e.g. the success prediction of 1975 M_w 7.0 Haicheng earthquake largely relies on the ~1-day foreshock activity (Wang et al., 2006). Traditionally, two end-member models are proposed to explain the triggering relationship between the foreshocks and mainshock (Dodge et al., 1996): the cascade model and the pre-slip model. The cascade model describes the seismic sequence as the cascade failure of isolated asperities, where each event is triggered by the stress transfer from the previous earthquake (Helmstetter et al., 2003; Felzer et al., 2004; Ellsworth and Bulut, 2018; Yoon et al., 2019). Thus, the initiation process of mainshock and foreshocks are identical, which lead to an unpredictable nature of the mainshock. On the other end, the pre-slip model regards the foreshocks as the byproduct of the nucleation process of the mainshock, where accelerating aseismic slip is accompanied. It is a deterministic model, because theoretical and laboratory studies have shown that the nucleation size, i.e. the area of pre-slip, scales with the final size of the mainshock (Dieterich, 1978; 1992; Ampuero and Rubin, 2008; Johnson et al., 2013). The different implications for earthquake predictability make it important to discriminate between different foreshock-mainshock triggering mechanisms.

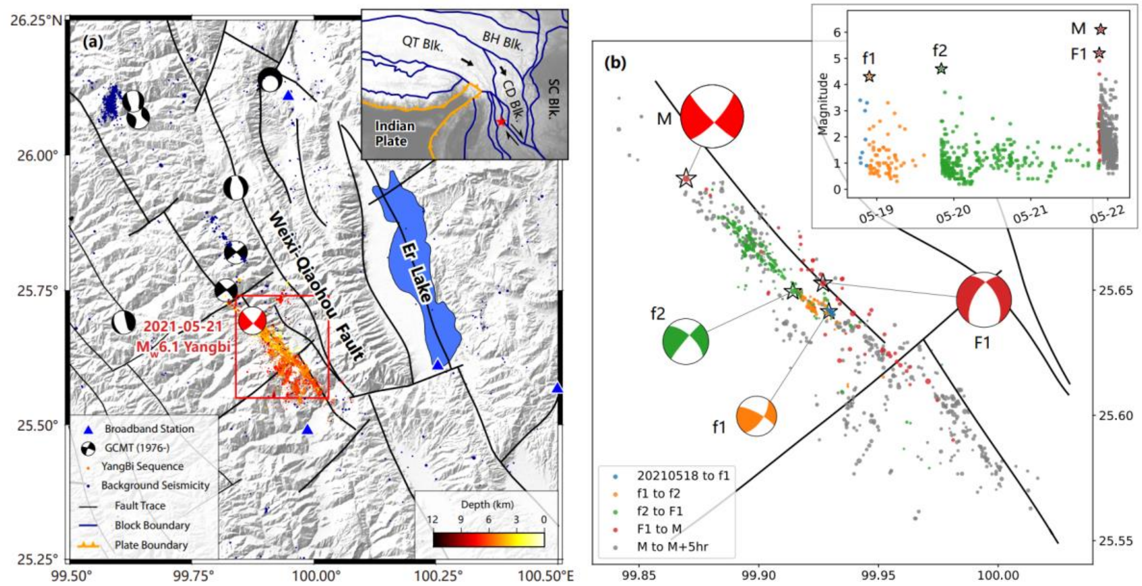

Figure 5.1. Tectonic background and foreshock sequence. (a) Tectonic background of the Yangbi earthquake. In the main plot, fault traces are plotted by black lines, and come from Wang et al. (2021a). The interseismic background seismicity and Yangbi seismic sequence are plotted by blue and orange dots respectively, with the focal depth color-coded. Focal mechanism of GCMT since 1976 is plotted by black beachballs. Blue triangles mark the broadband stations. In the insert plot, the plate boundary and active block boundary are plotted by orange and blue lines, respectively. Main blocks, i.e. Qiangtang block (QT), Bayan Har block (BH), Chuandian block (CD), and South China block (SC), are noted, with their relative motion marked. (b) The Yangbi foreshock sequence. The study time period is divided by the major foreshocks (*f1*, *f2*, and *F1*) and the mainshock (*M*). Seismic catalog comes from Zhou et al. (2021a). The focal mechanisms of the mainshock and largest foreshocks are determined by multi-point-source inversion, and that of the first two smaller foreshocks comes from Yang et al. (2021).

The 2021 M_w 6.1 Yangbi earthquake that strikes the Yunnan province of southwest China is a typical large earthquake with prominent foreshock activity (Figure 5.1). It occurs near the southwestern boundary of Chuandian block (Zhang et al., 2003) dominated by right-lateral strike-slip motion (Shen et al., 2005). The aftershock of Yangbi earthquake reveals an NW-SE trending fault that is subparallel with the major active fault, i.e. Weixi-Qiaohou fault (Figure 1a). The Yangbi sequence is composed of the 21st May M_w 6.1 mainshock (denoted as *M*) and three major foreshocks (Figure 5.1b): the 18th May M_w 4.3 (*f1*), the 19th May M_w 4.6 (*f2*), and the 21st May M_w 5.2 earthquake (*F1*). Moment tensor inversion results in right-lateral focal mechanism for these four events (Yang et al., 2021), which is also consistent with the major fault trend. The foreshocks are located in the middle of the mainshock co-seismic fault segment, all of which show clear unilateral rupture, indicated by the relative location between the epicenter and their aftershocks (Figure 5.1b): *f1* and *f2* rupture to northwest, while *F1* mainly rupture to southeast with certain bilateral component.

Up to date, a few discussions are published on the triggering relation between those major foreshocks and the Yangbi mainshock, but no consistent conclusions are reached (e.g., Lei et al., 2021; Zhang et al., 2021; Liu et al., 2022b; Sun et al., 2022). It is not surprising, since the conclusions on foreshock formation can vary by different analysis techniques and data conditions (Mignan, 2014). As an example, Ellsworth and Bulut (2018) made detailed event relocation and source spectra analysis to investigate the inter-event triggering effect of the 1999 Izmit foreshocks, which turned out to be a cascading sequence, instead of precursory aseismic slip loading proposed by Bouchon et al. (2011). Thus, the modeling of Coulomb stress with well-constraint event location and finite faulting model is necessary in such discussions. Fortunately, the rather dense regional seismic network in the Yunnan province of China made such analysis possible in Yangbi. Such well-recorded continental large earthquake with intense foreshock activity is rare, and thus provides a valuable chance to generate a well-depicted case for the seismological community. Moreover, the Yangbi earthquake is the largest event that occurs in southwest Chuandian block since the 1996 M_w 6.6 Lijiang earthquake (Han et al., 2004; Ji et al., 2017) and is one of the largest earthquake in China that has clear foreshock activity since the 1975 M_w 7.0 Haicheng earthquake (Xu et al., 1982; Wang et al., 2006), the 2010 M_w 6.9 Yushu earthquake (Ni et al., 2010), and the 2014 M_w 6.9 Yutian earthquake (Cheng et al., 2014). Thus, an in-depth study in the Yangbi sequence has implications on not only the foreshock mechanism but also the seismic hazard of southwest China.

In this study, we follow a similar strategy as Ellsworth and Bulut (2018), but focus on larger events with finite source and rupture directivity, to investigate the triggering mechanism of Yangbi sequence. We first determine the local fault structure based on the rupture directivity, aftershock distribution, and the focal mechanism. Secondly, we delineate the finite rupture area for each major foreshock based on aftershocks and spectral ratio analysis. Finally, we model the evolution of Coulomb stress, based on which we interpret the causality of each major event.

5.2 Data and Methods

5.2.1 Seismic Catalog

We adopt a high-resolution seismic catalog constructed by Zhou et al. (2021a) with deep learning and matched filter. The catalog contains 7943 well-located events in the Yangbi source region from 2021-05-01 to 2021-05-28, which covers the foreshock and early-aftershock period that is interested in this study. The construction of this catalog utilized an AI-based phase picker to obtain the template catalog (Zhou et al., 2019) and matched filter to augment the templates (Zhou et al., 2021b). Such strategy gives reliable and highly complete detection, and thus the catalog reaches a complete magnitude of M_L 1.0, and a minimum magnitude of M_L -1.0. The relocation process utilized cross-correlated differential travel times, which provides sub-sampling-rate precision (<0.01-s), leading to a relative location uncertainty of ~10m laterally and ~20m vertically in the hypoDD inversion process (Waldhauser, 2001; Zhou et al., 2021a). Note that the real location uncertainty is larger than that given by least-square criteria.

5.2.2 Spectral Ratio Analysis

We use a spectral ratio method to extract the source spectrum of the Yangbi foreshocks to determine their rupture directivity and source parameters. This method utilizes empirical Green’s function (EGF) to remove the wave propagation effect and site response in the target foreshock seismogram (Chen and Shearer, 2013; Ross and Ben-Zion, 2016; Ellsworth and Bulut, 2018; Yoon et al., 2019). EGFs are selected as smaller events (usually >1 magnitude smaller) that occur near the target event, so that they can be considered as point source and share similar ray paths with the target event. Thus, on the same station, the ratio between target and EGF spectra represents the source spectrum of target event, which contains the seismic source information, e.g. rupture area, coseismic slip, stress drop, etc. In the Yangbi sequence, we select the aftershocks of the target foreshock as EGF, which is both large enough to be clearly recorded on selected stations, and small enough to be considered as a point source. This leads to 6 to 10 EGFs with the magnitude range from M_L 2.6-3.5 for *f1* and *f2*, and M_L 2.9-4.1 for *F1*.

The rupture directivity can be revealed by the azimuthal variation of source spectrum (Calderoni et al., 2015; Calderoni et al., 2017). Based on the dynamic rupture theory, stations facing the rupture propagation direction are expected to observe a source-time function (STF) of shorter duration and higher amplitude; or, in the frequency domain, a higher corner frequency on the source spectrum (Haskell, 1964). Thus, we apply two sets of comparison on the source spectrum observed on two sides of the target earthquake: one set along fault-parallel direction and another along fault-normal direction. For unilateral rupture, the contrast of corner frequency along fault-parallel would be larger than the fault-normal one; for bilateral rupture, both directions have weak contrasts, but fault-parallel stations would record larger high-frequency components.

For the estimation of rupture area, we use fault-normal stations to obtain the corner frequency that has little directivity effect. We calculate the S-wave spectrum with a multi-taper algorithm (Prieto et al., 2009), and normalize it by its seismic moment (Ross and Ben-Zion, 2016). We adopt several strategies to improve the stability of spectral ratio calculation: (1) the initial result is smoothed in log-scale by interpolation and sampling on every 0.025 of log(f); (2) for each event-station pair, we utilize a multi-window strategy (Imanishi and Ellsworth, 2006; Uchida et al., 2007; Yoon et al., 2019): three 10-s sliding windows with a 1.5-s stride are applied, where the first window starts from the S wave arrival. The spectrum of these sliding windows is averaged on the log scale; (3) the spectrum of different EGFs are stacked in the log-scale, since they have similar shape and amplitude (Ross and Ben-Zion, 2016). The final spectral ratio is obtained by dividing the target spectrum with the stacked EGF spectrum.

To estimate source parameters from spectral ratio, we first fit the omega-square source model proposed by Boatwright (1980) for the estimation of corner frequency:

$$\frac{u_1(f)}{u_2(f)} = \frac{M_{01}}{M_{02}} \sqrt{\frac{1 + \left(\frac{f}{f_{c2}}\right)^4}{1 + \left(\frac{f}{f_{c1}}\right)^4}} \, , \tag{5.1}$$

where sub-index 1 and 2 represent the target event and EGF, respectively; u is the spectrum, M_0 is the seismic moment, f_c is the corner frequency. Grid search of the moment ratio M_{01}/M_{02} and two corner frequency f_{c1} and f_{c2} is applied to fit the spectral ratio. In this process, the summed difference between predicted and observed spectral ratio on a frequency band of 0.2-20 Hz is minimized in the logarithm scale. The source radius is estimated according to Madariaga (1976)'s theory, assuming a constant rupture velocity of $0.9v_s$:

$$r = \frac{0.21v_s}{f_c} \, , \tag{5.2}$$

where v_s is the S wave velocity, which is set as 3.4 km/s, based on the local velocity structure (Liu et al., 2021). The average slip on the circular fault is thus:

$$D = \frac{M_0}{\mu\pi r^2} \, , \tag{5.3}$$

where μ is the shear modulus, and is set to 32 GPa. The static stress drop is estimated by Eshelby (1957)'s equation:

$$\Delta\sigma = \frac{7}{16}\frac{M_0}{r^3} \; . \tag{5.4}$$

5.2.3 Multi-Point-Source Moment Tensor Inversion

We adopt multi-point-source (MPS) inversion technique (Yue and Lay, 2020) to resolve the moment tensor of the largest foreshock and the mainshock. The MPS method utilize different subevents to model three-component broad-band records in the near field. It is primarily developed by Kikuchi and Kanamori (1982, 1986, 1991), and is improved by Yue and Lay (2020) with an iterative inversion algorithm. In this method, a priori constraints are set on the search time window of subevents, their potential location (mesh grids), and the shape of STF. The algorithm finally provides an estimation of the location, initiative time, focal mechanism, and moment of each subevent. This method has advantages for the largest foreshock of Yangbi, which is followed by two immediate aftershock that contaminate the tail wave (see Section 5.3.2). Thus, we want to refine the results obtained by gCAP method (e.g., Lei et al., 2021; Zhang et al., 2021). It is worth mentioning that polarity-based methods are not suitable as well, because of the imperfect station coverage and that most stations record upward polarity for *F1*.

To apply the MPS method in Yangbi, we first select 14 stations with epicentral distances between 30-160km for the largest foreshock, and 12 stations between 40-200km for the mainshock, considering the clipping effect of the nearest stations. All original waveforms are preprocessed by removing the instrumental response, band-pass filtering to 0.01-0.5 Hz, and down-sampling to 10 Hz. Event waveforms are cut from 10-s before the initial P arrivals and ending with 130-s and 100-s time windows for foreshock and mainshock separately. For the computation of Green's function, we adopt the regional velocity model developed by joint-inversion of body and surface wave (Liu et al., 2021). The Green's function is computed with wavenumber-frequency integration algorithm (Zhu and Rivera, 2002) for each preset spatial grid. The spatial grids are distributed in a potential rupture area of about 15*6 km^2. For the largest foreshock and the mainshock, we respectively sliced 10*6 grids and 10*5 grids (Figure S10), considering the distribution of aftershocks. The selection of search time windows, i.e. window length and number of subevents, is based on the visual inspection on waveform and the inversion process. For the largest foreshock, we used two subevents that occur between 0-5 s and 5-10 s; for the mainshock, we use three subevents during 0-3 s, 5-8 s, and 8-15 s.

5.3 Results and Discussion

5.3.1 Rupture Directivity and Source Parameters of the Major Foreshocks

We first investigate the rupture directivity of the major foreshocks, since it is debatable in some published results (Lei et al., 2021; Zhang et al., 2021; Liu et al., 2022a; Liu et al., 2022b), and is essential in the determination of rupture area. As demonstrated in Section 5.2.2, we use the spectral ratio observed on different stations to determine the directivity. Based on the aftershock distribution and local fault traces (Figure 5.1b), we consider the major fault trend (SE-NW) as the possible rupture direction. Thus, we made two sets of comparisons along fault-normal and fault-parallel direction (Figure 5.2, and Figure S1a for adopted stations). It is obvious that the fault-parallel spectral ratios show

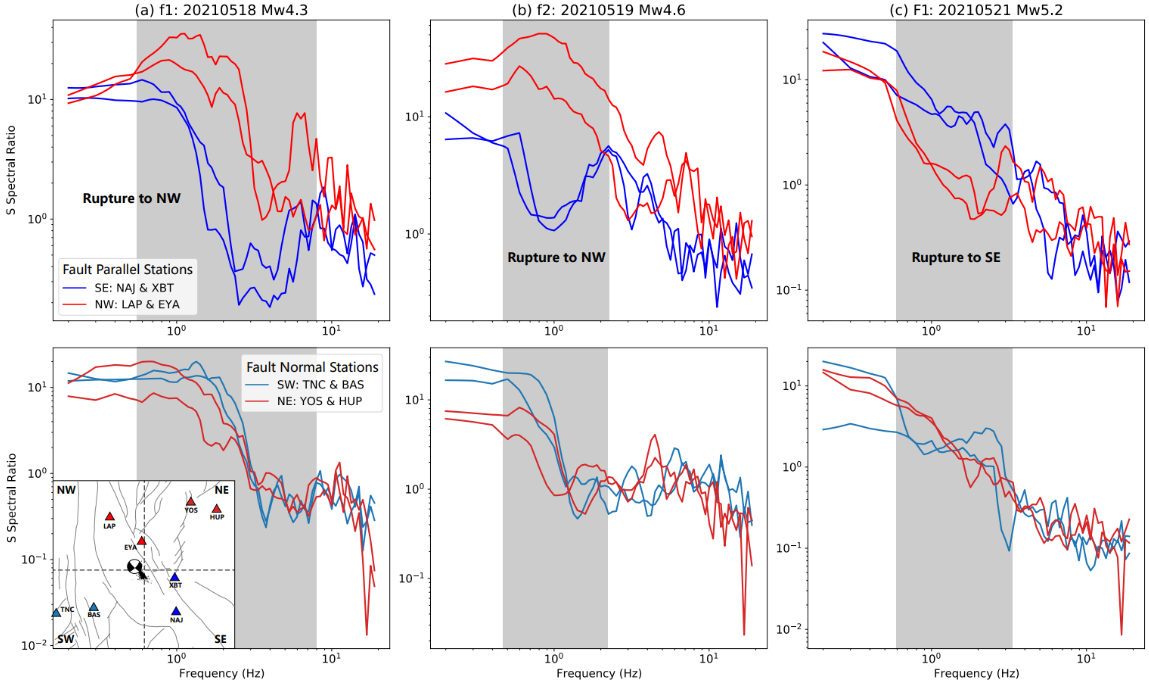

Figure 5.2 Spectral ratio comparison for directivity determination. (a), (b), and (c) plot the spectral ratio comparison of the foreshock *f1*, *f2*, and *F1*, respectively. The first and second line show the comparison along fault-parallel and fault-normal direction. The station used for the comparison is shown in the inset, with their color represent the quadrant. Each line represents a spectral ratio observation on one station, with the color mark its azimuthal quadrant. The frequency bands with significant contrasts are highlighted by gray patches.

more significant contrast, indicating that the rupture mainly occurs along the major fault trend, and that *f1* & *f2* rupture to the NW direction, while *F1* rupture to SE. This conclusion agrees with the relative location between the epicenter and aftershocks, but disagrees with Lei et al. (2021) that obtained a NE rupture for *F1* event, based on waveform fitting assuming different nodal planes. However, their waveform inversion utilized a 70-s time window for S wave, which is biased by two immediate large aftershocks (see next section), and there are no mapped NE-trending conjugate faults associated with *F1*, nor do its aftershocks distribute along that direction, as in other catalogs built with AI picker or matched filter (Liu et al., 2022a). Thus, our spectral ratio analysis determines that the Yangbi sequence is associated with faults that strike in NW-SE direction.

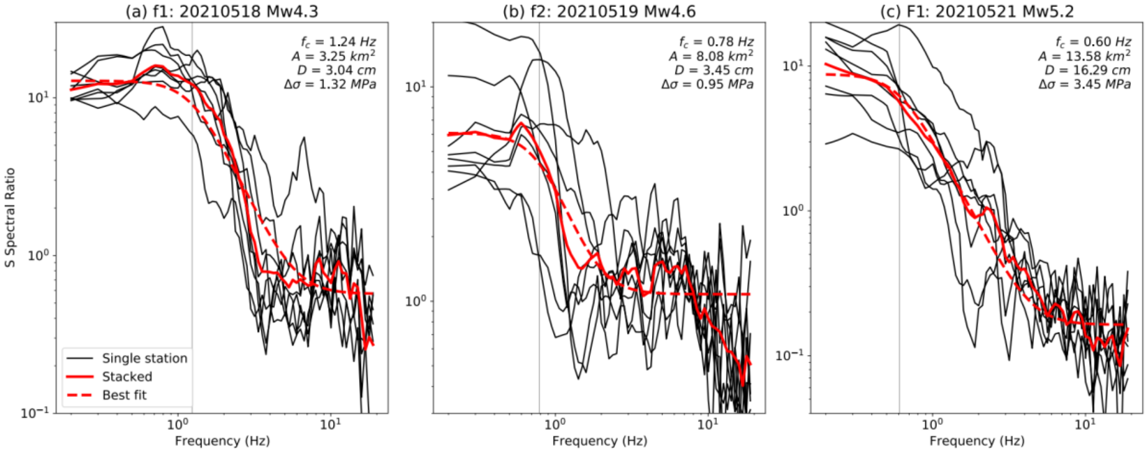

Figure 5.3. Spectral ratio analysis. (a), (b), and (c) plot the spectral ratio analysis of the foreshock *f1*, *f2*, and *F1*, respectively. The black lines, solid red lines, and dashed red lines denote the spectral ratio on single stations, stacked spectral ratio, and the best fit to Boatwright model to the stacked spectral ratio. The vertical gray line marks the estimated corner frequency.

We then extract source parameters for these major foreshocks with fault-normal stations, where directivity effect is minimized. The spectral ratios on different stations have consistent shape, and the resulting stacked spectral ratio is smooth, fitting well with the Boatwright model (Figure 5.3). The spectra fitting gives an estimation of corner frequency, which is directly related to the rupture area, assuming Madariaga (1976)'s dynamic model (Equ. 5.2): for *f1*, *f2* and *F1*, we got 3.25 km^2, 8.08 km^2, and 13.58 km^2, respectively. The amount of slip and stress drop are also estimated by combining the moment magnitude. We find that *f1* & *f2* have relatively low stress drop of ~1.0 MPa and a coseismic slip of 3 cm, while *F1* has a ~3.5-MPa stress drop and a ~16-cm coseismic slip (Figure 5.3).

5.3.2 Analysis of the Largest Foreshock

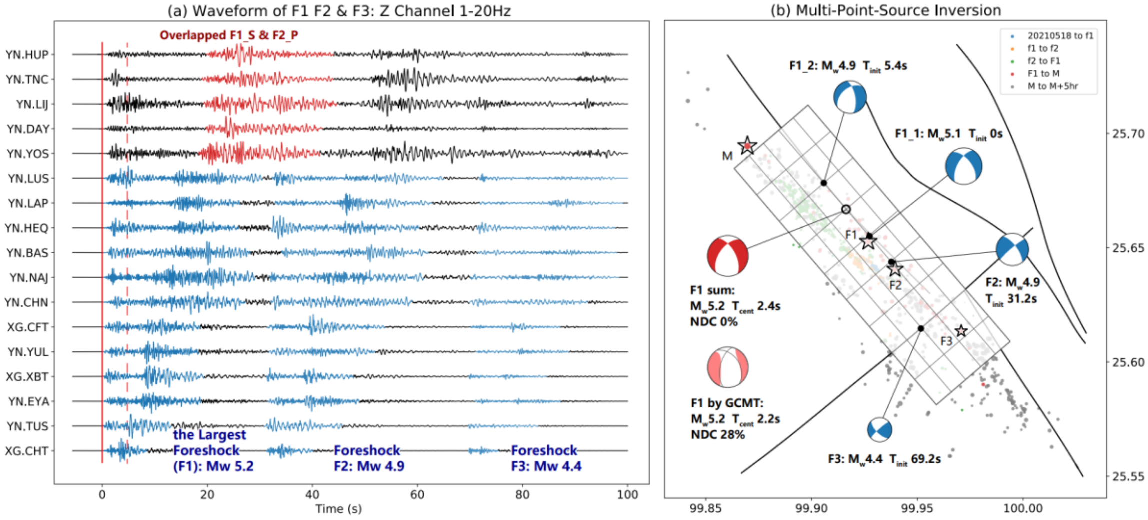

Figure 5.4. Multi-point-source (MPS) inversion for the largest foreshock (*F1*) and its two immediate aftershocks (*F2* & *F3*). (a) Waveform of *F1*, *F2*, and *F3*. The Z-channel waveform is band-pass filtered to 1-20Hz, and is aligned with the initial P wave arrival of *F1*. The onset of P waves of *F1* is marked by vertical red line, and that of the second subevent of *F1* (i.e. *F1_2*) is marked by dashed red line. The earthquake signal of *F1-3* are highlighted in blue. The relative remote stations with the S wave of F1 and P wave of F2 overlapped are marked in red. (b) The MPS inversion result of *F1-3*. The subevents of the whole sequence are marked in blue, with their centroid location distributed on the preset mesh grids. Note that *F1* is separated by two subevents, and the summarized moment tensor plot in red, with a comparison with that by GCMT plot in light-red.

By inspecting the waveform of *F1*, we found that this largest foreshock of Yangbi is followed by two immediate aftershocks: M_w 4.9 *F2* and M_w 4.4 *F3* (Figure 5.4a). This raises challenges in the moment inversion process, since the waveform of different events are overlapped. Thus, as demonstrated in Section 5.2.3, we apply MPS inversion technique to *F1-3*, which is designed to resolve complex rupture process, and is not affected by overlapping waveforms. Results show that the largest foreshock *F1* is composed of two subevents (Figure 5.4b), where the second and smaller subevent *F1_2* initiates after ~5 s, with its centroid locates at the NW of the first one. The temporal separation is significantly

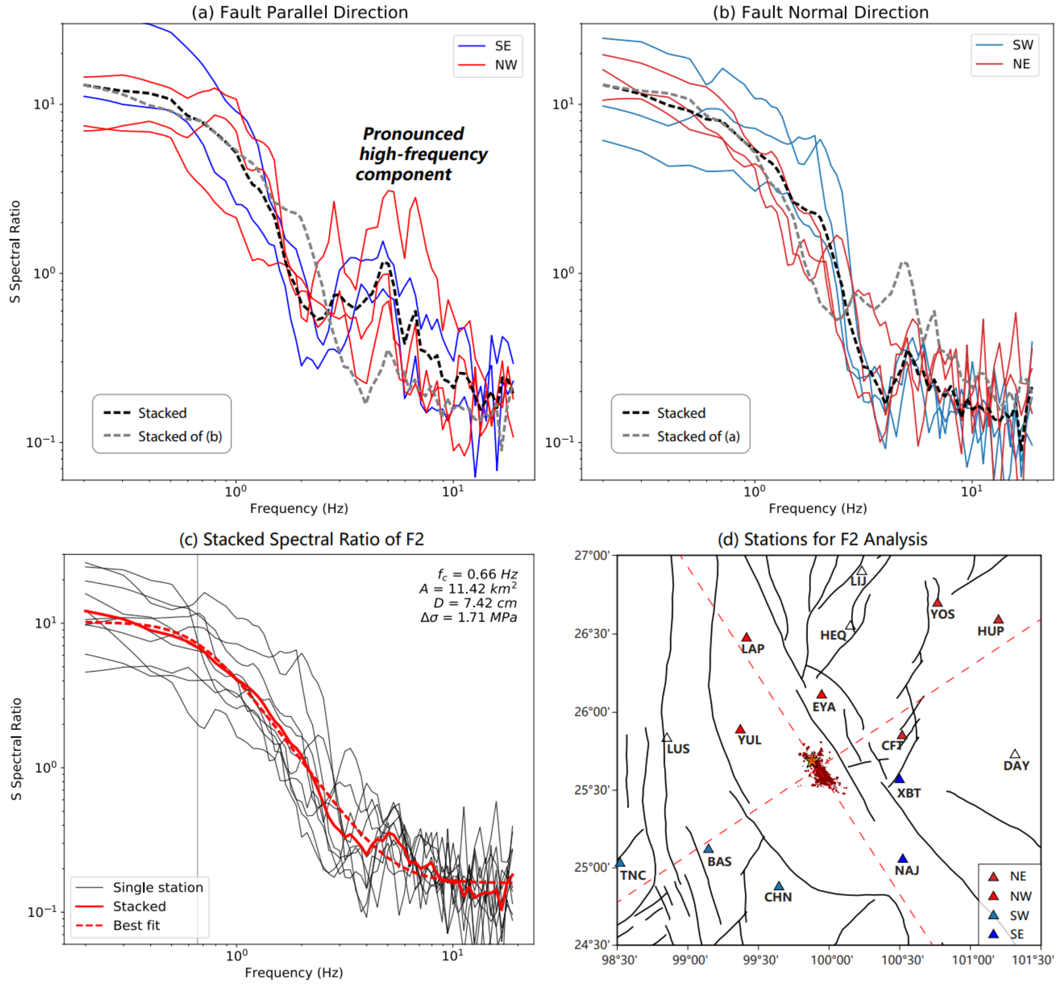

Figure 5.5. Spectral ratio analysis of *F2*. (a) & (b) are two sets of spectral ratio comparisons along fault-parallel and fault-normal direction, respectively. The dash lines are the stacked and averaged spectral ratio. (c) plots the stacked and fitted spectral ratio. The markers have the same meaning as in Figure 5.3. (d) shows the station distribution used in this analysis. Seismic stations are plotted in triangles, fault traces are plotted in black lines, and reference fault-parallel and fault-normal trend are marked by red dashed lines.

larger than the duration of an M ~5 earthquake, which probably indicates that *F1_1* and *F1_2* are two independent events that both rupture to SE. The summarized moment tensor of *F1* shows a ~60° NE dipping nodal plane and certain normal faulting component. This result is consistent with GCMT result, though our result show neglectable non-double-couple (NDC) component (Figure 5.4b). It is not surprising, since GCMT inverse long-window tele-seismic waveforms that represents an overall moment tensor including all three events, and that our MPS results show different dip angles between *F1-3*, which indicates geometrical complexity that can cause NDC in the summarized moment tensor (Julian et al., 1998).

The first immediate aftershock, i.e. *F2*, has a similarly large magnitude, thus may play an important role in triggering the mainshock, while is ignored by published results. We apply the spectral ratio analysis demonstrated in Section 5.2.2 to resolve its rupture source parameters. Note that the spectrum analysis is done with S-wave, which is less biased by the waveform of *F1*. We first examine the rupture directivity. The two-direction comparisons both show weak contrast in corner frequency, indicating bilateral rupturing (Figure 5.5a-b). However, the fault parallel stations observed pronounced high-frequency component (Figure 5.5a), suggesting that *F2* also rupture along the major fault trend. Thus, we adopt the fault-normal stations to extract its source parameters, as in the last section. We obtain a similarly large rupture area (~11 km^2), but a much smaller coseismic slip (~7 cm) and stress drop (~1.7 MPa).

5.3.3 Construction of Fault Model

To prepare for the Coulomb stress calculation, we construct a fault model that delineates the local fault structure and rupture area of each major foreshock. The fault geometry is determined by the aftershock distribution, focal mechanism, and the mapped local fault traces. The local fault data show a clear left-lateral step-over feature (Figure 5.6a), and that the Yangbi mainshock and first two smaller major foreshocks (*f1* & *f2*) are located off the mapped trace. However, the aftershocks on the NW of epicenter show a clear trend that connects to another mapped fault segment, indicating that the major fault is continuous at depth (Figure 5.6a). This fault segment associated with *M*, *f1*, and *f2* (denoted as *Fault_M*) is probably near-vertical, suggested by their focal mechanisms (Figure 5.1b, 5.6). The largest foreshock *F1* and its aftershocks are not on *Fault_M*, and are more likely to occur on the mapped segment (denoted as *Fault_F*), which is dipping to NE, as indicated by the focal mechanism (Figure 4b, 6a), the relative location between surface fault trace and microseismic events at depth (Figure 6a), and the aftershock distribution (cross-section CC' in Figure 5.7c). The dip angle of *Fault_F* is likely variable along strike, because the dip angle in the focal mechanisms of *F1* & *F2* are different, and that the aftershock trace is gradually merging with the surface fault trace (Figure 6). The two fault segments (*Fault_M* & *Fault_F*) intersect at the mapped stepover, where multiple unmapped conjugate faults are imaged by aftershocks, indicating geometrical complexity. This fault segment probably continues to SE at depth, while the surface trace alters to the mapped stepover, which is supported by the focal mechanism of *F3* and the third subevent of *M* that dip to SW (Figure 5.6). Though a connected fault makes rupture easier to propagate, the geometrical complexity slows down or even terminates the mainshock rupture, as shown in our MPS inversion (Figure 5.6b) and other studies utilizing joint inversion of InSAR & GPS data (Li et al., 2022) or InSAR & seismic data (Figure 5.7b, Wang et al., 2022a).

The rupture surface of major foreshocks is constrained jointly by aftershock distribution and spectrum-determined rupture area. As demonstrated in the last paragraph, the first two major foreshocks *f1* & *f2* occur on *Fault_M*, which is a near-vertical fault with pure right-lateral strike-slip events initiate on it. Their rupture area is well depicted by the aftershock distribution, because most of the aftershocks occur on only one side of the epicenter (Figure 5.7a), and that the extension of immediate aftershocks is rather clear (see Section 5.3.5). We draw a rectangular rupture area of *f1* & *f2* based on their immediate aftershocks (Figure 5.7a-b), which is generally consistent with the rupture area estimated with spectrum analysis in Section 5.3.1 (Figure 5.3a, b).

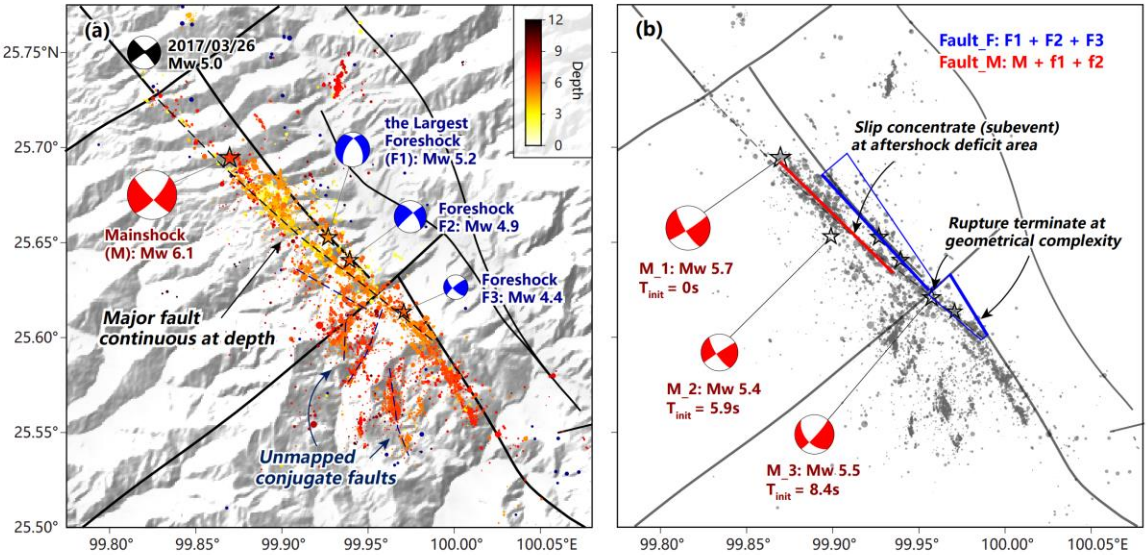

Figure 5.6. Fault geometry interpretation and MPS inversion of the mainshock. (a) Interpretation of fault geometry. The solid black lines are the mapped fault, the dashed black line is the unmapped major fault, and the dashed dark-blue lines are the unmapped conjugate faults. The blue beachballs mark the MPS-inversed focal mechanisms of the foreshock *F1-3*, and the hollow black stars mark their epicenters. (b) Simplified fault geometry and MPS inversion result of the mainshock. The solid red and blue line marks the simplified fault trace associated with the mainshock and the largest foreshock. The red beachballs mark the focal mechanisms of the mainshock subevents, and their centroid locations are marked by hollow stars.

For the largest foreshock *F1*, we first simplify the *Fault_F* as a 60° NE dipping fault that slips with a rake angle of -150° (right-lateral + normal faulting), based on the focal mechanism solution. However, the coseismic rupture cannot be directly imaged from aftershocks, because the immediate aftershocks occur on both sides of the epicenter (though mainly on the SE side), and the total associated rectangular area is significantly larger than that inferred from the spectral ratio method. Therefore, we adopt two end-member rupture models for *F1*, and show that this difference does not alter the interpretation of triggering relation (see Section 5.3.5), while only the preferred model and related Coulomb stress calculation is shown in the main text. The preferred model put the NW end of *F1* rupture on the location of the northernmost immediate aftershock, since the second subevent of *F1* locates on the NW of epicenter (Figure 5.4b). The southern end of *F1* rupture is set at the fault junction between the major fault and mapped conjugate fault (Figure 5.6a), which is also near the termination of the mainshock (*M_3*, Figure 6b). The top of *F1* rupture is set at 4 km, since the shallowest aftershock locates at 4 km, and that the shallower portion of the fault is probably near-vertical. This setting also agrees with the observed separation of the two fault traces at ground surface (see cross-section CC' in Figure 5.7c). This preferred model leads to a rupture area consistent with the spectral ratio analysis (Figure 5.3c), and the overall rupture directivity is to SE, as shown in Figure 2c. Further evidence in support or against this model may come from source-time function extraction and subsequent subevent location technique with a rather dense seismic network (e.g., López-Comino and Cesca, 2018; Wu et al., 2019a; Meng and Fan, 2021; Meng et al., 2021).

Another important event is the M_w 4.9 *F2*, i.e. the first and largest immediate aftershock of *F1*. As shown by spectrum analysis (see Section 5.3.2), *F2* is a bilateral rupture along *Fault_F* that has a similarly large rupture area as *F1*. Its rupture area is even harder to determine than *F1*, since we cannot decipher which aftershock is associated

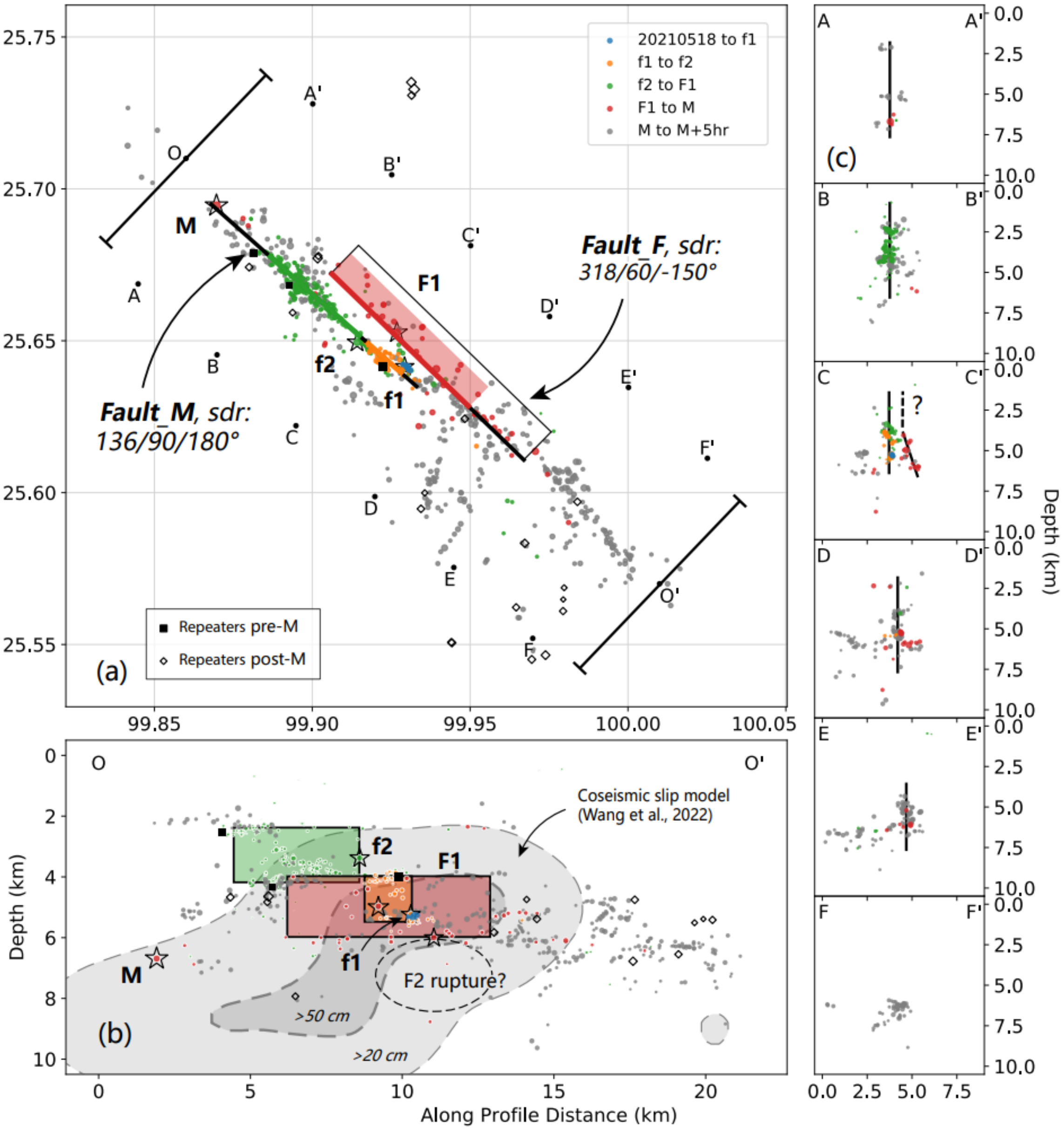

Figure 5.7. Distribution of seismic events and finite rupture model. (a) Map view, (b) cross-section along strike, and (c) fault-normal cross-sections. Events in different periods are denoted by colors. Four major foreshocks are marked by hollow stars. The simplified faults associated with the mainshock (*Fault_M*) and the largest foreshock (*Fault_F*) are denoted as thick black lines. The rupture length and area are marked by color line and patch in (a) and (b). The coseismic slip contour by Wang et al. (2022a) is plotted in (b). Repeating earthquakes pre- and post-mainshock is plotted in solid squares and hollow diamonds, respectively.

with $F2$. The best guess we can make is that $F2$ ruptures a deeper portion (Figure 5.7b), which avoids an immediate re-rupturing of the same asperity. Again, further investigations would require near-source stations that can resolve the down-dip rupturing behavior. Based on the above reasons, we decide not to include $F2$ in the Coulomb stress modeling, but will include it in our discussion in Section 5.3.5.

Our fault model of foreshocks forms a complementary pattern with the co-seismic rupture of the M_w 6.1 mainshock that concentrates at about 3-10 km initially and propagates towards the shallower portion at SE side at about 2-7 km (Figure 5.7b, Li et al., 2022; Wang et al., 2022a). This is a typical pattern for aftershock distribution and coseismic slip, as shown in many other case studies (e.g., Yue et al., 2017; Mendoza et al., 2019; Jiang et al., 2021b). This pattern of rupture is also consistent with the distribution of repeating earthquakes (see Section 5.3.5), which surrounds the ruptured patches and indicate the existence of afterslip (e.g., Shaddox et al., 2021). Based on this model, we can calculate the static Coulomb stress change induced by each foreshock.

5.3.4 Coulomb Stress Evolution

We calculate the static change of Coulomb failure stress (ΔCFS) with the Coulomb 3 software (Lin and Stein, 2004; Toda et al., 2005), which assumes a homogeneous elastic half-space. The fault patch and amount of slip are determined according to the previous section. The friction parameters are set as default: Coefficient of friction = 0.4, Poisson's ratio = 0.25, Young's modulus = $8*10^4$ MPa. We calculated the cumulated Coulomb stress change after each significant foreshock (Figure 5.8).

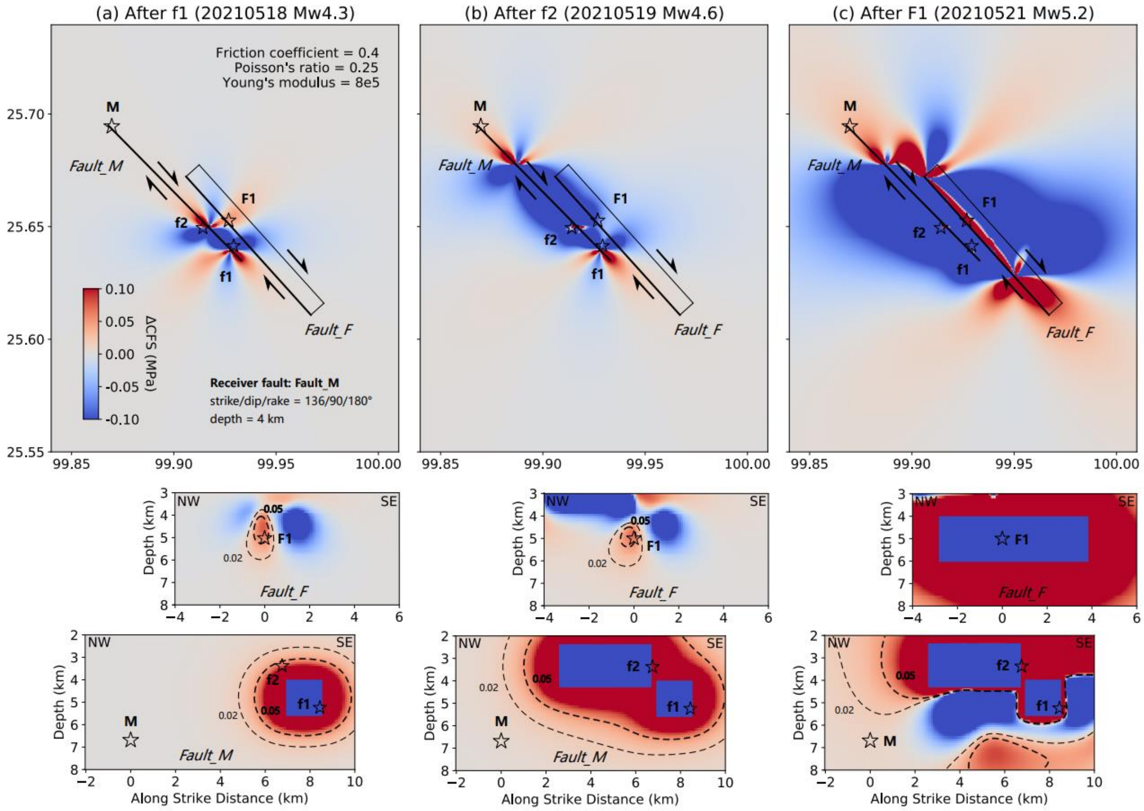

Figure 5.8. Evolution of Coulomb stress change. (a), (b), and (c) plot cumulated Coulomb stress change after *f1*, after *f2*, and after *F1*, respectively. The hypocenters are marked by stars. The upper and lower panels plot the map view with *Fault_M* as the receiver fault, and the cross-sections on *Fault_M* and *Fault_F*. Contours of 0.02 MPa and 0.05 MPa Coulomb stress increase are marked by dashed lines.

Results show that the foreshock *f1* causes a significant increase of ΔCFS near the hypocenter of *f2* (Figure 5.8a), indicating a cascade triggering. Note that *f1* also promotes the occurrence of *F1*, with a $\Delta CFS > 0.05\ MPa$. Similarly, the foreshock *f2* causes positive ΔCFS on both *F1* and *M* as well (Figure 5.8b). For *F1*, the net effect of *f1* & *f2* caused a $\Delta CFS > 0.05\ MPa$, which, is well above the traditionally considered threshold of 0.01 MPa for static triggering (e.g., Hardebeck et al., 1998; Ziv and Rubin, 2000; Parsons and Velasco, 2009). Note that the positive effect of *f2* on *Fault_F* rupturing is localized within 1-2 km, which covers the separation of these two faults. The occurrence

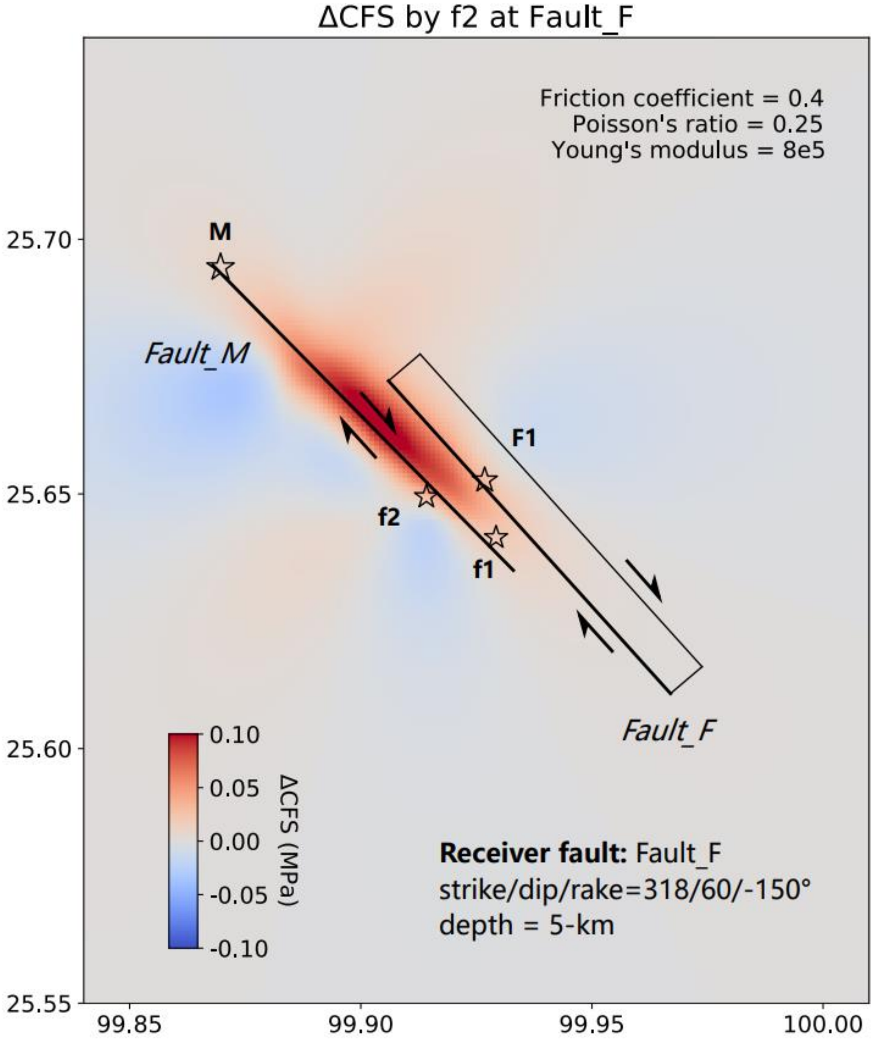

Figure 5.9. Coulomb stress change induced by *f2* with *Fault_F* as the receiver fault at a depth of 5 km.

of *F1* pushes the 0.02-MPa ΔCFS boundary closer to the hypocenter of *M*, which is also true for another rupture model of *F1* that is purely unilateral towards SE (Figure 5.10). This number is not significantly large compared with many statistical studies (e.g., King et al., 1994; Kilb et al., 2002), but is considered sufficient to explain the triggering in many other studies (Steacy et al., 2005, and references therein). More detailed discussions on the causality are presented in the next section.

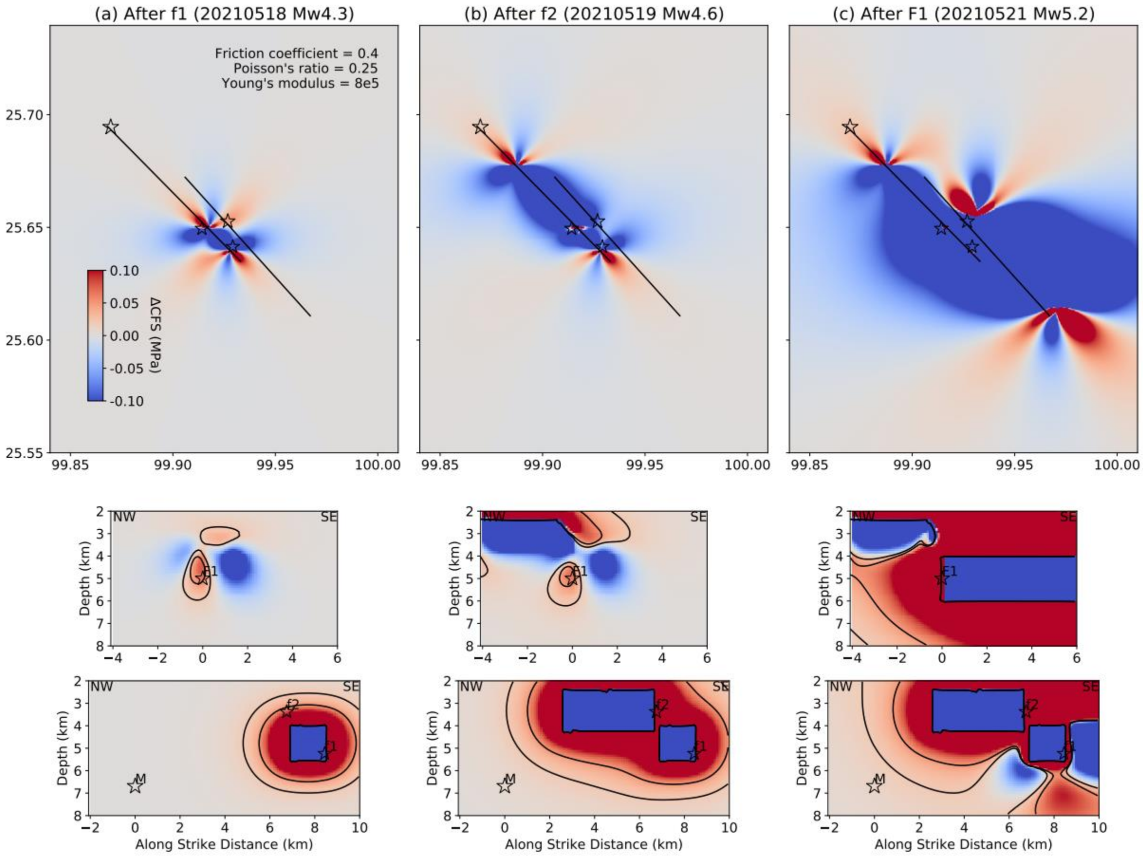

Figure 5.10. Coulomb stress evolution with *F1* as a purely uni-lateral rupture. The symbols have the same meaning as in Figure 5.8.

5.3.5 Interpretation of Inter-Event Triggering

5.3.5.1 How do the M_w 4.3 *f1* & M_w 4.6 *f2* initiate?

The initiation of *f1* is preceded by a micro-seismic swarm near the hypocenter (Figure 5.1b, 5.7a, 5.11a), probably indicating the nucleation process (Dieterich, 1992; Ampuero and Rubin, 2008). This pre-*f1* cluster is also observed in Liu et al. (2022b) and Liu et al. (2022a). Similar highly clustered seismicity before a major earthquake also exists in the 2019 M_w 6.4 Ridgecrest foreshock (Shelly, 2020a) and the 2007 M_w 4.6 Odaesan earthquake in Korea (Kim et al., 2010). Additional evidence for a pre-slip behavior comes from three M_w ~3.5 repeating earthquakes within the *f1*-cluster detected by Liu et al. (2022a). We also perform detection for repeating earthquakes that are considered as indicator for aseismic slip (Uchida and Bürgmann, 2019, and references therein). Following a similar procedure in Zhou et al. (2022b), waveform cross-correlation (CC) is utilized to detect event pairs with both a high waveform similarity and a small location separation. We first band-pass filter the waveforms to 1-12 Hz, and then (1) measure the waveform similarity with a 15-s time window starting from 1 s before P arrival, so that it covers both P & S waves, and (2) measure the differential S-P times with a P & S window of 3 s and 4 s, starting from 0.5 s before the phase arrival. For each event pair, we require an average CC >0.9 and at least 3 stations with Δ(S-P) $\leq$0.01 s. However, the pre-*f1* repeaters in Liu et al. (2022a) are not detected under such criteria, which may be resulted from different stations used.

The termination of *f1* can be explained by the clear isolation between *f1* & *f2* asperity in the fault-parallel profile (Figure 5.7b, 5.12c). The neighboring location of *f1* asperity & *f2* hypocenter and the large Coulomb stress increase (Figure 5.8a) strongly indicate a cascade triggering mechanism. However, the static triggering theory cannot explain the time delay between events (Freed, 2005; Steacy et al., 2005). It is probable that *f1* induced an afterslip that further stresses *f2*, as indicated by three M_L 1.5 repeaters (Figure 5.7, 5.11a, 5.12a) and a logarithmic expansion of aftershock zone (Figure 5.12c). It is also possible that the ~20-hr time delay between *f1* and *f2* indicates a nucleation process (Dieterich, 1992).

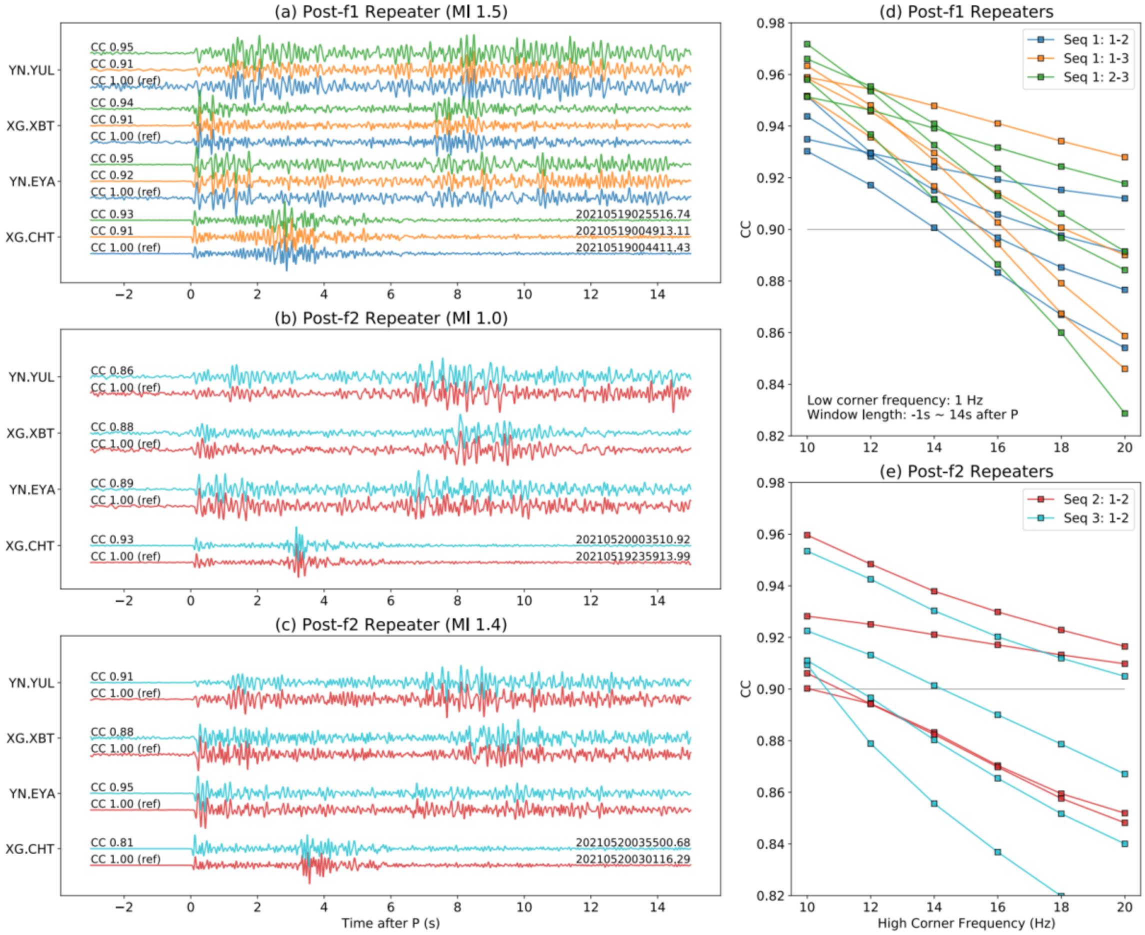

Figure 5.11. Repeater detection. (a-c) Repeater waveforms. The nearest four stations are plotted, with the Z-channel seismograms band-pass filtered to 1-20 Hz. (d-e) Relationship between CC values and frequency band. The CC values between each event pairs are calculated under different frequency band. The low corner frequency is kept as 1 Hz, with the high corner frequency ranges from 10-20 Hz.

5.3.5.2 How does the M_w 5.2 *F1* initiate?

As demonstrated in Section 5.3.4, *f2* itself causes a >0.01-MPa Coulomb stress increase on the NW segment of *Fault_F* (Figure 5.8b, 5.9), which is sufficient to support a static triggering relationship. However, *f1* also plays a role in preparing for the initiation of *F1*, and the Coulomb stress increase is localized around the *F1* hypocenter (Figure 5.8a).

Thus, it is probably *f1* that determines the hypocenter of *F1*. Another noticeable feature of the *f2*-induced ΔCFS is that it become negative above ~4 km (Figure 5.8b), which is the lower boundary of *f2* rupture area. This may confine the *F1* hypocenter below 4 km, as shown in our location result (Figure 5.7b, 5.11c). At the hypocentral depth of *F1* (~5 km), the positive effect of *f2* is more significant on the NW portion of *Fault_F* (Figure 5.8b), which favors a second subevent on NW (as in Figure 5.4b), and that the rupture of *F1* is more likely has an extension to NW, instead of a purely SE-propagating unilateral rupture, as argued in Section 5.3.3.

While the static Coulomb stress change of *f1* & *f2* is sufficient to explain the occurrence of *F1*, we want to note here that some possible aseismic evidences are also captured and may contribute to the triggering process. The aftershock zone of *f2* gradually expands along two sides of the coseismic rupture: ~1 km towards the NW side, and ~2 km to the SE side (events below and above the dashed lines in Figure 5.12a). This migration of aftershocks is probably driven by afterslip, since its evolution seems to follow a logarithmic pattern (Figure 5.12d), as is widely observed for afterslip (e.g., Kato, 2007; Peng and Zhao, 2009; Meng and Peng, 2016). Besides, two repeater doublets are detected after *f2* (Figure 9b-c, 10a), as is also observed in Zhu et al. (2022a) under a CC threshold of 0.9. Note that the SE-propagating afterslip occurs on the area above *f1*, which would cause a positive Coulomb stress change on *F1*. Again, this mechanism can well explain the time delay between the occurrence of *f2* and *F1*. The possible afterslip towards NW will be discussed in the next subsection. Moreover, like *f1*, the largest foreshock *F1* is also preceded by an increasing occurrence of micro-seismic events near its hypocenter, though in a much shorter period and with much fewer events (Figure 5.12b). This swarm may imply the existence of pre-slip during nucleation or is a mini mainshock-aftershock sequence triggered by the afterslip of *f2*.

5.3.5.3 How does the M$_w$ 6.1 *M* initiate?

Our Coulomb stress modeling shows that both *f2* and *F1* draw positive but relatively small ΔCFS on the mainshock hypocenter, but their summarized effect reaches a commonly adopted static triggering threshold of 0.01 MPa (Figure 5.8b-c). However, this may not be a satisfactory interpretation, since the short time interval between *F1* and *M* (~30 min) strongly indicates that the mainshock nucleation area has been critically stressed before *F1* or/and is significantly triggered by/after *F1*. Two other factors are likely incorporated in the triggering process: the afterslip of *f2* and the rupture of *F2*.

As pointed out in the last subsection, the logarithmic expansion of aftershock zone and the repeating aftershocks of *f2* indicate an afterslip migration. The NW-migrating afterslip would cause a positive Coulomb stress change on *M*, driving it closer to failure. Based on the aftershock evolution (Figure 5.12a-d), the average migration velocity is in the order of 1-10 km/d. However, the magnitude of *f2* is too small (M$_w$ 4.6) to generate visible afterslip for GPS, thus makes it difficult to validate the existence and extension of afterslip. Though no direct evidence in Yangbi, afterslip generated by M 4-5 or even smaller earthquakes have been observed in California with borehole strain data, and they tend to release a higher ratio of coseismic moment compared with that of large earthquakes (Hawthorne et al., 2016; Alwahedi and Hawthorne, 2019). Moreover, afterslip of M$_w$ >4.5 earthquakes are found to be common in the Anza segment of San Jacinto Fault, as indicated by the near-repeating earthquakes (detected with CC >0.9) and the correlated borehole strainmeter signal (Shaddox et al., 2021). If the *Fault_M* is already critically stressed before *F1*, it would be susceptible to small static stress change or even dynamic stress of *F1* (Freed, 2005; Yun et al., 2019).

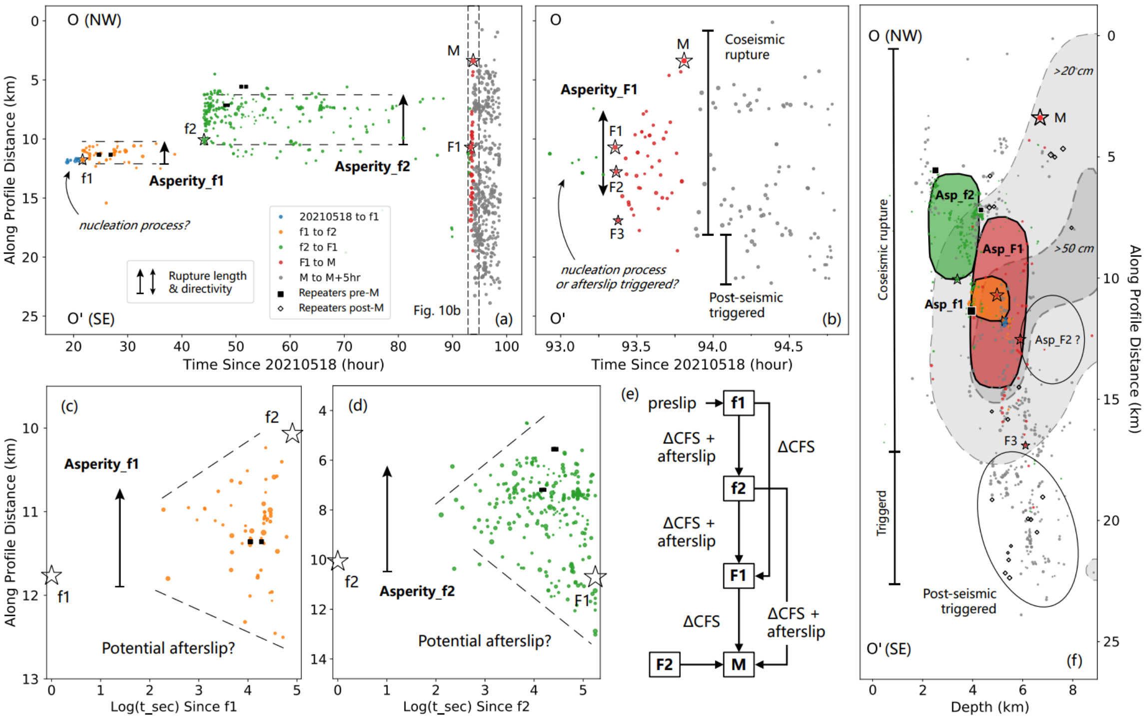

Figure 5.12. Migration pattern and interpretation of triggering mechanism. (a-b) plot seismicity migration along strike, with linear time scale. The reference points OO’ are the same as in Figure 5.7. The extension of different asperities and their rupture directivity are marked by vertical lines with arrow. (c-d) plot aftershock evolution after *f1* and *f2*, with the time plot in log-scale. (e) summarize our interpretation of foreshock mechanism. (f) plot fault-parallel cross-section, with the rough boundary of asperity delineated by solid lines. The coseismic slip model by Wang et al. (2022a) is plotted by gray dashed contours and color patches. Repeating earthquakes pre-, and post-mainshock are plotted in solid squares and hollow diamonds, respectively.

We point out in Section 3.3 that the rupture area of *F2* is hard to determine, which prevents us from obtaining an accurate ΔCFS modeling. However, *F2* has a comparable magnitude (M_w 4.9) as the largest foreshock *F1*, and the NW end of its rupture area probably reaches the $F1$ epicenter (Figure 5.7b, 5.12c), which suggests a non-negligible triggering effect. Similar to the ΔCFS by pure-unilateral $F1$ rupture model (Figure 5.10), we suspect that $F2$ could cause a 0.01-0.02-MPa Coulomb stress increase, which is comparably large as the contribution from $F1$.

It is noteworthy that the rupture process is less controlled by the ΔCFS pattern compared with its initiation, because the static stress transfer is 1-2 orders smaller than the dynamic stress that really controls the dynamic rupture (Heaton, 1990; Day et al., 1998). This can explain why a large portion of the mainshock rupture falls into the stress shadow of $F1$ (Figure 5.8c). However, it is probable that both the stress shadow and the fault step over (Figure 5.6b) slow down the rupture, cause the termination near $F3$. This rupture extension is consistent with the coseismic slip model (Li et al., 2022; Wang et al., 2022a), the MPS results (Figure 5.6b, Section 5.3.3), the distribution of repeating aftershocks (Figure 5.7b, 5.12c), and a ~20-min delay in the occurrence of aftershocks on SE (Figure 5.12b). We attribute the post-seismically triggered aftershocks (Figure 5.12b,f) to the effect of static stress transfer and post-seismic deformations.

In summary, the occurrence of Yangbi mainshock is probably a joint result of multiple major foreshocks that combines both seismic and aseismic process (Figure 5.12e). It becomes the mainshock by chance, because its hypocenter is not the first to nucleate, or those major foreshocks would likely become its aftershock, or part of its rupture process. Such unpredictable feature fit better with the cascade model demonstrated in the Introduction Section (Helmstetter et al., 2003; Felzer et al., 2004; Ellsworth and Bulut, 2018; Yoon et al., 2019).

5.3.5.4 Comparison with Published Results

As discussed in previous subsections, we find that Yangbi sequence is basically a cascade sequence, while aseismic evidences probably exist and play an important role in the triggering process (Figure 5.12e). However, many published studies reach different conclusions. Here, we provide a brief review and comparisons on those results (Table 5.1).

Table 5.1. Comparison with published results on Yangbi foreshock mechanisms.

Interpretation	Reference	Evidence
Cascade-up and Aseismic Slip	This study	large enough ΔCFS indicate cascade triggering; pre-slip cluster, repeating foreshocks, and logarithmic expansion of aftershocks indicate aseismic slip
	Liu, M. et al., JGR 2022	large enough ΔCFS indicate cascade triggering; three repeating foreshocks imply aseismic slip
	Liu, X. et al., SRL 2022	no repeaters and a large ΔCFS favor cascade model; negative ΔCFS on the largest foreshock indicate additional mechanisms, i.e. aseismic slip
Cascade-up without Aseismic Slip	Zhu et al., EPSL 2022	large enough ΔCFS indicate cascade triggering; no repeaters, no consistent migration of seismicity
	Zhang et al., SRL 2021	no repeaters, no consistent migration direction, and no concentrated or accelerated small events
Fluid Upwelling	Lei et al., ASS 2021	the foreshock sequence shows tidal modulation: peaks of tidal strain coincide with the major events
	Sun et al., SRL 2022	high Vp/Vs body at a depth of 18-30 km below source area indicates existence of deep fluid

Similar as our conclusions, the cascade model is preferred by Zhang et al. (2021), Liu et al. (2022b), Liu et al. (2022a), and Zhu et al. (2022a). All of these studies point out that the major foreshocks occur in a random behavior, and there is no consistent migration direction. However, Zhang et al. (2021) and Zhu et al. (2022a) found no evidence supporting aseismic processes, while Liu et al. (2022b) argues that $F1$ is triggered by aseismic slip based on the fact that $f1$ & $f2$ cause a negative Coulomb stress change, and Liu et al. (2022a) detected three repeating foreshocks in the pre-$f1$ cluster. We consider all of the arguments have certain flaw: (1) we do observe some indicators for aseismic slip, e.g. the pre-slip cluster before $f1$, the repeating aftershocks, and logarithmic aftershock zone expansion (see Section 5.3.5); (2) the negative ΔCFS resulted in Liu et al. (2022b) is caused by an inaccurate event location and rupture model, which also cause an unphysical re-rupture of the $f1$ & $f2$ asperities; (3) Liu et al. (2022a) adopt a NE-trending $F1$ rupture, which leads to the majority of the $F1$ aftershocks falling into its stress shadow, and is inconsistent with our spectral ratio analysis (see Section 5.3.1).

The different opinions on the existence of aseismic process mainly come from the identification of repeating earthquakes (Liu et al., 2022a; Zhu et al., 2022a). As reviewed in Uchida (2019), the frequency band is critical in constraining the location separation, while this differs significantly in two published studies: Liu et al. (2022a) and Zhu et al. (2022a) adopted 1-7 Hz and 1-20 Hz band-pass filtering, respectively. Both studies rely solely on waveform similarity to detect repeaters, though in the validation stage they consider the rupture area and temporal behaviors as well. It is worth noting that different frequency bands lead to different CC values (Figure 5.11d-e), implying that a CC threshold of 0.95 under 1-7 Hz filtering may be a loose criteria, while under 1-20 Hz may become too strict. Thus, we explicitly constrain the location separation by measuring the differential S-P time with cross-correlation. Note that Δ(S-P) $\leq$0.01 s constrains the location separation within ~0.1 km, which is smaller than the typical rupture radius of a M_L 1 event. Further investigations on this issue may first require a combination of all existing stations, so that the uncertainty induced by fluctuating noise level can be suppressed.

Tidal modulation is proposed by Lei et al. (2021), who reaches this conclusion because the occurrence time of the major events coincide with the peak values of tidal strain. However, this inference is not rigorous, since (1) not all major events coincide with the tidal shear, normal, or Coulomb stress: the mainshock initiate at near-zero tidal normal and shear stress, and all major events initiate at times of near-zero or even negative tidal Coulomb stress; (2) the tidal effect causes too small stress change, which is 2-orders smaller than coseismic stress transfer; (3) the tidal strain and stress calculation is based on same fault geometry for all events, which is not supported by this study and other results (Lei et al., 2021; Liu et al., 2022a). Thus, the tidal triggering mechanism is not well-supported by the observations in Lei et al. (2021). Further evidence may come from the detection of seismic swarms and a long-term modulation of tidal volumetric strain on the swarms (e.g., Lei et al., 2011; Xue et al., 2018; Ross and Cochran, 2021; Wang et al., 2022b).

The tidal sensitive observation given by Lei et al. (2021) lead to another deduction that fluid plays an important role in the Yangbi sequence, which is also held by Sun et al.

(2022), who detected an area of high V_P/V_S ratio at about 18-30 km beneath the Yangbi sequence. However, both studies show no direct evidence for the existence of fluids and fluid upwelling, and the seismicity pattern in Yangbi is very different from that driven by fluid, e.g. 2009 L'Aquila sequence, where the seismicity migrates along a consistent direction and follows the fluid diffusion law (Di Luccio et al., 2010; Chiaraluce et al., 2011; Cabrera et al., 2022). It is worth further investigations on the existence and effects of fluid, e.g. extracting time-dependent V_P/V_S pattern (e.g., Di Luccio et al., 2010; Lin, 2020), long-term search for fluid-driven seismicity migration, and statistical analysis of source parameters (e.g., stress drop, Cabrera et al., 2022).

Overall, the inconsistency between different studies comes from the data and technique they adopt. Especially for the studies based on seismic data, many temporary stations are not publicly available, thus make it difficult to cross-validate the cataloging results. While some seismic dataset associated with this sequence was made openly available through peer-reviewed publications (e.g., Wang et al., 2021b; Liu et al., 2022a, and in this study), the majority of continuous seismic waveforms recorded by both temporary and permanent networks are only available to certain registered users. We believe that further efforts to make the entire dataset completely available can alleviate the uncertainty on the observations, and provide a clearer image for the Yangbi sequence.

5.3.6 Implications on Foreshock Triggering Models

As reviewed in the Introduction, cascade-up and pre-slip model are two end-member models for foreshock mechanism. However, with accumulating observational studies, the understanding becomes more complicated:

(1) The inter-event triggering in cascade model can be realized through aseismic slip as well, i.e. the afterslip of large foreshocks. For example, the 2016 M_w 7.0 Kumamoto earthquake is triggered by both the static stress change and the afterslip of M_w 6.2 foreshock (Kato et al., 2016). However, the inclusion of aseismic slip does not help predict the initiation time and size of the mainshock, which is similar as what we observed in Yangbi.

(2) Slow-slip events can be an external driven source that triggers both the foreshock and the mainshock. This kind of triggering mechanism is also widely observed, e.g. the 2011 M_w 9.0 Tohoku (Kato et al., 2012), the 2014 M_w 8.1 Iquique (Kato and Nakagawa, 2014; Ruiz et al., 2014), and the 2017 M_w 6.9 Valparaiso earthquake (Ruiz et al., 2017). Again, the aseismic slip in such mechanism does not provide predictability on the magnitude of mainshock, but the migration direction of foreshock sequence does give a clue of where the mainshock may occur. This mechanism serves as another model besides cascading and pre-slip model, and thus implies that only searching for aseismic-slip-indicators is not enough in the discrimination of foreshock triggering models.

(3) For the pre-slip nucleation phase, we still lack direct observations in the field. Near field observations with bore-hole strain meter have reported no similar nucleation signals so far (Roeloffs, 2006), even before the 2004 Parkfield earthquake (Johnston et al., 2006). Meng and Fan (2021) detect immediate foreshocks in the 2019 Ridgecrest aftershocks, but found that they follow mostly the cascade mode, with no scaling between the characteristic of their P wave and the magnitude of target event. Though Tape et al. (2018) reports possible nucleation signals in the strike-slip fault system in central Alaska, it comes in the form of very-low-frequency earthquakes, instead of significant foreshocks.

The closest case is reported by Jiang et al. (2022) in the 2011 Hawthorne seismic swarm, where a significant aseismic slip drives a seismic swarm, leading to a M4.6 mainshock. It may be interesting to perform large-scale statistics on the candidate pre-slip clusters like that preceding *f1* in our study.

(4) Multiple mechanisms can coexist in a foreshock-mainshock sequence. Based on recent laboratory observations, McLaskey (2019) proposes a rate-dependent cascade-up model that includes contributions from both cascade-up and pre-slip mechanism. Case studies have also indicated such dual-mode mechanism in foreshock sequences, e.g. the 2009 M_w 6.3 L'Aquila earthquake (Cabrera et al., 2022), the 2010 M_w 7.2 El-Mayor earthquake (Yao et al., 2020), and the 2019 M_w 7.1 Ridgecrest earthquake (Huang et al., 2020; Yue et al., 2021b).

5.4 Conclusions

In this study, we utilize seismological methods to characterize the 2021 Yangbi foreshock sequence, in order to better understand the triggering relationship between these major foreshocks and the mainshock. We find that the Yangbi sequence is associated with a rather complex fault geometry, with the mainshock and two smaller foreshocks occur on an unmapped near-vertical fault, and the largest foreshock occurs on a mapped stepover fault that dips to NE. The geometrical complexity confines the rupture extension of the mainshock and some foreshocks. Coulomb stress modeling shows that the foreshock triggering process can be explained by cascade triggering, while we also find evidence for aseismic slip that contributes to the triggering process. We conclude that the nucleation of mainshock is the result of multiple major foreshocks with both seismic and aseismic process, and that the formation of this foreshock-mainshock sequence is probably a coincidence. This detailed observation lend supports to the developed understanding on foreshock triggering mechanism: (1) the foreshock model is not limited to cascade-up & pre-slip, multiple mechanisms can operate together; and (2) aseismic slip does not always provide more predictability on the mainshock.

Chapter 6

Conclusions and Perspectives for Future Work

In this dissertation, I present two earthquake cataloging workflows: PALM and LoSAR, designed for intense seismic sequences and long-term observations, respectively. These tools offer a generalized approach to earthquake detection, making them suitable for seismic networks commonly deployed worldwide. Systematic tests demonstrate that our methods achieve higher detection completeness and accuracy compared to contemporary algorithms. Additionally, their high temporal stability and computational efficiency make them particularly helpful for studying fault zones and earthquake physics. Empowered by these technical developments, I conducted case studies on fault zones and seismic sequences, demonstrating that enhanced seismic observations can offer valuable insights into seismic hazard analysis and earthquake triggering mechanisms, as summarized in Chapter 4.6 and 5.4. In addition to further exploration of seismic catalogs for deeper insights, a clear direction for future work is to extract more information from continuous data. In this final chapter, I will outline three potential areas for future research, including (1) solve the remaining problems in earthquake detection, (2) resolve source parameters automatically to build comprehensive catalogs, and (3) detect slow earthquakes that are not routine cataloged or even reported.

6.1 Remaining Problems in Earthquake Detection

Most earthquake detection algorithms, including those presented in this dissertation, assume a relatively homogeneous 2D station distribution with an average inter-station distance of approximately 10 to 60 km and a spatial coverage within several degrees. This network configuration primarily limits the detected phases to direct P and S waves (i.e., Pg & Sg). However, when the network becomes sparse, with inter-station distances exceeding ~100 km, head waves (e.g. Pn & Sn) may be detected, complicating phase picking and association tasks. In such scenarios, accurately picking these phases is crucial for maintaining location accuracy. Similarly, in subduction zones where deep earthquakes occur, depth phases are crucial for constraining their focal depth. However, the lack of large-scale labeled datasets makes it challenging to train models capable of accurately picking these phases. Moreover, when aiming to build a global catalog with consistent detection capabilities, several questions arise: Do we need network-based phase detection algorithms? Could beamforming with small-aperture dense arrays aid in denoising? And how can we estimate location errors in regions with different station coverage?

In addition to the complexity of seismic phases, different types of seismic events, such as explosions and earthquakes, can share very similar waveform characteristics. As a result, it is common for explosion events to be falsely included in seismic catalogs, potentially biasing statistical analyses. Fortunately, many seismic networks provide manual classifications for blast events, and these anthropogenic explosions tend to cluster in time and space, enabling the automatic collection of rough training samples. Recent studies have already shown promising results in using deep learning to classify nonearthquake seismic events (e.g. Kong et al., 2022; Barama et al., 2023). However, it remains unclear how well these methods generalize across different regions and what potential challenges may arise when incorporating event classification algorithms into cataloging workflows. This event classification issue may be particularly pronounced in glacier regions, where various types of icequakes are mixed into the continuous data (Ekström and Stark, 2013; Podolskiy and Walter, 2016).

6.2 Seismic Source Parameters

In traditional catalogs, earthquake source parameters are typically limited to origin time, hypocenter location, and magnitude. However, earthquakes can also be associated with a fault plane, which can be described by a focal mechanism solution. This information is crucial for understanding regional tectonics and stress field (Hardebeck and Hauksson, 2001; Hardebeck and Michael, 2006). The HASH algorithm offers a convenient method for calculating focal mechanisms using P-wave polarity (Hardebeck and Shearer, 2002; 2003). However, accurately picking P-wave polarity can be challenging, especially due to emergent signals and stations located near the nodal plane azimuth. Researchers have attempted to train neural networks using large datasets of manually picked P-wave polarities, demonstrating improved polarity determination compared to traditional algorithms (Ross et al., 2018; Zhang et al., 2023a). However, tests show that current AI polarity pickers suffer from instability to the phase picking errors (Li et al., 2023a; Zhao et al., 2023), and a generalized pre-trained model like PhaseNet remains unavailable.

In addition to focal mechanisms, stress drop, energy radiation, and source-time functions also provide critical insights into earthquake dynamics. Studies have shown that even moderate-size earthquakes show rupture complexities that deviate from simple circular or point source models (e.g. Wu et al., 2019a; Meng and Fan, 2021). However, these source parameters are notoriously hard to constrain (Abercrombie, 2015; 2021), leaving many fundamental questions open to debate. For instance, how do stress drop and energy radiation scale with earthquake magnitude? How do small and large earthquakes differ in their rupture processes, particularly in rupture directivity and source-time functions? And how does source scaling relate to the properties of the fault zone? Thus, the technical issues have to be investigated first, including but not limited to: how to estimate the uncertainties? how do network configure affect the result? how much scatter is due to uncertainty and how much is real?

6.3 Slow Earthquakes

Beyond studying the earthquakes directly, another approach to understand them is by examining other types of seismic sources as proxies. Slow earthquakes, including tectonic tremor, low-frequency earthquakes (LFE), and very-low-frequency earthquakes (VLFE), are one such example and have been widely observed. These events represent a category of seismic signatures associated with slow fault slip, typically occur in subduction zones at frictional transition depth (~35 km) (Beroza and Ide, 2011). However, the advent of ocean-bottom seismic networks has led to the recent detections of shallow tremors and VLFEs along Nankai Trough and Japan Trench (Yamashita et al., 2015; Nishikawa et al., 2019). This prompts the question: How do these new observations reshape our understanding of earthquake mechanisms? In the full-magnitude spectrum (M_w 1-8), the distinct moment-duration scaling of fast and slow earthquakes suggests fundamental differences between them (Ide and Beroza, 2023). Yet, on the lower-magnitude end (M_w<6), this distinction becomes less pronounced (Peng and Gomberg, 2010; Takemura et al., 2022), and there are emerging evidence suggesting the opposite: Fan et al. (2022) observed a M_w 5.7 VLFE dynamically triggered in Cascadia, but with its moment-duration akin to fast earthquakes; Frank and Brodsky (2019) studied the sub-daily slow transients in Mexican subduction zone by calibrating LFE amplitudes, and obtained an earthquake-like scaling; Gomberg et al. (2016) found that both fast and slow earthquakes scaling can be interpreted by a single dislocation model. To address these complexities, a comprehensive catalog of slow earthquakes is essential.

Unfortunately, tremors are notoriously hard to detect due to their emergent seismic signals, lack of clear phase arrivals, and ambiguous start and end times. With conventional networks, tremors are typically detected using envelope cross-correlation (ECC) algorithm (Obara, 2002; Wech and Creager, 2008; Mizuno and Ide, 2019; Wech, 2021), which has been integrated into automatic systems like the Pacific Northwest Seismic Network (PNSN). ECC methods detect high-coherence signals across multiple stations via cross-correlation. However, a challenge with ECC is that it also identifies other coherent signals, such as earthquakes. To improve detection accuracy, Wech (2021) implemented spatiotemporal clustering criteria, which may introduce biases in the observed tremor distribution.

Moreover, since ECC does not provide P and S wave picks, tremor locations are poorly constrained, particularly in terms of depth. To address this issue, La Rocca et al. (2010) utilized dense array and correlation between horizontal and vertical channels to obtain S-P times; Rubin and Armbruster (2013) employed 3-station arrays, polarity analysis, and variable time windows to constrain the location; Li and Ghosh (2017) performed beamforming with multiple small-aperture dense arrays. These efforts have significantly improved tremor location accuracy, shedding light on tremor migration patterns. However, these algorithms may lack generalizability due to specific array configuration requirements.

Overall, compared to earthquake cataloging, the detection and location of slow earthquakes are less advanced, with many challenges yet to be addressed. My experience in solving earthquake detection problems has underscored the importance of aligning technical development with the scientific objectives. In particular, identifying appropriate evaluation metrics is just as crucial as developing innovative algorithms. Lastly, contrary to the tendency in academia to constantly pursue new methods, it is important not to overlook traditional algorithms. Some of these approaches may be highly effective but have failed due to poor implementation or overlooked criteria. Such oversights are common in geoscience, a relatively young field, where in many subdomains, only a few researchers have explored certain ideas.

References

Abercrombie, R. E. (2015). Investigating uncertainties in empirical Green's function analysis of earthquake source parameters, *Journal of Geophysical Research: Solid Earth*, *120*(6), 4263-4277, doi:https://doi.org/10.1002/2015JB011984.

Abercrombie, R. E. (2021). Resolution and uncertainties in estimates of earthquake stress drop and energy release, *Philosophical Transactions of the Royal Society A: Mathematical, Physical and Engineering Sciences*, *379*(2196), 20200131, doi:doi:10.1098/rsta.2020.0131.

Ader, T., et al. (2012). Convergence rate across the Nepal Himalaya and interseismic coupling on the Main Himalayan Thrust: Implications for seismic hazard, *Journal of Geophysical Research: Solid Earth*, *117*(B4), doi:10.1029/2011jb009071.

Ake, J., K. Mahrer, D. O'Connell, and L. Block (2005). Deep-Injection and Closely Monitored Induced Seismicity at Paradox Valley, Colorado, *Bulletin of the Seismological Society of America*, *95*(2), 664-683, doi:10.1785/0120040072.

Aki, K. (1965). Maximum likelihood estimate of b in the formula log N= a-bM and its confidence limits, *Bull. Earthq. Res. Inst., Tokyo Univ.*, *43*, 237-239.

Aktug, B., H. Ozener, A. Dogru, A. Sabuncu, B. Turgut, K. Halicioglu, O. Yilmaz, and E. Havazli (2016). Slip rates and seismic potential on the East Anatolian Fault System using an improved GPS velocity field, *Journal of Geodynamics*, *94-95*, 1-12, doi:https://doi.org/10.1016/j.jog.2016.01.001.

Allen, R. V. (1978). Automatic earthquake recognition and timing from single traces, *Bulletin of the Seismological Society of America*, *68*(5), 1521-1532.

Alwahedi, M. A., and J. C. Hawthorne (2019). Intermediate-Magnitude Postseismic Slip Follows Intermediate-Magnitude (M 4 to 5) Earthquakes in California, *Geophysical Research Letters*, *46*(7), 3676-3687, doi:https://doi.org/10.1029/2018GL081001.

Amorèse, D., J.-R. Grasso, and P. A. Rydelek (2010). On varying b-values with depth: results from computer-intensive tests for Southern California, *Geophysical Journal International*, *180*(1), 347-360, doi:10.1111/j.1365-246X.2009.04414.x.

Ampuero, J.-P., and A. M. Rubin (2008). Earthquake nucleation on rate and state faults – Aging and slip laws, *Journal of Geophysical Research: Solid Earth*, *113*(B1), doi:https://doi.org/10.1029/2007JB005082.

Bachmann, C. E., S. Wiemer, B. P. Goertz-Allmann, and J. Woessner (2012). Influence of pore-pressure on the event-size distribution of induced earthquakes, *Geophysical Research Letters*, *39*(9), doi:10.1029/2012gl051480.

Bahdanau, D., K. Cho, and Y. Bengio (2014). Neural machine translation by jointly learning to align and translate, *arXiv preprint arXiv:1409.0473*.

Bai, D., et al. (2010). Crustal deformation of the eastern Tibetan plateau revealed by magnetotelluric imaging, *Nature Geoscience*, *3*(5), 358-362, doi:10.1038/ngeo830.

Baillard, C., W. C. Crawford, V. Ballu, C. Hibert, and A. Mangeney (2013). An Automatic Kurtosis-Based P- and S-Phase Picker Designed for Local Seismic Networks, *Bulletin of the Seismological Society of America*, *104*(1), 394-409, doi:10.1785/0120120347.

Bao, X., et al. (2015). Two crustal low-velocity channels beneath SE Tibet revealed by joint inversion of Rayleigh wave dispersion and receiver functions, *Earth and Planetary Science Letters*, *415*, 16-24, doi:https://doi.org/10.1016/j.epsl.2015.01.020.

Barama, L., J. Williams, A. V. Newman, and Z. Peng (2023). Global Nuclear Explosion Discrimination Using a Convolutional Neural Network, *Geophysical Research Letters*, *50*(17), e2022GL101528, doi:https://doi.org/10.1029/2022GL101528.

Barbot, S., and J. R. Weiss (2021). Connecting subduction, extension and shear localization across the Aegean Sea and Anatolia, *Geophysical Journal International*, *226*(1), 422-445, doi:10.1093/gji/ggab078.

Barbot, S., H. Luo, T. Wang, Y. Hamiel, O. Piatibratova, M. T. Javed, C. Braitenberg, and G. Gurbuz (2023). Slip distribution of the February 6, 2023 Mw 7.8 and Mw 7.6, Kahramanmaraş, Turkey earthquake sequence in the East Anatolian Fault Zone, *Seismica*, *2*(3), doi:10.26443/seismica.v2i3.502.

Ben-Zion, Y., and C. G. Sammis (2003). Characterization of Fault Zones, *pure and applied geophysics*, *160*(3), 677-715, doi:10.1007/PL00012554.

Beroza, C. G. C., and S. Ide (2011). Slow Earthquakes and Nonvolcanic Tremor, *Annual Review of Earth and Planetary Sciences*, *39*(1), 271-296, doi:10.1146/annurev-earth-040809-152531.

Bletery, Q., O. Cavalié, J.-M. Nocquet, and T. Ragon (2020). Distribution of Interseismic Coupling Along the North and East Anatolian Faults Inferred From InSAR and GPS Data, *Geophysical Research Letters*, *47*(16), e2020GL087775, doi:https://doi.org/10.1029/2020GL087775.

Bletery, Q., and J.-M. Nocquet (2023). The precursory phase of large earthquakes, *Science*, *381*(6655), 297-301, doi:doi:10.1126/science.adg2565.

Boatwright, J. (1980). A spectral theory for circular seismic sources; simple estimates of source dimension, dynamic stress drop, and radiated seismic energy, *Bulletin of the Seismological Society of America*, *70*(1), 1-27, doi:10.1785/bssa0700010001.

Boore, D. M. (1989). The Richter scale: its development and use for determining earthquake source parameters, *Tectonophysics*, *166*(1), 1-14, doi:https://doi.org/10.1016/0040-1951(89)90200-X.

Bornstein, T., D. Lange, J. Münchmeyer, J. Woollam, A. Rietbrock, G. Barcheck, I. Grevemeyer, and F. Tilmann (2024). PickBlue: Seismic Phase Picking for Ocean Bottom Seismometers With Deep Learning, *Earth and Space Science*, *11*(1), e2023EA003332, doi:https://doi.org/10.1029/2023EA003332.

Bouchon, M., H. Karabulut, M. Aktar, S. Özalaybey, J. Schmittbuhl, and M.-P. Bouin (2011). Extended Nucleation of the 1999 Mw7.6 Izmit Earthquake, *Science*, *331*(6019), 877-880, doi:10.1126/science.1197341.

Bouchon, M., V. Durand, D. Marsan, H. Karabulut, and J. Schmittbuhl (2013). The long precursory phase of most large interplate earthquakes, *Nature Geoscience*, *6*(4), 299-302, doi:10.1038/ngeo1770.

Bulut, F., M. Bohnhoff, T. Eken, C. Janssen, T. Kılıç, and G. Dresen (2012). The East Anatolian Fault Zone: Seismotectonic setting and spatiotemporal characteristics of seismicity based on precise earthquake locations, *Journal of Geophysical Research: Solid Earth*, *117*(B7), doi:https://doi.org/10.1029/2011JB008966.

Bürgmann, R. (2018). The geophysics, geology and mechanics of slow fault slip, *Earth and Planetary Science Letters*, *495*, 112-134, doi:https://doi.org/10.1016/j.epsl.2018.04.062.

Cabrera, L., P. Poli, and W. B. Frank (2022). Tracking the Spatio-Temporal Evolution of Foreshocks Preceding the Mw 6.1 2009 L'Aquila Earthquake, *Journal of Geophysical Research: Solid Earth*, *127*(3), e2021JB023888, doi:https://doi.org/10.1029/2021JB023888.

Cakir, Z., et al. (2023). Arrest of the Mw 6.8 January 24, 2020 Elaziğ (Turkey) earthquake by shallow fault creep, *Earth and Planetary Science Letters*, *608*, 118085, doi:https://doi.org/10.1016/j.epsl.2023.118085.

Calderoni, G., A. Rovelli, Y. Ben-Zion, and R. Di Giovambattista (2015). Along-strike rupture directivity of earthquakes of the 2009 L'Aquila, central Italy, seismic sequence, *Geophysical Journal International*, *203*(1), 399-415, doi:10.1093/gji/ggv275.

Calderoni, G., A. Rovelli, and R. Di Giovambattista (2017). Rupture Directivity of the Strongest 2016–2017 Central Italy Earthquakes, *Journal of Geophysical Research: Solid Earth*, *122*(11), 9118-9131, doi:https://doi.org/10.1002/2017JB014118.

Cao, A., and S. S. Gao (2002). Temporal variation of seismic b-values beneath northeastern Japan island arc, *Geophysical Research Letters*, *29*(9), 48-41-48-43, doi:10.1029/2001gl013775.

Cavalié, O., and S. Jónsson (2014). Block-like plate movements in eastern Anatolia observed by InSAR, *Geophysical Research Letters*, *41*(1), 26-31, doi:https://doi.org/10.1002/2013GL058170.

Chai, C., M. Maceira, H. J. Santos-Villalobos, S. V. Venkatakrishnan, M. Schoenball, W. Zhu, G. C. Beroza, C. Thurber, and E. C. Team (2020). Using a Deep Neural Network and Transfer Learning to Bridge Scales for Seismic Phase Picking, *Geophysical Research Letters*, *47*(16), e2020GL088651, doi:https://doi.org/10.1029/2020GL088651.

Chamberlain, C. J., C. M. Boese, and J. Townend (2017). Cross-correlation-based detection and characterisation of microseismicity adjacent to the locked, late-interseismic Alpine Fault, South Westland, New Zealand, *Earth and Planetary Science Letters*, *457*, 63-72, doi:https://doi.org/10.1016/j.epsl.2016.09.061.

Chamberlain, C. J., W. B. Frank, F. Lanza, J. Townend, and E. Warren-Smith (2021). Illuminating the Pre-, Co-, and Post-Seismic Phases of the 2016 M7.8 Kaikōura Earthquake With 10 Years of Seismicity, *Journal of Geophysical Research: Solid Earth*, *126*(8), e2021JB022304, doi:https://doi.org/10.1029/2021JB022304.

Chen, C., and A. A. Holland (2016). PhasePApy: A Robust Pure Python Package for Automatic Identification of Seismic Phases, *Seismological Research Letters*, *87*(6), 1384-1396, doi:10.1785/0220160019.

Chen, K., J.-P. Avouac, S. Aati, C. Milliner, F. Zheng, and C. Shi (2020). Cascading and pulse-like ruptures during the 2019 Ridgecrest earthquakes in the Eastern California Shear Zone, *Nature Communications*, *11*(1), 22, doi:10.1038/s41467-019-13750-w.

Chen, X., P. M. Shearer, and R. E. Abercrombie (2012). Spatial migration of earthquakes within seismic clusters in Southern California: Evidence for fluid diffusion, *Journal of Geophysical Research: Solid Earth*, *117*(B4), doi:https://doi.org/10.1029/2011JB008973.

Chen, X., and P. M. Shearer (2013). California foreshock sequences suggest aseismic triggering process, *Geophysical Research Letters*, *40*(11), 2602-2607, doi:https://doi.org/10.1002/grl.50444.

Cheng, J., Y. Wen, J. Liu, and L. Zhou (2014). Earthquake sequence of the Yutian <i>M</i>_S7.3 earthquake on February 12, 2014 and its tectonic background, *Acta Seismologica Sinica*, *36*(3), 350, doi:10.3969/j.issn.0253-3782.2014.03.002.

Cheng, Y., E. Hauksson, and Y. Ben-Zion (2023). Refined Earthquake Focal Mechanism Catalog for Southern California Derived With Deep Learning Algorithms, *Journal of Geophysical Research: Solid Earth*, *128*(2), e2022JB025975, doi:https://doi.org/10.1029/2022JB025975.

Chiaraluce, L., L. Valoroso, D. Piccinini, R. Di Stefano, and P. De Gori (2011). The anatomy of the 2009 L'Aquila normal fault system (central Italy) imaged by high resolution foreshock and aftershock locations, *Journal of Geophysical Research: Solid Earth*, *116*(B12), doi:https://doi.org/10.1029/2011JB008352.

Cho, K., B. van Merrienboer, C. Gulcehre, D. Bahdanau, F. Bougares, H. Schwenk, and Y. Bengio (2014). Learning Phrase Representations using RNN Encoder-Decoder for Statistical Machine Translation, *arXiv e-prints*, arXiv:1406.1078.

Cochran, E. S., E. Wolin, D. E. McNamara, A. Yong, D. Wilson, M. Alvarez, N. van der Elst, A. McClain, and J. Steidl (2020). The U.S. Geological Survey's Rapid Seismic Array Deployment for the 2019 Ridgecrest Earthquake Sequence, *Seismological Research Letters*, doi:10.1785/0220190296.

Dal Zilio, L., and J.-P. Ampuero (2023). Earthquake doublet in Turkey and Syria, *Communications Earth & Environment*, *4*(1), 71, doi:10.1038/s43247-023-00747-z.

Davis, G. H., A. P. Bump, P. E. García, and S. G. Ahlgren (2000). Conjugate Riedel deformation band shear zones, *Journal of Structural Geology*, *22*(2), 169-190, doi:https://doi.org/10.1016/S0191-8141(99)00140-6.

Day, S. M. (1982). Three-dimensional simulation of spontaneous rupture: The effect of nonuniform prestress, *Bulletin of the Seismological Society of America*, *72*(6A), 1881-1902, doi:10.1785/bssa07206a1881.

Day, S. M., G. Yu, and D. J. Wald (1998). Dynamic stress changes during earthquake rupture, *Bulletin of the Seismological Society of America*, *88*(2), 512-522, doi:10.1785/bssa0880020512.

DeLong, S. B., G. E. Hilley, M. J. Rymer, and C. Prentice (2010). Fault zone structure from topography: Signatures of en echelon fault slip at Mustang Ridge on the San Andreas Fault, Monterey County, California, *Tectonics*, *29*(5), doi:https://doi.org/10.1029/2010TC002673.

Deng, Q., P. Zhang, Y. Ran, X. Yang, W. Min, and Q. Chu (2003). Basic characteristics of active tectonics of China, *Science in China Series D-Earth Sciences*, *46*(1006-9313), 356, doi:https://doi.org/10.1360/03yd9032.

Di Luccio, F., G. Ventura, R. Di Giovambattista, A. Piscini, and F. R. Cinti (2010). Normal faults and thrusts reactivated by deep fluids: The 6 April 2009 Mw 6.3 L'Aquila earthquake, central Italy, *Journal of Geophysical Research: Solid Earth*, *115*(B6), doi:https://doi.org/10.1029/2009JB007190.

Dieterich, J. H. (1978). Preseismic fault slip and earthquake prediction, *Journal of Geophysical Research: Solid Earth*, *83*(B8), 3940-3948, doi:https://doi.org/10.1029/JB083iB08p03940.

Dieterich, J. H. (1992). Earthquake nucleation on faults with rate-and state-dependent strength, *Tectonophysics*, *211*(1), 115-134, doi:https://doi.org/10.1016/0040-1951(92)90055-B.

Ding, H., Y. Zhou, Z. Ge, T. Taymaz, A. Ghosh, H. Xu, T. S. Irmak, and X. Song (2023). High-resolution seismicity imaging and early aftershock migration of the 2023 Kahramanmaraş (SE Türkiye) <i>M</i>_W7.9 & 7.8 earthquake doublet, *Earthquake Science*, *36*, 1-16, doi:10.1016/j.eqs.2023.06.002.

Dodge, D. A., G. C. Beroza, and W. L. Ellsworth (1996). Detailed observations of California foreshock sequences: Implications for the earthquake initiation process, *Journal of Geophysical Research: Solid Earth*, *101*(B10), 22371-22392, doi:https://doi.org/10.1029/96JB02269.

Ekström, G., and C. P. Stark (2013). Simple Scaling of Catastrophic Landslide Dynamics, *Science*, *339*(6126), 1416-1419, doi:doi:10.1126/science.1232887.

El-Isa, Z. H., and D. W. Eaton (2014). Spatiotemporal variations in the b-value of earthquake magnitude–frequency distributions: Classification and causes, *Tectonophysics*, *615-616*, 1-11, doi:https://doi.org/10.1016/j.tecto.2013.12.001.

Ellsworth, W. L., and F. Bulut (2018). Nucleation of the 1999 Izmit earthquake by a triggered cascade of foreshocks, *Nature Geoscience*, *11*(7), 531-535, doi:10.1038/s41561-018-0145-1.

Erdik, M., M. B. D. Tümsa, A. Pınar, E. Altunel, and A. C. Zülfikar (2023). A preliminary report on the February 6, 2023 earthquakes in Türkiye, *Temblor*, doi:http://doi.org/10.32858/temblor.297.

Eshelby, J. D. (1957). The determination of the elastic field of an ellipsoidal inclusion, and related problems, *Proceedings of the Royal Society of London. Series A. Mathematical and Physical Sciences*, *241*(1226), 376-396, doi:doi:10.1098/rspa.1957.0133.

Ezen-Can, A. (2020). A Comparison of LSTM and BERT for Small Corpus, *arXiv preprint arXiv:2009.05451*.

Fan, W., A. J. Barbour, J. J. McGuire, Y. Huang, G. Lin, E. S. Cochran, and R. Okuwaki (2022). Very Low Frequency Earthquakes in Between the Seismogenic and Tremor Zones in Cascadia?, *AGU Advances*, *3*(2), e2021AV000607, doi:https://doi.org/10.1029/2021AV000607.

Fang, L., J. Wu, W. Wang, Z. Lü, C. Wang, T. Yang, and Y. Cai (2013). Relocation of the mainshock and aftershock sequences of MS7.0 Sichuan Lushan earthquake, *Chinese Science Bulletin*, *58*(28), 3451-3459, doi:10.1007/s11434-013-6000-2.

Fang, Y., Z. Jiang, and A. Niu (2005). Analysis of Crustal Deformation in East Boundary of Sichuan-Yunnan Block, *Journal of Geodesy and Geodynamics*(03), 81-85.

Felzer, K. R., R. E. Abercrombie, and G. r. Ekström (2004). A Common Origin for Aftershocks, Foreshocks, and Multiplets, *Bulletin of the Seismological Society of America*, *94*(1), 88-98, doi:10.1785/0120030069.

Feng, T., S. Mohanna, and L. Meng (2022). EdgePhase: A Deep Learning Model for Multi-Station Seismic Phase Picking, *Geochemistry, Geophysics, Geosystems*, *23*(11), e2022GC010453, doi:https://doi.org/10.1029/2022GC010453.

Frank, W. B., and E. E. Brodsky (2019). Daily measurement of slow slip from low-frequency earthquakes is consistent with ordinary earthquake scaling, *Science Advances*, *5*(10), eaaw9386, doi:doi:10.1126/sciadv.aaw9386.

Freed, A. M. (2005). Earthquake Triggering by Static, Dynamic, and Postseismic Stress Transfer, *Annual Review of Earth and Planetary Sciences*, *33*(1), 335-367, doi:10.1146/annurev.earth.33.092203.122505.

Frémont, M.-J., and S. D. Malone (1987). High precision relative locations of earthquakes at Mount St. Helens, Washington, *Journal of Geophysical Research: Solid Earth*, *92*(B10), 10223-10236, doi:https://doi.org/10.1029/JB092iB10p10223.

Fu, Z., L. Xu, and Y. Wang (2020). Seismic Risk on the Northern Xiaojiang Fault Implied by the Latest and Nearest GPS Observations, *Pure and Applied Geophysics*, *177*(2), 661-679, doi:10.1007/s00024-019-02347-5.

Gallovič, F., J. Zahradník, V. Plicka, E. Sokos, C. Evangelidis, I. Fountoulakis, and F. Turhan (2020). Complex rupture dynamics on an immature fault during the 2020 Mw 6.8 Elazığ earthquake, Turkey, *Communications Earth & Environment*, *1*(1), 40, doi:10.1038/s43247-020-00038-x.

Ganev, P. N., J. F. Dolan, S. F. McGill, and K. L. Frankel (2012). Constancy of geologic slip rate along the central Garlock fault: implications for strain accumulation and release in southern California, *Geophysical Journal International*, *190*(2), 745-760, doi:10.1111/j.1365-246X.2012.05494.x.

Gao, D., H. Kao, and B. Wang (2021). Misconception of Waveform Similarity in the Identification of Repeating Earthquakes, *Geophysical Research Letters*, *48*(13), e2021GL092815, doi:https://doi.org/10.1029/2021GL092815.

Geiger, L. (1912). Probability method for the determination of earthquake epicenters from the arrival time only, *Bull. St. Louis Univ*, *8*(1), 56-71.

Geller, R. J., D. D. Jackson, Y. Y. Kagan, and F. Mulargia (1997). Earthquakes Cannot Be Predicted, *Science*, *275*(5306), 1616-1616, doi:doi:10.1126/science.275.5306.1616.

Gibbons, S. J., and F. Ringdal (2006). The detection of low magnitude seismic events using array-based waveform correlation, *Geophysical Journal International*, *165*(1), 149-166, doi:10.1111/j.1365-246X.2006.02865.x.

Goldberg, D. E., D. Melgar, V. J. Sahakian, A. M. Thomas, X. Xu, B. W. Crowell, and J. Geng (2020). Complex Rupture of an Immature Fault Zone: A Simultaneous Kinematic Model of the 2019 Ridgecrest, CA Earthquakes, *Geophysical Research Letters*, *47*(3), e2019GL086382, doi:https://doi.org/10.1029/2019GL086382.

Goldberg, D. E., et al. (2023). Rapid Characterization of the February 2023 Kahramanmaraş, Türkiye, Earthquake Sequence, *The Seismic Record*, *3*(2), 156-167, doi:10.1785/0320230009.

Gomberg, J., A. Wech, K. Creager, K. Obara, and D. Agnew (2016). Reconsidering earthquake scaling, *Geophysical Research Letters*, *43*(12), 6243-6251, doi:https://doi.org/10.1002/2016GL069967.

Gong, J., and W. Fan (2022). Seismicity, Fault Architecture, and Slip Mode of the Westernmost Gofar Transform Fault, *Journal of Geophysical Research: Solid Earth*, *127*(11), e2022JB024918, doi:https://doi.org/10.1029/2022JB024918.

Graves, A., and N. Jaitly (2014). Towards End-To-End Speech Recognition with Recurrent Neural Networks, in *Proceedings of the 31st International Conference on Machine Learning*, edited by P. X. Eric and J. Tony, pp. 1764--1772, PMLR, Proceedings of Machine Learning Research.

Gutenberg, B., and C. F. Richter (1944). Frequency of earthquakes in California, *Bulletin of the Seismological Society of America*, *34*(4), 185-188.

Güvercin, S. E., H. Karabulut, A. Ö. Konca, U. Doğan, and S. Ergintav (2022). Active seismotectonics of the East Anatolian Fault, *Geophysical Journal International*, *230*(1), 50-69, doi:10.1093/gji/ggac045.

Güvercin, S. E. (2024). 2023 Earthquake Doublet in Türkiye Reveals the Complexities of the East Anatolian Fault Zone: Insights from Aftershock Patterns and Moment Tensor Solutions, *Seismological Research Letters*, doi:10.1785/0220230317.

Han, Z.-j., S.-m. Guo, H.-f. Xiang, J.-s. Zhang, and Y.-k. Ran (2004). Seismotectonic environment of occurring the February 3, 1996 Lijiang M=7.0 earthquake, Yunnan province, *Acta Seismologica Sinica*, *17*(4), 453-463, doi:10.1007/s11589-004-0025-1.

Hanks, T. C., and H. Kanamori (1979). A moment magnitude scale, *Journal of Geophysical Research: Solid Earth*, *84*(B5), 2348-2350, doi:https://doi.org/10.1029/JB084iB05p02348.

Hannun, A., C. Case, J. Casper, B. Catanzaro, G. Diamos, E. Elsen, R. Prenger, S. Satheesh, S. Sengupta, and A. Coates (2014). Deep speech: Scaling up end-to-end speech recognition, *arXiv preprint arXiv:1412.5567*.

Hardebeck, J. L., J. J. Nazareth, and E. Hauksson (1998). The static stress change triggering model: Constraints from two southern California aftershock sequences, *Journal of*

Geophysical Research: Solid Earth, *103*(B10), 24427-24437, doi:https://doi.org/10.1029/98JB00573.

Hardebeck, J. L., and E. Hauksson (2001). Crustal stress field in southern California and its implications for fault mechanics, *Journal of Geophysical Research: Solid Earth*, *106*(B10), 21859-21882, doi:https://doi.org/10.1029/2001JB000292.

Hardebeck, J. L., and P. M. Shearer (2002). A New Method for Determining First-Motion Focal Mechanisms, *Bulletin of the Seismological Society of America*, *92*(6), 2264-2276, doi:10.1785/0120010200.

Hardebeck, J. L., and P. M. Shearer (2003). Using S/P Amplitude Ratios to Constrain the Focal Mechanisms of Small Earthquakes, *Bulletin of the Seismological Society of America*, *93*(6), 2434-2444, doi:10.1785/0120020236.

Hardebeck, J. L., and A. J. Michael (2006). Damped regional-scale stress inversions: Methodology and examples for southern California and the Coalinga aftershock sequence, *Journal of Geophysical Research: Solid Earth*, *111*(B11), doi:https://doi.org/10.1029/2005JB004144.

Haskell, N. A. (1964). Total energy and energy spectral density of elastic wave radiation from propagating faults, *Bulletin of the Seismological Society of America*, *54*(6A), 1811-1841, doi:10.1785/bssa05406a1811.

Hatem, A. E., and J. F. Dolan (2018). A Model for the Initiation, Evolution, and Controls on Seismic Behavior of the Garlock Fault, California, *Geochemistry, Geophysics, Geosystems*, *19*(7), 2166-2178, doi:https://doi.org/10.1029/2017GC007349.

Hauksson, E., W. Yang, and P. M. Shearer (2012). Waveform Relocated Earthquake Catalog for Southern California (1981 to June 2011), *Bulletin of the Seismological Society of America*, *102*(5), 2239-2244, doi:10.1785/0120120010.

Hauksson, E., and L. M. Jones (2020). Seismicity, Stress State, and Style of Faulting of the Ridgecrest-Coso Region from the 1930s to 2019: Seismotectonics of an Evolving Plate Boundary Segment, *Bulletin of the Seismological Society of America*, *110*(4), 1457-1473, doi:10.1785/0120200051.

Hauksson, E., C. Yoon, E. Yu, J. R. Andrews, M. Alvarez, R. Bhadha, and V. Thomas (2020). Caltech/USGS Southern California Seismic Network (SCSN) and Southern California Earthquake Data Center (SCEDC): Data Availability for the 2019 Ridgecrest Sequence, *Seismological Research Letters*, *91*(4), 1961-1970, doi:10.1785/0220190290.

Hawthorne, J. C., M. Simons, and J.-P. Ampuero (2016). Estimates of aseismic slip associated with small earthquakes near San Juan Bautista, CA, *Journal of Geophysical Research: Solid Earth*, *121*(11), 8254-8275, doi:https://doi.org/10.1002/2016JB013120.

Hayes, G. P., D. J. Wald, and R. L. Johnson (2012). Slab1.0: A three-dimensional model of global subduction zone geometries, *Journal of Geophysical Research: Solid Earth*, *117*(B1), doi:10.1029/2011jb008524.

Heaton, T. H. (1990). Evidence for and implications of self-healing pulses of slip in earthquake rupture, *Physics of the Earth and Planetary Interiors*, *64*(1), 1-20, doi:https://doi.org/10.1016/0031-9201(90)90002-F.

Helmstetter, A., D. Sornette, and J.-R. Grasso (2003). Mainshocks are aftershocks of conditional foreshocks: How do foreshock statistical properties emerge from aftershock laws, *Journal of Geophysical Research: Solid Earth*, *108*(B1), doi:https://doi.org/10.1029/2002JB001991.

Herrmann, M., and W. Marzocchi (2020). Inconsistencies and Lurking Pitfalls in the Magnitude–Frequency Distribution of High-Resolution Earthquake Catalogs, *Seismological Research Letters*, *92*(2A), 909-922, doi:10.1785/0220200337.

Hsu, Y.-F., I. Zaliapin, and Y. Ben-Zion (2024). Informative Modes of Seismicity in Nearest-Neighbor Earthquake Proximities, *Journal of Geophysical Research: Solid Earth*, *129*(3), e2023JB027826, doi:https://doi.org/10.1029/2023JB027826.

Huang, H., L. Meng, R. Bürgmann, W. Wang, and K. Wang (2020). Spatio-temporal foreshock evolution of the 2019 M 6.4 and M 7.1 Ridgecrest, California earthquakes, *Earth and Planetary Science Letters*, *551*, 116582, doi:https://doi.org/10.1016/j.epsl.2020.116582.

Hubert-Ferrari, A., L. Lamair, S. Hage, S. Schmidt, M. N. Çağatay, and U. Avşar (2020). A 3800 yr paleoseismic record (Lake Hazar sediments, eastern Turkey): Implications for the East Anatolian Fault seismic cycle, *Earth and Planetary Science Letters*, *538*, 116152, doi:https://doi.org/10.1016/j.epsl.2020.116152.

Husen, S., and J. Hardebeck (2010). Earthquake location accuracy, *Community Online Resource for Statistical Seismicity Analysis*, doi:10.5078/corssa-55815573.

Hussain, E., S. Kalaycıoğlu, C. W. D. Milliner, and Z. Çakir (2023). Preconditioning the 2023 Kahramanmaraş (Türkiye) earthquake disaster, *Nature Reviews Earth & Environment*, doi:10.1038/s43017-023-00411-2.

Hutton, K., J. Woessner, and E. Hauksson (2010). Earthquake Monitoring in Southern California for Seventy-Seven Years (1932–2008), *Bulletin of the Seismological Society of America*, *100*(2), 423-446, doi:10.1785/0120090130.

Hutton, L. K., and D. M. Boore (1987). The ML scale in Southern California, *Bulletin of the Seismological Society of America*, *77*(6), 2074-2094.

Ide, S., and G. C. Beroza (2023). Slow earthquake scaling reconsidered as a boundary between distinct modes of rupture propagation, *Proceedings of the National Academy of Sciences*, *120*(32), e2222102120, doi:doi:10.1073/pnas.2222102120.

Im, K., J.-P. Avouac, E. R. Heimisson, and D. Elsworth (2021). Ridgecrest aftershocks at Coso suppressed by thermal destressing, *Nature*, *595*(7865), 70-74, doi:10.1038/s41586-021-03601-4.

Imanishi, K., and W. L. Ellsworth (2006). Source Scaling Relationships of Microearthquakes at Parkfield, CA, Determined Using the SAFOD Pilot Hole Seismic Array, in *Earthquakes: Radiated Energy and the Physics of Faulting*, edited, pp. 81-90, doi:https://doi.org/10.1029/170GM10.

Ji, L., Q. Wang, J. Xu, and J. Feng (2017). The 1996 Mw 6.6 Lijiang earthquake: Application of JERS-1 SAR interferometry on a typical normal-faulting event in the northwestern Yunnan rift zone, SW China, *Journal of Asian Earth Sciences*, *146*, 221-232, doi:https://doi.org/10.1016/j.jseaes.2017.05.029.

Jia, Z., et al. (2023). The complex dynamics of the 2023 Kahramanmaraş, Turkey, <i>M</i>_w 7.8-7.7 earthquake doublet, *Science*, *381*(6661), 985-990, doi:doi:10.1126/science.adi0685.

Jiang, C., L. Fang, L. Fan, and B. Li (2021a). Comparison of the earthquake detection abilities of PhaseNet and EQTransformer with the Yangbi and Maduo earthquakes, *Earthquake Science*, *34*(5), 425-435, doi:10.29382/eqs-2021-0038.

Jiang, J., and N. Lapusta (2016). Deeper penetration of large earthquakes on seismically quiescent faults, *Science*, *352*(6291), 1293-1297, doi:doi:10.1126/science.aaf1496.

Jiang, J., and N. Lapusta (2017). Connecting depth limits of interseismic locking, microseismicity, and large earthquakes in models of long-term fault slip, *Journal of Geophysical Research: Solid Earth*, *122*(8), 6491-6523, doi:https://doi.org/10.1002/2017JB014030.

Jiang, J., Y. Bock, and E. Klein (2021b). Coevolving early afterslip and aftershock signatures of a San Andreas fault rupture, *Science Advances*, *7*(15), eabc1606, doi:doi:10.1126/sciadv.abc1606.

Jiang, X., X. Song, T. Li, and K. Wu (2023). Moment magnitudes of two large Turkish earthquakes on February 6, 2023 from long-period coda, *Earthquake Science*, *36*(2), 169-174, doi:https://doi.org/10.1016/j.eqs.2023.02.008.

Jiang, Y., S. V. Samsonov, and P. J. González (2022). Aseismic Fault Slip During a Shallow Normal-Faulting Seismic Swarm Constrained Using a Physically Informed Geodetic Inversion Method, *Journal of Geophysical Research: Solid Earth*, *127*(7), e2021JB022621, doi:https://doi.org/10.1029/2021JB022621.

Jin, Z., and Y. Fialko (2020). Finite Slip Models of the 2019 Ridgecrest Earthquake Sequence Constrained by Space Geodetic Data and Aftershock Locations, *Bulletin of the Seismological Society of America*, *110*(4), 1660-1679, doi:10.1785/0120200060.

Johnson, C. E., A. G. Lindh, and B. F. Hirshorn (1997). Robust regional phase association, *Report Rep. 94-621*.

Johnson, P. A., B. Ferdowsi, B. M. Kaproth, M. Scuderi, M. Griffa, J. Carmeliet, R. A. Guyer, P.-Y. Le Bas, D. T. Trugman, and C. Marone (2013). Acoustic emission and microslip precursors to stick-slip failure in sheared granular material, *Geophysical Research Letters*, *40*(21), 5627-5631, doi:https://doi.org/10.1002/2013GL057848.

Johnston, M. J. S., R. D. Borcherdt, A. T. Linde, and M. T. Gladwin (2006). Continuous Borehole Strain and Pore Pressure in the Near Field of the 28 September 2004 M 6.0 Parkfield, California, Earthquake: Implications for Nucleation, Fault Response, Earthquake Prediction, and Tremor, *Bulletin of the Seismological Society of America*, *96*(4B), S56-S72, doi:10.1785/0120050822.

Jones, L. M., and P. Molnar (1979). Some characteristics of foreshocks and their possible relationship to earthquake prediction and premonitory slip on faults, *Journal of Geophysical Research: Solid Earth*, *84*(B7), 3596-3608, doi:https://doi.org/10.1029/JB084iB07p03596.

Julian, B. R., A. D. Miller, and G. R. Foulger (1998). Non-double-couple earthquakes 1. Theory, *Reviews of Geophysics*, *36*(4), 525-549, doi:https://doi.org/10.1029/98RG00716.

Kaneko, Y., J.-P. Avouac, and N. Lapusta (2010). Towards inferring earthquake patterns from geodetic observations of interseismic coupling, *Nature Geoscience*, *3*(5), 363-369, doi:10.1038/ngeo843.

Karabacak, V., et al. (2023). The 2023 Pazarcık (Kahramanmaraş, Türkiye) earthquake (Mw 7.7): implications for surface rupture dynamics along the East Anatolian Fault Zone, *Journal of the Geological Society*, *180*(3), doi:10.1144/jgs2023-020.

Karabulut, H., S. E. Güvercin, J. Hollingsworth, and A. Ö. Konca (2023). Long silence on the East Anatolian Fault Zone (Southern Turkey) ends with devastating double earthquakes (6 February 2023) over a seismic gap: Implications for the seismic potential in the Eastern Mediterranean region, *Journal of the Geological Society*, *0*(ja), jgs2023-2021, doi:doi:10.1144/jgs2023-021.

Kato, A., K. Obara, T. Igarashi, H. Tsuruoka, S. Nakagawa, and N. Hirata (2012). Propagation of Slow Slip Leading Up to the 2011 Mw9.0 Tohoku-Oki Earthquake, *Science*, *335*(6069), 705-708, doi:10.1126/science.1215141.

Kato, A., and S. Nakagawa (2014). Multiple slow-slip events during a foreshock sequence of the 2014 Iquique, Chile Mw 8.1 earthquake, *Geophysical Research Letters*, *41*(15), 5420-5427, doi:https://doi.org/10.1002/2014GL061138.

Kato, A., and K. Obara (2014). Step-like migration of early aftershocks following the 2007 Mw 6.7 Noto-Hanto earthquake, Japan, *Geophysical Research Letters*, *41*(11), 3864-3869, doi:https://doi.org/10.1002/2014GL060427.

Kato, A., J. i. Fukuda, S. Nakagawa, and K. Obara (2016). Foreshock migration preceding the 2016 Mw 7.0 Kumamoto earthquake, Japan, *Geophysical Research Letters*, *43*(17), 8945-8953, doi:https://doi.org/10.1002/2016GL070079.

Kato, N. (2007). Expansion of aftershock areas caused by propagating post-seismic sliding, *Geophysical Journal International*, *168*(2), 797-808, doi:10.1111/j.1365-246X.2006.03255.x.

Kikuchi, M., and H. Kanamori (1982). Inversion of complex body waves, *Bulletin of the Seismological Society of America*, *72*(2), 491-506, doi:10.1785/bssa0720020491.

Kikuchi, M., and H. Kanamori (1986). Inversion of complex body waves-II, *Physics of the Earth and Planetary Interiors*, *43*(3), 205-222, doi:https://doi.org/10.1016/0031-9201(86)90048-8.

Kikuchi, M., and H. Kanamori (1991). Inversion of complex body waves—III, *Bulletin of the Seismological Society of America*, *81*(6), 2335-2350, doi:10.1785/bssa0810062335.

Kilb, D., J. Gomberg, and P. Bodin (2002). Aftershock triggering by complete Coulomb stress changes, *Journal of Geophysical Research: Solid Earth*, *107*(B4), ESE 2-1-ESE 2-14, doi:https://doi.org/10.1029/2001JB000202.

Kilb, D., and A. M. Rubin (2002). Implications of diverse fault orientations imaged in relocated aftershocks of the Mount Lewis, ML 5.7, California, earthquake, *Journal of Geophysical Research: Solid Earth*, *107*(B11), ESE 5-1-ESE 5-17, doi:10.1029/2001jb000149.

Kim, W.-Y., H. Choi, and M. Noh (2010). The 20 January 2007 Odaesan, Korea, Earthquake Sequence: Reactivation of a Buried Strike-Slip Fault?, *Bulletin of the Seismological Society of America*, *100*(3), 1120-1137, doi:10.1785/0120090069.

King, G. C. P., R. S. Stein, and J. Lin (1994). Static stress changes and the triggering of earthquakes, *Bulletin of the Seismological Society of America*, *84*(3), 935-953, doi:10.1785/bssa0840030935.

Kingma, D. P., and J. Ba (2014). Adam: A Method for Stochastic Optimization, *arXiv e-prints*, arXiv:1412.6980.

Klein, F. W. (2002). User's guide to HYPOINVERSE-2000, a Fortran program to solve for earthquake locations and magnitudes*Rep. 2331-1258*, US Geological Survey.

Kohler, M. D., H. Magistrale, and R. W. Clayton (2003). Mantle Heterogeneities and the SCEC Reference Three-Dimensional Seismic Velocity Model Version 3, *Bulletin of the Seismological Society of America*, *93*(2), 757-774, doi:10.1785/0120020017.

Konca, A. Ö., H. Karabulut, S. E. Güvercin, F. Eskiköy, S. Özarpacı, A. Özdemir, M. Floyd, S. Ergintav, and U. Doğan (2021). From Interseismic Deformation With Near-Repeating Earthquakes to Co-Seismic Rupture: A Unified View of the 2020 Mw6.8 Sivrice (Elazığ) Eastern Turkey Earthquake, *Journal of Geophysical Research: Solid Earth*, *126*(10), e2021JB021830, doi:https://doi.org/10.1029/2021JB021830.

Kong, Q., R. Wang, W. R. Walter, M. Pyle, K. Koper, and B. Schmandt (2022). Combining Deep Learning With Physics Based Features in Explosion-Earthquake Discrimination, *Geophysical Research Letters*, *49*(13), e2022GL098645, doi:https://doi.org/10.1029/2022GL098645.

La Rocca, M., D. Galluzzo, S. Malone, W. McCausland, and E. Del Pezzo (2010). Array analysis and precise source location of deep tremor in Cascadia, *Journal of Geophysical Research: Solid Earth*, *115*(B6), doi:https://doi.org/10.1029/2008JB006041.

Lay, T., and S. P. Nishenko (2022). Updated concepts of seismic gaps and asperities to assess great earthquake hazard along South America, *Proceedings of the National Academy of Sciences*, *119*(51), e2216843119, doi:doi:10.1073/pnas.2216843119.

Lei, J., and D. Zhao (2009). Structural heterogeneity of the Longmenshan fault zone and the mechanism of the 2008 Wenchuan earthquake (Ms 8.0), *Geochemistry, Geophysics, Geosystems*, *10*(10), doi:https://doi.org/10.1029/2009GC002590.

Lei, X., C. Xie, and B. Fu (2011). Remotely triggered seismicity in Yunnan, southwestern China, following the 2004 Mw9.3 Sumatra earthquake, *Journal of Geophysical Research: Solid Earth*, *116*(B8), doi:https://doi.org/10.1029/2011JB008245.

Lei, X., Z. Wang, S. Ma, and C. He (2021). A preliminary study on the characteristics and mechanism of the May 2021 M_S6.4 Yangbi earthquake sequence，Yunnan，China, *Acta Seismologica Sinica*, *43*(3), 261, doi:10.11939/jass.20210100.

Lengliné, O., and D. Marsan (2009). Inferring the coseismic and postseismic stress changes caused by the 2004 Mw = 6 Parkfield earthquake from variations of recurrence times of microearthquakes, *Journal of Geophysical Research: Solid Earth*, *114*(B10), doi:10.1029/2008jb006118.

Li, B., and A. Ghosh (2017). Near-continuous tremor and low-frequency earthquake activities in the Alaska-Aleutian subduction zone revealed by a mini seismic array, *Geophysical Research Letters*, *44*(11), 5427-5435, doi:https://doi.org/10.1002/2016GL072088.

Li, C., X. Shan, G. Zhang, C. Zhao, W. Gong, and Y. Zhang (2022). Slip Kinematics of the 2021 Yangbi Earthquake: Fore-Main-Aftershock Sequence Rupture along an Unknown Secondary Fault of the Weixi–Qiaohou Fault, *Seismological Research Letters*, doi:10.1785/0220210220.

Li, L., Q.-f. Chen, F. Niu, and J. Su (2011). Deep slip rates along the Longmen Shan fault zone estimated from repeating microearthquakes, *Journal of Geophysical Research: Solid Earth*, *116*(B9), doi:10.1029/2011jb008406.

Li, S., L. Fang, Z. Xiao, Y. Zhou, S. Liao, and L. Fan (2023a). FocMech-Flow: Automatic Determination of P-Wave First-Motion Polarity and Focal Mechanism Inversion and Application to the 2021 Yangbi Earthquake Sequence, *Applied Sciences*, *13*(4), 2233.

Li, S., X. Wang, T. Tao, Y. Zhu, X. Qu, Z. Li, J. Huang, and S. Song (2023b). Source Model of the 2023 Turkey Earthquake Sequence Imaged by Sentinel-1 and GPS Measurements: Implications for Heterogeneous Fault Behavior along the East Anatolian Fault Zone, *Remote Sensing*, *15*(10), 2618.

Li, X., Y. Ran, L. Chen, F. Wu, X. Ma, and J. Cao (2015). Late Quaternary Large Earthquakes on the Western Branch of the Xiaojiang Fault and Their Tectonic Implications, *Acta Geologica Sinica - English Edition*, *89*(5), 1516-1530, doi:10.1111/1755-6724.12561.

Li, X., D. Bai, X. Ma, Y. Chen, I. M. Varentsov, G. Xue, S. Xue, and I. Lozovsky (2019). Electrical resistivity structure of the Xiaojiang strike-slip fault system (SW China) and its tectonic implications, *Journal of Asian Earth Sciences*, *176*, 57-67, doi:https://doi.org/10.1016/j.jseaes.2019.01.031.

Li, Y., J.-M. Nocquet, X. Shan, and H. Jian (2021a). Heterogeneous interseismic coupling along the Xianshuihe-Xiaojiang fault system, eastern Tibet, *Journal of Geophysical Research: Solid Earth*, *n/a*(n/a), e2020JB021187, doi:https://doi.org/10.1029/2020JB021187.

Li, Z., Z. Shen, Y. Yang, E. Williams, X. Wang, and Z. Zhan (2021b). Rapid Response to the 2019 Ridgecrest Earthquake With Distributed Acoustic Sensing, *AGU Advances*, *2*(2), e2021AV000395, doi:https://doi.org/10.1029/2021AV000395.

Lin, G. (2020). Spatiotemporal variations of in situ Vp/Vs ratio within the Salton Sea Geothermal Field, southern California, *Geothermics*, *84*, 101740, doi:https://doi.org/10.1016/j.geothermics.2019.101740.

Lin, J., and R. S. Stein (2004). Stress triggering in thrust and subduction earthquakes and stress interaction between the southern San Andreas and nearby thrust and strike-slip faults, *Journal of Geophysical Research: Solid Earth*, *109*(B2), doi:https://doi.org/10.1029/2003JB002607.

Lin, X., J. Hao, D. Wang, R. Chu, X. Zeng, J. Xie, B. Zhang, and Q. Bai (2020). Coseismic Slip Distribution of the 24 January 2020 Mw 6.7 Doganyol Earthquake and in

Relation to the Foreshock and Aftershock Activities, *Seismological Research Letters*, *92*(1), 127-139, doi:10.1785/0220200152.

Liu, C., T. Lay, E. E. Brodsky, K. Dascher-Cousineau, and X. Xiong (2019). Coseismic Rupture Process of the Large 2019 Ridgecrest Earthquakes From Joint Inversion of Geodetic and Seismological Observations, *Geophysical Research Letters*, *46*(21), 11820-11829, doi:https://doi.org/10.1029/2019GL084949.

Liu, J., L. Zhang, and Y. Du (2020a). Seismic Hazard Assessment of the Mid-Northern Segment of Xiaojiang Fault Zone in Southwestern China Using Scenario Earthquakes, *Bulletin of the Seismological Society of America*, *110*(3), 1191-1210, doi:10.1785/0120190248.

Liu, M., M. Zhang, W. Zhu, W. L. Ellsworth, and H. Li (2020b). Rapid Characterization of the July 2019 Ridgecrest, California, Earthquake Sequence From Raw Seismic Data Using Machine-Learning Phase Picker, *Geophysical Research Letters*, *47*(4), e2019GL086189, doi:https://doi.org/10.1029/2019GL086189.

Liu, M., H. Li, L. Li, M. Zhang, and W. Wang (2022a). Multistage Nucleation of the 2021 Yangbi MS 6.4 Earthquake, Yunnan, China and Its Foreshocks, *Journal of Geophysical Research: Solid Earth*, *127*(5), e2022JB024091, doi:https://doi.org/10.1029/2022JB024091.

Liu, X., W. Xu, Z. He, L. Fang, and Z. Chen (2022b). Aseismic Slip and Cascade Triggering Process of Foreshocks Leading to the 2021 Mw 6.1 Yangbi Earthquake, *Seismological Research Letters*, doi:https://doi.org/10.1785/0220210263.

Liu, Y., H. Yao, H. Zhang, and H. Fang (2021). The Community Velocity Model V.1.0 of Southwest China, Constructed from Joint Body- and Surface-Wave Travel-Time Tomography, *Seismological Research Letters*, doi:10.1785/0220200318.

Lomax, A. (2020). Absolute Location of 2019 Ridgecrest Seismicity Reveals a Shallow Mw 7.1 Hypocenter, Migrating and Pulsing Mw 7.1 Foreshocks, and Duplex Mw 6.4 Ruptures, *Bulletin of the Seismological Society of America*, *110*(4), 1845-1858, doi:10.1785/0120200006.

Lomax, A., and A. Savvaidis (2022). High-Precision Earthquake Location Using Source-Specific Station Terms and Inter-Event Waveform Similarity, *Journal of Geophysical Research: Solid Earth*, *127*(1), e2021JB023190, doi:https://doi.org/10.1029/2021JB023190.

López-Comino, J. A., and S. Cesca (2018). Source Complexity of an Injection Induced Event: The 2016 Mw 5.1 Fairview, Oklahoma Earthquake, *Geophysical Research Letters*, *45*(9), 4025-4032, doi:https://doi.org/10.1029/2018GL077631.

Lu, W., Y. Zhou, Z. Zhao, H. Yue, and S. Zhou (2021). Aftershock sequence of the 2017 Mw 6.5 Jiuzhaigou, China earthquake monitored by an AsA network and its implication to fault structures and strength, *Geophysical Journal International*, *228*(3), 1763-1779, doi:10.1093/gji/ggab443.

Madariaga, R. (1976). Dynamics of an expanding circular fault, *Bulletin of the Seismological Society of America*, *66*(3), 639-666.

Mai, P. M., et al. (2023). The Destructive Earthquake Doublet of 6 February 2023 in South-Central Türkiye and Northwestern Syria: Initial Observations and Analyses, *The Seismic Record*, *3*(2), 105-115, doi:10.1785/0320230007.

Marzocchi, W., I. Spassiani, A. Stallone, and M. Taroni (2019). How to be fooled searching for significant variations of the b-value, *Geophysical Journal International*, *220*(3), 1845-1856, doi:10.1093/gji/ggz541.

McClusky, S., et al. (2000). Global Positioning System constraints on plate kinematics and dynamics in the eastern Mediterranean and Caucasus, *Journal of Geophysical Research: Solid Earth*, *105*(B3), 5695-5719, doi:https://doi.org/10.1029/1999JB900351.

McGill, S., and K. Sieh (1993). Holocene slip rate of the Central Garlock Fault in southeastern Searles Valley, California, *Journal of Geophysical Research: Solid Earth*, *98*(B8), 14217-14231, doi:https://doi.org/10.1029/93JB00442.

McLaskey, G. C. (2019). Earthquake Initiation From Laboratory Observations and Implications for Foreshocks, *Journal of Geophysical Research: Solid Earth*, *124*(12), 12882-12904, doi:https://doi.org/10.1029/2019JB018363.

Melgar, D., A. Ganas, T. Taymaz, S. Valkaniotis, B. W. Crowell, V. Kapetanidis, V. Tsironi, S. Yolsal-Çevikbilen, and T. Öcalan (2020). Rupture kinematics of 2020 January 24 Mw 6.7 Doğanyol-Sivrice, Turkey earthquake on the East Anatolian Fault Zone imaged by space geodesy, *Geophysical Journal International*, *223*(2), 862-874, doi:10.1093/gji/ggaa345.

Melgar, D., et al. (2023). Sub- and super-shear ruptures during the 2023 Mw 7.8 and Mw 7.6 earthquake doublet in SE Türkiye, *Seismica*, *2*(3), doi:10.26443/seismica.v2i3.387.

Mendoza, M. M., A. Ghosh, M. S. Karplus, S. L. Klemperer, S. N. Sapkota, L. B. Adhikari, and A. Velasco (2019). Duplex in the Main Himalayan Thrust illuminated by aftershocks of the 2015 Mw 7.8 Gorkha earthquake, *Nature Geoscience*, *12*(12), 1018-1022, doi:10.1038/s41561-019-0474-8.

Meng, H., and W. Fan (2021). Immediate Foreshocks Indicating Cascading Rupture Developments for 527 M 0.9 to 5.4 Ridgecrest Earthquakes, *Geophysical Research Letters*, *48*(19), e2021GL095704, doi:https://doi.org/10.1029/2021GL095704.

Meng, Q., S. Ni, and Z. Peng (2021). Complex Source Behaviors and Spatiotemporal Evolution of Seismicity During the 2015–2016 Earthquake Sequence in Cushing, Oklahoma, *Journal of Geophysical Research: Solid Earth*, *126*(6), e2021JB022168, doi:https://doi.org/10.1029/2021JB022168.

Meng, X., and Z. Peng (2016). Increasing lengths of aftershock zones with depths of moderate-size earthquakes on the San Jacinto Fault suggests triggering of deep creep in the middle crust, *Geophysical Journal International*, *204*(1), 250-261, doi:10.1093/gji/ggv445.

Mignan, A. (2014). The debate on the prognostic value of earthquake foreshocks: A meta-analysis, *Scientific Reports*, *4*(1), 4099, doi:10.1038/srep04099.

Mizuno, N., and S. Ide (2019). Development of a modified envelope correlation method based on maximum-likelihood method and application to detecting and locating deep tectonic tremors in western Japan, *Earth, Planets and Space*, *71*(1), 40, doi:10.1186/s40623-019-1022-x.

Mousavi, S. M., Y. Sheng, W. Zhu, and G. C. Beroza (2019a). STanford EArthquake Dataset (STEAD): A Global Data Set of Seismic Signals for AI, *IEEE Access*, *7*, 179464-179476, doi:10.1109/ACCESS.2019.2947848.

Mousavi, S. M., W. Zhu, Y. Sheng, and G. C. Beroza (2019b). CRED: A Deep Residual Network of Convolutional and Recurrent Units for Earthquake Signal Detection, *Scientific Reports*, *9*(1), 10267, doi:10.1038/s41598-019-45748-1.

Mousavi, S. M., W. L. Ellsworth, W. Zhu, L. Y. Chuang, and G. C. Beroza (2020). Earthquake transformer—an attentive deep-learning model for simultaneous earthquake detection and phase picking, *Nature Communications*, *11*(1), 3952, doi:10.1038/s41467-020-17591-w.

Mousavi, S. M., and G. C. Beroza (2022). Deep-learning seismology, *Science*, *377*(6607), eabm4470, doi:doi:10.1126/science.abm4470.

Münchmeyer, J., et al. (2022). Which Picker Fits My Data? A Quantitative Evaluation of Deep Learning Based Seismic Pickers, *Journal of Geophysical Research: Solid Earth*, *127*(1), e2021JB023499, doi:https://doi.org/10.1029/2021JB023499.

Murru, M., R. Console, G. Falcone, C. Montuori, and T. Sgroi (2007). Spatial mapping of the b value at Mount Etna, Italy, using earthquake data recorded from 1999 to 2005, *Journal of Geophysical Research: Solid Earth*, *112*(B12), doi:https://doi.org/10.1029/2006JB004791.

Nanjo, K. Z. (2020). Were changes in stress state responsible for the 2019 Ridgecrest, California, earthquakes?, *Nature Communications*, *11*(1), 3082, doi:10.1038/s41467-020-16867-5.

Neo, J. C., Y. Huang, D. Yao, and S. Wei (2020). Is the Aftershock Zone Area a Good Proxy for the Mainshock Rupture Area?, *Bulletin of the Seismological Society of America*, *111*(1), 424-438, doi:10.1785/0120190200.

Neves, M., Z. Peng, and G. Lin (2022). A High-Resolution Earthquake Catalog for the 2004 Mw 6 Parkfield Earthquake Sequence Using a Matched Filter Technique, *Seismological Research Letters*, *94*(1), 507-521, doi:10.1785/0220220206.

Ni, S., W. Wang, and L. Li (2010). The April 14th, 2010 Yushu earthquake, a devastating earthquake with foreshocks, *Science China Earth Sciences*, *53*(6), 791-793, doi:10.1007/s11430-010-0083-2.

Nicholson, C., L. Seeber, P. Williams, and L. R. Sykes (1986). Seismic evidence for conjugate slip and block rotation within the San Andreas Fault System, southern California, *Tectonics*, *5*(4), 629-648, doi:10.1029/TC005i004p00629.

Niksejel, A., and M. Zhang (2024). OBSTransformer: a deep-learning seismic phase picker for OBS data using automated labelling and transfer learning, *Geophysical Journal International*, *237*(1), 485-505, doi:10.1093/gji/ggae049.

Nishikawa, T., T. Matsuzawa, K. Ohta, N. Uchida, T. Nishimura, and S. Ide (2019). The slow earthquake spectrum in the Japan Trench illuminated by the S-net seafloor observatories, *Science*, *365*(6455), 808-813, doi:doi:10.1126/science.aax5618.

Obara, K. (2002). Nonvolcanic Deep Tremor Associated with Subduction in Southwest Japan, *Science*, *296*(5573), 1679-1681, doi:10.1126/science.1070378.

Ogata, Y. (1988). Statistical Models for Earthquake Occurrences and Residual Analysis for Point Processes, *Journal of the American Statistical Association*, *83*(401), 9-27, doi:10.1080/01621459.1988.10478560.

Ogden, C. S., and I. D. Bastow (2021). The crustal structure of the Anatolian Plate from receiver functions and implications for the uplift of the central and eastern Anatolian plateaus, *Geophysical Journal International*, *229*(2), 1041-1062, doi:10.1093/gji/ggab513.

Oskin, M., L. Perg, E. Shelef, M. Strane, E. Gurney, B. Singer, and X. Zhang (2008). Elevated shear zone loading rate during an earthquake cluster in eastern California, *Geology*, *36*(6), 507-510, doi:10.1130/g24814a.1.

Park, Y., G. C. Beroza, and W. L. Ellsworth (2023). A Mitigation Strategy for the Prediction Inconsistency of Neural Phase Pickers, *Seismological Research Letters*, doi:10.1785/0220230003.

Parsons, T., and A. A. Velasco (2009). On near-source earthquake triggering, *Journal of Geophysical Research: Solid Earth*, *114*(B10), doi:https://doi.org/10.1029/2008JB006277.

Patton, J. M., M. R. Guy, H. M. Benz, R. P. Buland, B. K. Erickson, and D. S. Kragness (2016). Hydra—The National Earthquake Information Center's 24/7 seismic monitoring, analysis, catalog production, quality analysis, and special studies tool suite, *Report Rep. 2016-1128*, Reston, VA.

Peng, B., E. Alcaide, Q. Anthony, A. Albalak, S. Arcadinho, H. Cao, X. Cheng, M. Chung, M. Grella, and K. K. GV (2023). Rwkv: Reinventing rnns for the transformer era, *arXiv preprint arXiv:2305.13048*.

Peng, Z., and P. Zhao (2009). Migration of early aftershocks following the 2004 Parkfield earthquake, *Nature Geoscience*, *2*(12), 877-881, doi:10.1038/ngeo697.

Peng, Z., and J. Gomberg (2010). An integrated perspective of the continuum between earthquakes and slow-slip phenomena, *Nature Geoscience*, *3*(9), 599-607, doi:10.1038/ngeo940.

Petersen, G. M., P. Büyükakpinar, F. O. Vera Sanhueza, M. Metz, S. Cesca, K. Akbayram, J. Saul, and T. Dahm (2023). The 2023 Southeast Türkiye Seismic Sequence: Rupture of a Complex Fault Network, *The Seismic Record*, *3*(2), 134-143, doi:10.1785/0320230008.

Podolskiy, E. A., and F. Walter (2016). Cryoseismology, *Reviews of Geophysics*, *54*(4), 708-758, doi:https://doi.org/10.1002/2016RG000526.

Pousse-Beltran, L., E. Nissen, E. A. Bergman, M. D. Cambaz, É. Gaudreau, E. Karasözen, and F. Tan (2020). The 2020 Mw 6.8 Elazığ (Turkey) Earthquake Reveals Rupture Behavior of the East Anatolian Fault, *Geophysical Research Letters*, *47*(13), e2020GL088136, doi:https://doi.org/10.1029/2020GL088136.

Prieto, G. A., R. L. Parker, and F. L. Vernon Iii (2009). A Fortran 90 library for multitaper spectrum analysis, *Computers & Geosciences*, *35*(8), 1701-1710, doi:https://doi.org/10.1016/j.cageo.2008.06.007.

Ren, C., et al. (2024). Supershear triggering and cascading fault ruptures of the 2023 Kahramanmaraş, Türkiye, earthquake doublet, *Science*, *383*(6680), 305-311, doi:doi:10.1126/science.adi1519.

Ren, Z. (2013). Geometry and deformation features of the most recent co-seismic surface ruptures along the Xiaojiang Fault and its tectonic implications for the Tibetan Plateau, *Journal of Asian Earth Sciences*, *77*, 21-30, doi:https://doi.org/10.1016/j.jseaes.2013.08.016.

Richter, C. F. (1935). An instrumental earthquake magnitude scale*, *Bulletin of the Seismological Society of America*, *25*(1), 1-32.

Roeloffs, E. A. (2006). Evidence for Aseismic Deformation Rate Changes Prior to Earthquakes, *Annual Review of Earth and Planetary Sciences*, *34*(1), 591-627, doi:10.1146/annurev.earth.34.031405.124947.

Ronald, E. W., T. P. Harding, and D. R. Seely (1973). Basic Wrench Tectonics, *AAPG Bulletin*, *57*(1), 74-96, doi:10.1306/819a424a-16c5-11d7-8645000102c1865d.

Ross, Z. E., and Y. Ben-Zion (2014). Automatic picking of direct P, S seismic phases and fault zone head waves, *Geophysical Journal International*, *199*(1), 368-381, doi:10.1093/gji/ggu267.

Ross, Z. E., and Y. Ben-Zion (2016). Toward reliable automated estimates of earthquake source properties from body wave spectra, *Journal of Geophysical Research: Solid Earth*, *121*(6), 4390-4407, doi:https://doi.org/10.1002/2016JB013003.

Ross, Z. E., E. Hauksson, and Y. Ben-Zion (2017a). Abundant off-fault seismicity and orthogonal structures in the San Jacinto fault zone, *Science Advances*, *3*(3), e1601946, doi:10.1126/sciadv.1601946.

Ross, Z. E., C. Rollins, E. S. Cochran, E. Hauksson, J.-P. Avouac, and Y. Ben-Zion (2017b). Aftershocks driven by afterslip and fluid pressure sweeping through a fault-fracture mesh, *Geophysical Research Letters*, *44*(16), 8260-8267, doi:https://doi.org/10.1002/2017GL074634.

Ross, Z. E., M.-A. Meier, and E. Hauksson (2018). P Wave Arrival Picking and First-Motion Polarity Determination With Deep Learning, *Journal of Geophysical Research: Solid Earth*, *123*(6), 5120-5129, doi:10.1029/2017jb015251.

Ross, Z. E., et al. (2019a). Hierarchical interlocked orthogonal faulting in the 2019 Ridgecrest earthquake sequence, *Science*, *366*(6463), 346-351, doi:10.1126/science.aaz0109.

Ross, Z. E., D. T. Trugman, E. Hauksson, and P. M. Shearer (2019b). Searching for hidden earthquakes in Southern California, *Science*, *364*(6442), 767-771, doi:10.1126/science.aaw6888.

Ross, Z. E., E. S. Cochran, D. T. Trugman, and J. D. Smith (2020). 3D fault architecture controls the dynamism of earthquake swarms, *Science*, *368*(6497), 1357-1361, doi:10.1126/science.abb0779.

Ross, Z. E., and E. S. Cochran (2021). Evidence for Latent Crustal Fluid Injection Transients in Southern California From Long-Duration Earthquake Swarms, *Geophysical Research Letters*, *48*(12), e2021GL092465, doi:https://doi.org/10.1029/2021GL092465.

Rubin, A. M., and J. G. Armbruster (2013). Imaging slow slip fronts in Cascadia with high precision cross-station tremor locations, *Geochemistry, Geophysics, Geosystems*, *14*(12), 5371-5392, doi:https://doi.org/10.1002/2013GC005031.

Ruiz, S., M. Metois, A. Fuenzalida, J. Ruiz, F. Leyton, R. Grandin, C. Vigny, R. Madariaga, and J. Campos (2014). Intense foreshocks and a slow slip event preceded the 2014 Iquique Mw 8.1 earthquake, *Science*, *345*(6201), 1165-1169, doi:10.1126/science.1256074.

Ruiz, S., et al. (2017). Nucleation Phase and Dynamic Inversion of the Mw 6.9 Valparaíso 2017 Earthquake in Central Chile, *Geophysical Research Letters*, *44*(20), 10,290-210,297, doi:https://doi.org/10.1002/2017GL075675.

Schmittbuhl, J., H. Karabulut, O. Lengliné, and M. Bouchon (2016). Long-lasting seismic repeaters in the Central Basin of the Main Marmara Fault, *Geophysical Research Letters*, *43*(18), 9527-9534, doi:https://doi.org/10.1002/2016GL070505.

Schoenball, M., N. C. Davatzes, and J. M. G. Glen (2015). Differentiating induced and natural seismicity using space-time-magnitude statistics applied to the Coso Geothermal field, *Geophysical Research Letters*, *42*(15), 6221-6228, doi:https://doi.org/10.1002/2015GL064772.

Scholz, C. H. (1968). The frequency-magnitude relation of microfracturing in rock and its relation to earthquakes, *Bulletin of the Seismological Society of America*, *58*(1), 399-415.

Scholz, C. H. (1988). The brittle-plastic transition and the depth of seismic faulting, *Geologische Rundschau*, *77*(1), 319-328, doi:10.1007/BF01848693.

Scholz, C. H. (2015). On the stress dependence of the earthquake b value, *Geophysical Research Letters*, *42*(5), 1399-1402, doi:10.1002/2014gl062863.

Scholz, C. H. (2019). *The mechanics of earthquakes and faulting*, Cambridge university press, doi:https://doi.org/10.1017/9781316681473.

Schorlemmer, D., and S. Wiemer (2005). Microseismicity data forecast rupture area, *Nature*, *434*(7037), 1086-1086, doi:10.1038/4341086a.

Schurr, B., et al. (2014). Gradual unlocking of plate boundary controlled initiation of the 2014 Iquique earthquake, *Nature*, *512*(7514), 299-302, doi:10.1038/nature13681.

Schurr, B., M. Moreno, A. M. Tréhu, J. Bedford, J. Kummerow, S. Li, and O. Oncken (2020). Forming a Mogi Doughnut in the Years Prior to and Immediately Before the 2014 M8.1 Iquique, Northern Chile, Earthquake, *Geophysical Research Letters*, *47*(16), e2020GL088351, doi:https://doi.org/10.1029/2020GL088351.

Shaddox, H. R., S. Y. Schwartz, and N. M. Bartlow (2021). Afterslip and Spontaneous Aseismic Slip on the Anza Segment of the San Jacinto Fault Zone, Southern California, *Journal of Geophysical Research: Solid Earth*, *126*(6), e2020JB020460, doi:https://doi.org/10.1029/2020JB020460.

Shan, B., X. Xiong, R. Wang, Y. Zheng, and S. Yang (2013). Coulomb stress evolution along Xianshuihe–Xiaojiang Fault System since 1713 and its interaction with Wenchuan earthquake, May 12, 2008, *Earth and Planetary Science Letters*, *377-378*, 199-210, doi:https://doi.org/10.1016/j.epsl.2013.06.044.

Shelly, D. R., G. C. Beroza, and S. Ide (2007). Non-volcanic tremor and low-frequency earthquake swarms, *Nature*, *446*(7133), 305-307, doi:10.1038/nature05666.

Shelly, D. R., W. L. Ellsworth, and D. P. Hill (2016). Fluid-faulting evolution in high definition: Connecting fault structure and frequency-magnitude variations during the 2014 Long Valley Caldera, California, earthquake swarm, *Journal of*

Geophysical Research: Solid Earth, *121*(3), 1776-1795, doi:https://doi.org/10.1002/2015JB012719.

Shelly, D. R., and J. L. Hardebeck (2019). Illuminating Faulting Complexity of the 2017 Yellowstone Maple Creek Earthquake Swarm, *Geophysical Research Letters*, *46*(5), 2544-2552, doi:10.1029/2018gl081607.

Shelly, D. R. (2020a). A High-Resolution Seismic Catalog for the Initial 2019 Ridgecrest Earthquake Sequence: Foreshocks, Aftershocks, and Faulting Complexity, *Seismological Research Letters*, doi:10.1785/0220190309.

Shelly, D. R. (2020b). A High-Resolution Seismic Catalog for the Initial 2019 Ridgecrest Earthquake Sequence: Foreshocks, Aftershocks, and Faulting Complexity, *Seismological Research Letters*, *91*(4), 1971-1978, doi:10.1785/0220190309.

Shelly, D. R., D. E. Goldberg, K. Z. Materna, R. J. Skoumal, J. L. Hardebeck, C. E. Yoon, W. L. Yeck, and P. S. Earle (2024). Subduction intraslab-interface fault interactions in the 2022 <i>M</i>_w 6.4 Ferndale, California, earthquake sequence, *Science Advances*, *10*(10), eadl1226, doi:doi:10.1126/sciadv.adl1226.

Shen, J., and Y. Wang (1999). Estimation of Seismic Risk of the Xiaojiang Active Fault Zone Using Slip Rate, *Journal of Seismological Research*(03), 251-259.

Shen, J., Y. Wang, and F. Song (2003). Characteristics of the active Xiaojiang fault zone in Yunnan, China: a slip boundary for the southeastward escaping Sichuan–Yunnan Block of the Tibetan Plateau, *Journal of Asian Earth Sciences*, *21*(10), 1085-1096, doi:https://doi.org/10.1016/S1367-9120(02)00185-2.

Shen, Z.-K., J. Lü, M. Wang, and R. Bürgmann (2005). Contemporary crustal deformation around the southeast borderland of the Tibetan Plateau, *Journal of Geophysical Research: Solid Earth*, *110*(B11), doi:10.1029/2004jb003421.

Shi, Y., and B. A. Bolt (1982). The standard error of the magnitude-frequency b value, *Bulletin of the Seismological Society of America*, *72*(5), 1677-1687.

Shi, Z., and G. Wang (2017). Evaluation of the permeability properties of the Xiaojiang Fault Zone using hot springs and water wells, *Geophysical Journal International*, *209*(3), 1526-1533, doi:10.1093/gji/ggx113.

Sirorattanakul, K., Z. E. Ross, M. Khoshmanesh, E. S. Cochran, M. Acosta, and J.-P. Avouac (2022). The 2020 Westmorland, California Earthquake Swarm as Aftershocks of a Slow Slip Event Sustained by Fluid Flow, *Journal of Geophysical Research: Solid Earth*, *127*(11), e2022JB024693, doi:https://doi.org/10.1029/2022JB024693.

Spada, M., T. Tormann, S. Wiemer, and B. Enescu (2013). Generic dependence of the frequency-size distribution of earthquakes on depth and its relation to the strength profile of the crust, *Geophysical Research Letters*, *40*(4), 709-714, doi:10.1029/2012gl054198.

Spinler, J. C., R. A. Bennett, M. L. Anderson, S. F. McGill, S. Hreinsdóttir, and A. McCallister (2010). Present-day strain accumulation and slip rates associated with southern San Andreas and eastern California shear zone faults, *Journal of Geophysical Research: Solid Earth*, *115*(B11), doi:https://doi.org/10.1029/2010JB007424.

Steacy, S., J. Gomberg, and M. Cocco (2005). Introduction to special section: Stress transfer, earthquake triggering, and time-dependent seismic hazard, *Journal of Geophysical Research: Solid Earth*, *110*(B5), doi:https://doi.org/10.1029/2005JB003692.

Sugan, M., S. Campanella, L. Chiaraluce, M. Michele, and A. Vuan (2023). The unlocking process leading to the 2016 Central Italy seismic sequence, *Geophysical Research Letters*, *n/a*(n/a), e2022GL101838, doi:https://doi.org/10.1029/2022GL101838.

Sun, H., Z. E. Ross, W. Zhu, and K. Azizzadenesheli (2023). Phase Neural Operator for Multi-Station Picking of Seismic Arrivals, *Geophysical Research Letters*, *50*(24), e2023GL106434, doi:https://doi.org/10.1029/2023GL106434.

Sun, J., H. Yue, Z. Shen, L. Fang, Y. Zhan, and X. Sun (2018). The 2017 Jiuzhaigou Earthquake: A Complicated Event Occurred in a Young Fault System, *Geophysical Research Letters*, *45*(5), 2230-2240, doi:10.1002/2017gl076421.

Sun, Q., Z. Guo, S. Pei, Y. V. Fu, and Y. J. Chen (2022). Fluids Triggered the 2021 Mw 6.1 Yangbi Earthquake at an Unmapped Fault: Implications for the Tectonics at the Northern End of the Red River Fault, *Seismological Research Letters*, *93*(2A), 666-679, doi:10.1785/0220210227.

Sutskever, I., O. Vinyals, and Q. V. Le (2014). Sequence to sequence learning with neural networks, *Advances in neural information processing systems*, *27*.

Sykes, L. R. (2021). Decadal seismicity prior to great earthquakes at subduction zones: Roles of major asperities and low-coupling zones, *International Journal of Geosciences*, *12*(9), 845-926, doi:https://doi.org/10.4236/ijg.2021.129046.

Takemura, S., S. Baba, S. Yabe, K. Emoto, K. Shiomi, and T. Matsuzawa (2022). Source Characteristics and Along-Strike Variations of Shallow Very Low Frequency Earthquake Swarms on the Nankai Trough Shallow Plate Boundary, *Geophysical Research Letters*, *49*(11), e2022GL097979, doi:https://doi.org/10.1029/2022GL097979.

Tan, Y. J., F. Waldhauser, W. L. Ellsworth, M. Zhang, W. Zhu, M. Michele, L. Chiaraluce, G. C. Beroza, and M. Segou (2021). Machine-Learning-Based High-Resolution Earthquake Catalog Reveals How Complex Fault Structures Were Activated during the 2016–2017 Central Italy Sequence, *The Seismic Record*, *1*(1), 11-19, doi:10.1785/0320210001.

Tape, C., S. Holtkamp, V. Silwal, J. Hawthorne, Y. Kaneko, J. P. Ampuero, C. Ji, N. Ruppert, K. Smith, and M. E. West (2018). Earthquake nucleation and fault slip complexity in the lower crust of central Alaska, *Nature Geoscience*, *11*(7), 536-541, doi:10.1038/s41561-018-0144-2.

Taymaz, T., et al. (2021). Source Mechanism and Rupture Process of the 24 January 2020 Mw 6.7 Doğanyol–Sivrice Earthquake obtained from Seismological Waveform Analysis and Space Geodetic Observations on the East Anatolian Fault Zone (Turkey), *Tectonophysics*, *804*, 228745, doi:https://doi.org/10.1016/j.tecto.2021.228745.

Thompson Jobe, J. A., et al. (2020). Evidence of Previous Faulting along the 2019 Ridgecrest, California, Earthquake Ruptures, *Bulletin of the Seismological Society of America*, *110*(4), 1427-1456, doi:10.1785/0120200041.

Toda, S., R. S. Stein, K. Richards-Dinger, and S. B. Bozkurt (2005). Forecasting the evolution of seismicity in southern California: Animations built on earthquake stress transfer, *Journal of Geophysical Research: Solid Earth*, *110*(B5), doi:https://doi.org/10.1029/2004JB003415.

Toda, S., and R. S. Stein (2022). Central shutdown and surrounding activation of aftershocks from megathrust earthquake stress transfer, *Nature Geoscience*, *15*(6), 494-500, doi:10.1038/s41561-022-00954-x.

Toda, S., R. S. Stein, A. D. Özbakir, H. Gonzalez-Huizar, V. Sevilgen, G. Lotto, and S. Sevilgen (2023). Stress change calculations provide clues to aftershocks in 2023 Türkiye earthquakes, *Temblor*, doi:http://doi.org/10.32858/temblor.295.

Tormann, T., S. Wiemer, S. Metzger, A. Michael, and J. L. Hardebeck (2013). Size distribution of Parkfield's microearthquakes reflects changes in surface creep rate, *Geophysical Journal International*, *193*(3), 1474-1478, doi:10.1093/gji/ggt093.

Trugman, D. T., P. M. Shearer, A. A. Borsa, and Y. Fialko (2016). A comparison of long-term changes in seismicity at The Geysers, Salton Sea, and Coso geothermal fields, *Journal of Geophysical Research: Solid Earth*, *121*(1), 225-247, doi:https://doi.org/10.1002/2015JB012510.

Trugman, D. T., and P. M. Shearer (2017). GrowClust: A Hierarchical Clustering Algorithm for Relative Earthquake Relocation, with Application to the Spanish Springs and Sheldon, Nevada, Earthquake Sequences, *Seismological Research Letters*, *88*(2A), 379-391, doi:10.1785/0220160188.

Trugman, D. T., and Z. E. Ross (2019). Pervasive Foreshock Activity Across Southern California, *Geophysical Research Letters*, *46*(15), 8772-8781, doi:https://doi.org/10.1029/2019GL083725.

Turin, G. (1960). An introduction to matched filters, *IRE Transactions on Information Theory*, *6*(3), 311-329, doi:10.1109/TIT.1960.1057571.

Tymofyeyeva, E., and Y. Fialko (2015). Mitigation of atmospheric phase delays in InSAR data, with application to the eastern California shear zone, *Journal of Geophysical Research: Solid Earth*, *120*(8), 5952-5963, doi:https://doi.org/10.1002/2015JB011886.

Uchida, N., T. Matsuzawa, W. L. Ellsworth, K. Imanishi, T. Okada, and A. Hasegawa (2007). Source parameters of a M4.8 and its accompanying repeating earthquakes off Kamaishi, NE Japan: Implications for the hierarchical structure of asperities and earthquake cycle, *Geophysical Research Letters*, *34*(20), doi:https://doi.org/10.1029/2007GL031263.

Uchida, N. (2019). Detection of repeating earthquakes and their application in characterizing slow fault slip, *Progress in Earth and Planetary Science*, *6*(1), 40, doi:10.1186/s40645-019-0284-z.

Uchida, N., and R. Bürgmann (2019). Repeating Earthquakes, *Annual Review of Earth and Planetary Sciences*, *47*(1), 305-332, doi:10.1146/annurev-earth-053018-060119.

Uchida, N., and R. Bürgmann (2021). A Decade of Lessons Learned from the 2011 Tohoku-Oki Earthquake, *Reviews of Geophysics*, *59*(2), e2020RG000713, doi:https://doi.org/10.1029/2020RG000713.

Uhrhammer, R. A., M. Hellweg, K. Hutton, P. Lombard, A. W. Walters, E. Hauksson, and D. Oppenheimer (2011). California Integrated Seismic Network (CISN) Local Magnitude Determination in California and Vicinity, *Bulletin of the Seismological Society of America*, *101*(6), 2685-2693, doi:10.1785/0120100106.

Ulrich, T., A.-A. Gabriel, J.-P. Ampuero, and W. Xu (2019). Dynamic viability of the 2016 Mw 7.8 Kaikōura earthquake cascade on weak crustal faults, *Nature Communications*, *10*(1), 1213, doi:10.1038/s41467-019-09125-w.

Utsu, T. (1961). A statistical study on the occurrence of aftershocks, *Geophysical magazine*, *30*(4), 521-605.

Utsu, T. (1970). Aftershocks and Earthquake Statistics(1) : Some Parameters Which Characterize an Aftershock Sequence and Their Interrelations, *Journal of the Faculty of Science, Hokkaido University. Series 7, Geophysics*, *3*(3), 129-195.

Vanacore, E. A., T. Taymaz, and E. Saygin (2013). Moho structure of the Anatolian Plate from receiver function analysis, *Geophysical Journal International*, *193*(1), 329-337, doi:10.1093/gji/ggs107.

Vaswani, A., N. Shazeer, N. Parmar, J. Uszkoreit, L. Jones, A. N. Gomez, Ł. Kaiser, and I. Polosukhin (2017). Attention is all you need, *Advances in neural information processing systems*, *30*.

Vidale, J. E., and P. M. Shearer (2006). A survey of 71 earthquake bursts across southern California: Exploring the role of pore fluid pressure fluctuations and aseismic slip as drivers, *Journal of Geophysical Research: Solid Earth*, *111*(B5), doi:https://doi.org/10.1029/2005JB004034.

Waldhauser, F., and W. L. Ellsworth (2000). A Double-Difference Earthquake Location Algorithm: Method and Application to the Northern Hayward Fault, California, *Bulletin of the Seismological Society of America*, *90*(6), 1353-1368, doi:10.1785/0120000006.

Waldhauser, F. (2001). hypoDD--A program to compute double-difference hypocenter locations, *U.S. Geological Survey Open-File Report 01-113*, 25 pp.

Waldhauser, F., and W. L. Ellsworth (2002). Fault structure and mechanics of the Hayward Fault, California, from double-difference earthquake locations, *Journal of Geophysical Research: Solid Earth*, *107*(B3), ESE 3-1-ESE 3-15, doi:10.1029/2000jb000084.

Waldhauser, F., W. L. Ellsworth, D. P. Schaff, and A. Cole (2004). Streaks, multiplets, and holes: High-resolution spatio-temporal behavior of Parkfield seismicity, *Geophysical Research Letters*, *31*(18), doi:10.1029/2004gl020649.

Waldhauser, F., and D. P. Schaff (2008). Large-scale relocation of two decades of Northern California seismicity using cross-correlation and double-difference methods, *Journal of Geophysical Research: Solid Earth*, *113*(B8), doi:10.1029/2007jb005479.

Walters, R. J., B. Parsons, and T. J. Wright (2014). Constraining crustal velocity fields with InSAR for Eastern Turkey: Limits to the block-like behavior of Eastern Anatolia, *Journal of Geophysical Research: Solid Earth*, *119*(6), 5215-5234, doi:https://doi.org/10.1002/2013JB010909.

Wang, C., W.D.Mooney, X. Wang, J. Wu, H. Lou, and F. Wang (2002). Study on 3-D Velocity Structure of Crust and Upper Mantle in Sichuan-Yunnan Region, China, *Acta Seismological Sinica*(01), 1-16.

Wang, F., M. Wang, Y. Wang, and Z.-K. Shen (2015). Earthquake potential of the Sichuan-Yunnan region, western China, *Journal of Asian Earth Sciences*, *107*, 232-243, doi:https://doi.org/10.1016/j.jseaes.2015.04.041.

Wang, G., Z. Wu, G. Peng, Z. Liu, R. Luo, X. Huang, and H. Chen (2021a). Seismogenic fault and it's rupture characteristics of 21 May, 2021 Yangbi Ms6.4 earthquake: analysis results from relocation of earthquake sequence, *Journal of Geomechanics (in Chinese)*, *27(4)*, 1-22.

Wang, H., M. Liu, J. Cao, X. Shen, and G. Zhang (2011). Slip rates and seismic moment deficits on major active faults in mainland China, *Journal of Geophysical Research: Solid Earth*, *116*(B2), doi:10.1029/2010jb007821.

Wang, K., Q.-F. Chen, S. Sun, and A. Wang (2006). Predicting the 1975 Haicheng Earthquake, *Bulletin of the Seismological Society of America*, *96*(3), 757-795, doi:10.1785/0120050191.

Wang, K., D. S. Dreger, E. Tinti, R. Bürgmann, and T. a. Taira (2020). Rupture Process of the 2019 Ridgecrest, California Mw 6.4 Foreshock and Mw 7.1 Earthquake Constrained by Seismic and Geodetic Data, *Bulletin of the Seismological Society of America*, *110*(4), 1603-1626, doi:10.1785/0120200108.

Wang, M., and Z.-K. Shen (2020). Present-Day Crustal Deformation of Continental China Derived From GPS and Its Tectonic Implications, *Journal of Geophysical Research: Solid Earth*, *125*(2), e2019JB018774, doi:10.1029/2019jb018774.

Wang, S., et al. (2021b). An accessible seismological dataset of 2021 Yangbi MS 6.4 earthquake, *Earthquake Science*, *34*(5), 460-464, doi:10.29382/eqs-2021-0026.

Wang, W., J. Wu, L. Fang, G. Lai, and Y. Cai (2017). Crustal thickness and Poisson's ratio in southwest China based on data from dense seismic arrays, *Journal of Geophysical Research: Solid Earth*, *122*(9), 7219-7235, doi:10.1002/2017jb013978.

Wang, W., J. He, X. Wang, Y. Zhou, J. Hao, L. Zhao, and Z. Yao (2022a). Rupture process models of the Yangbi and Maduo earthquakes that struck the eastern Tibetan Plateau in May 2021, *Science Bulletin*, *67*(5), 466-469, doi:https://doi.org/10.1016/j.scib.2021.11.009.

Wang, W., P. M. Shearer, J. E. Vidale, X. Xu, D. T. Trugman, and Y. Fialko (2022b). Tidal modulation of seismicity at the Coso geothermal field, *Earth and Planetary Science Letters*, *579*, 117335, doi:https://doi.org/10.1016/j.epsl.2021.117335.

Wdowinski, S. (2009). Deep creep as a cause for the excess seismicity along the San Jacinto fault, *Nature Geoscience*, *2*(12), 882-885, doi:10.1038/ngeo684.

Wech, A. G., and K. C. Creager (2008). Automated detection and location of Cascadia tremor, *Geophysical Research Letters*, *35*(20), doi:https://doi.org/10.1029/2008GL035458.

Wech, A. G. (2021). Cataloging Tectonic Tremor Energy Radiation in the Cascadia Subduction Zone, *Journal of Geophysical Research: Solid Earth*, *126*(10), e2021JB022523, doi:https://doi.org/10.1029/2021JB022523.

Weiss, J. R., et al. (2020). High-Resolution Surface Velocities and Strain for Anatolia From Sentinel-1 InSAR and GNSS Data, *Geophysical Research Letters*, *47*(17), e2020GL087376, doi:https://doi.org/10.1029/2020GL087376.

Wen, X.-z., S.-l. Ma, X.-w. Xu, and Y.-n. He (2008). Historical pattern and behavior of earthquake ruptures along the eastern boundary of the Sichuan-Yunnan faulted-block, southwestern China, *Physics of the Earth and Planetary Interiors*, *168*(1), 16-36, doi:https://doi.org/10.1016/j.pepi.2008.04.013.

Wesnousky, S. G. (2008). Displacement and Geometrical Characteristics of Earthquake Surface Ruptures: Issues and Implications for Seismic-Hazard Analysis and the Process of Earthquake Rupture, *Bulletin of the Seismological Society of America*, *98*(4), 1609-1632, doi:10.1785/0120070111.

Wetzler, N., T. Lay, E. E. Brodsky, and H. Kanamori (2018). Systematic deficiency of aftershocks in areas of high coseismic slip for large subduction zone earthquakes, *Science Advances*, *4*(2), eaao3225, doi:10.1126/sciadv.aao3225.

White, M. C. A., Y. Ben-Zion, and F. L. Vernon (2019). A Detailed Earthquake Catalog for the San Jacinto Fault-Zone Region in Southern California, *Journal of Geophysical Research: Solid Earth*, *124*(7), 6908-6930, doi:https://doi.org/10.1029/2019JB017641.

Wiemer, S., and M. Wyss (2000). Minimum Magnitude of Completeness in Earthquake Catalogs: Examples from Alaska, the Western United States, and Japan, *Bulletin of the Seismological Society of America*, *90*(4), 859-869, doi:10.1785/0119990114.

Withers, M., R. Aster, C. Young, J. Beiriger, M. Harris, S. Moore, and J. Trujillo (1998). A comparison of select trigger algorithms for automated global seismic phase and event detection, *Bulletin of the Seismological Society of America*, *88*(1), 95-106.

Woessner, J., and S. Wiemer (2005). Assessing the Quality of Earthquake Catalogues: Estimating the Magnitude of Completeness and Its Uncertainty, *Bulletin of the Seismological Society of America*, *95*(2), 684-698, doi:10.1785/0120040007.

Wu, J., T. Yang, W. Wang, Y. Ming, and T. Zhang (2013). Three dimensional P-wave velocity structure around Xiaojiang fault system and its tectonic implications, *Chinese Journal Of Geophysics*, *56*(7), 2257-2267, doi:10.6038/cjg20130713.

Wu, Q., X. Chen, and R. E. Abercrombie (2019a). Source Complexity of the 2015 Mw 4.0 Guthrie, Oklahoma Earthquake, *Geophysical Research Letters*, *46*(9), 4674-4684, doi:https://doi.org/10.1029/2019GL082690.

Wu, Z., X. Zhang, and K. Sun (2019b). China Seismic Experiment Site: scientific challenges, *Acta Geologica Sinica - English Edition*, *93*(S1), 273-273, doi:10.1111/1755-6724.14084.

Xu, C., Y. Zhang, S. Hua, X. Zhang, L. Xu, Y.-t. Chen, and T. Taymaz (2023a). Rapid source inversions of the 2023 SE Türkiye earthquakes with teleseismic and strong-motion data, *Earthquake Science*, *36*(4), 1-12, doi:10.1016/j.eqs.2023.05.004.

Xu, L., S. Mohanna, L. Meng, C. Ji, J.-P. Ampuero, Z. Yunjun, M. Hasnain, R. Chu, and C. Liang (2023b). The overall-subshear and multi-segment rupture of the 2023 Mw7.8 Kahramanmaraş, Turkey earthquake in millennia supercycle, *Communications Earth & Environment*, *4*(1), 379, doi:10.1038/s43247-023-01030-x.

Xu, S., B. Wang, L. M. Jones, X. Ma, and P. Shen (1982). The foreshock sequence of haicheng earthquake and earthquake swarm—the use of foreshock sequences in earthquake prediction, *Tectonophysics*, *85*(1), 91-105, doi:https://doi.org/10.1016/0040-1951(82)90079-8.

Xu, X., D. T. Sandwell, L. A. Ward, C. W. D. Milliner, B. R. Smith-Konter, P. Fang, and Y. Bock (2020). Surface deformation associated with fractures near the 2019 Ridgecrest earthquake sequence, *Science*, *370*(6516), 605-608, doi:10.1126/science.abd1690.

Xue, L., R. Bürgmann, D. R. Shelly, C. W. Johnson, and T. a. Taira (2018). Kinematics of the 2015 San Ramon, California earthquake swarm: Implications for fault zone structure and driving mechanisms, *Earth and Planetary Science Letters*, *489*, 135-144, doi:https://doi.org/10.1016/j.epsl.2018.02.018.

Yagi, Y., R. Okuwaki, B. Enescu, A. Kasahara, A. Miyakawa, and M. Otsubo (2016). Rupture process of the 2016 Kumamoto earthquake in relation to the thermal structure around Aso volcano, *Earth, Planets and Space*, *68*(1), 118, doi:10.1186/s40623-016-0492-3.

Yamashita, Y., et al. (2015). Migrating tremor off southern Kyushu as evidence for slow slip of a shallow subduction interface, *Science*, *348*(6235), 676-679, doi:doi:10.1126/science.aaa4242.

Yang, H., S. Yao, B. He, A. V. Newman, and H. Weng (2019). Deriving Rupture Scenarios From Interseismic Locking Distributions Along the Subduction Megathrust, *Journal of Geophysical Research: Solid Earth*, *124*(10), 10376-10392, doi:10.1029/2019jb017541.

Yang, Y., S. Hu, H. Yao, L. Fang, and J. Wu (2020). Crustal shear wave velocity and radial anisotropy in the Xiaojiang fault zone system (SE Tibet) revealed by ambient noise interferometry, *Tectonophysics*, *792*, 228594, doi:https://doi.org/10.1016/j.tecto.2020.228594.

Yang, Z., J. Liu, X.-M. Zhang, W. Deng, G. Du, and X. Wu (2021). A preliminary report of the Yangbi, Yunnan, Ms6.4 earthquake of May 21, 2021, *Earth and Planetary Physics*, *5*(4), 1-3, doi:10.26464/epp2021036.

Yao, D., Y. Huang, Z. Peng, and R. R. Castro (2020). Detailed Investigation of the Foreshock Sequence of the 2010 Mw7.2 El Mayor-Cucapah Earthquake, *Journal of Geophysical Research: Solid Earth*, *125*(6), e2019JB019076, doi:https://doi.org/10.1029/2019JB019076.

Yoon, C. E., N. Yoshimitsu, W. L. Ellsworth, and G. C. Beroza (2019). Foreshocks and Mainshock Nucleation of the 1999 Mw 7.1 Hector Mine, California, Earthquake, *Journal of Geophysical Research: Solid Earth*, *124*(2), 1569-1582, doi:https://doi.org/10.1029/2018JB016383.

Yoon, C. E., and D. R. Shelly (2024). Distinct Yet Adjacent Earthquake Sequences near the Mendocino Triple Junction: 20 December 2021 Mw 6.1 and 6.0 Petrolia, and 20 December 2022 Mw 6.4 Ferndale, *The Seismic Record*, *4*(1), 81-92, doi:10.1785/0320230053.

Yu, Z., and W. Wang (2022). LPPN: A Lightweight Network for Fast Phase Picking, *Seismological Research Letters*, *93*(5), 2834-2846, doi:10.1785/0220210309.

Yue, H., Z. E. Ross, C. Liang, S. Michel, H. Fattahi, E. Fielding, A. Moore, Z. Liu, and B. Jia (2017). The 2016 Kumamoto Mw = 7.0 Earthquake: A Significant Event in a Fault–Volcano System, *Journal of Geophysical Research: Solid Earth*, *122*(11), 9166-9183, doi:https://doi.org/10.1002/2017JB014525.

Yue, H., Y. Zhou, S. Zhou, Y. Huang, M. Li, L. Zhou, and Z. Liu (2018). The 2017 Jiuzhaigou Earthquake Aftershock-Monitoring Experimental Network: Network Design and Signal Enhancement Algorithm, *Seismological Research Letters*, *89*(5), 1671-1679, doi:10.1785/0220180046.

Yue, H., and T. Lay (2020). Resolving Complicated Faulting Process Using Multi-Point-Source Representation: Iterative Inversion Algorithm Improvement and Application to Recent Complex Earthquakes, *Journal of Geophysical Research: Solid Earth*, *125*(2), e2019JB018601, doi:https://doi.org/10.1029/2019JB018601.

Yue, H., Z.-K. Shen, Z. Zhao, T. Wang, L. Zhao, and X. Song (2021a). A distributed shear zone near the northern margin of the Tibetan Plateau accommodates plateau expansion and growth, *(submitted)*.

Yue, H., J. Sun, M. Wang, Z. Shen, M. Li, L. Xue, W. Lu, Y. Zhou, C. Ren, and T. Lay (2021b). The 2019 Ridgecrest, California earthquake sequence: Evolution of seismic and aseismic slip on an orthogonal fault system, *Earth and Planetary Science Letters*, *570*, 117066, doi:https://doi.org/10.1016/j.epsl.2021.117066.

Yun, N., S. Zhou, H. Yang, H. Yue, and L. Zhao (2019). Automated Detection of Dynamic Earthquake Triggering by the High-Frequency Power Integral Ratio, *Geophysical Research Letters*, *46*(22), 12977-12985, doi:https://doi.org/10.1029/2019GL083913.

Zaliapin, I., and Y. Ben-Zion (2020). Earthquake Declustering Using the Nearest-Neighbor Approach in Space-Time-Magnitude Domain, *Journal of Geophysical Research: Solid Earth*, *125*(4), e2018JB017120, doi:https://doi.org/10.1029/2018JB017120.

Zhang, J., Z. Li, and J. Zhang (2023a). Simultaneous Seismic Phase Picking and Polarity Determination with an Attention-Based Neural Network, *Seismological Research Letters*, *94*(2A), 813-828, doi:10.1785/0220220247.

Zhang, L., Y. Liu, D. Li, H. Yu, and C. He (2022a). Geometric Control on Seismic Rupture and Earthquake Sequence Along the Yingxiu-Beichuan Fault With Implications for the 2008 Wenchuan Earthquake, *Journal of Geophysical Research: Solid Earth*, *127*(12), e2022JB024113, doi:https://doi.org/10.1029/2022JB024113.

Zhang, L., J. Su, W. Wang, L. Fang, and J. Wu (2022b). Deep fault slip characteristics in the Xianshuihe-Anninghe-Daliangshan Fault junction region (eastern Tibet) revealed by repeating micro-earthquakes, *Journal of Asian Earth Sciences*, *227*, 105115, doi:https://doi.org/10.1016/j.jseaes.2022.105115.

Zhang, M., W. L. Ellsworth, and G. C. Beroza (2019). Rapid Earthquake Association and Location, *Seismological Research Letters*, *90*(6), 2276-2284, doi:10.1785/0220190052.

Zhang, M., M. Liu, T. Feng, R. Wang, and W. Zhu (2022c). LOC-FLOW: An End-to-End Machine Learning-Based High-Precision Earthquake Location Workflow, *Seismological Research Letters*, *93*(5), 2426-2438, doi:10.1785/0220220019.

Zhang, P., Q. Deng, G. Zhang, J. Ma, W. Gan, W. Min, F. Mao, and Q. Wang (2003). Active tectonic blocks and strong earthquakes in the continent of China, *Science in China Series D: Earth Sciences*, *46*(2), 13-24, doi:10.1360/03dz0002.

Zhang, S., and F. Xie (2001). Seismo-Tectonic Divisions of Strong Earthquakes (MS>=7.0) and Their Tectonic Geomorphology along Xianshuihe-Xiaojiang Fault Zone, *Acta Seismologica Sinica*(01), 36-44+111.

Zhang, Y., Y. An, F. Long, G. Zhu, M. Qin, Y. Zhong, Q. Xu, and H. Yang (2021). Short-Term Foreshock and Aftershock Patterns of the 2021 Ms 6.4 Yangbi Earthquake Sequence, *Seismological Research Letters*, *93*(1), 21-32, doi:10.1785/0220210154.

Zhang, Y., X. Tang, D. Liu, T. Taymaz, T. Eken, R. Guo, Y. Zheng, J. Wang, and H. Sun (2023b). Geometric controls on cascading rupture of the 2023 Kahramanmaraş earthquake doublet, *Nature Geoscience*, *16*(11), 1054-1060, doi:10.1038/s41561-023-01283-3.

Zhao, J., Z. Jiang, A. Niu, J. Liu, Y. Wu, W. Wei, X. Liu, and W. Yan (2015). Study on dynamic characteristics of fault locking and fault slip deficit in the eastern boundary of the Sichuan-Yunnan rhombic block, *Chinese Journal Of Geophysics*, *58*(03), 872-885, doi:10.6038/cjg20150316.

Zhao, L.-F., X.-B. Xie, J.-K. He, X. Tian, and Z.-X. Yao (2013). Crustal flow pattern beneath the Tibetan Plateau constrained by regional Lg-wave Q tomography, *Earth and Planetary Science Letters*, *383*, 113-122, doi:https://doi.org/10.1016/j.epsl.2013.09.038.

Zhao, M., Z. Xiao, M. Zhang, Y. Yang, L. Tang, and S. Chen (2023). DiTingMotion: A deep-learning first-motion-polarity classifier and its application to focal mechanism inversion, *Frontiers in Earth Science*, *11*, doi:10.3389/feart.2023.1103914.

Zhong, Y., and Y. J. Tan (2024). Deep-Learning-Based Phase Picking for Volcano-Tectonic and Long-Period Earthquakes, *Geophysical Research Letters*, *51*(12), e2024GL108438, doi:https://doi.org/10.1029/2024GL108438.

Zhou, S., Z. Xu, and X. Chen (2001). Analysis On The Source Characteristics Of The 1997 Jiashi Swarm, Western China, *Chinese Journal Of Geophysics*, *44*(05), 654-662.

Zhou, Y., S. Zhou, and J. Zhuang (2018). A test on methods for MC estimation based on earthquake catalog, *Earth and Planetary Physics*, *2*(2), 150-162, doi:10.26464/epp2018015.

Zhou, Y., H. Yue, Q. Kong, and S. Zhou (2019). Hybrid Event Detection and Phase-Picking Algorithm Using Convolutional and Recurrent Neural Networks, *Seismological Research Letters*, *90*(3), 1079-1087, doi:10.1785/0220180319.

Zhou, Y., A. Ghosh, L. Fang, H. Yue, S. Zhou, and Y. Su (2021a). A High-Resolution Seismic Catalog for the 2021 Ms6.4/Mw6.1 YangBi Earthquake Sequence, Yunnan, China: Application of AI picker and Matched Filter, *Earthquake Science*, *34*(5), 390-398, doi:10.29382/eqs-2021-0031.

Zhou, Y., H. Yue, L. Fang, S. Zhou, L. Zhao, and A. Ghosh (2021b). An Earthquake Detection and Location Architecture for Continuous Seismograms: Phase Picking, Association, Location, and Matched Filter (PALM), *Seismological Research Letters*, *93*(1), 413-425, doi:10.1785/0220210111.

Zhou, Y., C. Ren, A. Ghosh, H. Meng, L. Fang, H. Yue, S. Zhou, and Y. Su (2022a). Seismological Characterization of the 2021 Yangbi Foreshock-Mainshock Sequence, Yunnan, China: More than a Triggered Cascade, *Journal of Geophysical Research: Solid Earth*, *127*(8), e2022JB024534, doi:https://doi.org/10.1029/2022JB024534.

Zhou, Y., H. Yue, S. Zhou, L. Fang, Y. Zhou, L. Xu, Z. Liu, T. Wang, L. Zhao, and A. Ghosh (2022b). Microseismicity along Xiaojiang Fault Zone (Southeastern Tibetan Plateau) and the characterization of interseismic fault behavior, *Tectonophysics*, *833*, 229364, doi:https://doi.org/10.1016/j.tecto.2022.229364.

Zhou, Y., H. Ding, A. Ghosh, and Z. Ge (2024). Construction of Long-Term Seismic Catalog with Deep Learning: A Workflow for Localized Self-Attention RNN (LoSAR). *Journal of Geophysical Research: Solid Earth (under review)*, doi:10.22541/essoar.171412572.25170940/v1.

Zhu, G., H. Yang, Y. J. Tan, M. Jin, X. Li, and W. Yang (2022a). The cascading foreshock sequence of the Ms 6.4 Yangbi Earthquake in Yunnan, China, *Earth and Planetary Science Letters*, *591*, 117594, doi:https://doi.org/10.1016/j.epsl.2022.117594.

Zhu, J., Z. Li, and L. Fang (2022b). USTC-Pickers: a Unified Set of seismic phase pickers Transfer learned for China, *Earthquake Science*, *36*, 1-11.

Zhu, L., and L. A. Rivera (2002). A note on the dynamic and static displacements from a point source in multilayered media, *Geophysical Journal International*, *148*(3), 619-627, doi:10.1046/j.1365-246X.2002.01610.x.

Zhu, L., Z. Peng, J. McClellan, C. Li, D. Yao, Z. Li, and L. Fang (2019). Deep learning for seismic phase detection and picking in the aftershock zone of 2008 Mw7.9 Wenchuan Earthquake, *Physics of the Earth and Planetary Interiors*, *293*, 106261, doi:https://doi.org/10.1016/j.pepi.2019.05.004.

Zhu, W., and G. C. Beroza (2018). PhaseNet: a deep-neural-network-based seismic arrival-time picking method, *Geophysical Journal International*, *216*(1), 261-273, doi:10.1093/gji/ggy423.

Zhu, W., A. B. Hou, R. Yang, A. Datta, S. M. Mousavi, W. L. Ellsworth, and G. C. Beroza (2022c). QuakeFlow: a scalable machine-learning-based earthquake monitoring workflow with cloud computing, *Geophysical Journal International*, *232*(1), 684-693, doi:10.1093/gji/ggac355.

Zhu, W., I. W. McBrearty, S. M. Mousavi, W. L. Ellsworth, and G. C. Beroza (2022d). Earthquake Phase Association Using a Bayesian Gaussian Mixture Model, *Journal of Geophysical Research: Solid Earth*, *127*(5), e2021JB023249, doi:https://doi.org/10.1029/2021JB023249.

Zhuang, J., Y. Ogata, and D. Vere-Jones (2002). Stochastic Declustering of Space-Time Earthquake Occurrences, *Journal of the American Statistical Association*, *97*(458), 369-380.

Ziv, A., and A. M. Rubin (2000). Static stress transfer and earthquake triggering: No lower threshold in sight?, *Journal of Geophysical Research: Solid Earth*, *105*(B6), 13631-13642, doi:https://doi.org/10.1029/2000JB900081.